MODELING DEFORMATIONS IN VISCOELASTIC MATERIALS UNDERGOING MICROSTRUCTURAL CHANGES DUE TO MECHANICAL STIMULUS

A Dissertation

by

RUYUE SONG

Submitted to the Office of Graduate and Professional Studies of
Texas A&M University
in partial fulfillment of the requirements for the degree of

DOCTOR OF PHILOSOPHY

Chair of Committee,	Anastasia Muliana
Committee Members,	Alan Freed
	Matt Pharr
	Jean-Briac le Graverend
Head of Department,	Andreas A. Polycarpou

December 2020

Major Subject: Mechanical Engineering

ABSTRACT

This study presents a thermodynamics framework for describing responses of viscoelastic materials undergoing microstructural changes when exposed to mechanical loadings. The constitutive models are derived based on multiple natural configuration theory, in order to accommodate the evolution of the material microstructures in a simplistic way. Within the multiple natural configuration theory, the microstructures of such materials are assumed to evolving between different stress-free natural configurations. In this study, two natural configurations are considered, i.e., the initial natural configuration which is associated with the microstructures at original state where no external stimuli are applied, and the final configuration which is associated with the microstructures where all possible microstructural changes are completed. Therefore, the net effect of any possible microstructural changes, can be incorporated into the constitutive model using an internal state variable, which quantifies percent amount of microstructural changes. Within the thermodynamics framework, a three-dimensional constitutive model is developed for polyoxymethylene (POM) polymer, as an example for viscoelastic homogeneous material. As an additional application, with plant tissue as an example, constitutive model is developed to predict the responses of general anisotropic and heterogeneous viscoelastic materials. Furthermore, the constitutive model is modified to describe responses of POM polymer and glass fiber reinforced polyamide (PA6GF40), under different mechanical loading histories and isothermal temperatures. Elevated temperatures accelerate the microstructural changes in the viscoelastic polymers, which are captured by the model. Mechanical responses of POM polymer, plant tissue and PA6GF40 composite, such as quasi-static, creep, cyclic, are simulated and validated by comparing the simulated responses with experimental data. With a relatively small number of material parameters,

the thermodynamically consistent models are capable of predicting the mechanical responses of viscoelastic materials undergoing microstructural changes. The multiple natural configurations based constitutive models are also computationally efficient, which makes them suitable for performing large scale structural analyses. As an application of the multiple natural configuration approach, structural analyses within shell finite element method are performed for a bilayer polymer comprising of different polymer constituents, e.g., elastic, viscoelastic, electro-active polymer, and light activated shape memory polymer (LASMP).

ACKNOWLEDGEMENTS

Upon the completion of my dissertation, I would like to express my deepest gratitude to all professors, colleagues, families and friends who guided and supported me through this endeavor.

First and foremost, I would like to express my sincere gratitude to my advisor Dr. Muliana, who guided and encouraged me through seven years of graduate education. Her motivation and enthusiasm always encourage me to keep pursuing higher goals, and will keep encourage me in life after graduation. Her patience, knowledge and continuous support made every second of my graduate study enjoyable. Also, I would like to thank the professors who serves in my dissertation committee: Professor Alan Freed, Professor Matt Pharr and Professor Jean-Briac le Graverend, for their insightful comments, continuous support and encouragement.

My sincere thanks also go to my classmates and labmates during my study at Texas A&M University. A special thanks to Junwei and Vahid, who help me a lot in the beginning of my study. I also would like to thank Yiming, Jian, Omid and Zaryab, who provide encouragement, support and friendship during my endeavor, and making my time at Texas A&M a great experience.

Finally, thanks to my parents, for their selfless and endless support financially and emotionally. Without their love I could never accomplish anything I have. I would like to thank my husband for his encouragement, patience and love.

CONTRIBUTORS AND FUNDING SOURCES

Contributors

This work was supervised by a dissertation committee consisting of Professor Anastasia Muliana and Professor Alan Freed, Professor Matt Pharr of the Department of Mechanical Engineering and Professor Jean-Briac le Graverend of the Department of Aerospace Engineering.

The experimental tests presented in Chapter IV and Chapter V were provided by Dr. Michael Berrer's group at the Polymer Competence Center Leoben (PCCL) Austria. The implementations of co-rotational finite element method in MATLAB in Chapter VI were conducted in part by Vahid Tajeddini of the Department of Mechanical Engineering and were published in 2017.

All other work conducted for the dissertation was completed by the student independently.

Funding Sources

This work was also made possible in part by the Air Force Office of Scientific Research (AFOSR) under Grant Number FA9550-14-1-0234, and the National Science Foundation (NSF) under Grant Number CMMI-1437086 and Grant Number CMMI 1761015.

TABLE OF CONTENTS

Page

LIST OF FIGURES

Page

LIST OF TABLES

Page

CHAPTER I

INTRODUCTION

The macroscopic response of materials when exposed to external stimuli (mechanical, thermal, electrical, etc.) is a manifestation of continuous changes in the microstructures of the materials. For example, when exposed to mechanical loadings, the long-chains of polymer networks can rearrange, reorient, break, slip, etc., leading to nonlinear and time-dependent mechanical responses. Depending on the extent of the prescribed stimuli, the microstructural changes can be permanent, i.e., upon removal of the external stimuli the materials do not regain their original microstructures and hence at the macroscopic scale permanent sets are observed accompanied by hysteretic responses. Figure 1 illustrates examples of mechanical responses of polyoxymethylene (POM) polymer under creep-recovery at different stress amplitude and holding time, indicating viscoelastic response (Song et al. [1]). At a relatively small stress and short-term loading, the polymer shows nearly fully recovery response upon removal of the stress and no apparent residual strain is observed. The corresponding hysteretic response is associated with the rearrangement of the polymer macromolecular networks, which is a dissipative process. Since POM is a semi-crystalline polymer, the deformation at this stage is due to straining of molecular chains of the interlamellar amorphous phase and rotation of lamellae stacks [2]. At a relatively large stress and long-term loading, the polymer undergoes more pronounced creep and hence upon removal of the load, residual strain is observed. The permanent deformation is associated with cavitation of the amorphous phase and fragmentation of the crystalline phase. As expected more severe loading conditions yield to more pronounced hysteretic area, indicating more energy being dissipated. In general, microstructural changes in polymers when subjected to a mechanical stimulus can take

place due to purely macromolecular reconfiguration without rupturing the molecular networks and from a chemorheological aspect, such as scission, crazing, fragmentation, etc.

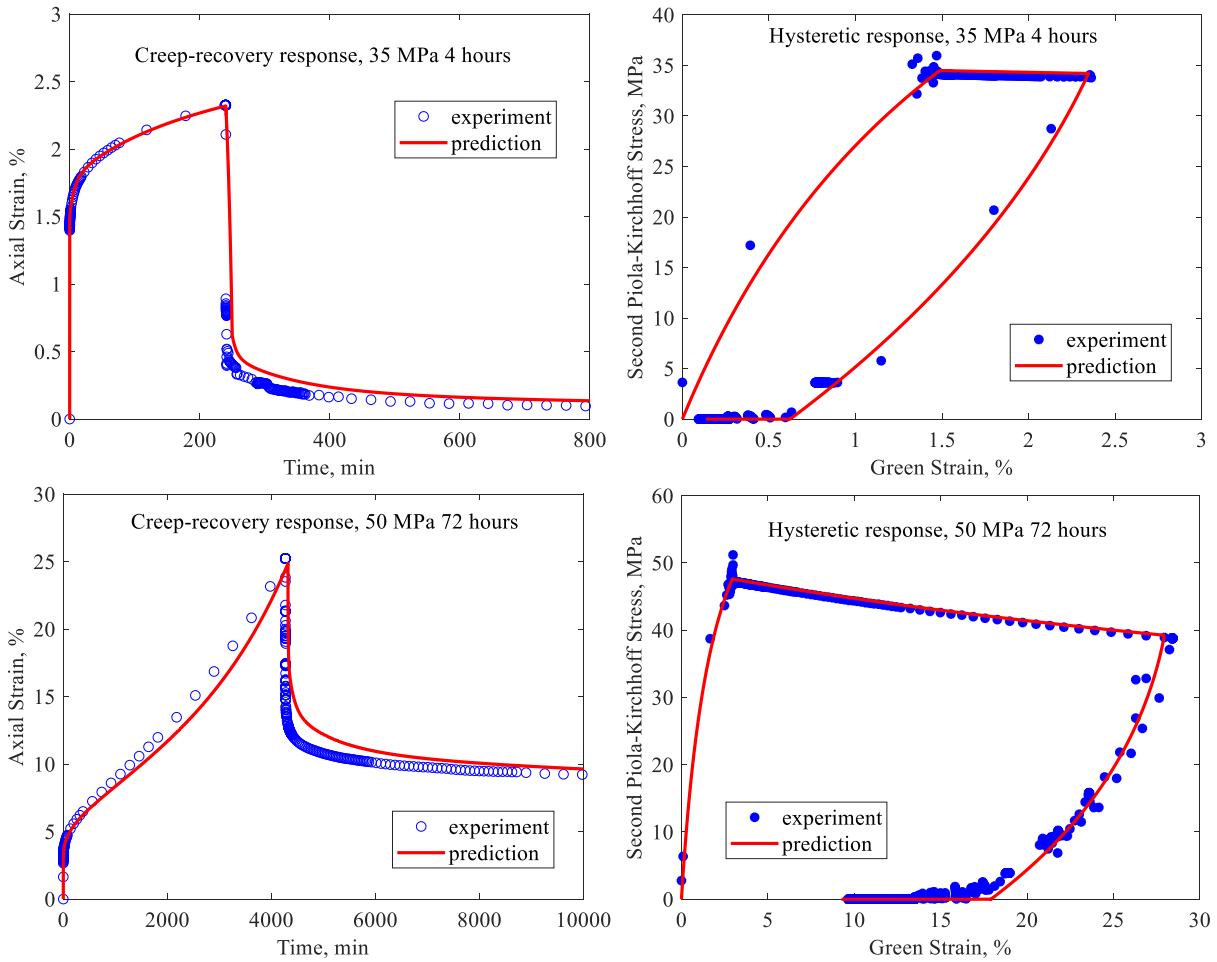

Figure 1 Creep-recovery responses of POM polymers and their corresponding hysteretic responses

Having said that deformations in materials generally present new material micro-mechanisms which affect the mechanical responses of these materials, and hence at the macroscopic scale hysteresis responses are observed. Many materials can exhibit significant microstructural changes when subjected to external stimuli, such as plastic deformations [3, 4], stimulus-responsive polymers [5], ferroelectric and ferromagnetic materials [6, 7], biological materials [8, 9], etc.

This study presents a thermodynamics framework for viscoelastic materials undergoing microstructural changes when exposed to mechanical loadings. The models are derived based on a multiple natural configuration theory in order to accommodate the evolution of the material microstructures in a simplistic way. In this study, the natural configuration is considered as a stress free configuration of the materials. The models are also extended to incorporate the heat generation due to energy dissipation from the microstructural changes. The accumulated heat generation can yield to significant increases in temperatures of the materials, and thus influence the mechanical responses of the materials. In order to demonstrate the ability of the models in describing the mechanical responses of materials undergoing microstructural changes, experimental data on POM polymers and plant cell walls are used.

1.1. Current Studies on the Modeling of Materials with Hysteresis Behaviors

Hysteresis behaviors can be widely observed in materials undergoing deformations due to mechanical and non-mechanical stimuli. Polymers and metals are common examples of materials which exhibit hysteresis behaviors when subjected to mechanical loadings. There have been many phenomenological models developed to predict the hysteresis behaviors of materials, such as the plastic and/or viscoplastic models for metals [10, 11] and viscoelastic models for polymers [12-15]. These phenomenological models are often expressed in general differential or integral form, and they are generally capable in capturing response of materials under various loading history. These types of constitutive models often lead to mathematical complexity, which often require numerical methods to determine their responses. Another approach in modeling response of materials is by using empirical models, where the mathematical functions and their corresponding material parameters are obtained from observing the experimental data. Such constitutive models

can also incorporate the effect of microstructural changes (diffusional transport by dislocation, dislocation climb and glide, grain boundary sliding, etc.) in order to describe the macroscopic constitutive models for materials. Examples of such models can be found in Amin et al. [16], Sherby and Weertman [17], Frost et al. [18], Gabb and Welsch [19], Orlova [20], etc. By considering dominant mechanism of microstructural changes under different loading conditions, deformation-mechanism maps can be constructed [18] [21]. Deformation-mechanism maps are very useful for engineering applications, especially for material selection and life prediction, due to the simplicity in the implementation of empirical models. However, the accuracy and ability of the empirical models are often limited to fixed loading conditions.

In this research, constitutive material models incorporating microstructural changes are formulated for viscoelastic materials. The model is based on a multiple natural configuration approach, which is discussed below. As the body undergoes deformations, its natural configuration also changes corresponding to the newly formed microstructures. There have been many constitutive models formulated for mathematically describing the viscoelastic response of polymers, as documented by Green and Rivlin [22], Findley et al. [13], Pipkin [14], Christensen [15], Wineman [23], De Pascalis et al. [24], etc. Most of these models assume a viscoelastic body to have one natural configuration associated with it and ignore the effect of microstructural changes, and these models predict full recovery of the specimens upon unloading and after sufficient recovery time. In order to describe the permanent deformations observed in materials, many viscoplastic models have been considered (De Souza Neto et al. [25], Lubliner [26], Chaboche [27]). These models suggest that the character of the response changes dramatically due to changes in the underlying microstructure of the body, after the loading reaches a critical threshold. For example, before the threshold is reached the material might behave elastically (does not dissipate

any energy), and once the threshold is reached the material behavior changes to that of an inelastic body (dissipating energy). Another approach to mathematically describe the hysteretic and permanent deformation behaviors in materials is by introducing damage parameters, and the material properties change with the damage parameters [28-30]. In both viscoplastic and damage motivated models, a variety of damage parameters and criteria based on them are often necessary to capture responses of materials at various stages of loading-unloading histories.

Microstructure-based models which analyze the macromolecular network structure of the material have been developed to simulate the time-dependent inelastic responses for polymers. Tobolsky et al. [31] modeled the relaxation of rubberlike materials by considering the rupture of networks with long-chain molecules. Similar ideas can also be found from Andrews et al. [32], Leaderman [33], Wineman and Shaw [34, 35], etc. Arruda and Boyce [36] proposed an eight chain model by describing the cooperative nature of polymer network deformation. In their research, the deformation of rubber is related to the orientation of molecular chain. The evolution of molecular chain is incorporated into the constitutive model through a material parameter which represents the limitation of chain extensibility. Similar constitutive models for rubber-like materials can also be found from Wu and Van Der Giessen [37], Nguyen et al. [38] and Kuhl et al. [39]. Thermodynamically-based constitutive models also have been developed to simulate the hysteresis responses of polymers [40, 41]. In the model proposed by Krairi and Doghri, constitutive relations are developed from the thermodynamics of irreversible processes. The rate of energy dissipation during irreversible processes is expressed as the difference between input power and Helmholtz free energy, which accounts for the dissipations due to viscoelasticity, viscoplasticity, and damage. In their model, the total strain is decomposed into the viscoelastic and viscoplastic (irreversible) parts. The constitutive relation between stress and viscoelastic strain is obtained from the second

law of thermodynamics, where the rate of dissipation due to viscoelastic deformation has to be nonnegative. The viscoplastic (irreversible) part of strain is calculated from evolution laws in a manner similar to the simulation for the plastic deformation.

1.2. Multiple Natural Configuration Theory

Another approach to model macroscopic responses of materials undergoing microstructural changes is based on a multiple natural configuration approach. Within the multiple natural configuration approach, the macroscopic response naturally evolves with the continuous changes in the microstructures, and therefore it does not require defining different mathematical expressions associated with different phenomena (e.g., elastic, plastic, damage, etc.) in order to describe different responses at various loading stages. The approach incorporates the net effect of various microstructural changes in materials without precisely modeling the detailed microstructural changes. Thus, the model can be directly correlated to the macroscopic experimental data, which represent the net (overall) response of materials. The idea of multiple natural configuration approach was introduced by Rajagopal and coworkers in 1990s [4, 42]. The actual microstructural changes in materials when exposed to external stimuli can be very complex, and might be impossible to analyze in great detail by incorporating all possible deformation mechanisms experienced by the microstructures. Within the multiple natural configuration theory, the microstructural changes are incorporated into the constitutive model by using internal state variables which indicate the evolution between different configurations. The multiple natural configuration approach was initially developed to model twinning of polycrystalline metals [43-45]. During twinning, the material possesses two stress-free configurations, the original configuration which corresponding to untwined material and the final configuration corresponding

to fully twinned material. Then at intermediate state, the partially twinned configuration can be modeled as the juxtaposition of the original and final natural configurations [45]. Recently, the idea of multiple natural configuration has been extended to describe other material behaviors, such as viscoelastic fluid [22, 46, 47], shape memory alloys and shape memory polymers [48-50], piezoelectric composites [51, 52], Mullins effect in rubberlike materials [53], and even the growth of tumor [54]. The multiple natural configuration approach is very promising for simulation applications in solid mechanics, fluid mechanics and biomechanics fields.

1.3. Research Objectives and Scope

The scope of this study is to formulate a thermodynamic framework in order to describe the macroscopic responses of viscoelastic materials undergoing microstructural changes when subjected to various mechanical loadings. The constitutive models are developed base on the theory of multiple natural configuration. In order to recognize that the natural configurations associated with a body could evolve due to external stimuli consider a polymer under uniaxial tension (Figure 2). The natural configuration of the body is the configuration that the polymeric body takes in the absence of any mechanical stimuli. In this study, the natural configuration is considered as a stress-free configuration. When the polymer is deformed so that its configuration lies outside the domain of elastic response, say the state O', then upon unloading the polymer will display a response that is different from the original elastic response. Thus, when unloaded from the states denoted by A', B', and C', the body will tend to the associated with the natural configurations corresponding to the body at the states A', B', and C', etc., namely the configurations corresponding to the states A, B, and C. The response from these natural configurations being different from the original elastic response as well as possibly from each

other. As will be discussed later, within the multiple natural configuration approach, the macroscopic response naturally evolves with the continuous changes in the microstructures, and therefore it does not require defining different mathematical expressions associated with different phenomena (e.g., elastic, plastic, damage, etc.) in order to capture the entire loading histories.

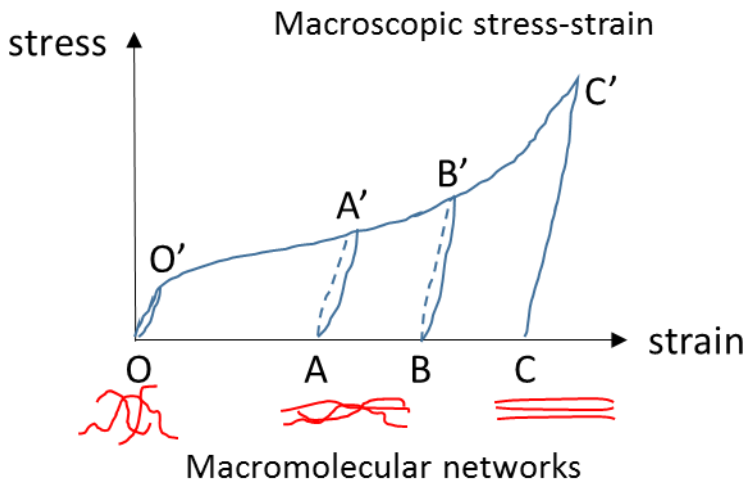

Figure 2 An illustration of multiple natural configurations

The research objectives are:

1. Formulate constitutive models for viscoelastic materials undergoing microstructural changes when subjected to mechanical loadings. The models will be used to describe the macroscopic response of POM polymers (Chapter 2) and plant cell walls, which have polymers as building blocks (Chapter 3), under various histories of mechanical loadings. In Chapter 2 the formulation and prediction are discussed for a homogenous material, while in Chapter 3 the model is extended for heterogeneous material.
2. Extend the viscoelastic constitutive model to include the temperature effect. The process of microstructural changes dissipates energy, which will cause temperature increases in the materials, and hence affecting the properties of materials. Once formulated, the framework

with thermo-viscoelastic behaviors can be used to study cyclic and fatigue behaviors in materials.

3. Implement the above models within finite element analyses, which will be used to analyze responses of structures under various boundary conditions and loading histories.

CHAPTER II

A THERMODYNAMICS FRAMEWORK FOR VISCOELASTIC ISOTROPIC HOMOGENEOUS MATERIALS[*]

A three-dimensional constitutive model is formulated for materials undergoing microstructural changes due to prescribed mechanical loading. The model is used to describe responses of POM polymers. Under external stimuli, the material deforms, and the microstructure of the material evolves from its original natural configuration to a different (new) natural configuration where all microstructural change has completed, i.e., all macromolecular chains in polymers are broken. Material parameters for the two natural configurations are calibrated from creep responses at different stress levels. The amount of new network being generated, i.e., the amount of broken macromolecular chain, is considered as an internal state variable that describes the evolution of the natural configurations. The simulation gives reasonable predictions when compared with quasi-static and creep test data. The constitutive model, the characterization of material parameters, and the simulation results are presented in this chapter.

2.1. Constitutive Model

In this section, a constitutive model to describe the viscoelastic response of a body that accounts for the effect of microstructural changes in the polymer networks on the overall (macroscopic) response of polymers is presented. The model is derived within the context of a multiple natural configuration approach. It is assumed that due to mechanical loading, the polymer microstructures

[*] Reprinted with permission from "A thermodynamically consistent model for viscoelastic polymers undergoing microstructural changes" by Song, R., Muliana, A., & Rajagopal, K, 2019. International Journal of Engineering Science, 142, 106-124, Copyright [2019] by Elsevier.

are evolving between two natural configurations, which are stress free. The first (original) configuration is associated with the initial microstructures of the polymer, and the second (final) configuration is associated with the configuration that corresponds to the situation after complete microstructural changes have taken place (no more macromolecular chains are put into place). The polymers under consideration are in the glassy state, and thus small deformation gradient problems are considered. However, the materials still can exhibit nonlinear viscoelastic responses, which are incorporated in the nonlinear constitutive equations. The linearized strain is given by the expression $\boldsymbol{\varepsilon} = \frac{1}{2}\left(\frac{\partial \mathbf{u}}{\partial \mathbf{X}} + \left(\frac{\partial \mathbf{u}}{\partial \mathbf{X}} \right)^{T} \right)$, where $\mathbf{u} = \mathbf{x} - \mathbf{X}$ is the displacement and $\mathbf{x} = \chi\left(\mathbf{X}, t\right)$ is the motion of a particle that is at $\mathbf{X}$ in a stress-free reference configuration.

To recapitulate, the body in question, in general, is assumed to be comprised of two components, each with a different microstructure (a two-network polymer each network possessing a distinct microstructure). Initially, the body consists in just one network and as the deformation proceeds the network junctions of the polymer break and a new network comes into being. Each of these networks has its own "natural configuration". Each of these networks has two distinct energy storage mechanisms and also has an energy dissipation mechanism. The purely elastic response of the network is denoted with subscript (E) and the one that is capable of both storing and dissipating energy will be denoted with a subscript (VS) to express the fact that it is a viscoelastic network.

The Gibbs free energy associated with the body as a whole, consisting in both the networks, is of the following form:

$$G = G(\boldsymbol{\sigma}_{(VS)_E}, \boldsymbol{\sigma}_E, \alpha) = G_1(\boldsymbol{\sigma}_{(VS)_E}, \alpha) + G_2(\boldsymbol{\sigma}_E, \alpha) \tag{1}$$

where $\boldsymbol{\sigma}$ is the stress tensor and α is a scalar parameter that takes the value between 0 and 1, that is a measure of the microstructural changes that has been undergone by the original material. While it could be thought of as the mass fraction of the new network present it could also be viewed as a parameter that is a measure of a type of microstructure[1]. When α=0, the response of the polymer is comprised that of only with the original network, and for α=1 the response is only due to the final (newly formed) network. That is, the Gibbs potential associate with the original network is $G(\boldsymbol{\sigma}_{(VS)_E}, \boldsymbol{\sigma}_E, 0)$ and that of the new network is $G(\boldsymbol{\sigma}_{(VS)_E}, \boldsymbol{\sigma}_E, 1)$. The function $G(\boldsymbol{\sigma}_{(VS)_E}, \boldsymbol{\sigma}_E, \alpha)$ need not necessarily be a linear function of α.

The Helmholtz free energy per unit volume and its rates are:

$$\psi = G - \frac{\partial G}{\partial \boldsymbol{\sigma}_{(VS)_E}} \bullet \boldsymbol{\sigma}_{(VS)_E} - \frac{\partial G}{\partial \boldsymbol{\sigma}_E} \bullet \boldsymbol{\sigma}_E \tag{2}$$

$$\dot{\psi} = \frac{\partial G}{\partial \alpha}\dot{\alpha} - \frac{d}{dt}\left(\frac{\partial G}{\partial \boldsymbol{\sigma}_{(VS)_E}}\right) \bullet \boldsymbol{\sigma}_{(VS)_E} - \frac{d}{dt}\left(\frac{\partial G}{\partial \boldsymbol{\sigma}_E}\right) \bullet \boldsymbol{\sigma}_E \tag{3}$$

As a result of microstructural changes, permanent deformations can occur in the materials upon unloading. As we shall be concerned with problems involving small strains, we shall assume an additive decomposition of the total strain:

$$\boldsymbol{\varepsilon} = \boldsymbol{\varepsilon}_{(VS)} + \boldsymbol{\varepsilon}_E + \boldsymbol{\varepsilon}_P \tag{4}$$

where $\boldsymbol{\varepsilon}_P$ is the permanent strain that would depend on the microstructural changes ($\boldsymbol{\varepsilon}_P = \mathbf{0}$ when α=0), and $\boldsymbol{\varepsilon}_E = -\frac{\partial G}{\partial \boldsymbol{\sigma}_E}$. Also, $\boldsymbol{\varepsilon}_{(VS)_E} = -\frac{\partial G}{\partial \boldsymbol{\sigma}_{(VS)_E}}$. Using the linearized strain as a measure of the

[1] The multiple natural configuration approach incorporates the net effect of microstructural changes in polymers, which could be associated with various phenomena such as network reconfiguration, scission, fragmentation, etc. However, in case a single dominant physical mechanism of polymer macromolecular changes due to mechanical loading can be identified, e.g., scission, the internal state variable α can be used to represent a fractional change of such specific physical mechanism.

deformation and then assuming that such strains are additive needs some justification. The classical model for linear viscoelastic response[2] uses the linearized strain as a measure and this model is often misused in situations wherein the displacement gradients are not small and thus the nonlinear part of the strain cannot be ignored. In the problem that we are considering, the error in neglecting the nonlinearities in the deformation gradients is approximately 11% for the axial strain level of 25%, however as the simplification that such an assumption offers is tremendous we use the linearized strain as the measure of deformation in carrying out our analysis. A detailed discussion of the nature and consequences of such an approximation is provided in the following section concerning the implementation of the constitutive model.

With regard to the viscoelastic components, we have the elastic recovery (subscript $(VS)_E$) and dissipative (subscript $(VS)_D$) parts:

$$\boldsymbol{\varepsilon}_{VS} = \boldsymbol{\varepsilon}_{(VS)_E} = \boldsymbol{\varepsilon}_{(VS)_D} \tag{5}$$

where

$$\boldsymbol{\varepsilon}_{(VS)_E} = -\frac{\partial G}{\partial \boldsymbol{\sigma}_{(VS)_E}} \rightarrow -\frac{d}{dt}\left(\frac{\partial G}{\partial \boldsymbol{\sigma}_{E}}\right) = \dot{\boldsymbol{\varepsilon}}_{(VS)_E} = \dot{\boldsymbol{\varepsilon}}_{(VS)} \tag{6}$$

The stress borne by the elastic element is given by:

$$\boldsymbol{\sigma} = \boldsymbol{\sigma}_E \tag{7}$$

and within the viscoelastic solid component, we have

$$\boldsymbol{\sigma}_{VS} = \boldsymbol{\sigma}_{(VS)_E} + \boldsymbol{\sigma}_{(VS)_D} \tag{8}$$

Next, we define the rate of mechanical dissipation through:

[2] The classical linear viscoelastic model should be rightly referred to as the classical linearized viscoelastic model as the strain that is used is the linearized strain. Thus, in keeping with linearized elasticity the linear viscoelastic model is not frame indifferent. It is an approximation that only holds for small strains though it is used indiscriminately for large strains.

$$\xi = \boldsymbol{\sigma}\dot{\boldsymbol{\varepsilon}} - \dot{\psi} \tag{9}$$

As a consequence of Eqs. (3), (4), and (6), Eq. (9) yields:

$$\xi = \left(\boldsymbol{\sigma} - \boldsymbol{\sigma}_{(VS)_E}\right)\dot{\boldsymbol{\varepsilon}}_{(VS)_E} + \boldsymbol{\sigma}\dot{\boldsymbol{\varepsilon}}_P - \frac{\partial G}{\partial \alpha}\dot{\alpha} = \boldsymbol{\sigma}_{(VS)_D}\dot{\boldsymbol{\varepsilon}}_{(VS)_D} + \boldsymbol{\sigma}\dot{\boldsymbol{\varepsilon}}_P - \frac{\partial G}{\partial \alpha}\dot{\alpha} = \xi_D + \boldsymbol{\sigma}\dot{\boldsymbol{\varepsilon}}_P - \frac{\partial G}{\partial \alpha}\dot{\alpha} \tag{10}$$

As mentioned above, the permanent strain $\boldsymbol{\varepsilon}_P$ should depend on α, and thus, Eq. (10) can be rewritten as:

$$\xi = \xi_D + \left(\boldsymbol{\sigma}\frac{\partial \boldsymbol{\varepsilon}_P}{\partial \alpha} - \frac{\partial G}{\partial \alpha}\right)\dot{\alpha} = \xi_D + F_\alpha \dot{\alpha} \tag{11}$$

We assume the following function for the Gibbs potential for the problem under consideration:

$$\begin{aligned} G_1\left(\boldsymbol{\sigma}_{(VS)_E}, \alpha\right) &= -\left[\left(1-\alpha\right)\left(\frac{A_1}{2} I^2_{(VS)_E} + B_1 II_{(VS)_E}\right) + \alpha\left(\frac{A_2}{2} I^2_{(VS)_E} + B_2 II_{(VS)_E}\right)\right] \\ G_2\left(\boldsymbol{\sigma}_E, \alpha\right) &= -\left[\left(1-\alpha\right)\left(\frac{C_1}{2} I^2_E + D_1 II_E\right) + \alpha\left(\frac{C_2}{2} I^2_E + D_2 II_E\right)\right] \end{aligned} \tag{12}$$

where I and II are the first and second invariants associated with the stress of the viscous and elastic stress components, i.e.,

$$\begin{aligned} I_{(VS)_E} &= \mathrm{tr}(\boldsymbol{\sigma}_{(VS)_E}); \quad II_{(VS)_E} = \frac{1}{2}\mathrm{tr}\left(\boldsymbol{\sigma}_{(VS)_E}\right)^2 \\ I_E &= \mathrm{tr}(\boldsymbol{\sigma}_E); \quad II_E = \frac{1}{2}\mathrm{tr}\left(\boldsymbol{\sigma}_E\right)^2 \end{aligned} \tag{13}$$

and the parameters A, B, C, and D are the material parameters associated with the initial (subscript '*1*') and final (subscript '*2*') configurations. In this study, as will be demonstrated later, the instantaneous response of the POM polymer cannot be captured by a relation as in Eq. (12), and therefore we modify the second form of the Gibbs potential as:

$$\begin{aligned} G_2\left(\boldsymbol{\sigma}_E, \alpha\right) = -\left(1-\alpha\right)\left(C_1\left(\frac{e^{\beta^i I_E}}{\beta^i} - I_E\right) + D_1\left(\frac{e^{\delta^i\sqrt{2II_E}}}{\delta^i} - \sqrt{2II_E}\right)\right) - \\ \alpha\left(C_2\left(\frac{e^{\beta^f I_E}}{\beta^f} - I_E\right) + D_2\left(\frac{e^{\delta^f\sqrt{2II_E}}}{\delta^f} - \sqrt{2II_E}\right)\right) \end{aligned} \tag{14}$$

We further consider the following form for the rate of mechanical dissipation in Eq. (10):

$$\xi_D = (1-\alpha)\mathbf{K_1}\boldsymbol{\sigma}_{(VS)_D}.\boldsymbol{\sigma}_{(VS)_D} + \alpha\mathbf{K_2}\boldsymbol{\sigma}_{(VS)_D}.\boldsymbol{\sigma}_{(VS)_D} \tag{15}$$

where **K** is a fourth order tensor associated with the viscosity of the material. Further confining our study to isotropic materials, Eq. (15) can be written as:

$$\xi_D = (1-\alpha)\left[\frac{\lambda_1}{2} I^2_{(VS)_D} + \eta_1 II_{(VS)_D}\right] + \alpha\left[\frac{\lambda_2}{2} I^2_{(VS)_D} + \eta_2 II_{(VS)_D}\right] \tag{16}$$

where λ and η are material parameters associated with the viscosity of the polymer and $I_{(VS)_D}$, $II_{(VS)_D}$ are the first and second invariants of $\boldsymbol{\sigma}_{(VS)_D}$.

The elastic strains associated with the two networks can be obtained from either Eq. (12) or (14). Eq. (12) gives the following relation for isotropic materials:

$$\boldsymbol{\varepsilon}_{(VS)_E} = -\frac{\partial G}{\partial \boldsymbol{\sigma}_{(VS)_E}} = (1-\alpha)\left[A_1 I_{(VS)_E}\mathbf{I} + B_1\boldsymbol{\sigma}_{(VS)_E}\right] + \alpha\left[A_2 I_{(VS)_E}\mathbf{I} + B_2\boldsymbol{\sigma}_{(VS)_E}\right] \tag{17}$$

$$\boldsymbol{\varepsilon}_E = -\frac{\partial G}{\partial \boldsymbol{\sigma}_E} = (1-\alpha)\left[C_1 I_E\mathbf{I} + D_1\boldsymbol{\sigma}_E\right] + \alpha\left[C_2 I_E\mathbf{I} + D_2\boldsymbol{\sigma}_E\right] \tag{18}$$

It is seen from Eq. (18) that for a linear elastic isotropic material, we have the following relations $C_1 = -\frac{\nu}{E^i}, D_1 = \frac{1+\nu}{E^i}, C_2 = -\frac{\nu}{E^f}, D_2 = \frac{1+\nu}{E^f}$ and E and ν are the instantaneous elastic modulus and Poisson's ratio, respectively. The above parameters can also vary with α. The superscripts '*i*' and '*f*' denote the properties corresponding to the initial and final configurations, respectively. The potential in Eq. (14) results in

$$\begin{aligned}\boldsymbol{\varepsilon}_E = -\frac{\partial G}{\partial \boldsymbol{\sigma}_E} = (1-\alpha)&\left[C_1\left(e^{\beta^i I_E} - 1\right)\mathbf{I} + D_1\left(\frac{e^{\delta^i\sqrt{2II_E}} - 1}{\sqrt{2II_E}}\right)\boldsymbol{\sigma}_E\right] + \\ \alpha&\left[C_2\left(e^{\beta^f I_E} - 1\right)\mathbf{I} + D_2\left(\frac{e^{\delta^f\sqrt{2II_E}} - 1}{\sqrt{2II_E}}\right)\boldsymbol{\sigma}_E\right]\end{aligned} \tag{19}$$

Muliana et al. [55] used a nonlinear constitutive form presented in Eq. (19) for polymers in the absence of microstructural changes, i.e., $\boldsymbol{\varepsilon}_E = C\left(e^{\beta I_E}-1\right)\mathbf{I} + D\left(\frac{e^{\delta\sqrt{2II_E}}-1}{\sqrt{2II_E}}\right)\boldsymbol{\sigma}_E$, and they showed that upon linearization, the model reduces to a linear elastic response, $\boldsymbol{\varepsilon}_E = C\beta I_E\mathbf{I} + D\delta\boldsymbol{\sigma}_E$, where $C\beta = -\frac{\nu}{E}$, $D\delta = \frac{1+\nu}{E}$ and E and ν are the elastic modulus and Poisson's ratio, respectively. From the first and second terms of the right hand side of the rate of mechanical dissipation in Eq. (16), we can obtain the rate of strain associated with the viscoelastic responses:

$$\dot{\boldsymbol{\varepsilon}}_{(VS)} = \dot{\boldsymbol{\varepsilon}}_{(VS)_E} = \alpha\left[\lambda_2 I_{(VS)_D}\mathbf{I} + \eta_2\boldsymbol{\sigma}_{(VS)_D}\right] + (1-\alpha)\left[\lambda_1 I_{(VS)_D}\mathbf{I} + \eta_1\boldsymbol{\sigma}_{(VS)_D}\right] \tag{20}$$

When the above relations are considered for the viscoelastic constitutive model for the isotropic materials discussed above, we have six material parameters (A, B, C, D, λ, η) for each configuration. It is noted that the above material parameters have physical interpretation, corresponding to the compliance and inverse of viscosity of the polymers. This illustrates that the macroscopic properties, i.e., moduli and viscosity, of materials are associated with the microstructural configuration of the materials. Altering the microstructural configurations in the materials, due to either processing or exposure to external stimuli, will result in different macroscopic properties, as should be expected.

In dealing with viscoelastic response, more than one final component is often considered, especially when describing the long-term response of materials. In such a situation, the Gibbs potential $G_1\left(\boldsymbol{\sigma}_{(VS1)_E}, \boldsymbol{\sigma}_{(VS2)_E}, ...\boldsymbol{\sigma}_{(VSM)_E}\right)$ and the rate of dissipation $\xi_D\left(\boldsymbol{\sigma}_{(VS1)_D}, \boldsymbol{\sigma}_{(VS2)_D}, ...\boldsymbol{\sigma}_{(VSM)_D}\right)$ can be modified to include additional networks in the viscoelastic components, such as:

$$G_1\left(\boldsymbol{\sigma}_{(VS)_E}, \alpha\right) = -\sum_{m=1}^{M}\left[(1-\alpha)\left(\frac{A_{1m}}{2}I^2_{(VS)_E} + B_{1m}II_{(VS)_E}\right) + \alpha\left(\frac{A_{2m}}{2}I^2_{(VS)_E} + B_{2m}II_{(VS)_E}\right)\right] \tag{21}$$

$$\xi_D = \sum_{m=1}^{M} \alpha \left[\frac{(\lambda_2)_m}{2} I^2_{(VSm)_D} + (\eta_2)_m II_{(VSm)_D} \right] + (1-\alpha) \left[\frac{(\lambda_1)_m}{2} I^2_{(VSm)_D} + (\eta_1)_m II_{(VSm)_D} \right] \quad (22)$$

Consequently, the strain associated with the viscoelastic component and its rate are:

$$\boldsymbol{\varepsilon}_{(VS)_E} = -\sum_{m=1}^{M} \frac{\partial G}{\partial \boldsymbol{\sigma}_{(VSm)_E}} = \sum_{m=1}^{M} (1-\alpha) \left[A_{1m} I_{(VSm)_E} \mathbf{I} + B_{1m} \boldsymbol{\sigma}_{(VSm)_E} \right] + \alpha \left[A_{2m} I_{(VSm)_E} \mathbf{I} + B_{2m} \boldsymbol{\sigma}_{(VSm)_E} \right] \quad (23)$$

$$\dot{\boldsymbol{\varepsilon}}_{(VS)_D} = \sum_{m=1}^{M} \alpha \left[(\lambda_2)_m I_{(VSm)_D} \mathbf{I} + (\eta_2)_m \boldsymbol{\sigma}_{(VSm)_D} \right] + (1-\alpha) \left[(\lambda_1)_m I_{(VSm)_D} \mathbf{I} + (\eta_1)_m \boldsymbol{\sigma}_{(VSm)_D} \right] \quad (24)$$

The total strain can then be determined by:

$$\boldsymbol{\varepsilon} = \sum_{m=1}^{M} \boldsymbol{\varepsilon}_{(VSm)} + \boldsymbol{\varepsilon}_E + \boldsymbol{\varepsilon}_P \quad (25)$$

The constitutive relation of the viscoelastic materials undergoing microstructural changes can then be determined by substituting Eqs. (17), (18) or (19), and (20) into Eq. (4), which results in ordinary differential equations (ODEs). In case multiple final components are considered, the relation is formed by substituting Eqs. (23), (18) or (19), and (24) into Eq. (25).

Finally we also need an activation function and a driving force for the microstructural changes. It is natural to assume that microstructural changes in the polymers undergoing creep are related to the macroscopic strains in the materials[3]. Increasing strains would potentially result in breaking of the macromolecular networks of the polymers (scission). While healing in polymers is possible, in this study we neglect the possibility of healing. It is noted that as the amount of the new network (microstructural changes) in the polymer increases, the amount of the original network decreases. Formation of the new network and reduction of the original network are

[3] Since one can never know if the reference configuration from which strain is measured is free of residual stress or permanent set induced by prior deformation using measures based on strain or stress is not philosophically sound (see Alagappan et al. (2016) for a discussion concerning the use of strain or stress measures for changes in microstructures.)

assumed to occur at the same rate. The formation of the new network is determined by the activation function:

$$A(\boldsymbol{\varepsilon}) = f(\boldsymbol{\varepsilon}) - I_{cr} \tag{26}$$

where I_{cr} is the critical value associated with the total strains that determines the formation of the new network. When loading takes place and the corresponding function $f(\boldsymbol{\varepsilon})$ is less than the current value of I_{cr} there is no formation of the new network. However, when loading results in $f(\boldsymbol{\varepsilon})$ to be greater than the current value of I_{cr}, then I_{cr} needs to be updated to $I_{cr} = f(\boldsymbol{\varepsilon})$, and the equality condition in Eq. (26) is now satisfied and therefore a new network is formed. We also need to define the amount of new network being formed, which is assumed to depend on the second invariant of the total strain:

$$\alpha(\boldsymbol{\varepsilon}) = \alpha(II_{\boldsymbol{\varepsilon}}) \tag{27}$$

The activation function and the function that describes microstructural changes will be discussed later during the material calibrations.

The driving force F_α for the microstructural changes in Eq. (11) can be obtained once the form of the permanent strain evolving with the microstructural changes $\boldsymbol{\varepsilon}_P(\alpha)$ is defined. When the Gibbs potential is expressed as in Eq. (12), the driving force is:

$$\begin{aligned} F_\alpha = {} & \boldsymbol{\sigma}\frac{\partial \boldsymbol{\varepsilon}_P}{\partial \alpha} + \left(\frac{A_2}{2} I^2_{(VS)_E} + B_2 II_{(VS)_E}\right) - \left(\frac{A_1}{2} I^2_{(VS)_E} + B_1 II_{(VS)_E}\right) + \left(\frac{C_2}{2} I^2_E + D_2 II_E\right) - \left(\frac{C_1}{2} I^2_E + D_1 II_E\right) \\ & + \alpha \frac{\partial\left(\frac{A_2}{2} I^2_{(VS)_E} + B_2 II_{(VS)_E}\right)}{\partial \alpha} + (1-\alpha)\frac{\partial\left(\frac{A_1}{2} I^2_{(VS)_E} + B_1 II_{(VS)_E}\right)}{\partial \alpha} + \alpha \frac{\partial\left(\frac{C_2}{2} I^2_{(VS)_E} + D_2 II_{(VS)_E}\right)}{\partial \alpha} \\ & + (1-\alpha)\frac{\partial\left(\frac{C_1}{2} I^2_{(VS)_E} + D_1 II_{(VS)_E}\right)}{\partial \alpha} \end{aligned} \tag{28}$$

When the instantaneous part of the Gibbs potential is expressed as in Eq. (14), the driving force in Eqs. (28) becomes:

$$
\begin{aligned}
F_\alpha = {} & \boldsymbol{\sigma}\frac{\partial \boldsymbol{\varepsilon}_P}{\partial \alpha} + \left(\frac{A_2}{2} I_{(VS)_E}^2 + B_2 II_{(VS)_E}\right) - \left(\frac{A_1}{2} I_{(VS)_E}^2 + B_1 II_{(VS)_E}\right) + \\
& \alpha \frac{\partial\left(\frac{A_2}{2} I_{(VS)_E}^2 + B_2 II_{(VS)_E}\right)}{\partial \alpha} + (1-\alpha)\frac{\partial\left(\frac{A_1}{2} I_{(VS)_E}^2 + B_1 II_{(VS)_E}\right)}{\partial \alpha} \\
& \left(C_2\left(\frac{e^{\beta^f I_E}}{\beta^f} - I_E\right) + D_2\left(\frac{e^{\delta^f \sqrt{2II_E}}}{\delta^f} - \sqrt{2II_E}\right)\right) - \left(C_1\left(\frac{e^{\beta^i I_E}}{\beta^i} - I_E\right) + D_1\left(\frac{e^{\delta^i \sqrt{2II_E}}}{\delta^i} - \sqrt{2II_E}\right)\right) \\
& + \alpha \frac{\partial\left(C_2\left(\frac{e^{\beta^f I_E}}{\beta^f} - I_E\right) + D_2\left(\frac{e^{\delta^f \sqrt{2II_E}}}{\delta^f} - \sqrt{2II_E}\right)\right)}{\partial \alpha} + (1-\alpha)\frac{\partial\left(C_1\left(\frac{e^{\beta^i I_E}}{\beta^i} - I_E\right) + D_1\left(\frac{e^{\delta^i \sqrt{2II_E}}}{\delta^i} - \sqrt{2II_E}\right)\right)}{\partial \alpha}
\end{aligned}
\tag{29}
$$

It is necessary for the rate of mechanical dissipation in Eq. (11) to be nonnegative. From the evolution of the viscoelastic mechanical response, we have $\xi_D \geq 0$, and thus we need $F_\alpha \dot{\alpha} \geq 0$. Since we assume that there is no healing in the materials, during unloading and recovery we have $\dot{\alpha} = 0$ and thus $F_\alpha \dot{\alpha} = 0$ meaning the rate of mechanical dissipation is nonnegative. During loading and creep that trigger formation of the new network ($\dot{\alpha} \geq 0$), it is necessary for $F_\alpha \geq 0$. The form for $\boldsymbol{\varepsilon}_P(\alpha)$ should be chosen so that $\boldsymbol{\sigma}\frac{\partial \boldsymbol{\varepsilon}_P}{\partial \alpha} \geq 0$. When the function in Eq. (28) is considered, the non-negative dissipative rate leads to the following restriction on the material parameters, i.e., $E^i \geq E^f$; $\nu^i \geq \nu^f$, which is naturally obtained when we calibrate the material parameters from the experiment. When the function in Eq. (29) is used, it is necessary for $\left(C_2\left(\frac{e^{\beta^f I_E}}{\beta^f} - I_E\right) + D_2\left(\frac{e^{\delta^f \sqrt{2II_E}}}{\delta^f} - \sqrt{2II_E}\right)\right) - \left(C_1\left(\frac{e^{\beta^i I_E}}{\beta^i} - I_E\right) + D_1\left(\frac{e^{\delta^i \sqrt{2II_E}}}{\delta^i} - \sqrt{2II_E}\right)\right)$ to be greater than or equal to zero for any stress value. With the parameter values for C and D as shown in the material parameter characterization section, it is easy to prove that the restriction is satisfied for uniaxial loading conditions.

The above constitutive relation is solved numerically, by using finite difference method. The algorithm to compute the creep strain is summarized as follow: Assume at time *t*, the creep stress tensor $\boldsymbol{\sigma}$, creep strain tensor $\boldsymbol{\varepsilon}(t)$, volume fraction of newly formulated network $\alpha(t)$, and stress tensor $\boldsymbol{\sigma}_{(VSm)_D}(t)$ within each delayed component are known. In order to calculate the creep strain at time $t+\Delta t$, $\alpha(t)$ and $\boldsymbol{\sigma}_{(VSm)_D}(t)$ are substituted into Eq. (20) to calculate the rates of dissipative strain $\dot{\boldsymbol{\varepsilon}}_{(VSm)}(t+\Delta t)$. The instantaneous, elastic strain tensor $\boldsymbol{\varepsilon}_E(t+\Delta t)$ can be calculated from Eq. (19) using $\alpha(t)$ and $\boldsymbol{\sigma}$, while viscoelastic strain generated by each delayed component can be obtained by equation $\boldsymbol{\varepsilon}_{(VSm)}(t+\Delta t)=\boldsymbol{\varepsilon}_{(VSm)}(t)+\dot{\boldsymbol{\varepsilon}}_{(VSm)}(t+\Delta t)\Delta t$. The total creep strain at time $t+\Delta t$ can be computed by Eq. (25). Finally, volume fraction of newly formulated configuration $\alpha(t+\Delta t)$ and stress tensor $\boldsymbol{\sigma}_{(VSm)_D}(t+\Delta t)$ for each delayed component are calculated from Eq. (27) and Eq. (17), respectively, to apply as inputs for next time step. To ensure the accuracy of this differential model, the value for Δt is set to be a small number. In this research, we choose $\Delta t = 0.5\,\text{min}$.

2.2. Implementation of the Constitutive Model

The above constitutive model is corroborated using experimental data on polyoxymethylene (POM) under uniaxial tensile tests. A ramp loading with a constant displacement rate (1 mm/s), corresponding to 0.87%/s nominal (engineering) strain rate, creep under constant loads as well as recovery tests were performed. The ramp loading was carried out until specimens failed at around 25% engineering strain. The creep-recovery tests were conducted at different load amplitude and duration. It will be seen later that depending on the magnitude of load and duration of loading, the POM polymer can experience microstructural changes, which can be associated with the breaking

of the polymer networks. When microstructural changes take place, upon unloading and recovery the macroscopic response of polymers show permanent set, which is a new stress free natural configuration. Both axial and in-plane transverse deformations were measured during the tests. A detailed discussion of the experiment can be found in Muliana et al. [55, 56].

For the POM polymer under consideration, the failure strain is around 25%. From the recorded axial and transverse deformations, we can construct the axial and lateral stretch, and the corresponding axial and lateral displacement gradients, i.e., $\frac{\partial u_1}{\partial X_1}$ and $\frac{\partial u_2}{\partial X_2}$. The engineering strains are determined as $\varepsilon_{11} = \frac{\partial u_1}{\partial X_1};\ \varepsilon_{22} = \varepsilon_{33} = \frac{\partial u_2}{\partial X_2};\ \varepsilon_{12} = \varepsilon_{13} = \varepsilon_{23} = 0$. In order to justify the choice of engineering strain, instead of using nonlinear strains, we quantify percent errors when neglecting the higher order displacement gradients. For the displacement gradient $\frac{\partial u_1}{\partial X_1} = 0.25;\ \frac{1}{2}\left(\frac{\partial u_1}{\partial X_1}\right)^2 = 0.03125$; the percent error in neglecting the higher order term when determining the strain is around 11%. As most of the data are below the failure strain of 25%, the percent error in considering the engineering strain is less than 11% in most of the results. The engineering strain measure is used due to its simplicity in formulating the model and obtaining the solutions.

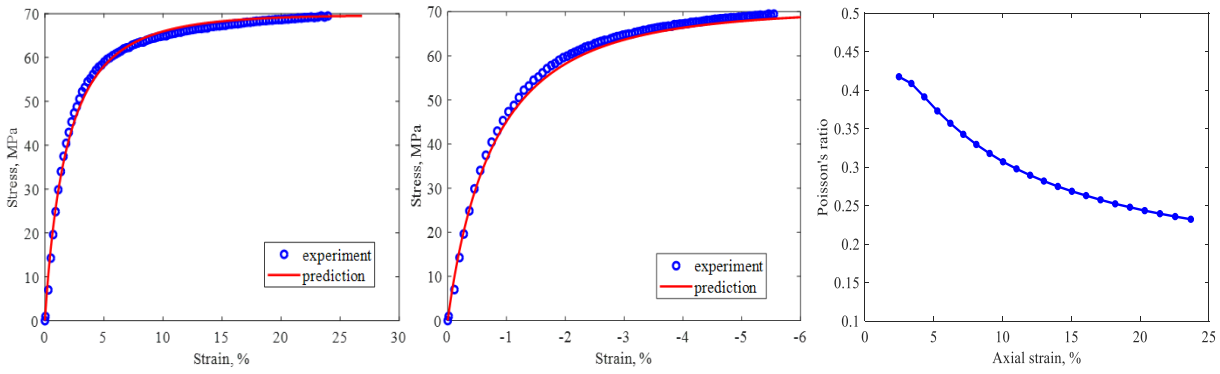

Figure 3 A ramp loading at a constant strain rate, showing axial response (left) and lateral response (middle), and Poisson's ration (right)

The axial and lateral responses under ramp loading (Figure 3) are used to calibrate the material parameters associated with the elastic response in Eq. (19). Hence, the stress tensor of the elastic component $\boldsymbol{\sigma}_E$ and invariants I_E, II_E can be written as:

$$\boldsymbol{\sigma}_E = \begin{bmatrix} \sigma_E & 0 & 0 \\ 0 & 0 & 0 \\ 0 & 0 & 0 \end{bmatrix}, I_E = \sigma_E, II_E = \frac{1}{2}\sigma_E^2 \tag{30}$$

Substituting Eq. (30) into Eq. (19), the elastic strain components are written as:

$$\begin{aligned} \varepsilon_{11}^E &= (1-\alpha)\left[C_1\left(e^{\beta^i \sigma_E} - 1\right) + D_1\left(e^{\delta^i \sigma_E} - 1\right)\right] + \alpha\left[C_2\left(e^{\beta^f \sigma_E} - 1\right) + D_2\left(e^{\delta^f \sigma_E} - 1\right)\right] \\ \varepsilon_{22}^E &= \varepsilon_{33}^E = (1-\alpha)C_1\left(e^{\beta^i \sigma_E} - 1\right) + \alpha C_2\left(e^{\beta^f \sigma_E} - 1\right) \\ \varepsilon_{12}^E &= \varepsilon_{13}^E = \varepsilon_{23}^E = 0 \end{aligned} \tag{31}$$

As discussed before, upon linearization, we have $C\beta = -\frac{\nu}{E}$, $D\delta = \frac{1+\nu}{E}$ and hence:

$$C_1\beta^i = -\frac{\nu}{E_E^i}, \quad D_1\delta^i = \frac{1+\nu}{E_E^i}, \quad C_2\beta^f = -\frac{\nu}{E_E^f}, \quad D_2\delta^f = \frac{1+\nu}{E_E^f} \tag{32}$$

where E_E and ν are the instantaneous elastic modulus and Poisson's ratio, and superscripts '*i*' and '*f*' denote the properties corresponding to the initial and final configurations, respectively. We also plot the ratio of the lateral to axial strains against the axial strain corresponding to the ramp loading in Figure 3. It is seen the 'corresponding Poisson's ratio' varies as the polymer is being stretched. Thus, we suggest the following form for the Poisson's function:

$$\nu(\alpha) = \alpha\nu^f + (1-\alpha)\nu^i \tag{33}$$

which also implies:

$$\nu(\alpha) = -\frac{(1-\alpha)C_1\left(e^{\beta^i \sigma_E} - 1\right) + \alpha C_2\left(e^{\beta^f \sigma_E} - 1\right)}{(1-\alpha)\left[C_1\left(e^{\beta^i \sigma_E} - 1\right) + D_1\left(e^{\delta^i \sigma_E} - 1\right)\right] + \alpha\left[C_2\left(e^{\beta^f \sigma_E} - 1\right) + D_2\left(e^{\delta^f \sigma_E} - 1\right)\right]} \tag{34}$$

Furthermore, we assume that $\delta^i = \beta^i, \delta^f = \beta^f$, and from Eqs. (33) and (34) we can show that

$$-\frac{C_1}{C_1+D_1}=-\frac{C_2}{C_2+D_2}=\nu(\alpha) \tag{35}$$

Combining Eq. (32) and Eq. (35), and let $C^i=C_1(\alpha=0)$, $C^f=C_2(\alpha=1)$, $D^i=D_1(\alpha=0)$, $D^f=D_1(\alpha=1)$, we have:

$$\begin{aligned}
C_1&=-\frac{\nu(\alpha)}{E^i\beta^i}=(1+\alpha)C^i+\frac{\alpha\nu^f}{\nu^i}C^i\\
C_2&=-\frac{\nu(\alpha)}{E^f\beta^f}=\alpha C^f+\frac{(1-\alpha)\nu^i}{\nu^f}C^f\\
D_1&=\frac{1+\nu(\alpha)}{E^i\beta^i}=(1+\alpha)D^i+\frac{\alpha(1+\nu^f)}{1+\nu^i}D^i\\
D_2&=\frac{1+\nu(\alpha)}{E^f\beta^f}=\alpha D^f+\frac{(1+\alpha)(1+\nu^i)}{1+\nu^f}D^f
\end{aligned} \tag{36}$$

The responses near zero stress, i.e., $\alpha\approx 0$, are used to determine C^i,β^i,D^i,δ^i (note that $\delta^i=\beta^i$). As discussed above, $C^i\beta^i=-\frac{\nu^i}{E^i}$, $D^i\delta^i=\frac{1+\nu^i}{E^i}$. The remaining information concerning the responses are used to calibrate C^f,β^f,D^f,δ^f (also noted $\delta^f=\beta^f$). The Poisson's ratio associated with the elastic response in the initial configuration is determined by taking the ratio of the lateral and axial strains of the ramp loading at a relatively low axial strain (<3%), i.e., $\nu^i=-\frac{\varepsilon_{22}}{\varepsilon_{11}}=0.42$, and the Poisson's ratio associated with the elastic response in the final configuration is determined at the highest value of axial strain (~25%), i.e., $\nu^f=-\frac{\varepsilon_{22}}{\varepsilon_{11}}=0.25$. We can also determine this value by examining the creep responses at the highest strain (see Figure 4), which gives $\nu^f=-\frac{-7\%}{25.5\%}=0.28$. It is seen that the two values of ν^f from the elastic responses in the ramp and creep loading are very close. In this study, we take $\nu^f=0.28$.

Simultaneously, we also define the amount of the new network being formed (Eq. (27)) during the ramp loading until failure occurs, as given below:

$$\alpha(\boldsymbol{\varepsilon}) = \alpha(\mathrm{II}_\varepsilon) = \left(\frac{J_2(\boldsymbol{\varepsilon})}{J_2^{\max}}\right)^{\kappa} \tag{37}$$

where the maximum second strain invariant is at failure strains, i.e., $\varepsilon_{11}^{\max} = 25.2\%; \varepsilon_{22}^{\max} = \varepsilon_{33}^{\max} = -7\%$, which gives $J_2^{\max} = 0.0367$ are obtained from the highest creep strains under 50 MPa, shown in Figure 4. The calibrated value for κ is 0.63. The irrecoverable strains are determined from the long-term recovery data $\varepsilon_{11}^{ir} = 8.2\%; \varepsilon_{22}^{ir} = \varepsilon_{33}^{ir} = -2.3\%$, shown in Figure 4. We consider the following permanent strains:

$$\boldsymbol{\varepsilon}_P = h(\alpha)\boldsymbol{\varepsilon}^{ir} = \left[\alpha(\mathrm{II}_\varepsilon)\right]^n \boldsymbol{\varepsilon}^{ir} = \left(\frac{J_2(\boldsymbol{\varepsilon})}{J_2^{\max}}\right)^{\kappa n} \boldsymbol{\varepsilon}^{ir} \tag{38}$$

The calibrated value for n is 1.8. Table 1 summarizes the calibrated values.

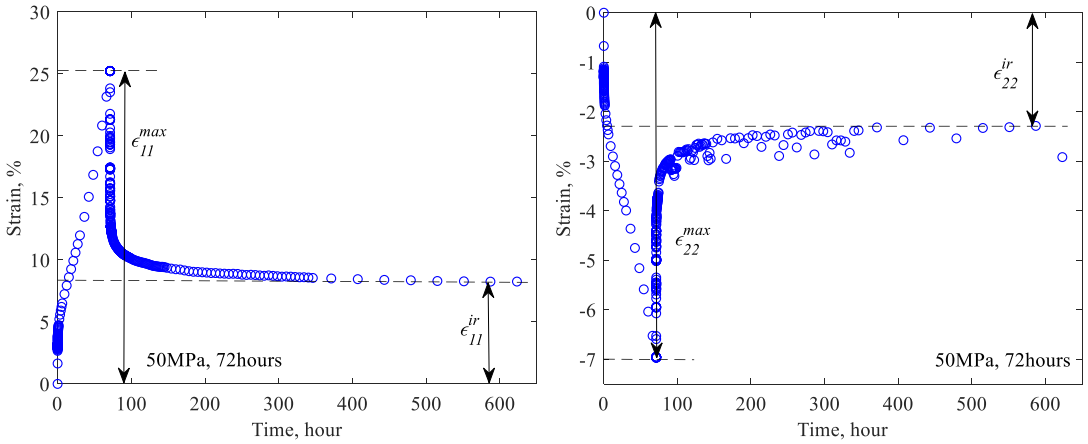

Figure 4 Creep-recovery responses under 50 MPa, showing axial response (top) and lateral response (bottom)

Table 1 Instantaneous parameters

Parameter	Value at initial configuration (superscript i)	Value at final configuration (superscript f)
C	-4.048×10^{-3}	-6.370×10^{-3}
$\beta\,(MPa^{-1})$	0.025	0.036
D	13.615×10^{-3}	29.118×10^{-3}
$\delta\,(MPa^{-1})$	0.025	0.036
ν	0.42	0.28

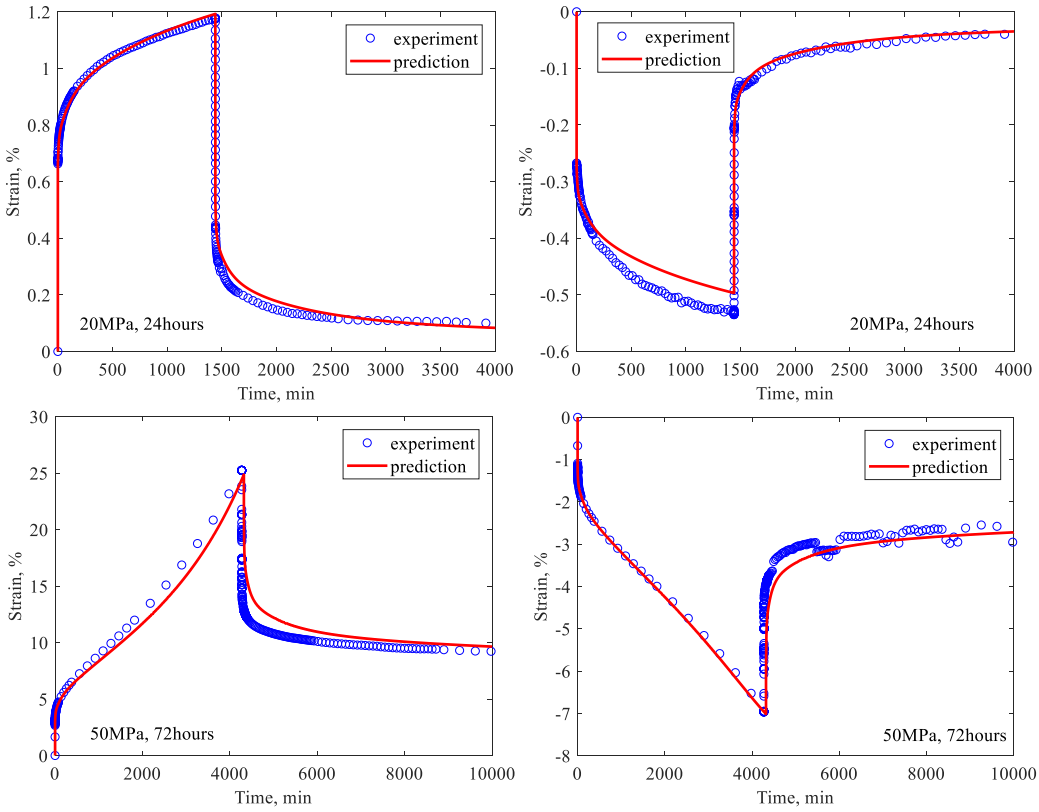

Figure 5 Creep-recovery responses under axial stresses 20 MPa and 50 MPa

Next, we determine the dissipative components of the model using the creep responses at two stress levels, i.e., 20 MPa and 50 MPa, shown in Figure 5. We have a relatively long-term response and therefore the models in Eqs. (23) and (24) are considered. Similar to Eq. (36), from Eq. (23) and Eq. (24), for an isotropic material, we have:

$$
\begin{aligned}
A_{1m} &= -\frac{\nu_m(\alpha)}{E_m^i}; \quad A_{2m} = -\frac{\nu_m(\alpha)}{E_m^f} \\
B_{1m} &= \frac{1+\nu_m(\alpha)}{E_m^i}; \quad B_{2m} = \frac{1+\nu_m(\alpha)}{E_m^f} \\
\lambda_{1m} &= -\frac{\nu_m(\alpha)}{\mu_m^i}; \quad \lambda_{2m} = -\frac{\nu_m(\alpha)}{\mu_m^f} \\
\eta_{1m} &= \frac{1+\nu_m(\alpha)}{\mu_m^i}; \quad \eta_{2m} = \frac{1+\nu_m(\alpha)}{\mu_m^f}
\end{aligned}
\tag{39}
$$

The creep response at 20 MPa gives a relatively small strain, i.e., $\alpha \approx 0$ and is used to determine the parameters A_{1m}, B_{1m}, while the creep response at 50 MPa is used to calibrate A_{2m}, B_{2m}. Based on the experimental data of the ratio of the lateral and axial strain from the ramp and creep loadings in Figure 3 and Figure 4, it is assumed that the ratio of the transverse strain to the axial strain does not depend on time, so that $\nu_m(\alpha) = \nu(\alpha)$ and hence $\nu_m^i = \nu^i$ and $\nu_m^f = \nu^f$. This assumption will be validated by comparing the lateral creep-recovery responses for all stress levels. Furthermore, the dissipative part in Eq. (24) leads to $\lambda_{1m} = -\frac{\nu(\alpha)}{\mu_m^i}$; $\lambda_{1m} + \eta_{1m} = \frac{1}{\mu_m^i}$ and $\lambda_{2m} = -\frac{\nu(\alpha)}{\mu_m^f}$; $\lambda_{2m} + \eta_{2m} = \frac{1}{\mu_m^f}$, where μ_m^i, μ_m^f are the viscosity parameters. It is often convenient to relate the characteristics of creep time to the viscosity of materials. We consider several components of the final network, $\mu_m^i = E_m^i \tau_m$ and $\mu_m^f = E_m^f \tau_m$, where τ_m is the characteristic time. In this study, we have 8 components for the final network and we pick the characteristic time as shown in Table 2. Therefore, we only need to calibrate the values for E_m^i and E_m^f from the creep responses at 20 MPa and 50 MPa, respectively, as shown in Figure 5. From the values in Table 2 and the Poisson's ratios associated with the elastic responses of the initial and final configurations, we can determine the values for $\lambda_{1m}, \eta_{1m}, \lambda_{2m}, \eta_{2m}$ if needed.

Table 2 Time-dependent parameters

Individual network m	τ_m (min)	E_m^{in} (GPa)	E_m^{f} (GPa)
1	5	48.80	1.98
2	10	47.33	2.43
3	100	20.26	1.44
4	500	27.02	3.70
5	1000	16.06	1.61
6	5000	1318.7	4.00
7	10000	5.53	0.36
8	50000	3.84	3.84

Using the calibrated material parameters in Table 1 and Table 2, we simulate the creep-recovery responses of POM polymers under different stress levels and holding periods. Figure 6-Figure 9 summarize the responses comparing experiments and simulation.

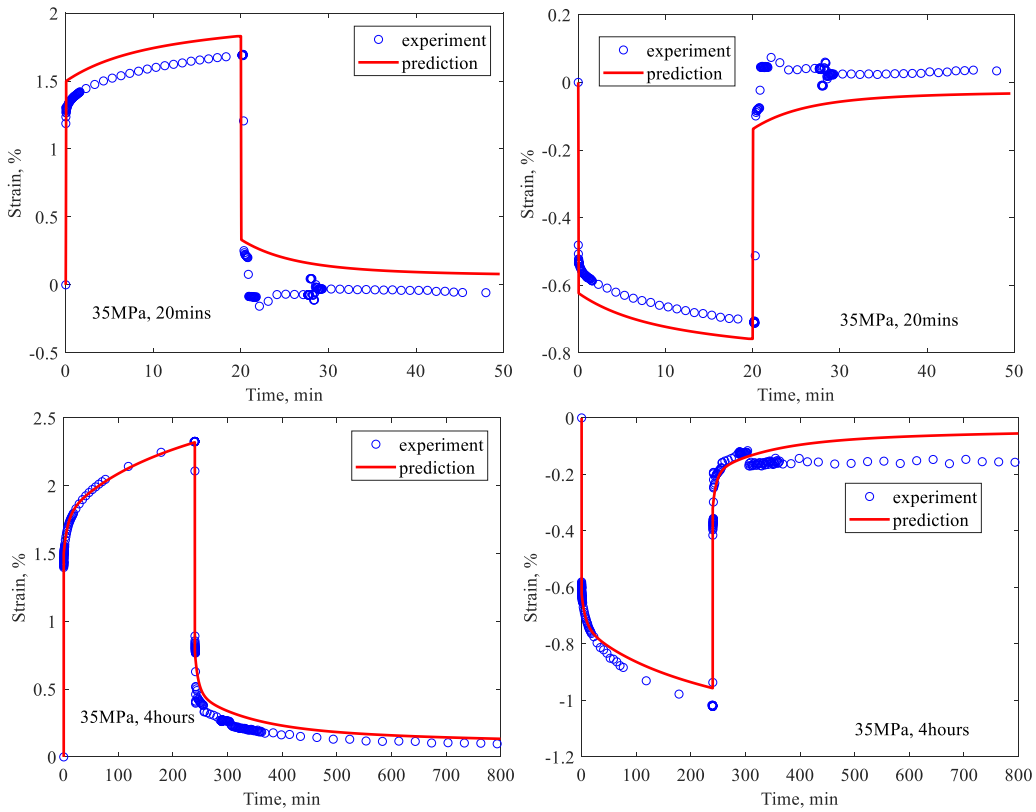

Figure 6 Creep-recovery responses under 35 MPa

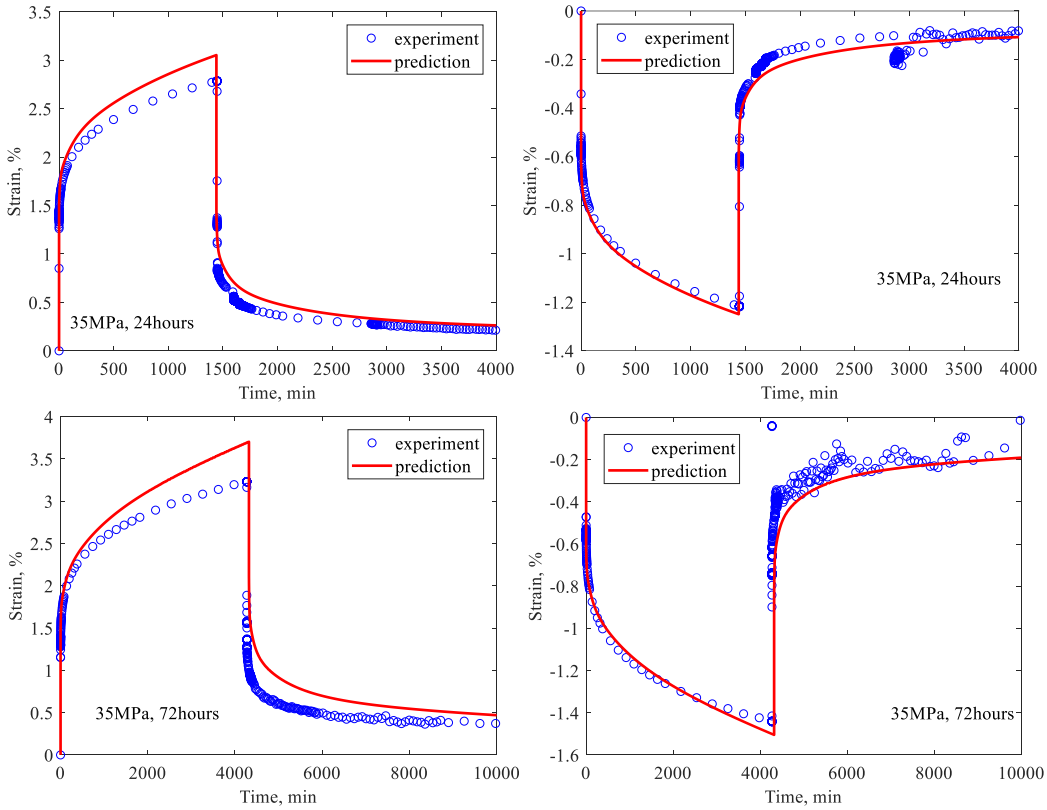

Figure 6 Continued

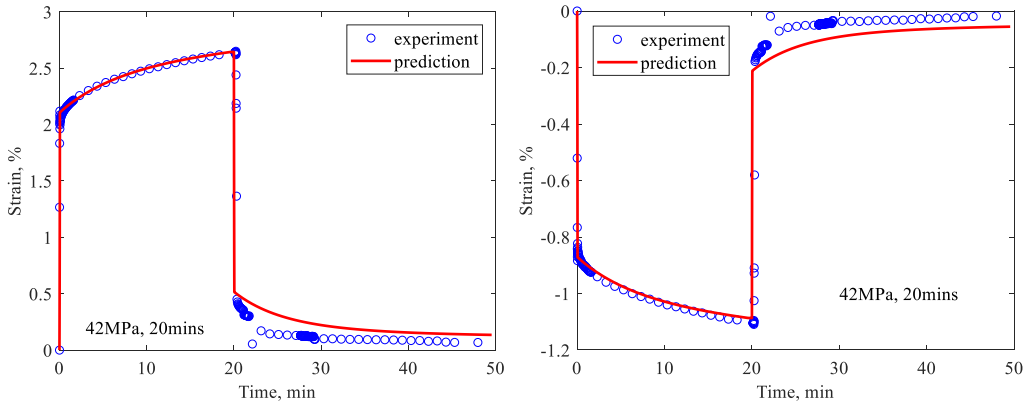

Figure 7 Creep-recovery responses under 42 MPa

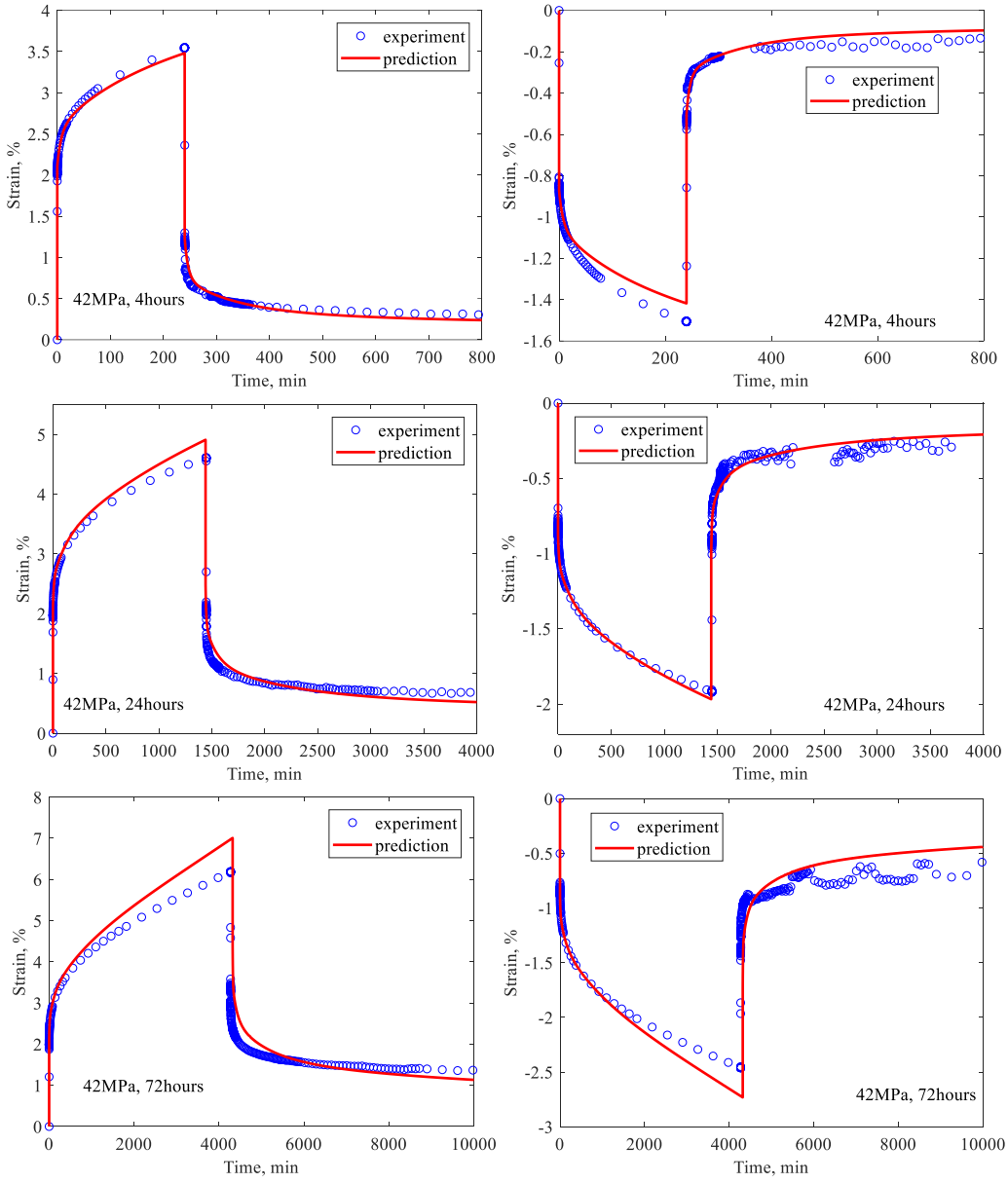

Figure 7 Continued

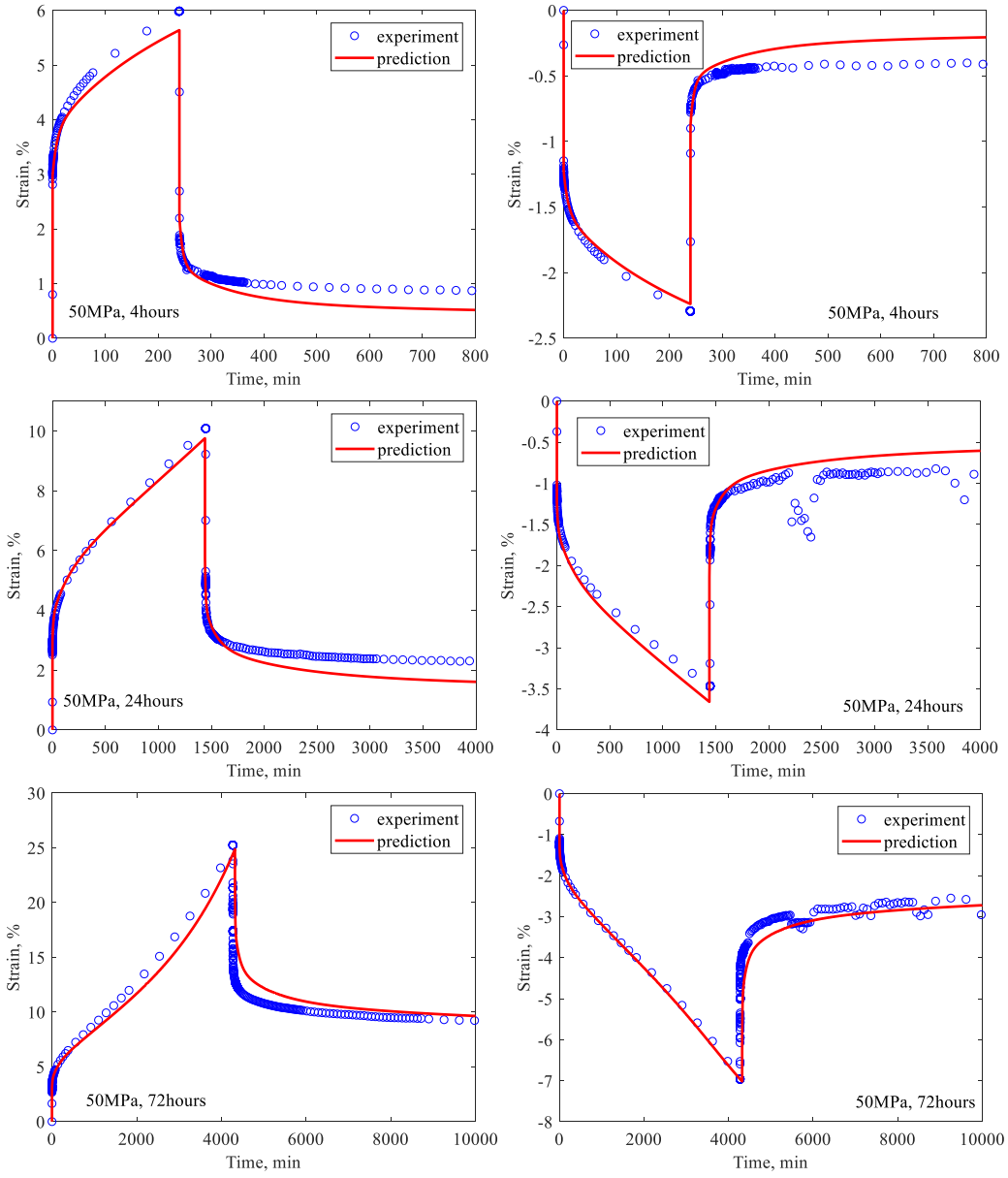

Figure 8 Creep-recovery responses under 50 MPa

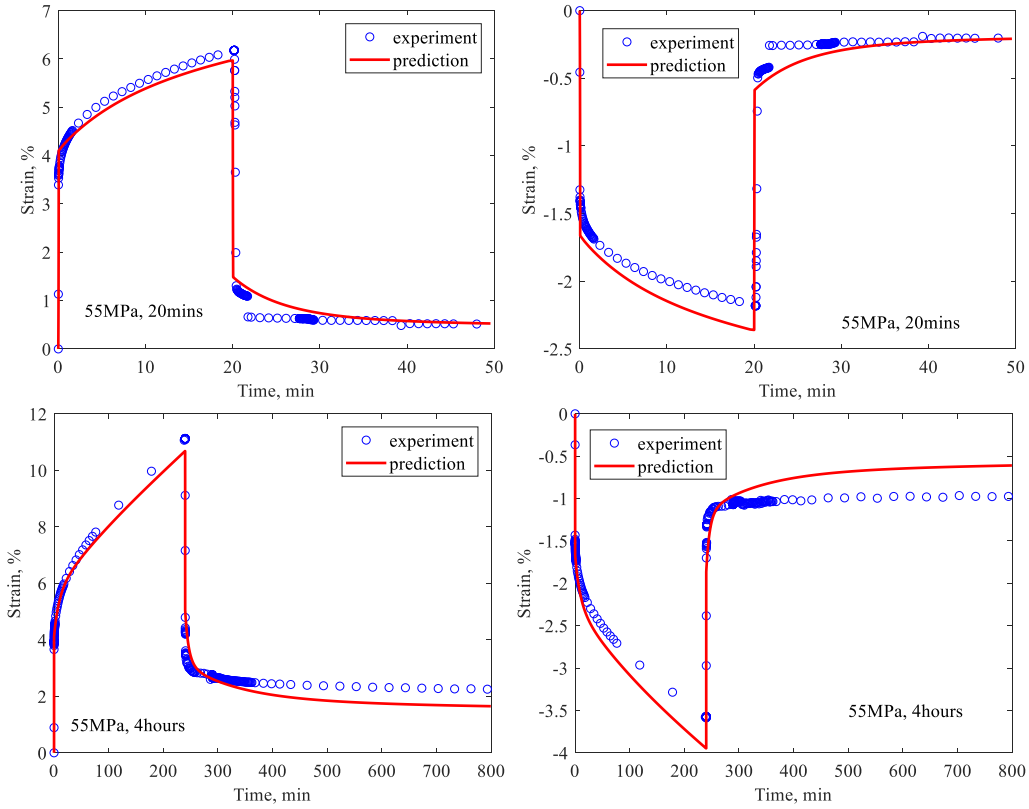

Figure 9 Creep-recovery responses under 55 MPa

CHAPTER III

A THERMODYNAMICS FRAMEWORK FOR GENERAL ANISOTROPIC AND HETEROGENEOUS MATERIALS[*]

As an additional application for the multiple natural configuration theory discussed in Chapter II, in this section, a constitutive model is developed to predict the responses of general anisotropic and heterogeneous materials. As examples of applications, hysteretic responses of plant cell walls are studied and the effect of microstructural changes, i.e., fibril reorientations, viscoelastic behaviors of fibers and matrix, possible sliding between fibers and fiber-matrix, etc., is incorporated through an internal state variable. Plant tissue experiences viscoelastic behaviors because its components, such as cellulose and lignin are polymers with long chain and multiple network microstructures. Their macromolecular networks lead to viscoelastic behaviors when they are subjected to mechanical loadings. In living tissues, the existence of fluid can also amplify the viscoelastic response of the stems. Because of these polymer-like properties, a time-dependent constitutive model similar with the model for POM polymer is developed in this section. Plant stems also share similar structure with fiber-reinforced composites. Therefore, nonlinear hysteresis responses of plant stem are also analyzed by applying multiple configuration theory on composites.

3.1. Constitutive Material Models

A general multi-axial constitutive model that can be used for describing anisotropic response of materials is discussed here. To calibrate the properties in the multi-axial model, experimental tests beyond a simple uniaxial test are required. The Gibbs free energy is expressed in terms of stress

[*] Reprinted with permission from "Modeling mechanical behaviors of plant stems undergoing microstructural changes" by Song, R., & Muliana, A., 2019. Mechanics of Materials, 139, 103175, Copyright [2019] by Elsevier.

tensor comprising elastic (*N*) and viscoelastic (*V*) components, $G = G(\boldsymbol{\sigma}_V, \boldsymbol{\sigma}_N, \alpha)$ and the total strain tensor is given as:

$$\boldsymbol{\varepsilon} = \boldsymbol{\varepsilon}_e + \boldsymbol{\varepsilon}_p \tag{40}$$

where $\boldsymbol{\varepsilon}_e = \boldsymbol{\varepsilon}_V = \boldsymbol{\varepsilon}_N$, $\boldsymbol{\varepsilon}_V = \boldsymbol{\varepsilon}_V^e + \boldsymbol{\varepsilon}_V^d$ and $\boldsymbol{\varepsilon}_p$ is the permanent strain tensor. The elastic strains are determined from $\boldsymbol{\varepsilon}_N = -\dfrac{\partial G}{\partial \boldsymbol{\sigma}_N}$ and $\boldsymbol{\varepsilon}_V^e = -\dfrac{\partial G}{\partial \boldsymbol{\sigma}_V}$. The total stress is $\boldsymbol{\sigma} = \boldsymbol{\sigma}_N + \boldsymbol{\sigma}_V$. The rate of the mechanical dissipation is given as:

$$\xi = \boldsymbol{\sigma}_V \dot{\boldsymbol{\varepsilon}}_V^d + \boldsymbol{\sigma} \dot{\boldsymbol{\varepsilon}}_p - \frac{\partial G}{\partial \alpha}\dot{\alpha} = \xi_D + \left(\boldsymbol{\sigma} \frac{\partial \boldsymbol{\varepsilon}_P}{\partial \alpha} - \frac{\partial G}{\partial \alpha} \right) \dot{\alpha} = \xi_D + F_\alpha \dot{\alpha} \tag{41}$$

For a general multi-axial response, the Gibbs free energy can be expressed as:

$$G(\boldsymbol{\sigma}_V, \boldsymbol{\sigma}_N, \alpha) = -\left[\alpha \mathbf{S}_V^f \boldsymbol{\sigma}_V . \boldsymbol{\sigma}_V + (1-\alpha) \mathbf{S}_V^i \boldsymbol{\sigma}_V . \boldsymbol{\sigma}_V \right] - \left[\alpha \mathbf{S}_N^f \boldsymbol{\sigma}_N . \boldsymbol{\sigma}_N + (1-\alpha) \mathbf{S}_N^i \boldsymbol{\sigma}_N . \boldsymbol{\sigma}_N \right] \tag{42}$$

where $\mathbf{S}_V^f, \mathbf{S}_V^i, \mathbf{S}_N^f, \mathbf{S}_N^i$ are fourth order tensors associated with the compliance of the materials. The components of the above tensors should be determined from experiments, which will indicate the isotropy or anisotropy nature of the materials. The rate of the mechanical dissipation associated with the viscoelastic response is given as:

$$\xi_D = \alpha \mathbf{K}^f \boldsymbol{\sigma}_V . \boldsymbol{\sigma}_V + (1-\alpha) \mathbf{K}^i \boldsymbol{\sigma}_V . \boldsymbol{\sigma}_V \tag{43}$$

where $\mathbf{K}^f$ and $\mathbf{K}^i$ are fourth order tensors associated with the inverse viscosity of the materials.

Finally, the elastic and viscoelastic strain tensors can be determined from the Gibbs energy in Eq. (42) and the rate of the dissipative strain can be obtained from Eq. (43):

$$\boldsymbol{\varepsilon}_V^e = \alpha 2 \mathbf{S}_V^f \boldsymbol{\sigma}_V + (1-\alpha) 2 \mathbf{S}_V^i \boldsymbol{\sigma}_V \tag{44}$$

$$\boldsymbol{\varepsilon}_N = \alpha 2 \mathbf{S}_N^f \boldsymbol{\sigma}_N + (1-\alpha) 2 \mathbf{S}_N^i \boldsymbol{\sigma}_N \tag{45}$$

$$\dot{\boldsymbol{\varepsilon}}_V^d = \alpha 2 \mathbf{K}^f \boldsymbol{\sigma}_V + (1-\alpha) 2 \mathbf{K}^i \boldsymbol{\sigma}_V \tag{46}$$

The driving force for the microstructural changes is now given as:

$$F_\alpha = \boldsymbol{\sigma}\frac{\partial \boldsymbol{\varepsilon}_p}{\partial \alpha} + \mathbf{S}_V^f \boldsymbol{\sigma}_V.\boldsymbol{\sigma}_V - \mathbf{S}_V^i \boldsymbol{\sigma}_V.\boldsymbol{\sigma}_V + \mathbf{S}_N^f \boldsymbol{\sigma}_N.\boldsymbol{\sigma}_N - \mathbf{S}_N^i \boldsymbol{\sigma}_N.\boldsymbol{\sigma}_N \tag{47}$$

The function for $\boldsymbol{\varepsilon}_p(\alpha)$ can be formed based on available experimental data, as discussed above.

The multi-axial constitutive model can also be modified to simulate the mechanical responses for heterogeneous materials, given the volume fractions of each phases. Constitutive model for heterogeneous material with two layers is discussed below as an example. Similar with Eq. (42), for a general three-dimensional response, the Gibbs free energy for the heterogeneous material can be written as:

$$\begin{aligned} &G(\boldsymbol{\sigma}_{V1}, \boldsymbol{\sigma}_{N1}, \boldsymbol{\sigma}_{V2}, \boldsymbol{\sigma}_{N2}, \alpha_1, \alpha_2) \\ &= c\left[-\alpha_1 \mathbf{S}_{V1}^f \boldsymbol{\sigma}_{V1}.\boldsymbol{\sigma}_{V1} - (1-\alpha_1)\mathbf{S}_{V1}^i \boldsymbol{\sigma}_{V1}.\boldsymbol{\sigma}_{V1}\right] + (1-c)\left[-\alpha_2 \mathbf{S}_{N2}^f \boldsymbol{\sigma}_{N2}.\boldsymbol{\sigma}_{N2} - (1-\alpha_2)\mathbf{S}_{N2}^i \boldsymbol{\sigma}_{N2}.\boldsymbol{\sigma}_{N2}\right] \end{aligned} \tag{48}$$

where c is the volume fraction of first layer of the heterogeneous material. Subscript '1' and '2' denote properties associated with first layer and second layer, respectively.

The rate of mechanical dissipation is defined as the difference between mechanical power and the rate of internal energy:

$$\begin{aligned} \xi &= c\boldsymbol{\sigma}_1 \dot{\boldsymbol{\varepsilon}}_1 + (1-c)\boldsymbol{\sigma}_2 \dot{\boldsymbol{\varepsilon}}_2 - \dot{u} \\ &= c\left(\boldsymbol{\sigma}_{V1}\dot{\boldsymbol{\varepsilon}}_{V1}^d + \boldsymbol{\sigma}_1 \dot{\boldsymbol{\varepsilon}}_{p1}\right) - \frac{\partial G}{\partial \alpha_1}\dot{\alpha}_1 + (1-c)\left(\boldsymbol{\sigma}_{V2}\dot{\boldsymbol{\varepsilon}}_{V2}^d + \boldsymbol{\sigma}_2 \dot{\boldsymbol{\varepsilon}}_{p2}\right) - \frac{\partial G}{\partial \alpha_2}\dot{\alpha}_2 \\ &= \xi_D + \left(c\boldsymbol{\sigma}_1 \frac{\partial \boldsymbol{\varepsilon}_{p1}}{\partial \alpha_1} - \frac{\partial G}{\partial \alpha_1}\right)\dot{\alpha}_1 + \left[(1-c)\boldsymbol{\sigma}_2 \frac{\partial \boldsymbol{\varepsilon}_{p2}}{\partial \alpha_2} - \frac{\partial G}{\partial \alpha_2}\right]\dot{\alpha}_2 = \xi_D + cF_{\alpha 1}\dot{\alpha}_1 + (1-c)F_{\alpha 2}\dot{\alpha}_2 \end{aligned} \tag{49}$$

where $F_{\alpha 1}$ and $F_{\alpha 2}$ denote the driving forces for microstructural changes in first layer and second layer, respectively, while ξ_D represents the rate of mechanical dissipation associated with the viscoelastic response:

$$\xi_D = c\left[\alpha_1 \mathbf{K}_1^f \boldsymbol{\sigma}_{V1}.\boldsymbol{\sigma}_{V1} + (1-\alpha_1)\mathbf{K}_1^i \boldsymbol{\sigma}_{V1}.\boldsymbol{\sigma}_{V1}\right] + (1-c)\left[\alpha_2 \mathbf{K}_2^f \boldsymbol{\sigma}_{V2}.\boldsymbol{\sigma}_{V2} + (1-\alpha_2)\mathbf{K}_2^i \boldsymbol{\sigma}_{V2}.\boldsymbol{\sigma}_{V2}\right] \tag{50}$$

Similar with Eqs. (44)-(46), the delayed and relaxed strain tensors within each layer can be derived from Gibbs free energy and the rate of mechanical dissipation:

$$\boldsymbol{\varepsilon}_{V1}^{e}=\alpha_1 2\mathbf{S}_{V1}^{f}\boldsymbol{\sigma}_{V1}+(1-\alpha_1)2\mathbf{S}_{V1}^{i}\boldsymbol{\sigma}_{V1},\boldsymbol{\varepsilon}_{V2}^{e}=\alpha_2 2\mathbf{S}_{V2}^{f}\boldsymbol{\sigma}_{V2}+(1-\alpha_2)2\mathbf{S}_{V2}^{i}\boldsymbol{\sigma}_{V2} \tag{51}$$

$$\boldsymbol{\varepsilon}_{N1}=\alpha_1 2\mathbf{S}_{N1}^{f}\boldsymbol{\sigma}_{N1}+(1-\alpha_1)2\mathbf{S}_{N1}^{i}\boldsymbol{\sigma}_{N1},\boldsymbol{\varepsilon}_{N2}=\alpha_2 2\mathbf{S}_{N2}^{f}\boldsymbol{\sigma}_{N2}+(1-\alpha_2)2\mathbf{S}_{N2}^{i}\boldsymbol{\sigma}_{N2} \tag{52}$$

$$\dot{\boldsymbol{\varepsilon}}_{V1}^{d}=\alpha_1 2\mathbf{K}_{1}^{f}\boldsymbol{\sigma}_{V1}+(1-\alpha_1)2\mathbf{K}_{1}^{i}\boldsymbol{\sigma}_{V1},\dot{\boldsymbol{\varepsilon}}_{V2}^{d}=\alpha_2 2\mathbf{K}_{2}^{f}\boldsymbol{\sigma}_{V2}+(1-\alpha_2)2\mathbf{K}_{2}^{i}\boldsymbol{\sigma}_{V2} \tag{53}$$

For a two-layer heterogeneous material, we have:

$$\boldsymbol{\varepsilon}_1=\boldsymbol{\varepsilon}_2=\boldsymbol{\varepsilon},\boldsymbol{\sigma}=c\boldsymbol{\sigma}_1+\left(1-c\right)\boldsymbol{\sigma}_2 \tag{54}$$

The constitutive relation between $\boldsymbol{\varepsilon}$ and $\boldsymbol{\sigma}$ can be derived by combining Eqs. (51)-(54).

3.2. An Application of the Model for Nonlinear Hysteretic Responses of Cell Walls

3.2.1 Model Formulation

In this chapter, we present a one-dimensional reduction of the above models since the currently available data in literature for plant tissue mainly report stress-strain along the loading axis. Both cellulose fibrils and matrix are polymers with long chain and multiple network microstructures. When subjected to mechanical loadings they exhibit pronounced viscoelastic behaviors due to the movements of the long macromolecular chains. We present a model for a viscoelastic response, which consists of the elastic (*N*) and viscoelastic (*V*) components. The Gibbs free energy is of the form $G=G(\sigma_V,\sigma_N,\alpha)$, and the specific Helmholtz free energy and its rates are:

$$\psi=G-\frac{\partial G}{\partial\sigma_V}\sigma_V-\frac{\partial G}{\partial\sigma_N}\sigma_N \tag{55}$$

$$\dot{\psi}=\frac{\partial G}{\partial\alpha}\dot{\alpha}-\frac{d}{dt}\left(\frac{\partial G}{\partial\sigma_V}\right)\sigma_V-\frac{d}{dt}\left(\frac{\partial G}{\partial\sigma_N}\right)\sigma_N \tag{56}$$

We assume that the delayed and relaxed components produce the same strain. In this research, a solid-like viscoelastic response is assumed. The 'reversible' strain is written as ε_e. Hence, we have:

$$\varepsilon_e = \varepsilon_V = \varepsilon_N \tag{57}$$

Within the viscoelastic part, we have the elastic recovery and dissipative parts:

$$\varepsilon_V = \varepsilon_V^e + \varepsilon_V^d \tag{58}$$

where

$$\varepsilon_V^e = -\frac{\partial G}{\partial \sigma_V} \rightarrow \dot{\varepsilon}_V^e = -\frac{d}{dt}\left(\frac{\partial G}{\partial \sigma_V}\right) = \dot{\varepsilon}_e - \dot{\varepsilon}_V^d \tag{59}$$

The total strain is assumed to be the superposition of the reversible viscoelastic strain and the permanent strain due to the microstructural change:

$$\varepsilon = \varepsilon_e + \varepsilon_p = \varepsilon_e + \alpha\varepsilon_{\max} \tag{60}$$

where the permanent strain is assumed to be proportional to microstructural change, and $\varepsilon_{\max}$ is the maximum permanent strain. The overdot in Eqs. (56) and (59) denotes the time derivative. It is also noted that the stress is an additive decomposition of the elastic and viscoelastic parts: $\sigma = \sigma_N + \sigma_V$.

Next, we define the rate of mechanical dissipation:

$$\xi = \sigma\dot{\varepsilon} - \dot{\psi} \tag{61}$$

Substituting Eqs. (56)-(60) into Eq. (61) gives:

$$\xi = \sigma_V\left(\dot{\varepsilon} - \dot{\varepsilon}_r - \dot{\varepsilon}_V^d\right) + \sigma_N\left(\dot{\varepsilon} - \dot{\varepsilon}_r\right) - \frac{\partial G}{\partial \alpha}\dot{\alpha} = \sigma_V\dot{\varepsilon}_V^d + \left(\sigma\varepsilon_{\max} - \frac{\partial G}{\partial \alpha}\right)\dot{\alpha} \tag{62}$$

We consider the following form of the Gibbs potential:

$$G(\sigma_V, \sigma_N, \alpha) = -\left(\frac{\alpha\sigma_V^2}{2E_{Vf}} + \frac{(1-\alpha)\sigma_V^2}{2E_{Vo}}\right) - \left(\frac{\alpha\sigma_N^2}{2E_{Nf}} + \frac{(1-\alpha)\sigma_N^2}{2E_{No}}\right) + f(\alpha) \tag{63}$$

The above potential gives the following constitutive equations for the elastic and viscoelastic parts:

$$\varepsilon_N = -\frac{\partial G}{\partial \sigma_N} = \frac{\alpha \sigma_N}{E_{Nf}} + \frac{(1-\alpha)\sigma_N}{E_{No}} \tag{64}$$

$$\varepsilon_V = \varepsilon_V^e + \varepsilon_V^d = -\frac{\partial G}{\partial \sigma_V} + \varepsilon_V^d = \frac{\alpha \sigma_V}{E_{Vf}} + \frac{(1-\alpha)\sigma_V}{E_{Vo}} + \varepsilon_V^d \tag{65}$$

$$\dot{\varepsilon}_V^d = \left(\frac{\alpha}{\mu_f} + \frac{1-\alpha}{\mu_o} \right) \sigma_V \tag{66}$$

From Eqs. (63)-(66) we can see that there are three material parameters involved, which are moduli for the elastic and viscoelastic parts and viscosity for the viscoelastic part. They are referred as E_N, E_V, μ, respectively. These material parameters evolve with the mechanical loading. Thus, with regards to the initial and final microstructural configurations, we have the following material parameters: $E_{No}, E_{Vo}, \mu_o, E_{Nf}, E_{Vf}, \mu_f$. Equation (63) represents the stored energy from the elastic and viscoelastic responses. Recall the mechanical dissipation in Eq. (62), and with the Gibbs potential in Eq. (63), we have:

$$F = \sigma \varepsilon_{\max} - \frac{\partial G}{\partial \alpha} = \sigma \varepsilon_{\max} + \left(\frac{\sigma_V^2}{2E_{Vf}} - \frac{\sigma_V^2}{2E_{Vo}} \right) + \left(\frac{\sigma_N^2}{2E_{Nf}} - \frac{\sigma_N^2}{2E_{No}} \right) - \frac{\partial f(\alpha)}{\partial \alpha} \tag{67}$$

Eq. (67) presents the driving force for the microstructural changes. It is noted that it is necessary for the rate of mechanical dissipation in Eq. (62) to be non-negative and thus we can pick an expression for $f(\alpha)$ to satisfy the above constraint so that $F\dot{\alpha} \geq 0$. In this study, we neglect the free energy due to microstructural changes, and hence we take $f(\alpha) = 0$.

In many cases, experimental data pertinent to the time-dependent response are not being reported. In order to capture nonlinear hysteretic response, in absence of the viscous dissipation, we can reduce the above model by eliminating $\dot{\varepsilon}_V^d$ (letting $\frac{1}{\mu_i} = \frac{\alpha}{\mu_f} + \frac{(1-\alpha)}{\mu_o} = 0$). Thus, according to

Eqs. (57)-(58) and (65)-(66), the reversible part of the model reduced to an elastic response with a modulus of elasticity as a material parameter. The only stress involved is σ and the elastic moduli at the initial and final configurations become $E_o = E_{Vo} + E_{No}$ and $E_f = E_{Vf} + E_{Nf}$, respectively. It is noted that the elastic moduli for the elastic material behavior are associated with the instantaneous moduli in viscoelastic materials. Thus, the Gibbs potential in Eq. (63) reduces to:

$$G(\alpha,\sigma) = -\left(\frac{\alpha\sigma^2}{2E_f} + \frac{(1-\alpha)\sigma^2}{2E_o}\right) \tag{68}$$

The parameters E_o and E_f are the material stiffness at the initial configuration $(\alpha = 0)$ and final configuration $(\alpha = 1)$, respectively. Following a standard procedure in imposing the thermo-dynamics relations, the rate of the mechanical dissipation is:

$$\xi = \sigma\dot{\varepsilon}_p - \frac{\partial G}{\partial \alpha}\dot{\alpha} = \sigma\left(\dot{\varepsilon} - \dot{\varepsilon}_e\right) - \frac{\partial G}{\partial \alpha}\dot{\alpha} \tag{69}$$

where the reversible strain, defined as the superposition of elastic strains of the two configurations, can be derived from Gibbs free energy:

$$\varepsilon_e = -\frac{\partial G}{\partial \sigma} = \frac{\alpha\sigma}{E_f} + \frac{(1-\alpha)\sigma}{E_o} \tag{70}$$

The rate of dissipation associated with the microstructural changes are expressed in Eq. **Error! Reference source not found.**. The term $\sigma\left(\dot{\varepsilon} - \dot{\varepsilon}_e\right)$ is related to the permanent strain due to microstructural changes. As discussed above, we need to satisfy the constraint $\xi \geq 0$, and we also need to define the evolution of the microstructural changes due to the deformation. These will be discussed later during the material characterization from available experimental data.Finally, the total energy dissipation is defined as:

$$W_d = \oint \xi dt \geq 0 \tag{71}$$

3.2.2 Material Parameter Characterization from Experimental Data

In this section we discuss the determination of material parameters in the above model in capturing the nonlinear hysteretic response of plant cell wall undergoing microstructural changes. For this purpose, we first used data of wet wood tissue of spruce (*Picea abies*), provided by Burgert [57]. The data were discussed for time-independent response, thus we eliminate the viscous dissipation part and use the Gibbs potential given in Eq. (63). Before we proceed with the material parameter characterization, we need to identify the relation between the evolution of the microstructural changes and the deformation. Figure 10 shows the hysteretic response of the tested wet wood tissue of spruce. It is seen that multiple loading-unloading cycles lead to a sequence of permanent deformations, which are associated with changes in the microstructures of the cell wall. The unloading-reloading cycles also show significant hysteretic loops.

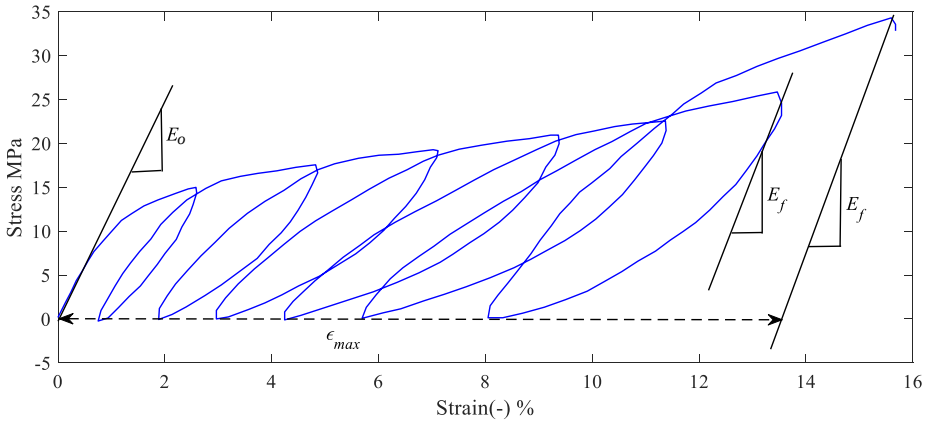

Figure 10 Calibration of material parameters E_o, E_f and $\varepsilon_{\max}$ from experimental data on wet wood tissue of spruce [57]

The material modulus at the initial configuration, E_o, is calibrated by taking the slope when the strain is zero, while the modulus at the final configuration E_f is calibrated at the maximum

unloading strain, where a complete microstructural change has taken place, $\alpha \approx 1$. It is assumed that the permanent strain is proportional to the extent of microstructural change α:

$$\varepsilon - \varepsilon_e = \alpha \varepsilon_{\max} \rightarrow \left(\dot{\varepsilon} - \dot{\varepsilon}_e\right) = \dot{\alpha} \varepsilon_{\max} \tag{72}$$

where $\varepsilon_{\max}$ is the maximum remanent strain, as depicted in Figure 10. The value for $\varepsilon_{\max}$ is calculated by using the maximum strain minus the reversible part of the strain at the maximum load. The calibration results for wet wood tissue of spruce are $E_o = 1.189 GPa$, $E_f = 1.757 GPa$ and $\varepsilon_{\max} = 13.65\%$. From Eqs. **Error! Reference source not found.** and (72), the strain is given as:

$$\varepsilon = \frac{\alpha \sigma}{E_f} + \frac{(1-\alpha)\sigma}{E_o} + \alpha \varepsilon_{\max} \tag{73}$$

The rate of energy dissipation in Eq. **Error! Reference source not found.** can now be written as:

$$\xi = \sigma \dot{\varepsilon}_p - \frac{\partial G}{\partial \alpha} \dot{\alpha} = \sigma \varepsilon_{\max} \dot{\alpha} - \frac{\partial G}{\partial \alpha} \dot{\alpha} = F \dot{\alpha} \tag{74}$$

where *F* is the driving force for the microstructural changes due to mechanical loading. As stated above we ignore the free energy associated with the microstructural changes, and the expression of *F* is:

$$F = \sigma \varepsilon_{max} - \frac{\partial G}{\partial \alpha} = \sigma \varepsilon_{max} + \sigma^2 \left(\frac{1}{2E_f} - \frac{1}{2E_o} \right) \tag{75}$$

Since at the initial stage (α =0 and σ =0), the microstructural changes have not yet taken place and *F*=0. Also from Eq. (73), the microstructural change is explicitly expressed as:

$$\alpha = \frac{\varepsilon - \dfrac{\sigma}{E_o}}{\dfrac{\sigma}{E_f} - \dfrac{\sigma}{E_o} + \varepsilon_{max}} \tag{76}$$

Now in order to examine the relation between the driving force F and microstructural changes α, we plot the outer loop of the hysteretic response, shown in Figure 11. Once the parameters $E_o, E_f, \varepsilon_{\max}$ have been determined, the experimental plot of F-α can be constructed from Eqs. (75) and (76). We then mathematically describe the F-α relationship. This can be done by using a weighted superposition of kernels of the Preisach-Krasnoselskii operator, which is described in Mayergoyz [58], [59]. The Preisach-Krasnoselskii approach describes a phenomenological hysteretic model of any physical behavior. In this study, we consider the Preisach-Krasnoselskii operator with the number of hysteron N=5050. The number of hysterons in Preisach-Krasnoselskii operator describes the smoothness of the response. The prediction of the minor loops at several loading-unloading cycles is also shown in Figure 11. The material parameters are summarized in Table 3.

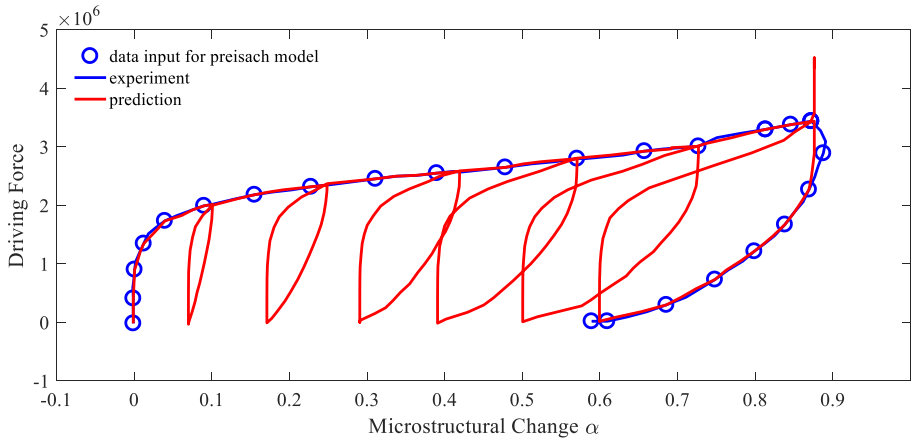

Figure 11 Relation between driving force and microstructural change for wet wood tissue of spruce during calibration of the Preisach-Krasnoselskii operator

Table 3 Material parameters for different tissue

Tissue type	$E_o(GPa)$	$E_f(GPa)$	$\varepsilon_{\max}(\%)$	N
Wet wood tissue of spruce (*Picea abies*)	1.189	1.757	13.65	5050
Isolated sclerenchyma tissue of *Aristolochia macrophylla*	3.542	4.984	4.24	5050
Outer strengthening tissue of *Aristolochia macrophylla*	1.552	1.552	2.91	5050
Inner core tissue of *Aristolochia macrophylla*	0.262	0.262	8.37	5050

The hysteretic response of a plant cell wall with microstructural changes is then determined from Eqs. (73), (75), and F-α relationship through the use of the Preisach-Krasnoselskii operator. Finally we show the prediction of the stress-strain hysteretic response of a wet wood tissue of spruce (*Picea abies*), tested by Burgert [57], in Figure 12 below. Overall the model is capable of capturing the entire hysteretic response.

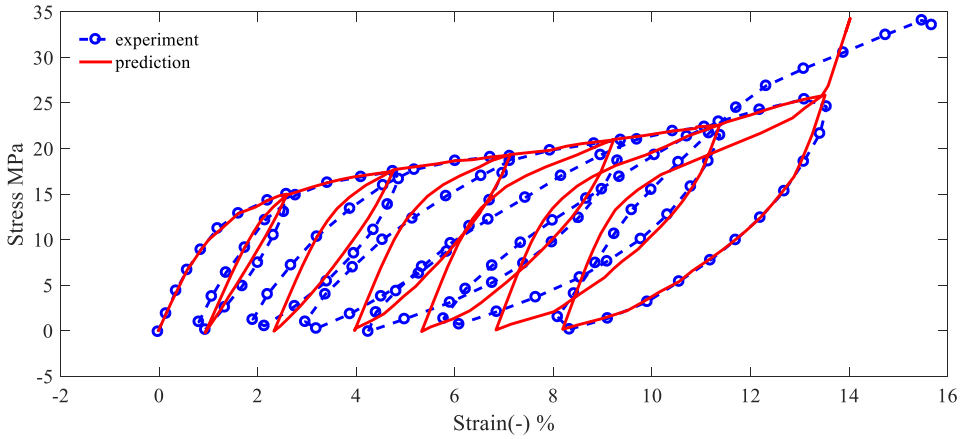

Figure 12 Modeling result of wet wood tissue of spruce

We also test the approach using a hysteretic response of a different plant cell wall. We consider an isolated sclerenchyma tissue of *Aristolochia macrophylla* tested by Köhler and Spatz [60]. The same procedure as discussed above is used to calibrate the material parameters in the model, which are listed in Table 3. Figure 13 shows the simulation results for isolated

sclerenchyma tissue of *Aristolochia macrophylla*. For both cyclic and quasi static responses, the model gives a reasonably good prediction compared to experimental result.

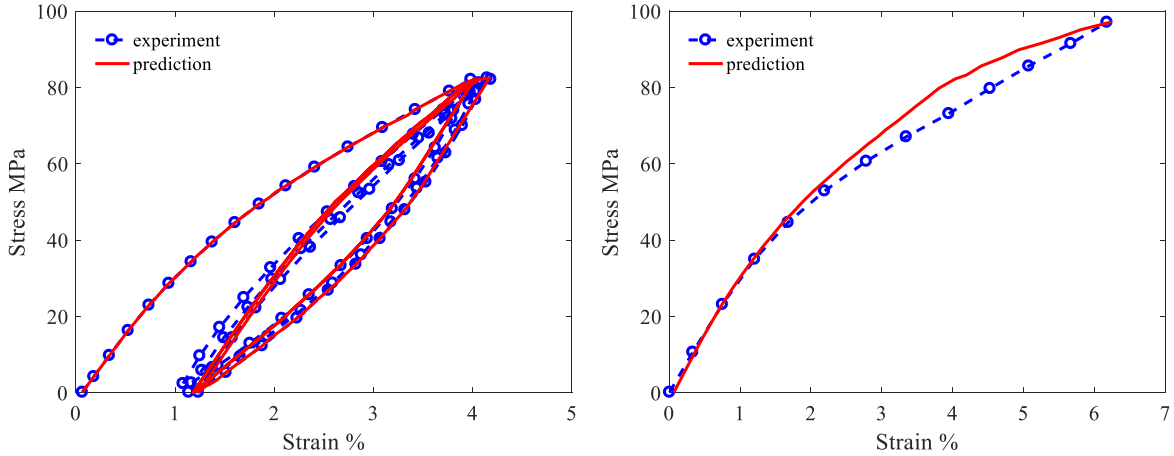

Figure 13 Simulation results for isolated sclerenchyma tissue of *Aristolochia macrophylla*. Left: cyclic response. Right: Quasi static response.

3.2.3 Investigation of the Effect of Viscoelasticity on the Hysteretic Response

Köhler and Spatz [60] discussed the viscoelastic effect of the overall hysteretic response of the isolated sclerenchyma tissue of *Aristolochia macrophylla*. The time-dependence is shown by the variation in the amount of energy dissipation with loading rates. However, they did not provide detailed time-dependent responses, e.g., creep, stress relaxation, etc., which makes it difficult, or impossible, to calibrate the parameters needed for the viscoelastic response (E_N, E_V, μ). As we can see from Eqs. (64) and (65), when $\varepsilon_V^d = 0$, the constitutive relations become:

$$\begin{aligned} \varepsilon_N &= -\frac{\partial G}{\partial \sigma_N} = \frac{\alpha \sigma_N}{E_{Nf}} + \frac{(1-\alpha)\sigma_N}{E_{No}} \\ \varepsilon_V &= -\frac{\partial G}{\partial \sigma_V} = \frac{\alpha \sigma_V}{E_{Vf}} + \frac{(1-\alpha)\sigma_V}{E_{Vo}} \end{aligned} \tag{77}$$

Together with the kinematic condition shown in Eq. (57) and equilibrium condition $\sigma = \sigma_N + \sigma_V$, the reversible strain derived from Eq. (77) can be written as follow:

$$\left(E_N + E_V\right)\varepsilon_e = \sigma \tag{78}$$

where

$$\begin{aligned} \frac{1}{E_V} &= \frac{\alpha}{E_{Vf}} + \frac{(1-\alpha)}{E_{Vo}} \\ \frac{1}{E_N} &= \frac{\alpha}{E_{Nf}} + \frac{(1-\alpha)}{E_{No}} \end{aligned} \tag{79}$$

The calibration of elastic moduli at initial and final configuration for time-independent constitutive relation shown in Eq. (78) were discussed in previous section. From Eq. (79), the elastic modulus at the initial state $\left(E_N + E_V\right)|_{\alpha=0} = E_o = E_{No} + E_{Vo}$; at final state, $\left(E_N + E_V\right)|_{\alpha=1} = E_f = E_{Nf} + E_{Vf}$. The values for E_o and E_f are depicted in Table 3. For the purpose of a qualitative study, we take $E_{No} = E_{Vo} = \frac{1}{2}E_o$ and $E_{Nf} = E_{Vf} = \frac{1}{2}E_f$. For the viscosity parameter μ, we set the characteristic time $\tau = 2000s$, hence we have $\mu_o = \tau E_{Vo}$ and $\mu_f = \tau E_{Vf}$. The above material parameters $E_{No}, E_{Vo}, \mu_o, E_{Nf}, E_{Vf}, \mu_f$ can be easily determined if we have the experimental data reported in time-domain, i.e., stress-strain-time, at the initial and final configurations, see previous work of Muliana et al. [56].

The relation between the microstructural change α and driving force F for the time-dependent model is assumed to be the same as the one from the time-independent model, which can be determined by examining the outerloop of the time-independent hysteresis loop, as discussed in the previous section.

A qualitative study for the effect of viscoelasticity on hysteresis behavior is depicted in Figure 14. The loading stress cycles between 0MPa and 80MPa, and energy dissipations per cycle

are calculated for different loading rates. The left figure in Figure 14 shows the energy dissipation for the first three cycles. As we can see from the figure, the energy dissipation of the first cycle is significantly larger than the second and third cycle. The reason for a higher energy dissipation for the first cycle is because more pronounced microstructural changes and time-dependent effect occur during first cycle, therefore more energy are dissipated. As reloading continues, the response is closer to the relaxed stage and microstructural changes vary between the reloading-unloading strains (1.8-4.8%), and hence smaller energy dissipation is seen. Thus, it can be seen that there are two sources of energy dissipation, which are from the microstructural changes and delayed response owing to the viscoelastic effect. Figure 15 shows time-dependent hysteresis responses of cycles 1-3, respectively, at loading rate $\dot{\sigma} = 1 \times 10^{-2}\, MPa / s$. As we can see from Figure 15(a), more deformation occurs during first cycle, which leads to more pronounced energy dissipation, as shown in Figure 14(left). From Figure 15(b) and (c), we can see that the shapes of hysteresis loop for cycle 2 and cycle 3 are almost the same, which means the response reaches to the steady-state. The right figure of Figure 14 shows the ratio between the dissipated energy and stored energy for the third cycle. Initially the energy dissipation increases with stress rate, then after reaching to a peak, energy dissipation decreases with increasing stress rate. The relation between energy dissipation and stress rate depicted in Figure 14 shows that the model can capture the same trend as the experimental result reported by Köhler and Spatz [60]. The time-dependent model adequately describes the effect of viscoelasticity on the hysteresis response.

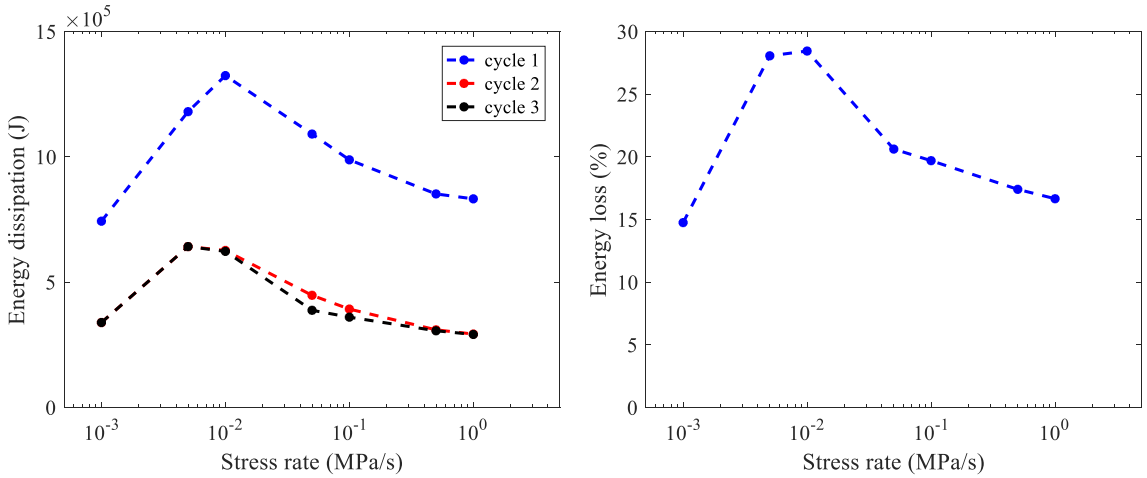

Figure 14 Quantitative study for the effect of viscoelasticity on hysteresis behavior

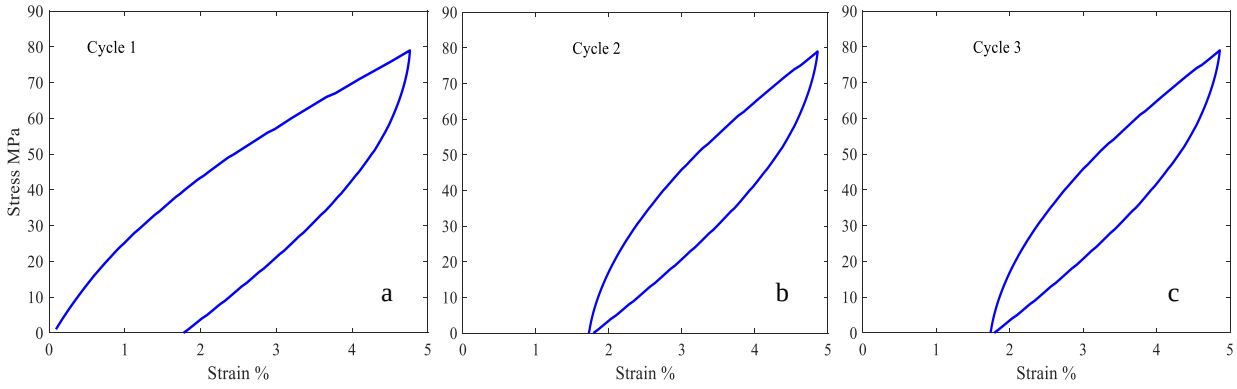

Figure 15 Time-dependent hysteresis response at stress rate $\dot{\sigma} = 1 \times 10^{-2} MPa / s$

A simulation for creep responses using the time-dependent model is depicted in Figure 16. Two stress levels, 40MPa (left) and 80MPa (right), are considered in this analysis. The loading stress is held for 1 hour. From Figure 16, we can see that the time-dependent model is capable of generating a creep-recovery curve similar to a typical linear viscoelastic material. However, unlike a linear viscoelastic material, the instantaneous deformations shown in Figure 16 during loading and unloading are not the same. The difference in the instantaneous deformations is attributed to the continuous microstructural changes during creep. Comparing the left figure of Figure 16 to the right figure, we can see that the difference in the instantaneous deformations during loading and

unloading is more obvious for the larger stress, indicating more microstructural changes occur at 80MPa. Figure 16 clearly presents the two sources of an energy dissipation: the dissipation due to a microstructural change and the dissipation due to a viscoelastic effect.

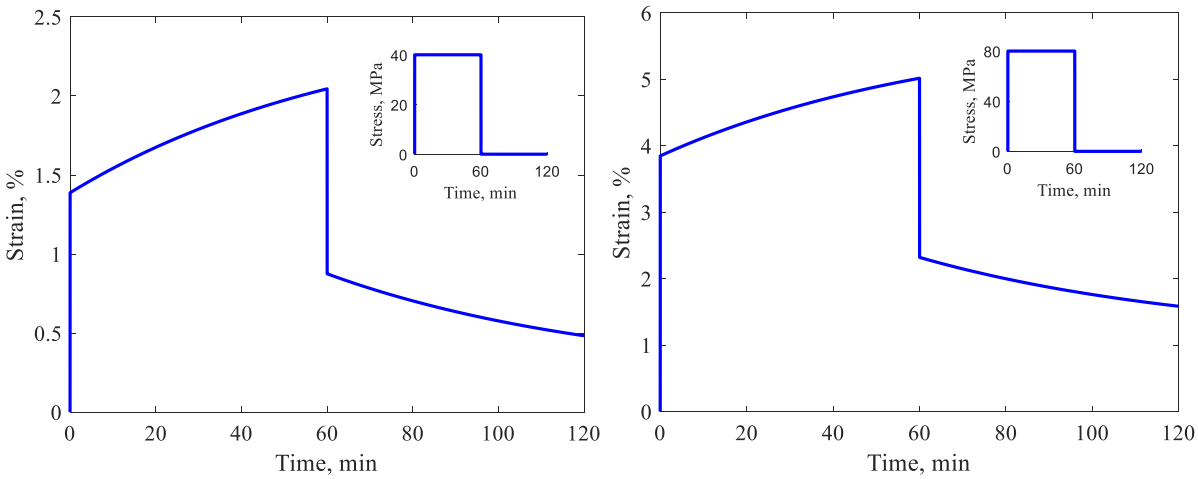

Figure 16 Creep responses generated by time-dependent model

3.3. Predicting Nonlinear Hysteretic Responses of Plant Stems

Plant stems comprise of multiple constituents with different microstructural morphologies. In a simplistic way, they can be considered as composites having outer strengthening tissue and inner core. The outer strengthening tissue consists of collenchyma, parenchyma, and sclerenchyma while the inner core comprises of phloem, xylem bundles, interfascicular parenchyma and pith [60]. We can predict the overall response of composites by incorporating different responses of the constituents and amount of the constituents in the composites, i.e., using a micromechanics model. In this study, we attempt to use a simple micromechanics model in order to capture the overall nonlinear hysteretic response of plant stems. We assume the stems as composites comprising of two different constituents (Figure 17), i.e., outer strengthening tissue and inner core, as tested by Köhler and Spatz [60].

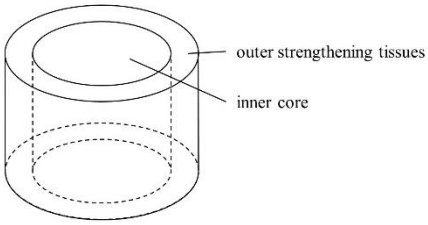

Figure 17 Structure of plant tissue (stalk)

Similar to the simulation of individual plant tissues discussed above, we assume both the outer ring and inner core experience microstructural changes when subjected to external stimuli. For a composite with two constituents, the Gibbs potential of the whole stalk is written as:

$$G(c,\alpha_1,\alpha_2,\sigma_1,\sigma_2)=(1-c)\left[-\left(\frac{\alpha_1\sigma_1^{\,2}}{2E_{1f}}+\frac{(1-\alpha_1)\sigma_1^{\,2}}{2E_{1o}}\right)\right]+c\left[\left(\frac{\alpha_2\sigma_2^{\,2}}{2E_{2f}}+\frac{(1-\alpha_2)\sigma_2^{\,2}}{2E_{2o}}\right)\right] \tag{80}$$

where

c: Volume fraction for inner core tissue

σ_1,σ_2: Independent variables represent stresses applied on the outer skin and inner core, respectively.

E_{1o},E_{1f}: Moduli of the outer strengthening tissue at $\alpha_1=0$ (initial state) and $\alpha_1=1$ (complete microstructural change), respectively.

E_{2in},E_{2f}: Moduli of the inner core tissue at $\alpha_2=0$ and $\alpha_2=1$, respectively.

Following Eq. (74), the rate of energy dissipation for the whole stalk is written as:

$$\xi=(1-c)\sigma_1\left(\dot{\varepsilon}_1-\dot{\varepsilon}_{1e}\right)+c\sigma_2\left(\dot{\varepsilon}_2-\dot{\varepsilon}_{2e}\right)-\frac{\partial G}{\partial\alpha_1}\dot{\alpha}_1-\frac{\partial G}{\partial\alpha_2}\dot{\alpha}_2 \tag{81}$$

The elastic strains for the outer skin and inner core tissues are:

$$\begin{aligned}(1-c)\varepsilon_{1e} &= -\frac{\partial G}{\partial \sigma_1} = (1-c)\left[\frac{\alpha_1\sigma_1}{E_{1f}} + \frac{(1-\alpha_1)\sigma_1}{E_{1o}}\right] \\ c\varepsilon_{2e} &= -\frac{\partial G}{\partial \sigma_2} = c\left[\frac{\alpha_2\sigma_2}{E_{2f}} + \frac{(1-\alpha_2)\sigma_2}{E_{2o}}\right]\end{aligned} \tag{82}$$

and we also assumed that

$$\begin{aligned}\varepsilon_1 - \varepsilon_{1e} = \alpha_1\varepsilon_{1\max} &\rightarrow \dot{\varepsilon}_1 - \dot{\varepsilon}_{1e} = \dot{\alpha}_1\varepsilon_{1\max} \\ \varepsilon_2 - \varepsilon_{2e} = \alpha_2\varepsilon_{2\max} &\rightarrow \dot{\varepsilon}_2 - \dot{\varepsilon}_{2e} = \dot{\alpha}_2\varepsilon_{2\max}\end{aligned} \tag{83}$$

From Eqs. (82) and (83), the strains for the outer strengthening and inner core are:

$$\begin{aligned}\varepsilon_1 &= \alpha_1\varepsilon_{1\max} + \left[\frac{\alpha_1\sigma_1}{E_{1f}} + \frac{(1-\alpha_1)\sigma_1}{E_{1o}}\right] \\ \varepsilon_2 &= \alpha_2\varepsilon_{2\max} + \left[\frac{\alpha_2\sigma_2}{E_{2f}} + \frac{(1-\alpha_2)\sigma_2}{E_{2o}}\right]\end{aligned} \tag{84}$$

Substituting Eqs. (82) and (83) into Eq.(81), the rate of energy dissipation for the whole stalk is:

$$\xi = \left[(1-c)\sigma_1\varepsilon_{1\max} - \frac{\partial G}{\partial \alpha_1}\right]\dot{\alpha}_1 + \left(c\sigma_2\varepsilon_{2\max} - \frac{\partial G}{\partial \alpha_2}\right)\dot{\alpha}_2 = (1-c)F_1\dot{\alpha}_1 + cF_2\dot{\alpha}_2 \tag{85}$$

where F_1 and F_2 are the driving forces for microstructural changes of the outer skin tissue and inner core tissue, respectively, which are:

$$\begin{aligned}F_1 &= \sigma_1\varepsilon_{1\max} + \sigma_1^{\,2}\left(\frac{1}{2E_{1f}} - \frac{1}{2E_{1o}}\right) \\ F_2 &= \sigma_2\varepsilon_{2\max} + \sigma_2^{\,2}\left(\frac{1}{2E_{2f}} - \frac{1}{2E_{2o}}\right)\end{aligned} \tag{86}$$

The microstructural changes of the outer skin and inner core are:

$$\alpha_1 = \frac{\varepsilon_1 - \dfrac{\sigma_1}{E_{1o}}}{\dfrac{\sigma_1}{E_{1f}} - \dfrac{\sigma_1}{E_{1o}} + \varepsilon_{1max}}; \qquad \alpha_2 = \frac{\varepsilon_2 - \dfrac{\sigma_2}{E_{2o}}}{\dfrac{\sigma_2}{E_{2f}} - \dfrac{\sigma_2}{E_{2o}} + \varepsilon_{2max}} \tag{87}$$

For stalks with a structure shown in Figure 17, the following kinematic and equilibrium equations for the axial loading are:

$$\begin{aligned} &\varepsilon_1 = \varepsilon_2 = \varepsilon \\ &\sigma = (1-c)\sigma_1 + c\sigma_2 \end{aligned} \tag{88}$$

From Eqs. (84) and (88) the constitutive equation for the stalk is:

$$\left[\frac{(1-c)}{\frac{\alpha_1}{E_{1f}} + \frac{1-\alpha_1}{E_{1o}}} + \frac{c}{\frac{\alpha_2}{E_{2f}} + \frac{1-\alpha_2}{E_{2o}}} \right] \varepsilon = \sigma + \frac{\alpha_1 (1-c)\varepsilon_{1\max}}{\frac{\alpha_1}{E_{1f}} + \frac{1-\alpha_1}{E_{1o}}} + \frac{\alpha_2 c \varepsilon_{2\max}}{\frac{\alpha_2}{E_{2f}} + \frac{1-\alpha_2}{E_{2o}}} \tag{89}$$

Figure 18 shows the stress-strain behaviors of the outer strengthening and inner core tissues of *Aristolochia macrophylla* stem. The experimental data are obtained from Köhler and Spatz [60]. For each of the outer and inner core tissues, material parameters are determined from the stress-strain in Figure 18. The corresponding driving force and microstructural changes for the outer strengthening and inner core tissues are obtained from Eqs. (86) and (87), as depicted in Figure 19. The material parameters are listed in Table 3. Figure 20 presents a prediction of a nonlinear response of *Aristolochia macrophylla* stem. The volume content of the inner core is determined by varying its value to give the best result of the overall response of the stalk. In this study, the volume content of 0.6 is chosen. Figure 21 shows the simulation of cyclic response for *Aristolochia macrophylla* stem, where input stress is varied between 0MPa and 16MPa. For comparison, the hysteretic responses of the outer skins and inner core are also shown.

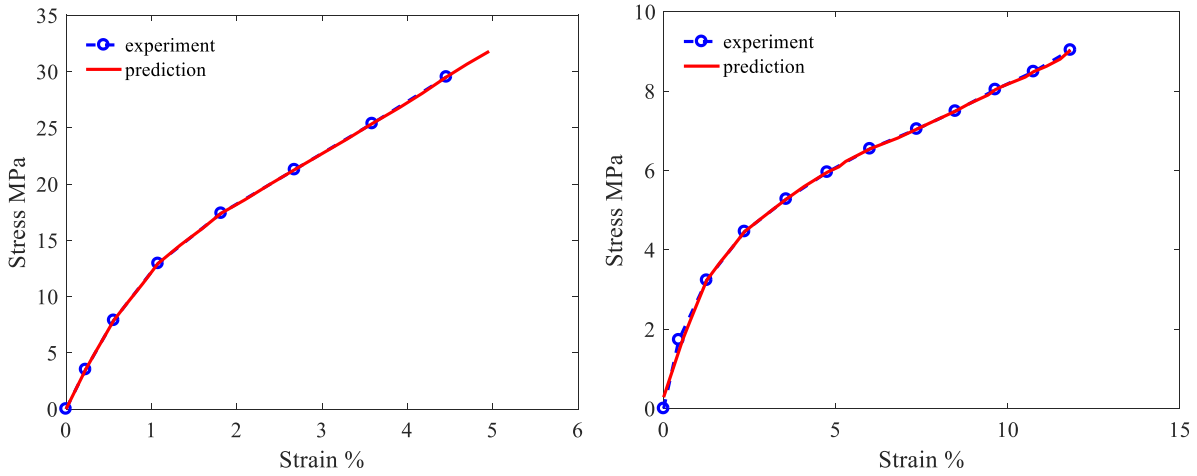

Figure 18 Simulation of strain-stress responses for outer skin and inner core of the *Aristolochia macrophylla* stem. Left: simulation for outer skin tissue. Right: simulation for inner core. Experimental data are obtained from Köhler and Spatz [60]

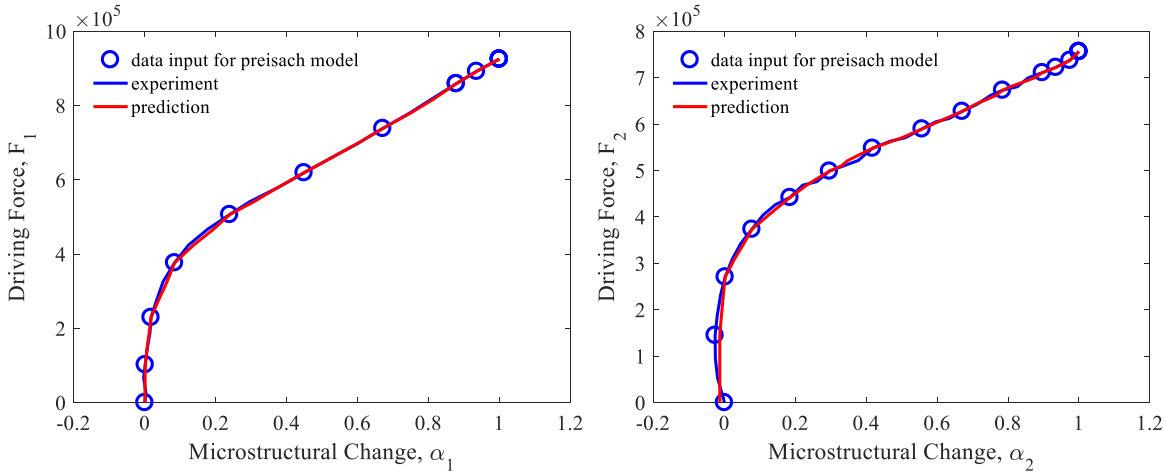

Figure 19 Relation between driving force and microstructural change for *Aristolochia macrophylla* tissue

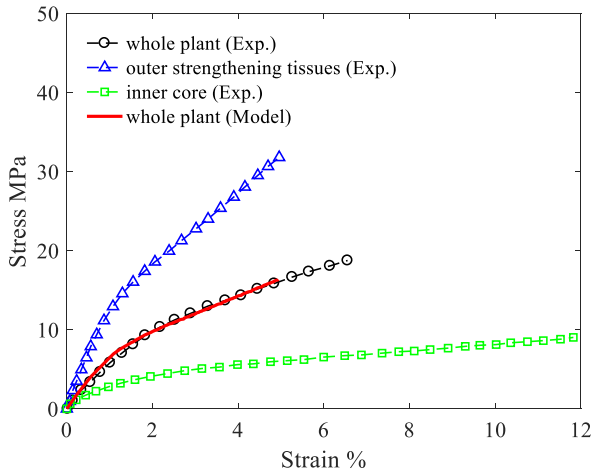

Figure 20 Response of the *Aristolochia macrophylla* stem with inner core volume fraction of 0.6

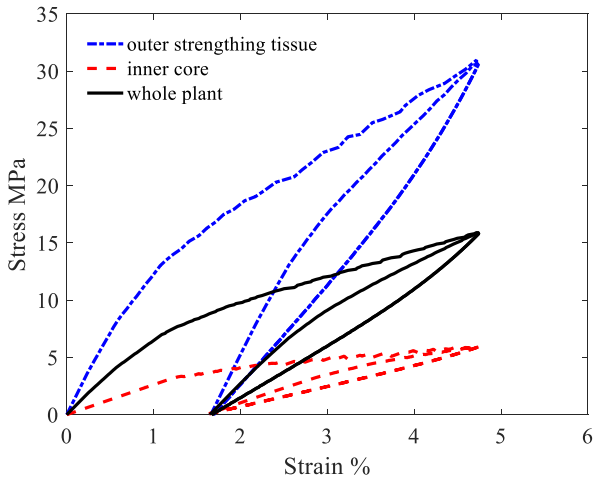

Figure 21 Simulation for the cyclic response of *Aristolochia macrophylla* stem

CHAPTER IV

THE INFLUENCE OF TEMPERATURES ON THE MICROSTRUCTURAL CHANGES IN VISCOELASTIC MATERIALS

In this chapter, multiple natural configuration approach is adopted to describe viscoelastic responses of polyoxymethylene (POM) with different molecular weight and degree of crystallinity, under different loading conditions (uniaxial tension and uniaxial compression), loading histories (loading-unloading, creep-recovery), and temperatures. Similar with the concept discussed in chapters II and III, the multiple natural configuration approach incorporates the net effect of different microstructural changes in materials, and the macroscopic response of a material is predicted by modeling the natural evolution between two configurations. Since the mechanical response for thermoplastic semi-crystalline polymers depend on the evolutions of their macromolecular networks, which are influenced by ambient temperatures, in this chapter, the thermodynamic framework discussed in Chapter II and Chapter III is extended to incorporate the temperature effect.

4.1. Experimental Tests

Three different POM materials with trademark names Delrin 100, Delrin 500, and Delrin 900 were processed and tested by Dr. Michael Berrer's group at the Polymer Competence Center Leoben (PCCL) Austria. The granular form of the materials was obtained from DuPont™ (E. I. du Pont de Nemours and Company, Wilmington Delaware, United States). The specimens were processed by a compression molding process (see a discussion in Usman 2019). The molecular weight and degree of crystallinity of the materials are given in Table 4. The glass transition temperature (Tg)

of the specimens is ???. Dogbone thin plates were used for uniaxial tensile testing. For uniaxial compression testing, the specimens were cut from the tensile bar**.** The initial cut length for the samples was 12 mm. The Milling machine Deckel (Bull & Straunz A-1092 Wien, Austria) in combination with a special self-developed clamping rod was used to grind the surfaces in order to obtain specimens with a height of 10 mm and precisely parallel surfaces. The tensile and compression specimens were loaded along the injection molding direction.

Table 4 Molecular weight and degree of crystallinity

Polymer type	Mw (g/mol)
Delrin 100	145997
Delrin 500	99488
Delrin 900	91690

The uniaxial tensile test was done according to ISO 527-1 standard. The tests were performed at different temperatures, ranging from -30^{o}C to 110^{o}C. The tests were conducted on a tensile testing machine of the type Zwick Z250 (Zwick GmbH & CO. KG Germany). To achieve the different temperatures, a temperature chamber was used together with the machine set up. Liquid Nitrogen was used inside the chamber for achieving the lower temperatures 0°C and -30°C. Before the start of the test every sample was put inside the chamber for minimum 10 min to attain the required temperature. An extensometer was used with the machine setup to record axial displacements. A cooling system was also connected to the machine to save the load cell from the higher temperatures 80°C and 110°C. The samples were clamped with mechanical clamps which were closed with the help of a torque wrench. The torque wrench was used to apply the same closing force every time and hence to keep the same conditions in all tests. The following loading

histories were considered: a ramp loading with a constant rate 1 mm/min, a loading-unloading at a rate 1 mm/min and a peak load around 70% of max load, and a creep-recovery test.

The compression tests were conducted by following the standard ISO 604 and the same temperatures as for tensile testing were considered. The machine used for uniaxial compression tests was universal testing machine of the type Instron 5500 (Instron LTD; High Wycombe, UK). The following loading histories were performed: a loading-unloading at a rate 0.085 mm/min and a peak load around 70% of max load, and a creep-recovery test.

During testing, both tension and compression, axial force and axial displacement were recorded and the engineering stress-strain measures were then determined. As expected increasing testing temperatures results in more compliant mechanical response of the polymers. Delrin 100, which has the highest weight average molecular weight, exhibits significantly larger deformations compared to Delrin 500 and Delrin 900, while insignificant differences in the maximum load and initial moduli were observed in the polymers with different molecular weight. Loading induces microstructural changes in the polymers, which are macroscopically observed by the permanent deformation upon removal of the load. The extent of microstructural changes in the polymers increases with increasing loading amplitude, as expected, and increasing temperatures accelerates the microstructural changes, as depicted in Figure 22 and Figure 23. Higher molecular weight, which indicates longer macromolecular chains and higher entanglement results in more compliant behaviors and thus slightly accelerating microstructural changes for the tension specimens, as shown in Figure 24. From the experiments, we can also conclude that at early loading, the tension and compressive responses are similar, which can be seen from the characterized initial slopes of the stress-strain responses (instantaneous moduli) in Figure 25. This should be expected as at early loading the responses are associated with the initial microstructures of the polymers. However,

tension and compressive loads induce different microstructural changes to the polymers, and from observing the permanent deformations, tension induces more pronounced microstructural changes in the polymers. Our conjecture is that the microstructural changes under tension could be associated to both void accumulation in the amorphous phase and slip mechanisms in the crystalline phase. Under compression, void formation would be absent, and the microstructural changes could be attributed to the slip mechanisms. Less microstructural changes under compression are also seen by smaller hysteretic areas compared to the ones under tension.

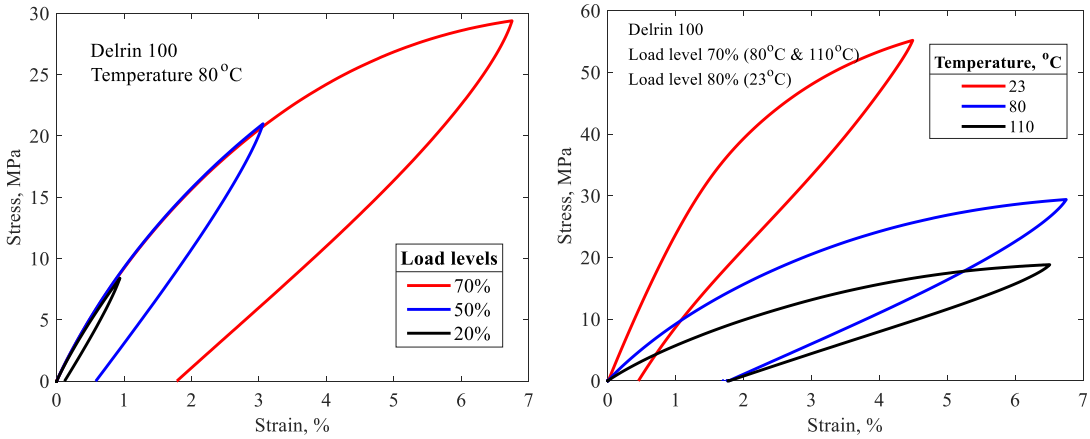

Figure 22 Loading-unloading tensile response of Delrin 100

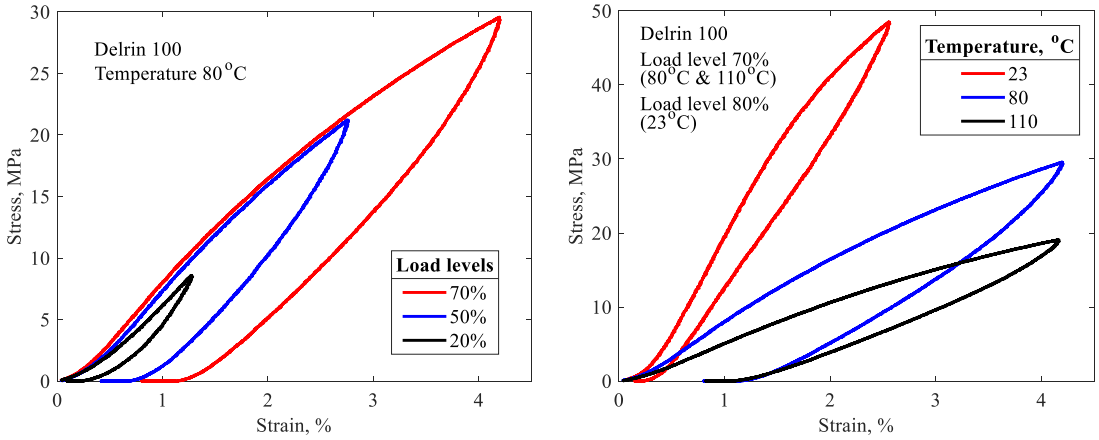

Figure 23 Loading-unloading comp response of Delrin 100

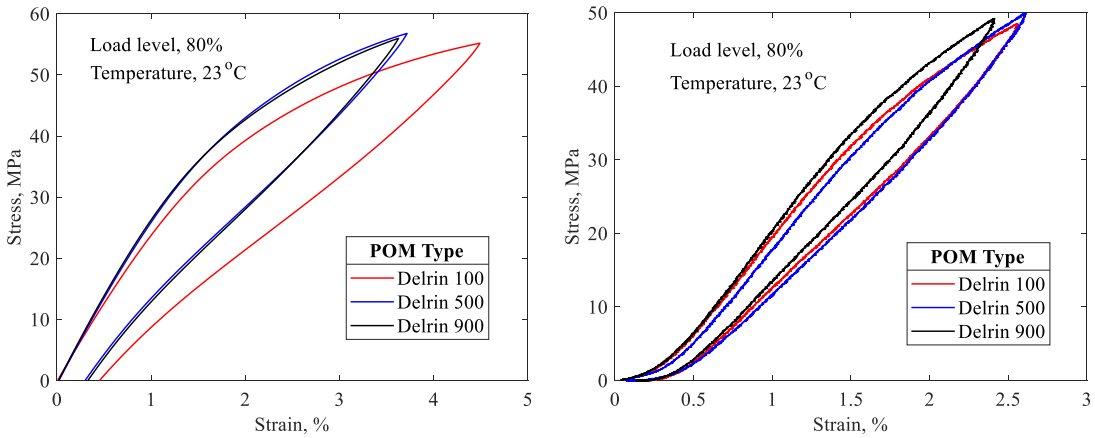

Figure 24 Loading-unloading responses for all polymers under tension (left) and compression (right)

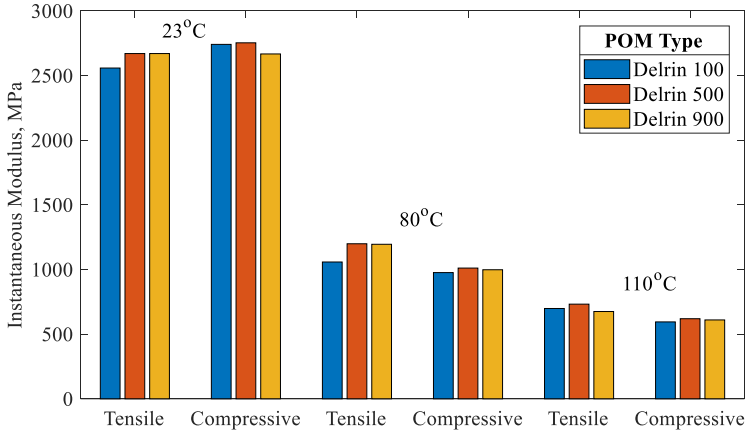

Figure 25 Instantaneous moduli under tension and compression

4.2. Constitutive Model Formulation

This section discusses a constitutive material model for semi-crystalline polymers subjected to thermal and mechanical stimuli. The model considers continuous changes in the microstructures of polymers with loadings and these microstructural changes depend on the loading rate and ambient temperature. It is assumed that the polymer microstructures are evolving between two natural configurations, which are stress free. The first configuration is associated with the initial microstructures of the polymer, and the second configuration is associated with the final

microstructures, where complete changes have taken place. Both initial and final microstructures are capable to store and dissipate energy, i.e., viscoelastic bodies.

In deriving the model, we start by defining the Gibbs free energy:

$$G = G(\boldsymbol{\sigma}_V^E, \boldsymbol{\sigma}_E, T, \alpha) = G_1(\boldsymbol{\sigma}_V^E, T, \alpha) + G_2(\boldsymbol{\sigma}_E, T, \alpha) \tag{90}$$

where G_1 represents the Gibbs free energy of both microstructures which can store and dissipate energy (viscoelastic response) and G_2 represents the Gibbs free energy of elastic response. The two stresses $\boldsymbol{\sigma}_V^E$ and $\boldsymbol{\sigma}_E$ represent stress tensors for viscoelastic response and elastic response, respectively, and T is the temperature. The evolution from initial configuration to final configuration is described with the parameter α, whose value ranges from 0 to 1. The parameter α represents the volume fraction of the newly generated (final) microstructure. When α=0, the response of the polymer is comprised that of only the original microstructure, and for α=1 the response is only due to the final microstructure.

The internal energy of the body can then be derived from the Gibbs free energy:

$$u = G + T\eta - \frac{\partial G}{\partial \boldsymbol{\sigma}_V^E} \cdot \boldsymbol{\sigma}_V^E - \frac{\partial G}{\partial \boldsymbol{\sigma}_E} \cdot \boldsymbol{\sigma}_E \tag{91}$$

where $\eta = -\dfrac{\partial G}{\partial T}$ is the specific entropy. Recall the second law of thermodynamics:

$$\xi = \boldsymbol{\sigma} \cdot \dot{\boldsymbol{\varepsilon}} - \dot{u} + T\dot{\eta} \geq 0 \tag{92}$$

where ξ is the rate of mechanical dissipation.

Since we consider small deformation gradient responses, the total strain can be decomposed into the elastic and viscoelastic parts. Also, microstructural changes result in permanent deformations in the material upon unloading. The total strain is given as:

$$\boldsymbol{\varepsilon} = \boldsymbol{\varepsilon}_E + \boldsymbol{\varepsilon}_V + \boldsymbol{\varepsilon}_P \tag{93}$$

The irreversible strain $\boldsymbol{\varepsilon}_P$ depends on microstructural change. For the elastic strain, we have:

$$\boldsymbol{\varepsilon}_E = -\frac{\partial G}{\partial \boldsymbol{\sigma}_E} \tag{94}$$

While for the viscoelastic strain, we have both elastic recovery and dissipative parts:

$$\boldsymbol{\varepsilon}_V = \boldsymbol{\varepsilon}_V^E = \boldsymbol{\varepsilon}_V^D = -\frac{\partial G}{\partial \boldsymbol{\sigma}_V^E} \tag{95}$$

The stress in the body is given as:

$$\boldsymbol{\sigma} = \boldsymbol{\sigma}_E = \boldsymbol{\sigma}_V^E + \boldsymbol{\sigma}_V^D \tag{96}$$

Substituting Eqs (91), (93), (94), and (95) into the rate of into the rate of mechanical dissipation in Eq. (92), we have:

$$\xi = \left(\boldsymbol{\sigma} - \boldsymbol{\sigma}_V^E\right) \cdot \dot{\boldsymbol{\varepsilon}}_V + (\boldsymbol{\sigma} \cdot \dot{\boldsymbol{\varepsilon}}_P - \frac{\partial G}{\partial \alpha}\dot{\alpha}) = \boldsymbol{\sigma}_V^E \cdot \dot{\boldsymbol{\varepsilon}}_V + (\boldsymbol{\sigma} \cdot \dot{\boldsymbol{\varepsilon}}_P - \frac{\partial G}{\partial \alpha}\dot{\alpha}) = \xi_D + \xi_\alpha \tag{97}$$

ξ_D and ξ_α in Eq. (97) represent the mechanical dissipation due to viscoelastic response and dissipation due to microstructural change, respectively. Since irreversible strain $\boldsymbol{\varepsilon}_P$ depends on α, ξ_α can be written as:

$$\xi_\alpha = (\boldsymbol{\sigma} \cdot \dot{\boldsymbol{\varepsilon}}_P - \frac{\partial G}{\partial \alpha}\dot{\alpha}) = (\boldsymbol{\sigma} \cdot \frac{\partial \boldsymbol{\varepsilon}_P}{\partial \alpha} - \frac{\partial G}{\partial \alpha})\dot{\alpha} = F_\alpha \dot{\alpha} \tag{98}$$

where F_α is the driving force conjugate with microstructural change α.

Equations (90)-(98) describe a general model formulation for viscoelastic polymers undergoing microstructural changes from the initial to final configurations. The next step is to choose specific forms for the Gibbs free energy, the rate of mechanical dissipation, and the evolution parameters, all of which depend on the specific materials being studied. When linear viscoelastic responses are considered for both initial and final microstructures, the following forms can be considered for the Gibbs free energy and rate of mechanical dissipation:

$$G_1(\boldsymbol{\sigma}_V^E, T, \alpha) = -\frac{1}{2}\left[(1-\alpha)\mathbf{C}_i(T)\boldsymbol{\sigma}_V^E \cdot \boldsymbol{\sigma}_V^E + \alpha \mathbf{C}_f(T)\boldsymbol{\sigma}_V^E \cdot \boldsymbol{\sigma}_V^E\right] \tag{99}$$

$$G_2(\boldsymbol{\sigma}_E, T, \alpha) = -\frac{1}{2}\left[(1-\alpha)\mathbf{D}_i(T)\boldsymbol{\sigma}_E \cdot \boldsymbol{\sigma}_E + \alpha \mathbf{D}_f(T)\boldsymbol{\sigma}_E \cdot \boldsymbol{\sigma}_E\right] \tag{100}$$

$$\xi_D = (1-\alpha)\mathbf{K}_i(T)\boldsymbol{\sigma}_V^D \cdot \boldsymbol{\sigma}_V^D + \alpha \mathbf{K}_f(T)\boldsymbol{\sigma}_V^D \cdot \boldsymbol{\sigma}_V^D \tag{101}$$

where $\mathbf{C}_i(T)$ and $\mathbf{C}_f(T)$ are the compliance tensors of the viscoelastic component of the initial and final microstructures, respectively, $\mathbf{D}_i(T)$ and $\mathbf{D}_f(T)$ are the compliance tensors of the instantaneous elastic component of the initial and final microstructures, respectively, and $\mathbf{K}_i(T)$ and $\mathbf{K}_f(T)$ are the inverse viscosity tensors of the initial and final microstructures, respectively. All of these tensors involve material properties that depend on temperatures. In this study, the evolution of microstructures is assumed to depend on the total strain in the material, $\alpha(\boldsymbol{\varepsilon})$, as previously studied by Muliana et al. [56]. When the materials do not exhibit linear responses[4], different forms can be chosen for the Gibbs free energy and rate of mechanical dissipation, which will be discussed later in this manuscript.

In this study, we assume that both initial and final microstructures comprise of isotropic viscoelastic bodies, the Gibbs free energy and rate of mechanical energy dissipation can be simplified as:

$$G_1 = -\left[(1-\alpha)\left(\frac{A_i(T)}{2}\left(I_V^E\right)^2 + B_i(T)\left(II_V^E\right)\right) + \alpha\left(\frac{A_f(T)}{2}\left(I_V^E\right)^2 + B_f(T)\left(II_V^E\right)\right)\right] \tag{102}$$

$$G_2 = -\left[(1-\alpha)\left(\frac{C_i(T)}{2}\left(I_E\right)^2 + D_i(T)\left(II_E\right)\right) + \alpha\left(\frac{C_f(T)}{2}\left(I_E\right)^2 + D_f(T)\left(II_E\right)\right)\right] \tag{103}$$

[4] A linear response of materials is considered whenever the response satisfies the superposition and proportionality of the inputs (loads).

$$\xi_D = \left[(1-\alpha)\left(\frac{\lambda_i(T)}{2}\left(I_V^D\right)^2 + \eta_i(T)\left(II_V^D\right) \right) + \alpha\left(\frac{\lambda_f(T)}{2}\left(I_V^D\right)^2 + \eta_f(T)\left(I_V^D\right) \right) \right] \tag{104}$$

In Eqs. (102)-(104) there are six scalar parameters $A_i(T), B_i(T), C_i(T), D_i(T), \lambda_i(T), \eta_i(T)$ that belong to the initial configuration, and six scalar parameters $A_f(T), B_f(T), C_f(T), D_f(T), \lambda_f(T), \eta_f(T)$ that belong to the final configuration. All of these parameters can vary with temperatures. The scalars *I* and *II* are the first and second invariants associated with the stress of the viscous and elastic stress components, i.e.,

$$\begin{aligned} I_V^E &= \mathrm{tr}(\boldsymbol{\sigma}_V^E); \quad II_V^E = \frac{1}{2}\mathrm{tr}\left(\boldsymbol{\sigma}_V^E\right)^2 \\ I_E &= \mathrm{tr}(\boldsymbol{\sigma}_E); \quad II_E = \frac{1}{2}\mathrm{tr}\left(\boldsymbol{\sigma}_E\right)^2 \\ I_V^D &= \mathrm{tr}(\boldsymbol{\sigma}_V^D); \quad II_V^D = \frac{1}{2}\mathrm{tr}\left(\boldsymbol{\sigma}_V^D\right)^2 \end{aligned} \tag{105}$$

The strain components from Eqs. (102)-(104) are then written as:

$$\boldsymbol{\varepsilon}_V^E = -\frac{\partial G}{\partial \boldsymbol{\sigma}_V^E} = (1-\alpha)\left[A_i(T) I_V^E \mathbf{I} + B_i(T)\boldsymbol{\sigma}_V^E \right] + \alpha\left[A_f(T) I_V^E \mathbf{I} + B_f(T)\boldsymbol{\sigma}_V^E \right] \tag{106}$$

$$\boldsymbol{\varepsilon}_E = -\frac{\partial G}{\partial \boldsymbol{\sigma}_E} = (1-\alpha)\left[C_i(T) I_E \mathbf{I} + D_i(T)\boldsymbol{\sigma}_E \right] + \alpha\left[C_f(T) I_E \mathbf{I} + D_f(T)\boldsymbol{\sigma}_E \right] \tag{107}$$

$$\dot{\boldsymbol{\varepsilon}}_V = \dot{\boldsymbol{\varepsilon}}_V^D = \alpha\left[\frac{\lambda_i}{2} I_V^D \mathbf{I} + \eta_i \boldsymbol{\sigma}_V^D \right] + (1-\alpha)\left[\frac{\lambda_f}{2} I_V^D \mathbf{I} + \eta_f \boldsymbol{\sigma}_V^D \right] \tag{108}$$

where **I** is the identity matrix of order 3. When the materials only exhibit elastic response, the viscous strain and its rate are equal to zero, and $C_i = \frac{-\nu_i}{E_i}; D_i = \frac{1+\nu_i}{E_i}; C_f = \frac{-\nu_f}{E_f}; D_f = \frac{1+\nu_f}{E_f};$ where E_i, ν_i are the elastic modulus and Poisson's ratio corresponding to the initial microstructures of the polymer, and E_f, ν_f are the elastic modulus and Poisson's ratio associated with the final microstructures of the polymers. Having said that the different properties attributed to different

microstructures of polymers, either from processing or microstructural changes by exposure to external stimuli, should be expected. When a relatively low load is prescribed in which the load does not induce any microstructural changes, then the material responses are attributed to the response of the initial microstructures, i.e., $\alpha = 0$.

In case the responses cannot be described by a linear model, different forms for the Gibbs free energy and rate of mechanical dissipation can be considered. In our previous study on POM polymers (Muliana et al. [56]), we found that the elastic (instantaneous) behaviors of POM could not be adequately capture by a linear model and hence a nonlinear relation was considered. The following form can be considered for G_2:

$$G_2\left(\boldsymbol{\sigma}_E, T, \alpha\right) = -\left(1-\alpha\right)\left(D_i\left(T\right)\left(\frac{e^{\beta_i(T)\sqrt{\left(I_E\right)^2}}}{\beta_i\left(T\right)} - I_E \right)\frac{I_E}{\left|I_E\right|} + H_i\left(T\right)\left(\frac{e^{\delta_i(T)\sqrt{2II_E}}}{\delta_i\left(T\right)} - \sqrt{2II_E} \right)\right) - \alpha\left(D_f\left(T\right)\left(\frac{e^{\beta_f(T)\sqrt{\left(I_E\right)^2}}}{\beta_f\left(T\right)} - I_E \right)\frac{I_E}{\left|I_E\right|} + H_f\left(T\right)\left(\frac{e^{\delta_f(T)\sqrt{2II_E}}}{\delta_f\left(T\right)} - \sqrt{2II_E} \right)\right) \tag{109}$$

The corresponding elastic strain is:

$$\boldsymbol{\varepsilon}_E = -\frac{\partial G}{\partial \boldsymbol{\sigma}_E} = (1-\alpha)\left[D_i\left(T\right)\left(e^{\beta_i(T)\sqrt{\left(I_E\right)^2}} - 1\right)\frac{I_E}{\left|I_E\right|}\mathbf{I} + H_i\left(T\right)\left(\frac{e^{\delta_i(T)\sqrt{2II_E}} - 1}{\sqrt{2II_E}} \right)\boldsymbol{\sigma}_E \right] + \alpha\left[D_f\left(T\right)\left(e^{\beta_f(T)\sqrt{\left(I_E\right)^2}} - 1\right)\frac{I_E}{\left|I_E\right|}\mathbf{I} + H_f\left(T\right)\left(\frac{e^{\delta_f(T)\sqrt{2II_E}} - 1}{\sqrt{2II_E}} \right)\boldsymbol{\sigma}_E \right] \tag{110}$$

Upon linearization, Eq. (110) reduces to a linear elastic response:

$$\boldsymbol{\varepsilon}_E = (1-\alpha)\left[D_i\left(T\right)\beta_i\left(T\right)I_E\mathbf{I} + H_i\left(T\right)\delta_i\left(T\right)\boldsymbol{\sigma}_E \right] + \alpha\left[D_f\left(T\right)\beta_f\left(T\right)I_E\mathbf{I} + H_f\left(T\right)\delta_f\left(T\right)\boldsymbol{\sigma}_E \right] \tag{111}$$

where $D\beta = -\frac{\nu}{E}$, $\mathrm{H}\delta = \frac{1+\nu}{E}$ and E and ν are the elastic modulus and Poisson's ratio, respectively. Subscripts i and f represent the initial and final configurations, respectively.

To describe long-term response of materials, it is often necessary to include more than one viscoelastic component. Additional viscoelastic components can be added to the G_1 and ξ_D, and thus the viscoelastic strain component is written as $\boldsymbol{\varepsilon}_V = \sum_{m=1}^{N} \boldsymbol{\varepsilon}_{Vm}$. We will discuss this later in the model implementation.

We also need a driving force for the microstructural changes. It is assumed that microstructural changes in the polymers are related to the macroscopic strains in the materials. It is noted that as the amount of the new microstructure in the polymer increases, the amount of the initial microstructure decreases, which is assumed to occur at the same rate. The amount of microstructural change is assumed to depend on the second invariant of the total strain:

$$\alpha(\boldsymbol{\varepsilon}) = \alpha(II_{\varepsilon}) \tag{112}$$

The amount of permanent strain will then depend on the microstructural changes, which is:

$$\boldsymbol{\varepsilon}_p(\alpha) = f\left(\alpha(II_{\varepsilon})\right) \tag{113}$$

The function that describes microstructural changes and permanent strain will be discussed later during the material calibrations.

The driving force F_α for the microstructural changes in Eq. (98) can be obtained once the form of the permanent strain evolving with the microstructural changes $\boldsymbol{\varepsilon}_P(\alpha)$ is defined. It is necessary for the rate of mechanical dissipation in Eq. (97) to be nonnegative. From the evolution of the viscoelastic mechanical response, we have $\xi_D \geq 0$, and thus we need $F_\alpha \dot{\alpha} \geq 0$. Since we assume that there is no healing in the materials, during unloading and recovery we have $\dot{\alpha} = 0$ and thus $F_\alpha \dot{\alpha} = 0$ meaning the rate of mechanical dissipation is nonnegative. During loading and creep that trigger formation of the new network ($\dot{\alpha} \geq 0$), it is necessary for $F_\alpha \geq 0$. The form for

$\boldsymbol{\varepsilon}_P(\alpha)$ should be chosen so that $\boldsymbol{\sigma}\dfrac{\partial \boldsymbol{\varepsilon}_P}{\partial \alpha} \geq 0$. We will then have restrictions to material parameters in order to satisfy the constraint in Eq. (92). We will discuss this later in the model implementation.

4.3. Material Parameter Calibrations and Predictions

The experimental tests were conducted under uniaxial loading, in tension and compression. The nonzero stress component is $\sigma_{11} = \sigma = \sigma_V^E + \sigma_V^D$. The axial strain components are $\varepsilon_{E11} = \varepsilon_E; \varepsilon_{V11} = \varepsilon_V; \varepsilon_{P11} = \varepsilon_P$ and the total axial strain is $\varepsilon = \varepsilon_E + \varepsilon_V + \varepsilon_P$. As will be shown later, when multiple viscoelastic components are considered, the total axial strain is $\varepsilon = \varepsilon_E + \sum_{m=1}^{N} \varepsilon_{Vm} + \varepsilon_P$.

From Eq. (110) the axial elastic strain component reduces to:

$$\begin{aligned}\varepsilon_E = (1-\alpha)\left[D_i(T)\left(e^{\beta_i(T)\sqrt{(\sigma_E)^2}} - 1\right) + H_i(T)\left(e^{\delta_i(T)\sqrt{(\sigma_E)^2}} - 1\right)\right] sign(\sigma_E) + \\ \alpha\left[D_f(T)\left(e^{\beta_f(T)\sqrt{(\sigma_E)^2}} - 1\right) + H_f(T)\left(e^{\delta_f(T)\sqrt{(\sigma_E)^2}} - 1\right)\right] sign(\sigma_E)\end{aligned} \tag{114}$$

Considering $\beta_i(T) = \delta_i(T);\ \beta_f(T) = \delta_f(T)$, Eq. (114) reduces to:

$$\begin{aligned}\varepsilon_E &= (1-\alpha)\left[\left(D_i(T) + H_i(T)\right)\left(e^{\beta_i(T)\sqrt{(\sigma_E)^2}} - 1\right)\right] + \alpha\left[\left(D_f(T) + H_f(T)\right)\left(e^{\beta_f(T)\sqrt{(\sigma_E)^2}} - 1\right)\right] sign(\sigma_E) \\ &= (1-\alpha)\left[C_i(T)\left(e^{\beta_i(T)\sqrt{(\sigma_E)^2}} - 1\right)\right] + \alpha\left[C_f(T)\left(e^{\beta_f(T)\sqrt{(\sigma_E)^2}} - 1\right)\right] sign(\sigma_E)\end{aligned} \tag{115}$$

From Eq. (115), upon linearization we have $C_i(T)\beta_i(T) = \dfrac{1}{E_i(T)};\ C_f(T)\beta_f(T) = \dfrac{1}{E_f(T)}$, which are obtained by taking α=0 and α=1, respectively. The elastic moduli of the initial and final configurations depend on temperatures. Taking the viscoelastic strain and its rate from Eqs. (106) and (108) and considering multiple viscoelastic components, the axial viscoelastic strain and its rate are rewritten as:

$$\varepsilon_V = \sum_{m=1}^{N}(1-\alpha)\left[\frac{1}{E_{im}(T)}\sigma_V^E\right] + \alpha\left[\frac{1}{E_{fm}(T)}\sigma_V^E\right] \tag{116}$$

$$\dot{\varepsilon}_V = \sum_{m=1}^{N}(1-\alpha)\left[\frac{1}{\mu_{im}(T)}\sigma_V^D\right] + \alpha\left[\frac{1}{\mu_{fm}(T)}\sigma_V^D\right] \tag{117}$$

where $E_{im}(T), E_{fm}(T)$ are the elastic constants of each viscoelastic component associated with the initial and final microstructures, respectively, and $\mu_{im}(T), \mu_{fm}(T)$ are the viscosities of each viscoelastic component associated with the initial and final microstructures.

4.3.1. Material Calibration at Room Temperature

From Eqs. (115)-(117) there are four parameters that need to be calibrated for the elastic strain component and four parameters for each component in the viscoelastic strain component. The material parameters of the elastic strain components were calibrated from the loading and unloading region (Figure 26), with an assumption that the time-dependent response was quite insignificant due to a relatively fast loading. The material parameters in the viscoelastic strain were calibrated from the long-term creep responses (Figure 27). During this process, it is also necessary to calibrate the corresponding microstructural evolution $\alpha(\varepsilon)$ and permanent strain $\varepsilon_P(\alpha)$. We considered the following forms:

$$\alpha(\varepsilon) = \left(\frac{\sqrt{\varepsilon^2}}{\varepsilon^{\max}}\right)^{\kappa} \tag{118}$$

$$\varepsilon_P = h(\alpha)\varepsilon^{ir} = \left(\frac{\sqrt{\varepsilon^2}}{\varepsilon^{\max}}\right)^{\kappa n}\varepsilon^{ir} \tag{119}$$

The material parameters for viscoelastic networks and parameters κ, n from Eqs. (118) and (119) are calibrated simultaneously from creep-recovery responses shown in Figure 27. The left figure

of Figure 27 depicts the creep response at relatively small stress level and short period, where microstructural evolution α is taken as zero. For POM, as shown in Figure 27 (right), the maximum failure strain in axial and lateral direction can be approximated as: $\varepsilon^{\max} = 25.2\%$. The microstructural evolution α corresponding to maximum strain $\varepsilon^{\max}$ is $\alpha = 1$ (final configuration). The calibrated value for parameter κ is 1.2. The irrecoverable strains are determined from the long-term recovery experimental data shown in Figure 27 (right) $\varepsilon^{ir} = 8.2\%$. The calibrated value for n is 1.8. The calibrated material parameters for viscoelastic networks are listed in Table 5.

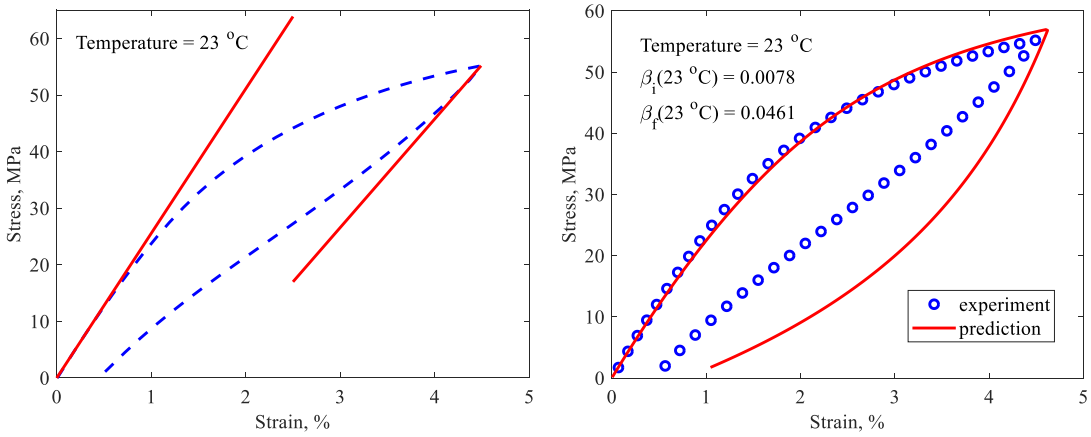

Figure 26 Loading-unloading response of Delrin 100 at room temperature

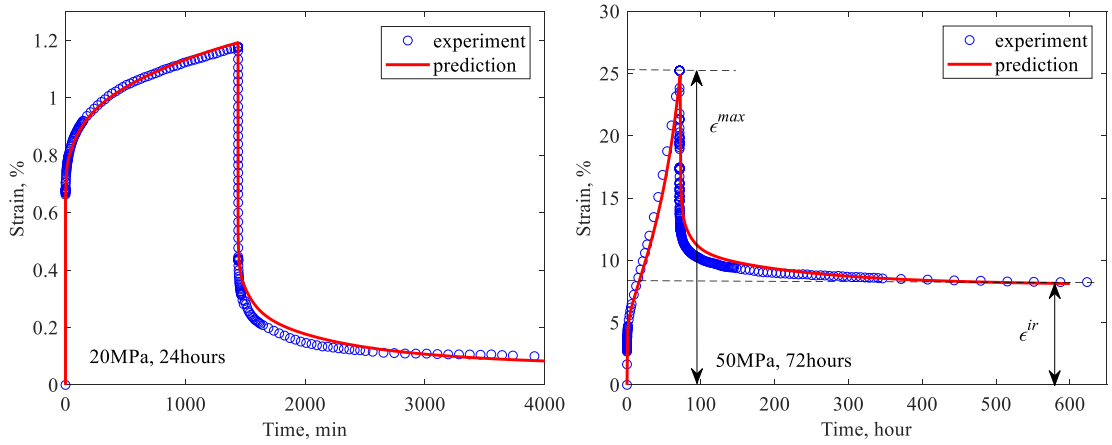

Figure 27 Calibration of material parameters of viscoelastic networks

Table 5 Time-dependent parameters at room temperature

Individual network *m*	τ_m (min)	E_{1m}^0 (GPa)	E_{2m}^0 (GPa)
1	5	48.80	1.98
2	10	47.33	2.43
3	100	20.26	1.44
4	500	27.02	3.70
5	1000	16.06	1.61
6	5000	1318.7	4.00
7	10000	5.53	0.36
8	50000	3.84	3.84

The instantaneous responses of the creep-recovery tests are calculated from Eq. (115). The instantaneous strain component is generated by elastic network, and the material parameters can be calibrated from loading-unloading tests. As shown in Figure 26, At room temperature, The values of parameters $E_i\left(23^oC\right)$, $E_f\left(23^oC\right)$, $\beta_i\left(23^oC\right)$ and $\beta_f\left(23^oC\right)$ can be calibrated from loading-unloading responses. The left figure of Figure 26 shows the calibration of elastic moduli from loading and unloading responses. It is assumed that $E^i = E^{loading}$ and $E^f = E^{unloading}$. At room temperature, we have $E^i = 2.558\text{GPa}$ and $E^f = 1.920\text{GPa}$. After elastic moduli at initial and final configurations are found, the values of parameters $\beta_i\left(23^oC\right)$ and $\beta_f\left(23^oC\right)$ can be determined by fitting the loading-unloading curve at room temperature, as shown in Figure 26 (right). The calibrated values are: $\beta_i\left(23^oC\right) = 0.0078$; $\beta_f\left(23^oC\right) = 0.0461$. After $\beta_i\left(23^oC\right)$ and $\beta_f\left(23^oC\right)$ are known, the values of parameters $C_i\left(23^oC\right)$ and $C_f\left(23^oC\right)$ can be determined from the following relations: $C_i(T)\beta_i(T) = \dfrac{1}{E_i(T)}$; $C_f(T)\beta_f(T) = \dfrac{1}{E_f(T)}$.

4.3.2. Calibration of Material Parameters at Elevated Temperatures

Eq. (115) is used to calibrate the elastic responses at different temperatures $E_i(T)$, $E_f(T)$, $\beta_i(T)$ and $\beta_f(T)$, following the same calibration process as in room temperature, as shown in Figure 28. The calibrated values are listed in Table 6. As depicted in Table 6, elastic moduli at initial and final configuration are temperature-dependent. The elastic moduli under different temperatures are plotted in Figure 29. The relations between temperature and elastic moduli at initial and final configurations are described with exponential function and linear function, respectively, as shown in Eq. (120) below:

$$\begin{aligned} E_i(T) &= 3.59\times10^3 e^{-0.015T} \\ E_f(T) &= -16.24T + 2.289\times10^3 \end{aligned} \tag{120}$$

The temperature-dependent functions $\beta_i(T)$ and $\beta_f(T)$ can be calibrated by fitting the loading-unloading responses at elevated temperatures (Figure 28). The calibrated values at 80℃ and 110℃ are listed in Table 6. The normalized expressions of $\beta_i(T)$ and $\beta_f(T)$, $\frac{\beta_i(T)}{\beta_i(23^\circ C)}$ and $\frac{\beta_f(T)}{\beta_f(23^\circ C)}$ are plotted against temperature, as shown in Figure 30.

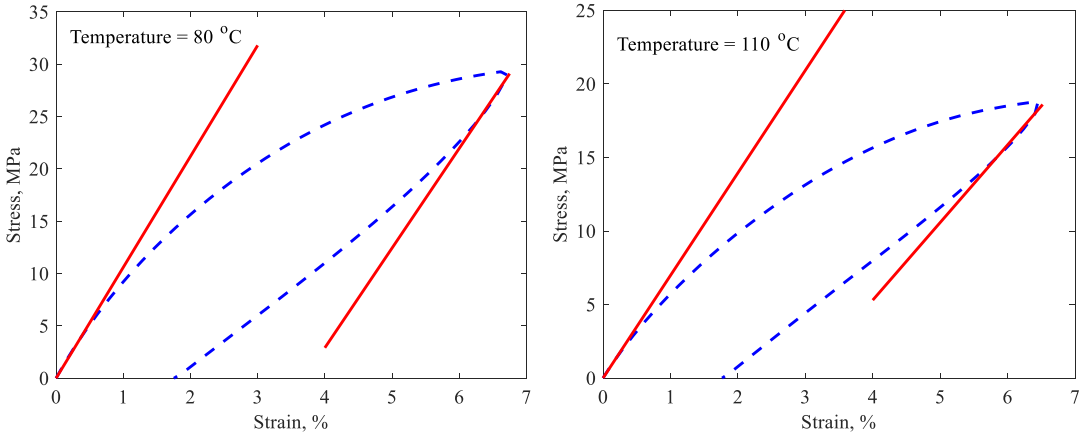

Figure 28 Top: calibration of elastic moduli at initial and final configuration; Bottom: calibration of $C_i(T)$ and $C_f(T)$ by fitting experimental data.

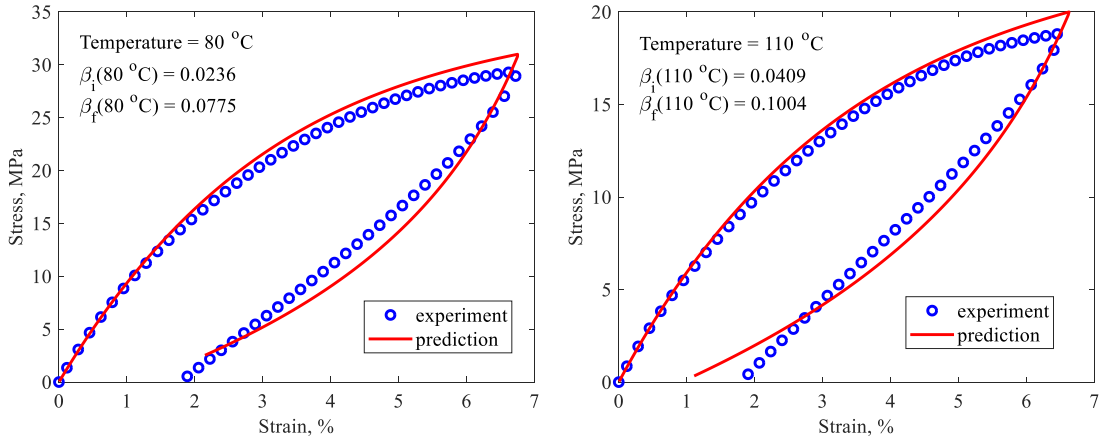

Figure 28 Continued

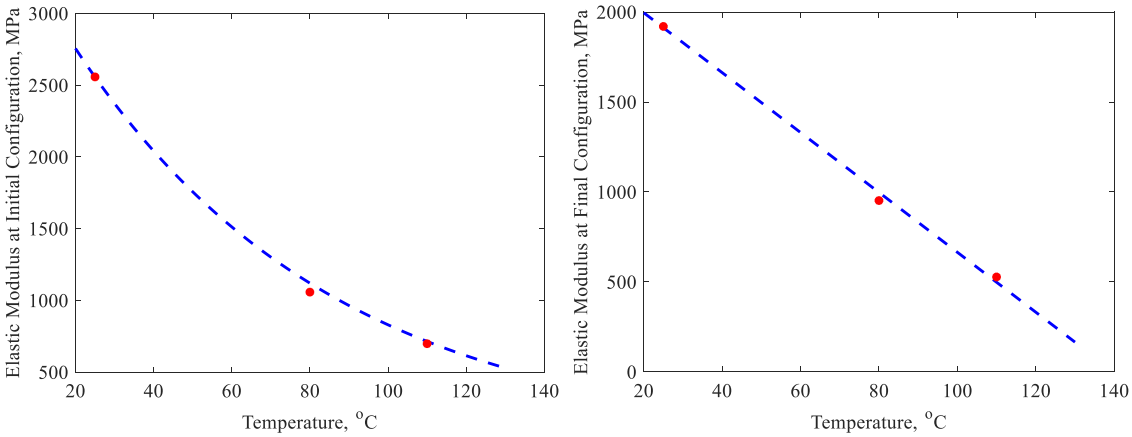

Figure 29 Relation between elastic moduli and temperature

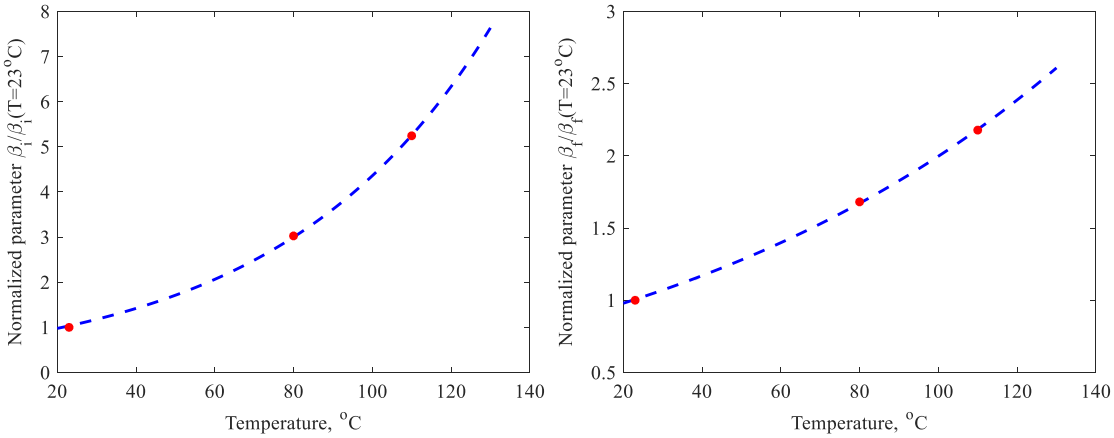

Figure 30 Relation between normalized parameters β_i, β_f and temperature

Table 6 Material parameters of elastic network (tensile)

Temperature, ℃	Type of POM	$E_i(T)$, MPa	$E_f(T)$, MPa	$\beta_i(T)$	$\beta_f(T)$
23	Derlin 100	2.558×10^3	1.920×10^3	0.0078	0.0461
	Derlin 500	2.670×10^3	1.939×10^3	0.0051	0.0456
	Derlin 900	2.759×10^3	2.143×10^3	0.0071	0.0413
80	Derlin 100	1.058×10^3	9.524×10^2	0.0236	0.0775
110	Derlin 100	6.984×10^2	5.278×10^2	0.0409	0.1004
	Derlin 500	7.320×10^2	6.675×10^2	0.0473	0.1006
	Derlin 900	6.750×10^2	6.774×10^2	0.05	0.1005

As expected from the calibrated moduli $E_i(T)$, $E_f(T)$, and nonlinear parameters $\beta_i(T)$ and $\beta_f(T)$, increasing the ambient temperature soften the polymers and increase the nonlinear mechanical response of the polymers. The relations between temperature and normalized parameters $\frac{\beta_i(T)}{\beta_i(23^oC)}$ and $\frac{\beta_f(T)}{\beta_f(23^oC)}$ are expressed with linear functions, as shown in Eq. (121) below:

$$\begin{aligned}\frac{\beta_i(T)}{\beta_i(23^oC)} &= 0.6723e^{0.01869T}\\ \frac{\beta_f(T)}{\beta_f(23^oC)} &= 0.8195e^{0.0089T}\end{aligned} \tag{121}$$

For the viscoelastic components, it is assumed that the temperature-dependent parameters in Eqs. (116), (117) can be written as the multiplication of a variable ($d_i(T)$, $d_f(T)$, etc.) and a constant (E_{im}^0, E_{fm}^0, etc.). Therefore, Eqs. (116), (117) can be rewritten as follow:

$$\begin{aligned}\varepsilon_V &= \sum_{m=1}^{M}\left[(1-\alpha)d_i(T)\frac{1}{E_{im}^0}\sigma_{Vm}^E+\alpha d_f(T)\frac{1}{E_{fm}^0}\sigma_{Vm}^E\right]\\ \dot{\varepsilon}_V &= \sum_{m=1}^{M}\left[(1-\alpha)b_i(T)\frac{1}{\mu_{im}^0}\left(\sigma-\sigma_{Vm}^E\right)+\alpha b_f(T)\frac{1}{\mu_{fm}^0}\left(\sigma-\sigma_{Vm}^E\right)\right]\end{aligned} \tag{122}$$

From Eq. (122) we have:

$$\begin{aligned}\frac{d_i(T)}{b_i(T)}\frac{\mu_{im}^0}{E_{im}^0}=\tau_{im}(T)\rightarrow a_i(T)\frac{\mu_{im}^0}{E_{im}^0}=\tau_{im}(T)\\ \frac{d_f(T)}{b_f(T)}\frac{\mu_{fm}^0}{E_{fm}^0}=\tau_{fm}(T)\rightarrow a_f(T)\frac{\mu_{fm}^0}{E_{fm}^0}=\tau_{fm}(T)\end{aligned} \tag{123}$$

In Eq. (123), $a_i(T)$ and $a_f(T)$ are the time-temperature shift factors for the initial and final configurations, respectively. Figure 31 shows the creep response for Derlin100 POM under stress 9MPa, 20MPa and temperature 80℃. The creep response shown in Figure 31 (left) is used to calibrate the values of $a_i(T)$ at initial configuration, while the creep response under stress 20MPa (Figure 31 (right)) with higher strain is used to calibrate $a_f(T)$ at final configuration. The values of $a_i(T)$ and $a_f(T)$ are adjusted until the prediction fits experimental data. The calibrated values are $a_1(80)=6.67; a_2(80)=1.82$.

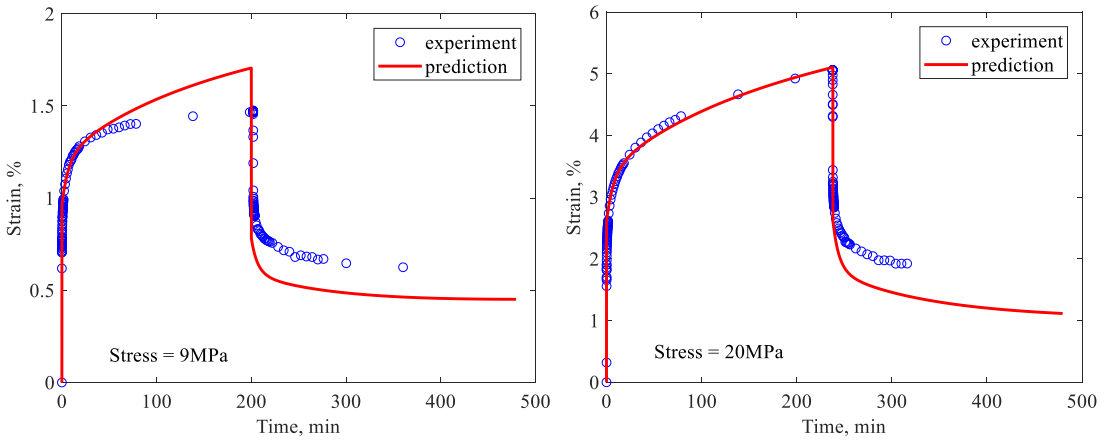

Figure 31 Creep responses at high temperature (80 ℃) of Delrin 100

4.3.3. Calibration of Material Parameters under Compressive Loading

Similar with the calibration of tensile elastic material parameters discussed above, material parameters governing compressive elastic network are calibrated from compressive loading-unloading responses. The elastic strain component under uniaxial compressive test can be written as:

$$\varepsilon_E^{comp} = (1-\alpha)\left[C_i(T)\left(e^{\beta_i(T)\sqrt{(\sigma_E)^2}}-1\right)\right]+\alpha\left[C_f^{comp}(T)\left(e^{\beta_f^{comp}(T)\sqrt{(\sigma_E)^2}}-1\right)\right]sign(\sigma_E) \qquad (124)$$

where:

$$C_i(T)\beta_i(T) = \frac{1}{E_i(T)}$$

$$C_f^{comp}(T)\beta_f^{comp}(T) = \frac{1}{E_f^{comp}(T)}$$

As shown in Eq. (124), under compressive loading, the instantaneous elastic responses for both initial and final configurations are also described with nonlinear exponential functions. Parameter α describes the evolution between initial configuration ($\varepsilon = 0$) and final configuration ($\varepsilon = \varepsilon_{\max}$). The relation between parameter α and strain ε is assumed the same with the relation for tensile responses, as depicted in Eq. (118). Since initial configurations for both tensile and compressive responses are defined the same at early loading, elastic material parameters for initial configuration in Eq. (124) are assumed the same with initial configuration parameters listed in Table 6 for tensile responses. Parameters for final configuration are calibrated from compressive loading-unloading responses.

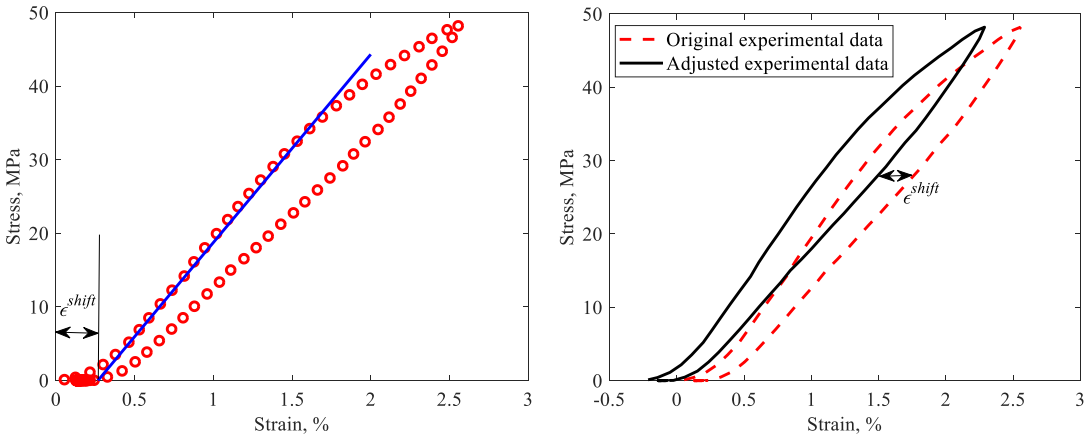

Figure 32 Adjustment for compressive loading-unloading data

As shown in the left figure of Figure 32, the initial stage of the compressive test is significantly softer compared with the rest of the stress-strain response. This behavior is due to the unsmooth top surface of the cylindrical specimen, and could be corrected by 'shifting' the stress-strain curve. It is assumed that the initial strain-stress response follows a linear relation: $\sigma = E_{in}^{comp}\varepsilon$, where $E_{in}^{comp} = E_{in}^{ten} = 2.558\text{GPa}$. As shown in Figure 32 (left), the amount of strain needs to be shifted is: $\varepsilon^{shift} = 0.267\%$. The adjusted data is depicted in the right figure of Figure 32.

The calibration of elastic material parameters at final configuration are depicted in Figure 33. At room temperature and high temperature (110℃), the values of $E_f^{comp}(T)$ and $\beta_f^{comp}(T)$ are adjusted until the prediction given by Eq. (124) could capture the experimental results reasonably well. The calibrated values are listed in Table 7.

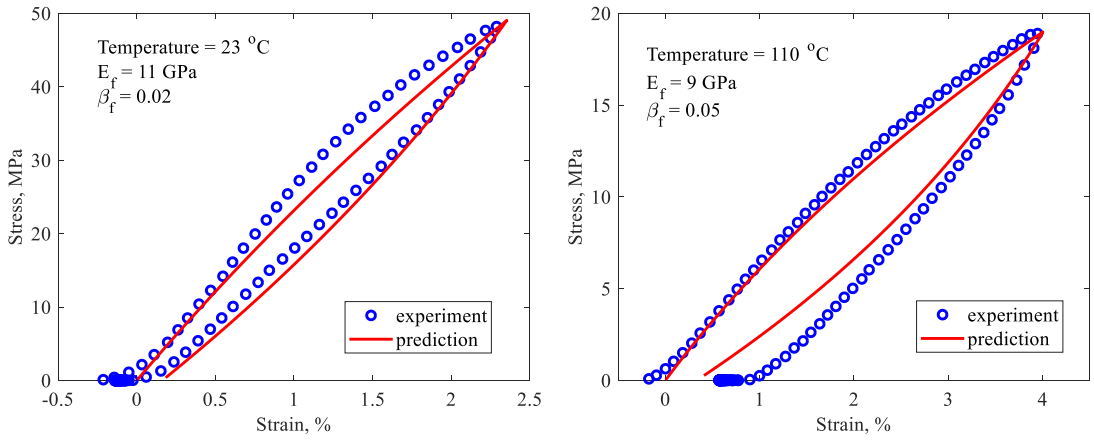

Figure 33 Calibration of elastic parameters of compressive responses for Delrin 100

Table 7 Material parameters of elastic network (compressive)

Temperature, ℃	Type of POM	$\beta_f^{comp}(T)$	$E_f^{comp}(T)$, GPa
23	Derlin 100	0.02	11
	Derlin 500	0.07	13
	Derlin 900	0.04	15
110	Derlin 100	0.05	9
	Derlin 500	0.10	10
	Derlin 900	0.08	10

Similar with tensile responses, it is assumed that both $\beta_f^{comp}(T)$ and $E_f^{comp}(T)$ can be written as exponential and linear functions of temperature, respectively. From the calibrated values under different temperatures listed in Table 7, the relations between temperature and parameters $\beta_f^{comp}(T)$ and $E_f^{comp}(T)$ could be expressed as follow:

$$\begin{aligned} \beta_f^{comp}(T) &= 5.244\times10^{-3}e^{-0.015T} \\ E_f^{comp}(T) &= -0.023T + 11.53 \end{aligned} \tag{125}$$

4.3.4. Calibration of Material Parameters of Delrin 500 and Delrin 900

Tensile, creep and compressive responses for other types of POM, Delrin 500 and Delrin 900 are also simulated. As we can see from the experimental data depicted in Figure 24, the difference between different types of POM is minor, and slight changes in the temperature-dependent functions are enough to capture the responses for all types of POM. The material parameters of viscoelastic networks for Delrin 500 and Delrin 900 are the same with the parameters calibrated from creep-recovery responses of Delrin 100, which means that the time-dependent responses for all types of POM could be captured with the same set of parameters. On the other hand, material parameters of the elastic strain component show slight difference for different types of POM.

Similar with Delrin 100, temperature-dependent elastic parameters $E_i(T)$, $E_f(T)$, $\beta_i(T)$ and $\beta_f(T)$ of Delrin 500 and Delrin 900 are calibrated from loading-unloading responses at room temperature and high temperature (110℃). These parameters are adjusted until the response calculated from Eq. (115) fits well with experimental data, as shown in Figure 34. The calibrated values are listed and compared with Delrin 100 in Table 6.

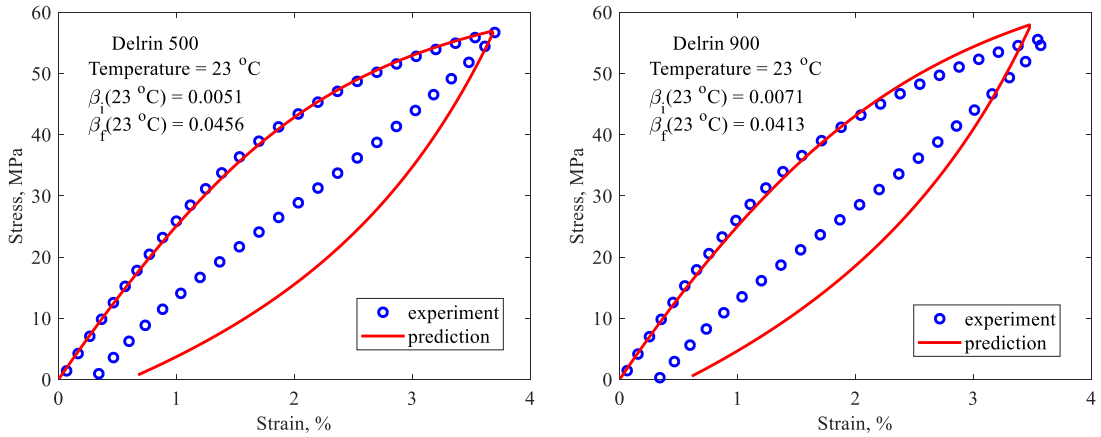

Figure 34 Calibration of tensile elastic parameters from loading-unloading responses

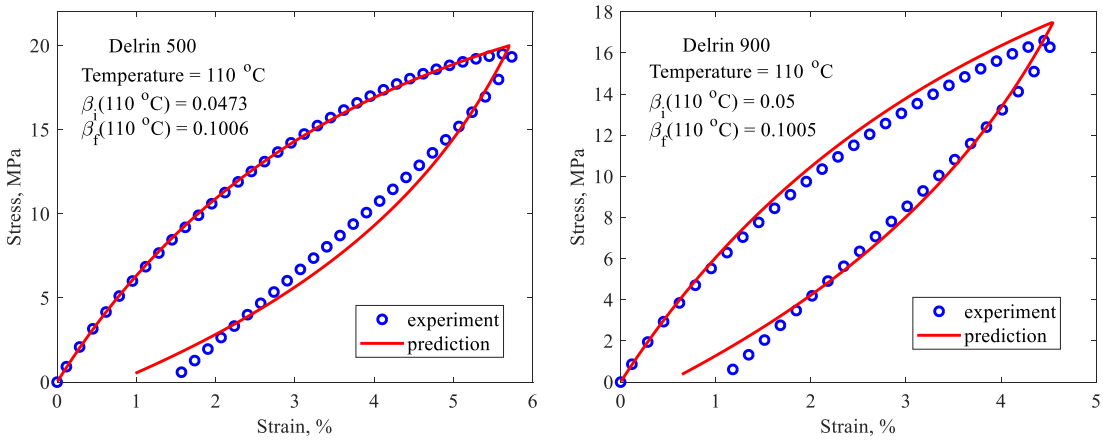

Figure 34 Continued

The format of mathematical expressions of temperature-dependent parameters $E_i(T)$, $E_f(T)$, $\beta_i(T)$ and $\beta_f(T)$ are assumed the same with Delrin 100, where $E_i(T)$, $\beta_i(T)$ and $\beta_f(T)$ can be written as exponentials function of temperature, and $E_f(T)$ is a linear function of temperature. Eq. (126) and Eq. (127) are used to relate the parameters listed in Table 6 with temperature for Delrin 500 and Delrin 900, respectively:

$$\begin{aligned} E_i(T) &= 3.93\times10^3 e^{-0.015T} \\ E_f(T) &= -14.71T + 2.268\times10^3 \\ \beta_i(T) &= 2.83\times10^{-3} e^{0.0256T} \\ \beta_f(T) &= 3.70\times10^{-2} e^{0.0091T} \end{aligned} \tag{126}$$

$$\begin{aligned} E_i(T) &= 4.06\times10^3 e^{-0.016T} \\ E_f(T) &= -16.95T + 2.523\times10^3 \\ \beta_i(T) &= 4.24\times10^{-3} e^{0.0224T} \\ \beta_f(T) &= 3.27\times10^{-2} e^{0.0102T} \end{aligned} \tag{127}$$

Compressive responses for Delrin 500 and Delrin 900 are also simulated with Eq. (124), with slight modification of the material parameters. Same with compressive response of Delrin 100, material parameters relate to initial configuration in Eq. (124) are assumed the same with the tensile initial configuration parameters listed in Table 6. The unknown temperature-dependent material

parameters in Eq. (124), $\beta_f^{comp}(T)$ and $E_f^{comp}(T)$, are calibrated from compressive loading-unloading responses at room temperature and 110℃. The values of these two parameters are adjusted simultaneously until the prediction from Eq. (124) fits well with experimental data, as shown in Figure 35. The calibrated values are listed and compared with parameters of Delrin 100 in Table 7.

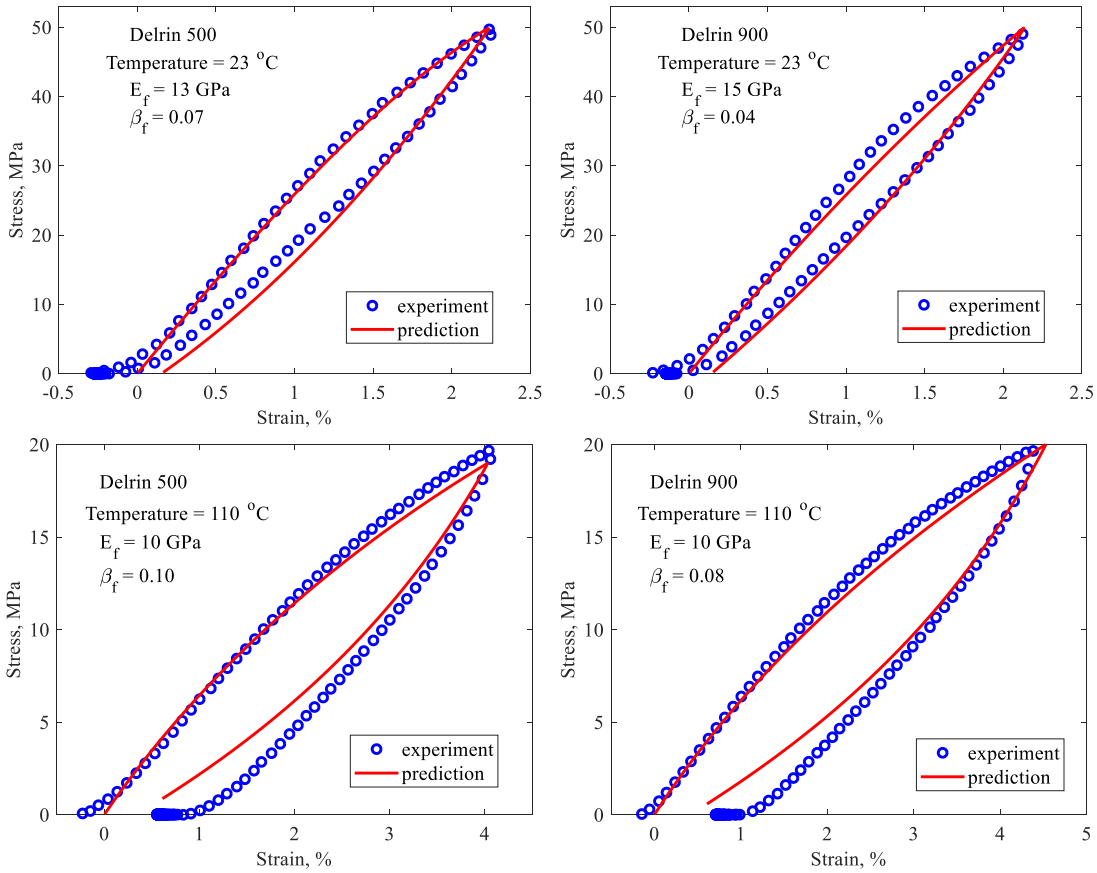

Figure 35 Calibration of compressive elastic parameters from loading-unloading responses

Following the conclusion for Delrin 100, it is assumed that $\beta_f^{comp}(T)$ and $E_f^{comp}(T)$ are exponential and linear functions of temperature, respectively. The temperature-dependent

functions of $\beta_f^{comp}(T)$ and $E_f^{comp}(T)$ for Delrin 500 and Delrin 900 are expressed in Eq. (128) and Eq. (129), respectively:

$$\begin{aligned} \beta_f^{comp}(T) &= 0.06154e^{0.0091T} \\ E_f^{comp}(T) &= -0.035T + 13.88 \end{aligned} \tag{128}$$

$$\begin{aligned} \beta_f^{comp}(T) &= 0.0333e^{0.0080T} \\ E_f^{comp}(T) &= -0.059T + 16.47 \end{aligned} \tag{129}$$

4.3.5. Model Prediction

Substituting the material parameters into constitute models discussed in section 4.2, creep responses, tensile and compressive loading-unloading responses for all types of POM are predicted and compared with experimental data. Figure 36 and Figure 37 depict the simulation of creep-recovery responses under room temperature and elevated temperature (80℃), respectively. The instantaneous responses in Figure 36 and Figure 37 are calcualted with Eq. (115), while the viscoelastic strain components are calcualted with Eqs. (116) and (117). The discrepancies in the recovery strains under stress 9 MPa in Figure 36 are attributed to experimental errors in obtaining strains below 0.2%. Overall, the conctitutive model with the calibrated material parameters could reasonably capture the creep response for all types of Delrin under varius temperatures.

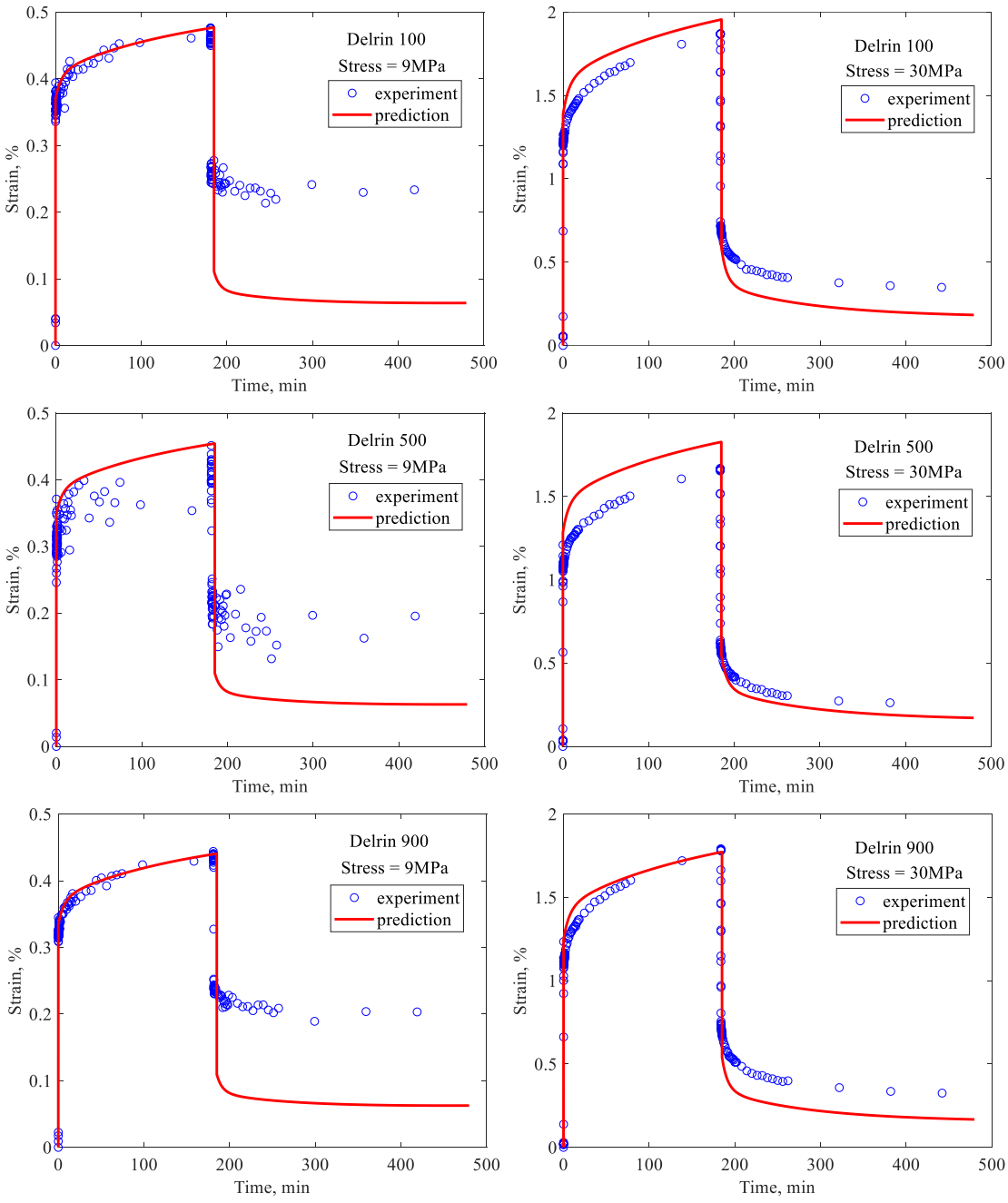

Figure 36 Creep-recovery responses at room temperature

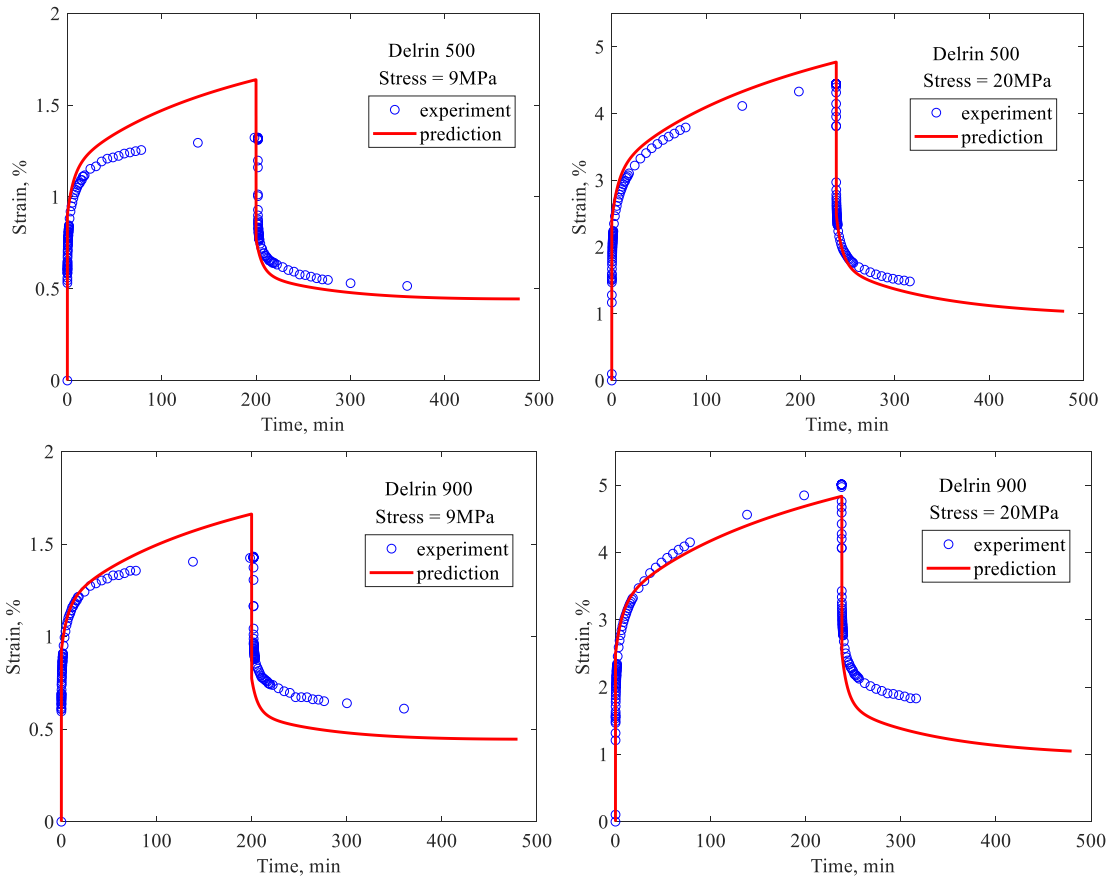

Figure 37 Creep-recovery responses at high temperature (80℃)

Constitutive model introduced in Eq. (115) are also applied to predict the tensile responses at different temperatures (Figure 38). The tensile tests depicted in Figure 38 are conducted at relatively high strain rates, therefore the time effect is quite negligible for the tensile responses. As shown in Figure 38, the temperature-dependent parameters calibrated from the loading-unloading responses could reasonably predict the tensile responses under temperatures varies from -30℃ to 110℃.

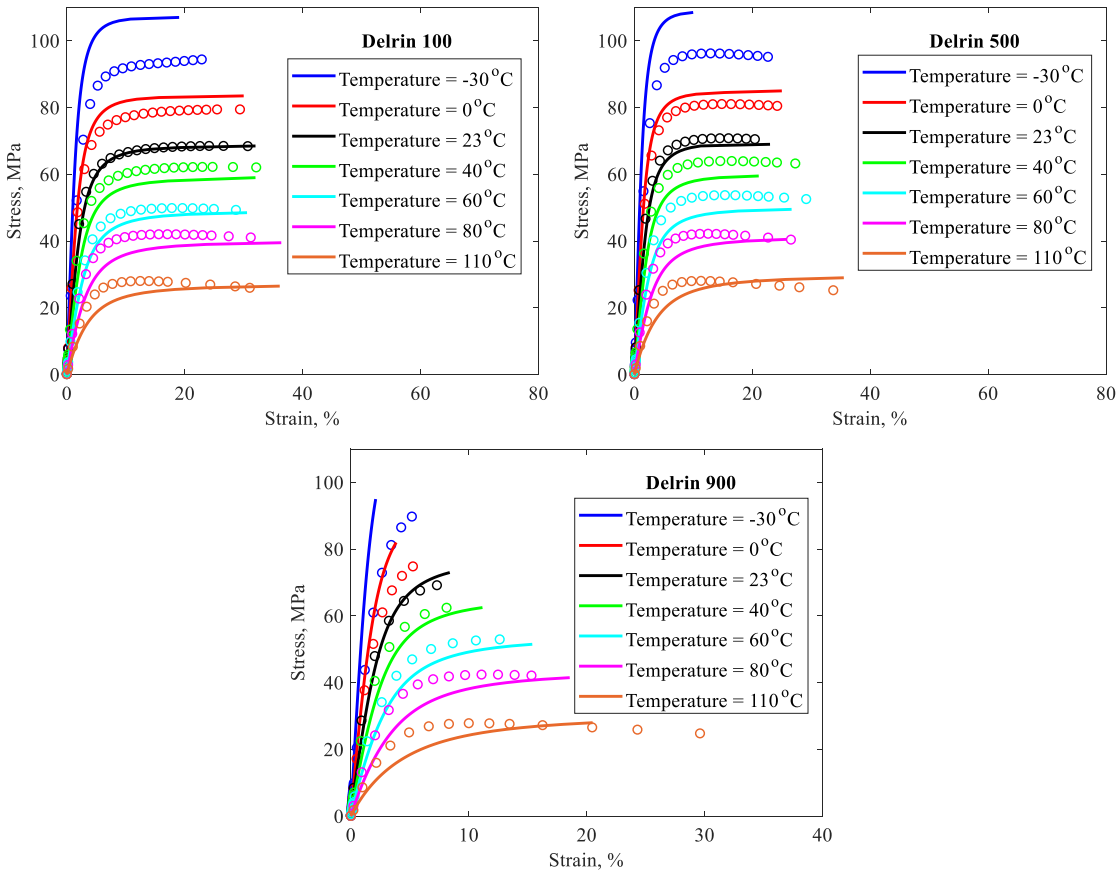

Figure 38 Tensile response (time-independent) at different temperatures

The loading-unloading responses under both uniaxial tensile and compressive loadings are also simulated in this research. Note that the strain rates for loading-unloading tests depicted in Figure 39 and Figure 40 are 1%/min for tensile tests and 0.85%/min for compressive tests. For the relatively slow strain rates, the time-effect cannot be ignored. Therefore both ε_E given by Eq. (115) and ε_V calculated from Eq. (116) contribute to the loading-unloading responses. Figure 39 shows the prediction of tensile loading-unloading responses of Delrin 500 and Delrin 900, under temperature 80°C. Figure 40 depicts the simulation of compressive loading-unloading responses for all types of POM, under temperatures 80°C. From Figure 39 and Figure 40, the temperature-

dependent expressions calibrated from loadings at 23℃ and 110℃ can reasonably predict the loading-unloading responses at 80℃.

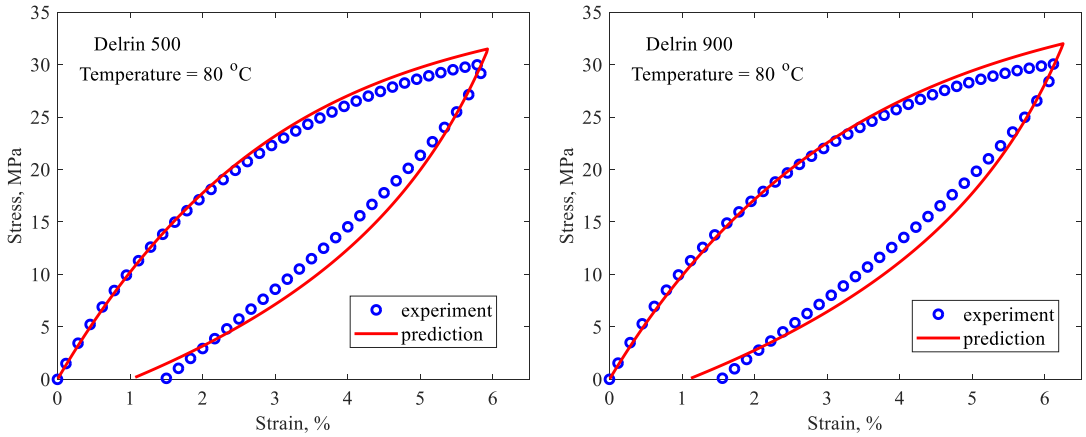

Figure 39 Tensile loading-unloading responses at 80℃. Left: Delrin 500; Right: Delrin 900

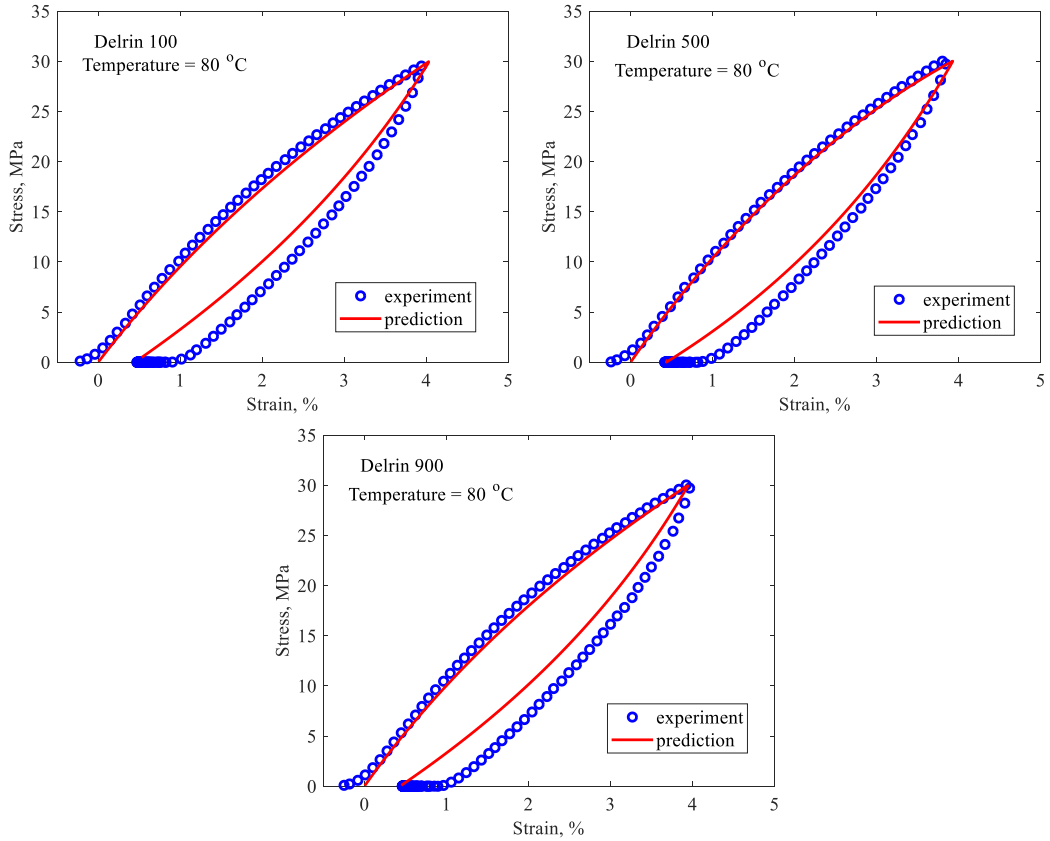

Figure 40 Compressive loading-unloading responses at 80℃ for all types of POM

CHAPTER V

TEMPERATURE-DEPENDENT CONSTITUTIVE MODEL FOR GENERAL ANISOTROPIC VISCOELASTIC MATERIALS

In this chapter, a three-dimensional, multiple natural configurations based constitutive model is developed to predict the time-dependent deformations of a transversely isotropic viscoelastic material. As an example, responses of glass fiber reinforced polyamide 6 with 40% glass fiber volume fraction (PA6GF40) along 0^o and 90^o fiber directions under different loading histories and at several isothermal temperatures are analyzed. Similar with the model discussed in Chapter IV, the constitutive model is derived from a thermodynamic framework which incorporates the temperature effect. Different loading histories, including quasi-static, cyclic and creep-recovery under different loading rates, loading amplitudes, and temperatures are predicted with the proposed constitutive model.

5.1. Formulation of Constitutive Model for Anisotropic Materials

The general formulation of temperature-dependent model for anisotropic viscoelastic materials undergoing microstructural change follows the same idea as introduced in Eqs. (91)-(101), Chapter IV. Recall when linear viscoelastic responses are considered for both initial and final microstructures, the following forms are considered for the Gibbs free energy and rate of mechanical dissipation:

$$G_1(\boldsymbol{\sigma}_V^E, T, \alpha) = -\frac{1}{2}\left[(1-\alpha)\mathbf{C}_i(T)\boldsymbol{\sigma}_V^E \cdot \boldsymbol{\sigma}_V^E + \alpha \mathbf{C}_f(T)\boldsymbol{\sigma}_V^E \cdot \boldsymbol{\sigma}_V^E\right] \tag{130}$$

$$G_2(\boldsymbol{\sigma}_E, T, \alpha) = -\frac{1}{2}\left[(1-\alpha)\mathbf{D}_i(T)\boldsymbol{\sigma}_E \cdot \boldsymbol{\sigma}_E + \alpha \mathbf{D}_f(T)\boldsymbol{\sigma}_E \cdot \boldsymbol{\sigma}_E\right] \tag{131}$$

$$\xi_D = (1-\alpha)\mathbf{K}_i(T)\boldsymbol{\sigma}_V^D \cdot \boldsymbol{\sigma}_V^D + \alpha \mathbf{K}_f(T)\boldsymbol{\sigma}_V^D \cdot \boldsymbol{\sigma}_V^D \tag{132}$$

In the above equations, $\mathbf{C}_i(T)$ and $\mathbf{C}_f(T)$ are the compliance tensors of the viscoelastic component of the initial and final microstructures, respectively, $\mathbf{D}_i(T)$ and $\mathbf{D}_f(T)$ are the compliance tensors of the instantaneous elastic component of the initial and final microstructures, respectively, and $\mathbf{K}_i(T)$ and $\mathbf{K}_f(T)$ are the inverse viscosity tensors of the initial and final microstructures, respectively.

In this study, for glass fiber reinforced polyamide (PA), we assume that both initial and final configurations comprise of transversely isotropic bodies. Spencer [61] discussed the strain energy function for a compressible, linear elastic transversely isotropic material. Following a similar idea, each of the compliance and inverse viscosity tensors in Eqs. (90)-(132) in each configuration is represented with five independent parameters. Therefore, the expressions of Gibbs free energy and rate of mechanical energy dissipation in Eqs. (90)-(132) for linear material responses can be rewritten as:

$$\begin{aligned} G_1 = &-(1-\alpha)\left(\frac{A_{1i}(T)}{2}\left(I_1^{VE}\right)^2 + A_{2i}(T) I_2^{VE} + A_{3i}(T) I_1^{VE} I_4^{VE} + \frac{A_{4i}}{2}(T)\left(I_4^{VE}\right)^2 + A_{5i}(T) I_5^{VE} \right) \\ &-\alpha\left(\frac{A_{1f}(T)}{2}\left(I_1^{VE}\right)^2 + A_{2f}(T) I_2^{VE} + A_{3f}(T) I_1^{VE} I_4^{VE} + \frac{A_{4f}}{2}(T)\left(I_4^{VE}\right)^2 + A_{5f}(T) I_5^{VE} \right) \end{aligned} \tag{133}$$

$$\begin{aligned} G_2 = &-(1-\alpha)\left(\frac{C_{1i}(T)}{2}\left(I_1^{E}\right)^2 + C_{2i}(T) I_2^{E} + C_{3i}(T) I_1^{E} I_4^{E} + \frac{C_{4i}}{2}(T)\left(I_4^{E}\right)^2 + C_{5i}(T) I_5^{E} \right) \\ &-\alpha\left(\frac{C_{1f}(T)}{2}\left(I_1^{E}\right)^2 + C_{2f}(T) I_2^{E} + C_{3f}(T) I_1^{E} I_4^{E} + \frac{C_{4f}}{2}(T)\left(I_4^{E}\right)^2 + C_{5f}(T) I_5^{E} \right) \end{aligned} \tag{134}$$

$$\begin{aligned} \xi_D = &-(1-\alpha)\left(\frac{\lambda_{1i}(T)}{2}\left(I_1^{VD}\right)^2 + \lambda_{2i}(T) I_2^{VD} + \lambda_{3i}(T) I_1^{VD} I_4^{VD} + \frac{\lambda_{4i}}{2}(T)\left(I_4^{VD}\right)^2 + \lambda_{5i}(T) I_5^{VD} \right) \\ &-\alpha\left(\frac{\lambda_{1f}(T)}{2}\left(I_1^{VD}\right)^2 + \lambda_{2f}(T) I_2^{VD} + \lambda_{3f}(T) I_1^{VD} I_4^{VD} + \frac{\lambda_{4f}}{2}(T)\left(I_4^{VD}\right)^2 + \lambda_{5f}(T) I_5^{VD} \right) \end{aligned} \tag{135}$$

where I_1 and I_2 are the first and second invariants of the stress tensor, and I_4, I_5 are functions of stress tensor and dyadic product $\mathbf{a}\otimes\mathbf{a}$. Vector $\mathbf{a}$ describes the fiber direction. The expressions of I_1, I_2, I_4 and I_5 are written as follow:

$$\begin{aligned}
&I_1^{VE}=\mathrm{tr}(\boldsymbol{\sigma}_V^E);\quad I_2^{VE}=\frac{1}{2}\mathrm{tr}\left(\boldsymbol{\sigma}_V^E\right)^2;\quad I_4^{VE}=\mathbf{a}\cdot\boldsymbol{\sigma}_V^E\cdot\mathbf{a};\quad I_5^{VE}=\mathbf{a}\cdot\left(\boldsymbol{\sigma}_V^E\right)^2\cdot\mathbf{a}\\
&I_1^{E}=\mathrm{tr}(\boldsymbol{\sigma}_E);\quad I_2^{E}=\frac{1}{2}\mathrm{tr}\left(\boldsymbol{\sigma}_E\right)^2;\quad I_4^{E}=\mathbf{a}\cdot\boldsymbol{\sigma}_E\cdot\mathbf{a};\quad I_5^{E}=\mathbf{a}\cdot\left(\boldsymbol{\sigma}_E\right)^2\cdot\mathbf{a}\\
&I_1^{VD}=\mathrm{tr}(\boldsymbol{\sigma}_V^D);\quad I_2^{VD}=\frac{1}{2}\mathrm{tr}\left(\boldsymbol{\sigma}_V^D\right)^2;\quad I_4^{VD}=\mathbf{a}\cdot\boldsymbol{\sigma}_V^D\cdot\mathbf{a};\quad I_5^{VD}=\mathbf{a}\cdot\left(\boldsymbol{\sigma}_V^D\right)^2\cdot\mathbf{a}
\end{aligned}\tag{136}$$

From Eqs. (133)-(135), for each compliance and inverse viscosity tensor in each configuration there are five temperature-dependent scalar parameters ($A_{1i}\sim A_{5i}$, $C_{1i}\sim C_{5i}$, etc.). These parameters corresponding to the five independent elastic constants of linear elastic transversely isotropic material.

The strain and strain rate components calculated from Gibbs potential given in Eqs. (133)-(135) are then written as:

$$\begin{aligned}
\boldsymbol{\varepsilon}_V^E=&(1-\alpha)\Big[\left(A_{1i}(T)\,\mathrm{tr}\left(\boldsymbol{\sigma}_V^E\right)+A_{3i}(T)\,\mathbf{a}\cdot\boldsymbol{\sigma}_V^E\cdot\mathbf{a}\right)\mathbf{I}+A_{2i}(T)\,\boldsymbol{\sigma}_V^E+\left(A_{3i}(T)\,\mathrm{tr}\left(\boldsymbol{\sigma}_V^E\right)+A_{4i}(T)\,\mathbf{a}\cdot\boldsymbol{\sigma}_V^E\cdot\mathbf{a}\right)\mathbf{a}\otimes\mathbf{a}\\
&+A_{5i}(T)\left(\mathbf{a}\otimes\mathbf{a}\cdot\boldsymbol{\sigma}_V^E+\boldsymbol{\sigma}_V^E\cdot\mathbf{a}\otimes\mathbf{a}\right)\Big]\\
&+\alpha\Big[\left(A_{1f}(T)\,\mathrm{tr}\left(\boldsymbol{\sigma}_V^E\right)+A_{3f}(T)\,\mathbf{a}\cdot\boldsymbol{\sigma}_V^E\cdot\mathbf{a}\right)\mathbf{I}+A_{2f}(T)\,\boldsymbol{\sigma}_V^E+\left(A_{3f}(T)\,\mathrm{tr}\left(\boldsymbol{\sigma}_V^E\right)+A_{4f}(T)\,\mathbf{a}\cdot\boldsymbol{\sigma}_V^E\cdot\mathbf{a}\right)\mathbf{a}\otimes\mathbf{a}\\
&+A_{5f}(T)\left(\mathbf{a}\otimes\mathbf{a}\cdot\boldsymbol{\sigma}_V^E+\boldsymbol{\sigma}_V^E\cdot\mathbf{a}\otimes\mathbf{a}\right)\Big]
\end{aligned}\tag{137}$$

$$\begin{aligned}
\boldsymbol{\varepsilon}_E=&(1-\alpha)\Big[\left(C_{1i}(T)\,\mathrm{tr}\left(\boldsymbol{\sigma}_E\right)+C_{3i}(T)\,\mathbf{a}\cdot\boldsymbol{\sigma}_E\cdot\mathbf{a}\right)\mathbf{I}+C_{2i}(T)\,\boldsymbol{\sigma}_E+\left(C_{3i}(T)\,\mathrm{tr}\left(\boldsymbol{\sigma}_E\right)+C_{4i}(T)\,\mathbf{a}\cdot\boldsymbol{\sigma}_E\cdot\mathbf{a}\right)\mathbf{a}\otimes\mathbf{a}\\
&+C_{5i}(T)\left(\mathbf{a}\otimes\mathbf{a}\cdot\boldsymbol{\sigma}_E+\boldsymbol{\sigma}_E\cdot\mathbf{a}\otimes\mathbf{a}\right)\Big]\\
&+\alpha\Big[\left(C_{1f}(T)\,\mathrm{tr}\left(\boldsymbol{\sigma}_E\right)+C_{3f}(T)\,\mathbf{a}\cdot\boldsymbol{\sigma}_E\cdot\mathbf{a}\right)\mathbf{I}+C_{2f}(T)\,\boldsymbol{\sigma}_E+\left(C_{3f}(T)\,\mathrm{tr}\left(\boldsymbol{\sigma}_E\right)+C_{4f}(T)\,\mathbf{a}\cdot\boldsymbol{\sigma}_E\cdot\mathbf{a}\right)\mathbf{a}\otimes\mathbf{a}\\
&+C_{5f}(T)\left(\mathbf{a}\otimes\mathbf{a}\cdot\boldsymbol{\sigma}_E+\boldsymbol{\sigma}_E\cdot\mathbf{a}\otimes\mathbf{a}\right)\Big]
\end{aligned}\tag{138}$$

$$\begin{aligned}\dot{\boldsymbol{\varepsilon}}_V = (1-\alpha)\Big[&\Big(\lambda_{1i}(T)\,\mathrm{tr}\big(\boldsymbol{\sigma}_V^D\big)+\lambda_{3i}(T)\,\mathbf{a}\cdot\boldsymbol{\sigma}_V^D\cdot\mathbf{a}\Big)\mathbf{I}+\lambda_{2i}(T)\,\boldsymbol{\sigma}_V^D+\Big(\lambda_{3i}(T)\,\mathrm{tr}\big(\boldsymbol{\sigma}_V^D\big)+\lambda_{4i}(T)\,\mathbf{a}\cdot\boldsymbol{\sigma}_V^D\cdot\mathbf{a}\Big)\mathbf{a}\otimes\mathbf{a}\\ &+\lambda_{5i}(T)\Big(\mathbf{a}\otimes\mathbf{a}\cdot\boldsymbol{\sigma}_V^D+\boldsymbol{\sigma}_V^D\cdot\mathbf{a}\otimes\mathbf{a}\Big)\Big]\\ +\alpha\Big[&\Big(\lambda_{1f}(T)\,\mathrm{tr}\big(\boldsymbol{\sigma}_V^D\big)+\lambda_{3f}(T)\,\mathbf{a}\cdot\boldsymbol{\sigma}_V^D\cdot\mathbf{a}\Big)\mathbf{I}+\lambda_{2f}(T)\,\boldsymbol{\sigma}_V^D+\Big(\lambda_{3f}(T)\,\mathrm{tr}\big(\boldsymbol{\sigma}_V^D\big)+\lambda_{4f}(T)\,\mathbf{a}\cdot\boldsymbol{\sigma}_V^D\cdot\mathbf{a}\Big)\mathbf{a}\otimes\mathbf{a}\\ &+\lambda_{5f}(T)\Big(\mathbf{a}\otimes\mathbf{a}\cdot\boldsymbol{\sigma}_V^D+\boldsymbol{\sigma}_V^D\cdot\mathbf{a}\otimes\mathbf{a}\Big)\Big]\end{aligned} \tag{139}$$

In this research, mechanical responses along fiber longitudinal direction (0°) and transverse direction (90°) are analyzed and validated with experimental results. Since no tests in directions other than 0° and 90° are available in this study, only three out of the five independent parameters can be calibrated from the available experimental tests. In this study, the number of independent parameters associated with each configuration is reduced to three. Therefore, in order to capture the responses under axial loadings in 0° and 90° directions, the Gibbs potential and rate of mechanical dissipation reduce to:

$$G_1 = -(1-\alpha)\left(\frac{A_{1i}(T)}{2}\left(I_1^{VE}\right)^2+A_{2i}(T)\,I_2^{VE}+\frac{A_{4i}}{2}(T)\left(I_4^{VE}\right)^2\right)-\alpha\left(\frac{A_{1f}(T)}{2}\left(I_1^{VE}\right)^2+A_{2f}(T)\,I_2^{VE}+\frac{A_{4f}}{2}(T)\left(I_4^{VE}\right)^2\right) \tag{140}$$

$$G_2 = -(1-\alpha)\left(\frac{C_{1i}(T)}{2}\left(I_1^{E}\right)^2+C_{2i}(T)\,I_2^{E}+\frac{C_{4i}}{2}(T)\left(I_4^{E}\right)^2\right)-\alpha\left(\frac{C_{1f}(T)}{2}\left(I_1^{E}\right)^2+C_{2f}(T)\,I_2^{E}+\frac{C_{4f}}{2}(T)\left(I_4^{E}\right)^2\right) \tag{141}$$

$$\xi_D = -(1-\alpha)\left(\frac{\lambda_{1i}(T)}{2}\left(I_1^{VD}\right)^2+\lambda_{2i}(T)\,I_2^{VD}+\frac{\lambda_{4i}}{2}(T)\left(I_4^{VD}\right)^2\right)-\alpha\left(\frac{\lambda_{1f}(T)}{2}\left(I_1^{VD}\right)^2+\lambda_{2f}(T)\,I_2^{VD}+\frac{\lambda_{4f}}{2}(T)\left(I_4^{VD}\right)^2\right) \tag{142}$$

By observing the experimental results of quasi-static tests, it can be seen that while the initial stress-strain relation can be described by a linear model, as strain increases, the stress-strain relation begins to show pronounced nonlinearly. Therefore, a different form of Gibbs free energy for elastic network is considered to result in a nonlinear model for the instantaneous response of final configuration. The relation of initial configuration is kept the same, to capture the linear initial response. The following form can be considered for G_2:

$$
\begin{aligned}
G_2 &= -(1-\alpha)\left(\frac{C_1(T)}{2}\left(I_1^E\right)^2 + C_2(T)I_2^E + \frac{C_4}{2}(T)\left(I_4^E\right)^2\right) \\
&-\alpha\left(D_1(T)\left(\frac{e^{\beta(T)\sqrt{\left(I_1^E\right)^2}}}{\beta(T)} - I_1^E\right)\frac{I_1^E}{\left|I_1^E\right|} + D_2(T)\left(\frac{e^{\delta(T)\sqrt{2I_2^E}}}{\delta(T)} - \sqrt{2I_2^E}\right) + D_4(T)\left(\frac{e^{\gamma(T)\sqrt{\left(I_4^E\right)^2}}}{\gamma(T)} - I_4^E\right)\frac{I_4^E}{\left|I_4^E\right|}\right)
\end{aligned}
\tag{143}
$$

The corresponding elastic strain can be written as:

$$
\begin{aligned}
\boldsymbol{\varepsilon}_E &= (1-\alpha)\left[C_1(T)I_1^E\mathbf{I} + C_2(T)\boldsymbol{\sigma}_E + \left(C_4(T)I_4^E\right)\mathbf{a}\otimes\mathbf{a}\right] \\
&+\alpha\left[D_1(T)\left(e^{\beta(T)\sqrt{\left(I_1^E\right)^2}} - 1\right)\frac{I_1^E}{\left|I_1^E\right|}\mathbf{I} + D_2(T)\left(\frac{e^{\delta(T)\sqrt{2I_2^E}} - 1}{\sqrt{2I_2^E}}\right)\boldsymbol{\sigma}_E + D_4(T)\left(e^{\gamma(T)\sqrt{\left(I_4^E\right)^2}} - 1\right)\frac{I_4^E}{\left|I_4^E\right|}\mathbf{a}\otimes\mathbf{a}\right]
\end{aligned}
\tag{144}
$$

Upon linearization, Eq. (144) reduces to a linear elastic response depicted as follow:

$$
\begin{aligned}
\boldsymbol{\varepsilon}_E &= (1-\alpha)\left[C_1(T)I_1^E\mathbf{I} + C_2(T)\boldsymbol{\sigma}_E + \left(C_4(T)I_4^E\right)\mathbf{a}\otimes\mathbf{a}\right] \\
&+\alpha\left[D_1(T)\beta(T)I_1^E\mathbf{I} + D_2(T)\delta(T)\boldsymbol{\sigma}_E + \left(D_4(T)\gamma(T)I_4^E\right)\mathbf{a}\otimes\mathbf{a}\right]
\end{aligned}
\tag{145}
$$

In this research, multiple viscoelastic components are added to the Gibbs potential G_1 and mechanical energy dissipation ξ_D to describe long-term time-dependent response of the material. Viscoelastic strain and its rate including multiple viscoelastic components can be written as:

$$
\begin{aligned}
\boldsymbol{\varepsilon}_V &= \sum_{m=1}^{N}\boldsymbol{\varepsilon}_{Vm} = (1-\alpha)\left[A_{1im}(T)I_{1m}^{VE}\mathbf{I} + A_{2im}(T)\boldsymbol{\sigma}_{Vm}^{E} + \left(A_{4im}(T)I_{4m}^{VE}\right)\mathbf{a}\otimes\mathbf{a}\right] \\
&+\alpha\left[A_{1fm}(T)I_{1m}^{VE}\mathbf{I} + A_{2fm}(T)\boldsymbol{\sigma}_{Vm}^{E} + \left(A_{4fm}(T)I_{4m}^{VE}\right)\mathbf{a}\otimes\mathbf{a}\right]
\end{aligned}
\tag{146}
$$

$$
\begin{aligned}
\dot{\boldsymbol{\varepsilon}}_V &= \sum_{m=1}^{N}\dot{\boldsymbol{\varepsilon}}_{Vm} = (1-\alpha)\left[\lambda_{1im}(T)I_{1m}^{VD}\mathbf{I} + \lambda_{2im}(T)\boldsymbol{\sigma}_{Vm}^{D} + \left(\lambda_{4im}(T)I_{4m}^{VD}\right)\mathbf{a}\otimes\mathbf{a}\right] \\
&+\alpha\left[\lambda_{1fm}(T)I_{1m}^{VD}\mathbf{I} + \lambda_{2fm}(T)\boldsymbol{\sigma}_{Vm}^{D} + \left(\lambda_{4fm}(T)I_{4m}^{VD}\right)\mathbf{a}\otimes\mathbf{a}\right]
\end{aligned}
\tag{147}
$$

Microstructural change α is related to the macroscopic strain in the material, as shown in Eq. (148). The amount of microstructural change is assumed as a power function depend on the second invariant of the total strain:

$$
\alpha(\boldsymbol{\varepsilon}) = \alpha(II_{\boldsymbol{\varepsilon}}) = \left(\frac{II_{\boldsymbol{\varepsilon}}}{II_{\varepsilon}^{\max}}\right)^n \tag{148}
$$

As the material evolving from initial configuration to final configuration, an irreversible deformation generates with the microstructural change. The amount of the generated permanent strain is assumed depend on both microstructural change and temperature, which can be expressed as follow:

$$\boldsymbol{\varepsilon}_p\left(\alpha,T\right)=f\left(\alpha(II_{\boldsymbol{\varepsilon}}),T\right)=\alpha(II_{\boldsymbol{\varepsilon}})^{\kappa(T)}\boldsymbol{\varepsilon}_p^{\max} \tag{149}$$

5.2. Material Parameter Calibrations

In this study, quasi-static, cyclic and creep-recovery tests were conducted under uniaxial loading, in both 0° and 90° fiber directions. For tests along 0° fiber direction, the nonzero stress component is $\sigma_{11}=\sigma_{E11}=\sigma_{V11}^{E}+\sigma_{V11}^{D}$. With multiple viscoelastic components considered, the total strain tensor can be written as:

$$\boldsymbol{\varepsilon}=\boldsymbol{\varepsilon}_E+\sum_{m=1}^{N}\boldsymbol{\varepsilon}_{Vm}+\boldsymbol{\varepsilon}_P \tag{150}$$

From Eq. (145), for uniaxial loadings in 0° fiber direction, the axial and lateral elastic strain components reduce to:

$$\begin{aligned}&\varepsilon_{E,axial}=\varepsilon_{E,11}=\left(1-\alpha\right)\left[C_1\left(T\right)+C_2\left(T\right)+C_4\left(T\right)\right]\sigma_{11}\\&+\alpha\left[D_1\left(T\right)\left(e^{\beta(T)\sqrt{(\sigma_{11})^2}}-1\right)+D_2\left(T\right)\left(e^{\delta(T)\sqrt{(\sigma_{11})^2}}-1\right)+D_4\left(T\right)\left(e^{\gamma(T)\sqrt{(\sigma_{11})^2}}-1\right)\right]sign(\sigma_{11})\\&\varepsilon_{E,lateral}=\varepsilon_{E,22}=\left(1-\alpha\right)C_1\left(T\right)\sigma_{11}+\alpha D_1\left(T\right)\left(e^{\beta(T)\sqrt{(\sigma_{11})^2}}-1\right)sign(\sigma_{11})\end{aligned} \tag{151}$$

For the nonlinear response of final configuration where stress-strain relation is expressed with an exponential function, we consider $\beta(T)=\delta(T)=\gamma(T)$. Therefore, Eq. (151) can be further reduced to:

$$\varepsilon_{E,axial}=\varepsilon_{E,11}=(1-\alpha)\left[C_1(T)+C_2(T)+C_4(T)\right]\sigma_{11}+\alpha\left[D_1(T)+D_2(T)+D_4(T)\right]\left(e^{\beta(T)\sqrt{(\sigma_{11})^2}}-1\right)sign(\sigma_{11})$$
$$\varepsilon_{E,lateral}=\varepsilon_{E,22}=(1-\alpha)C_1(T)\sigma_{11}+\alpha D_1(T)\left(e^{\beta(T)\sqrt{(\sigma_{11})^2}}-1\right)sign(\sigma_{11}) \quad (152)$$

Upon linearization, parameters in Eq. (152), $C_1(T)$, $C_2(T)$, $C_4(T)$, $D_1(T)$, $D_2(T)$, $D_4(T)$ and $\beta(T)$ can be related to linear elastic constants as follow. Substrates 'L' and 'T' in Eq. (153) indicate elastic constants in longitudinal (0°) and transverse (90°) direction, respectively.

$$\begin{aligned}
&C_1(T)+C_2(T)+C_4(T)=\frac{1}{E_L^{in}(T)}\\
&\left[D_1(T)+D_2(T)+D_4(T)\right]\beta(T)=\frac{1}{E_L^{f}(T)}\\
&C_1(T)=-\frac{\nu_{LT}(\alpha)}{E_L^{in}(T)}=-\frac{(1-\alpha)\nu_{LT}^{in}+\alpha\nu_{LT}^{f}}{E_L^{in}(T)}\\
&D_1(T)\beta(T)=-\frac{\nu_{LT}(\alpha)}{E_L^{f}(T)}=-\frac{(1-\alpha)\nu_{LT}^{in}+\alpha\nu_{LT}^{f}}{E_L^{in}(T)}
\end{aligned} \quad (153)$$

For viscoelastic network, under 0° uniaxial loading, axial and lateral viscoelastic strain and their rates can be rewritten as:

$$\begin{aligned}
&\varepsilon_{V,axial}=\varepsilon_{V,11}=\sum_{m=1}^{N}\varepsilon_{Vm,11}=(1-\alpha)\left[A_{1im}(T)+A_{2im}(T)+A_{4im}(T)\right]\sigma_{Vm,11}^{E}+\alpha\left[A_{1fm}(T)+A_{2fm}(T)+A_{4fm}(T)\right]\sigma_{Vm,11}^{E}\\
&\varepsilon_{V,lateral}=\varepsilon_{V,22}=\sum_{m=1}^{N}\varepsilon_{Vm,22}=(1-\alpha)A_{1im}(T)\sigma_{Vm,11}^{E}+\alpha A_{1fm}(T)\sigma_{Vm,11}^{E}\\
&\dot{\varepsilon}_{V,axial}=\dot{\varepsilon}_{V,11}=\sum_{m=1}^{N}\dot{\varepsilon}_{Vm,11}=(1-\alpha)\left[\lambda_{1im}(T)+\lambda_{2im}(T)+\lambda_{4im}(T)\right]\sigma_{Vm,11}^{D}+\alpha\left[\lambda_{1fm}(T)+\lambda_{2fm}(T)+\lambda_{4fm}(T)\right]\sigma_{Vm,11}^{D}\\
&\dot{\varepsilon}_{V,lateral}=\dot{\varepsilon}_{V,22}=\sum_{m=1}^{N}\dot{\varepsilon}_{Vm,22}=(1-\alpha)\lambda_{1im}(T)\sigma_{Vm,11}^{D}+\alpha\lambda_{1fm}(T)\sigma_{Vm,11}^{D}
\end{aligned} \quad (154)$$

where we have:

$$\begin{aligned}
&A_{1im}(T)+A_{2im}(T)+A_{4im}(T)=\frac{1}{E_{Lm}^{in}(T)};\quad A_{1im}(T)=-\frac{\nu_{LTm}(\alpha)}{E_{Lm}^{in}(T)}=-\frac{(1-\alpha)\nu_{LTm}^{in}+\alpha\nu_{LTm}^{f}}{E_{Lm}^{in}(T)}\\
&A_{1fm}(T)+A_{2fm}(T)+A_{4fm}(T)=\frac{1}{E_{Lm}^{f}(T)};\quad A_{1fm}(T)=-\frac{\nu_{LTm}(\alpha)}{E_{Lm}^{f}(T)}=-\frac{(1-\alpha)\nu_{LTm}^{in}+\alpha\nu_{LTm}^{f}}{E_{Lm}^{f}(T)}\\
&\lambda_{1im}(T)+\lambda_{2im}(T)+\lambda_{4im}(T)=\frac{1}{\mu_{Lm}^{in}(T)};\quad \lambda_{1im}(T)=-\frac{\nu_{LTm}(\alpha)}{\mu_{Lm}^{in}(T)}=-\frac{(1-\alpha)\nu_{LTm}^{in}+\alpha\nu_{LTm}^{f}}{\mu_{Lm}^{in}(T)}\\
&\lambda_{1fm}(T)+\lambda_{2fm}(T)+\lambda_{4fm}(T)=\frac{1}{\mu_{Lm}^{f}(T)};\quad \lambda_{1fm}(T)=-\frac{\nu_{LTm}(\alpha)}{\mu_{Lm}^{f}(T)}=-\frac{(1-\alpha)\nu_{LTm}^{in}+\alpha\nu_{LTm}^{f}}{\mu_{Lm}^{f}(T)}
\end{aligned} \quad (155)$$

In Eq. (155), $E_{Lim}(T)$ and $E_{Lfm}(T)$ are the elastic moduli corresponding with m^{th} viscoelastic component, associated with the initial and final microstructures, while $\mu_{Lim}(T), \mu_{Lfm}(T)$ are the viscosities of m^{th} viscoelastic component, associated with the initial and final microstructures, respectively. Substrate 'L' indicates elastic moduli and viscosities in longitudinal (0°) direction.

Similarly, for tests under uniaxial loading in 90° fiber direction, the only nonzero stress component is $\sigma_{22} = \sigma_{E22} = \sigma_{V22}^{E} + \sigma_{V22}^{D}$. Therefore, the axial and lateral elastic strain components reduce to:

$$\begin{aligned}
\varepsilon_{E,axial} &= \varepsilon_{E,22} = (1-\alpha)\left[C_1(T) + C_2(T)\right]\sigma_{22} + \alpha\left[D_1(T) + D_2(T)\right]\left(e^{\beta(T)\sqrt{(\sigma_{22})^2}} - 1\right) sign(\sigma_{22}) \\
\varepsilon_{E,lateral} &= \varepsilon_{E,11} = (1-\alpha) C_1(T)\sigma_{22} + \alpha D_1(T)\left(e^{\beta(T)\sqrt{(\sigma_{22})^2}} - 1\right) sign(\sigma_{22})
\end{aligned} \tag{156}$$

Where

$$\begin{aligned}
&C_1(T) + C_2(T) = \frac{1}{E_T^{in}(T)} \\
&\left[D_1(T) + D_2(T)\right]\beta(T) = \frac{1}{E_T^{f}(T)} \\
&C_1(T) = -\frac{\nu_{TL}(\alpha)}{E_T^{in}(T)} = -\frac{(1-\alpha)\nu_{TL}^{in} + \alpha\nu_{TL}^{f}}{E_T^{in}(T)} \\
&D_1(T)\beta(T) = -\frac{\nu_{TL}(\alpha)}{E_T^{f}(T)} = -\frac{(1-\alpha)\nu_{TL}^{in} + \alpha\nu_{TL}^{f}}{E_T^{in}(T)}
\end{aligned} \tag{157}$$

Comparing Eq. (157) with Eq. (153), the following relations must be satisfied for the compliance tensor to be symmetric:

$$\frac{\nu_{TL}^{in}}{E_T^{in}} = \frac{\nu_{LT}^{in}}{E_L^{in}}; \quad \frac{\nu_{TL}^{f}}{E_T^{f}} = \frac{\nu_{LT}^{f}}{E_L^{f}} \tag{158}$$

Deriving from Eqs. (153) and (157), parameters $C_1(T), C_2(T), C_4(T), D_1(T), D_2(T), D_4(T)$ and $\beta(T)$ can be written as functions of elastic constants of transversely isotropic material.

Under 90° uniaxial loading, axial and lateral viscoelastic strain and their rates can be rewritten as:

$$
\begin{aligned}
\varepsilon_{V,axial} &= \varepsilon_{V,22} = \sum_{m=1}^{N} \varepsilon_{Vm,22} = (1-\alpha)\left[A_{1im}(T) + A_{2im}(T)\right]\sigma_{Vm,22}^{E} + \alpha\left[A_{1fm}(T) + A_{2fm}(T)\right]\sigma_{Vm,22}^{E} \\
\varepsilon_{V,lateral} &= \varepsilon_{V,11} = \sum_{m=1}^{N} \varepsilon_{Vm,11} = (1-\alpha) A_{1im}(T)\sigma_{Vm,22}^{E} + \alpha A_{1fm}(T)\sigma_{Vm,22}^{E} \\
\dot{\varepsilon}_{V,axial} &= \dot{\varepsilon}_{V,22} = \sum_{m=1}^{N} \dot{\varepsilon}_{Vm,22} = (1-\alpha)\left[\lambda_{1im}(T) + \lambda_{2im}(T)\right]\sigma_{Vm,22}^{D} + \alpha\left[\lambda_{1fm}(T) + \lambda_{2fm}(T)\right]\sigma_{Vm,22}^{D} \\
\dot{\varepsilon}_{V,lateral} &= \dot{\varepsilon}_{V,11} = \sum_{m=1}^{N} \dot{\varepsilon}_{Vm,11} = (1-\alpha)\lambda_{1im}(T)\sigma_{Vm,22}^{D} + \alpha\lambda_{1fm}(T)\sigma_{Vm,22}^{D}
\end{aligned}
\tag{159}
$$

where we have:

$$
\begin{aligned}
&A_{1im}(T) + A_{2im}(T) = \frac{1}{E_{Tm}^{in}(T)}; \quad A_{1im}(T) = -\frac{\nu_{TLm}(\alpha)}{E_{Tm}^{in}(T)} = -\frac{(1-\alpha)\nu_{TLm}^{in} + \alpha\nu_{TLm}^{f}}{E_{Tm}^{in}(T)} \\
&A_{1fm}(T) + A_{2fm}(T) = \frac{1}{E_{Tm}^{f}(T)}; \quad A_{1fm}(T) = -\frac{\nu_{TLm}(\alpha)}{E_{Tm}^{f}(T)} = -\frac{(1-\alpha)\nu_{TLm}^{in} + \alpha\nu_{TLm}^{f}}{E_{Tm}^{f}(T)} \\
&\lambda_{1im}(T) + \lambda_{2im}(T) = \frac{1}{\mu_{Tm}^{in}(T)}; \quad \lambda_{1im}(T) = -\frac{\nu_{TLm}(\alpha)}{\mu_{Tm}^{in}(T)} = -\frac{(1-\alpha)\nu_{TLm}^{in} + \alpha\nu_{TLm}^{f}}{\mu_{Tm}^{in}(T)} \\
&\lambda_{1fm}(T) + \lambda_{2fm}(T) = \frac{1}{\mu_{Tm}^{f}(T)}; \quad \lambda_{1fm}(T) = -\frac{\nu_{TLm}(\alpha)}{\mu_{Tm}^{f}(T)} = -\frac{(1-\alpha)\nu_{TLm}^{in} + \alpha\nu_{TLm}^{f}}{\mu_{Tm}^{f}(T)}
\end{aligned}
\tag{160}
$$

In Eq. (160), for each viscoelastic component, it is required that $\frac{\nu_{TLm}^{in}}{E_{Tm}^{in}} = \frac{\nu_{LTm}^{in}}{E_{Lm}^{in}}$ and $\frac{\nu_{TLm}^{f}}{E_{Tm}^{f}} = \frac{\nu_{LTm}^{f}}{E_{Lm}^{f}}$, to make sure the compliance tensor of the viscoelastic component is symmetric. Together with Eq. (155), parameters $A_1(T)$, $A_2(T)$, $A_4(T)$, $\lambda_1(T)$, $\lambda_2(T)$ and $\lambda_4(T)$ can be expressed as functions of elastic constants and viscosities of transversely isotropic material.

5.2.1. Calibration of Material Parameters Associated with Elastic Network

As shown in Eqs. (152) and (156), in order to simulate the instantaneous response of anisotropic material PA6GF40, three independent parameters need to be calibrated for initial configuration and four parameters need to be calibrated for final configuration. These parameters are determined from cyclic tests under stress rates 5-7MPa/s and quasi-static tests under displacement rate 1mm/s, with an assumption that the time-dependent response under these relatively fast loading rates would be quite insignificant. Figure 41 shows the calibration of temperature-dependent elastic

moduli in both longitudinal and transverse directions. The maximum axial strain considered in this study is $\varepsilon^{\max} = 4.2\%$. It is assumed that when strain $\varepsilon = 4.2\%$, microstructural change $\alpha = 1$, i.e. the entire body evolved to its final configuration. As depicted in Figure 41, elastic modulus of initial configuration is calibrated by taking the slope of stress-strain curve at initial loading where $\varepsilon \approx 0$, while the elastic modulus of final configuration is calibrated from the unloading response from $\varepsilon \approx 4.2\%$ where $\alpha = 1$. The calibrated values are listed in Table 8. Recall that in Chapter IV, for thermoplastic polymer POM, the temperature-dependent elastic moduli for initial and final configurations are modeled as exponential and linear functions of temperature, respectively. For PA6GF40, similar relations between elastic moduli and temperature are assumed. Elastic moduli of initial and final configurations are modeled using exponential and linear functions of temperature, respectively. Their expressions are depicted as follow:

$$\begin{aligned} E_L^{in}(T) &= 10.91e^{-0.0050T} \\ E_L^{f}(T) &= 10.73 - 0.072T \\ E_T^{in}(T) &= 7.54e^{-0.0072T} \\ E_T^{f}(T) &= 6.15 - 0.042T \end{aligned} \tag{161}$$

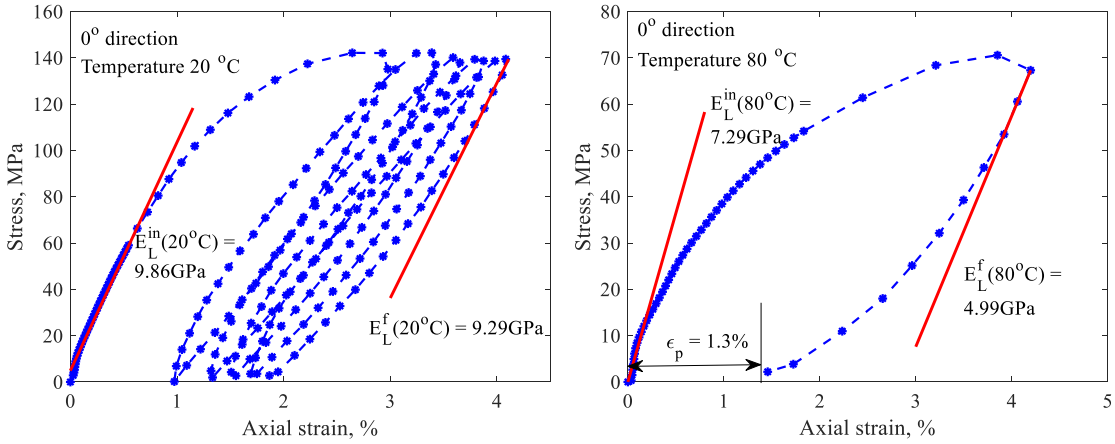

Figure 41 Calibration of temperature-dependent elastic moduli in longitudinal (0°) and transverse (90°) directions

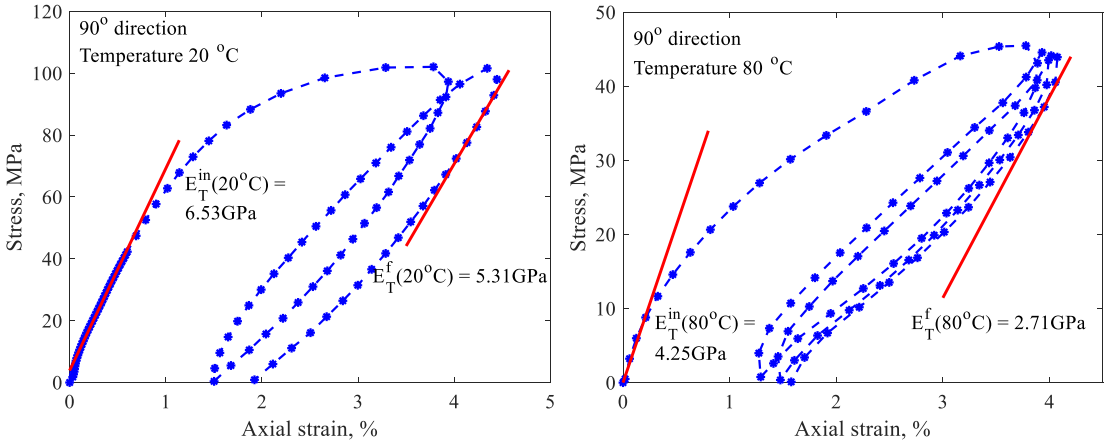

Figure 41 Continued

Table 8 Material parameters for elastic network

Temperature		20 ℃	80 ℃
Elastic modulus in longitudinal (0°) direction	E_L^{in} (GPa)	9.86	7.29
	E_L^{f} (Gpa)	9.29	4.99
Elastic modulus in transverse (90°) direction	E_T^{in} (Gpa)	6.53	4.25
	E_T^{f} (Gpa)	5.31	2.71
Poisson's ratio	ν_{TL}^{in}	0.2	0.2
	ν_{TL}^{f}	0.15	0.17
β		0.007	0.016
κ		1.8	1.05

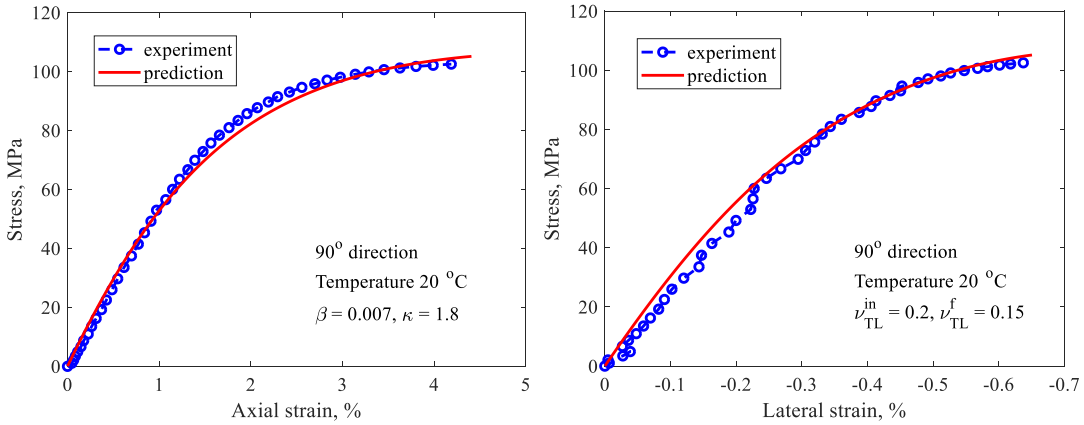

Figure 42 Left: calibration of temperature-dependent parameters β and κ; Right: calibration of Poisson's ratio

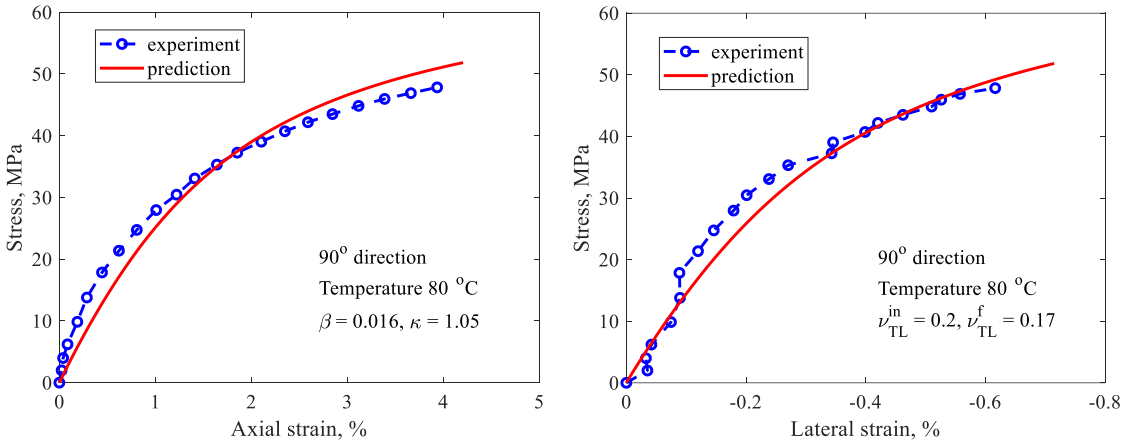

Figure 42 Continued

Temperature-dependent parameter $\beta(T)$ which describes the nonlinearity of the elastic response is calibrated from quasi-static tests under uniaxial loading in 90° direction, as shown in Figure 42. Since parameter $\beta(T)$ governs the nonlinearity of elastic response of final configuration, before the calibration of $\beta(T)$, it is necessary to define the evolutions of microstructural change α and permanent strain ε_p. The amount of the newly generated microstructural change α is assumed as a power function depends on the second invariant of the total strain. In this study, the relation between α and total strain is determined from axial responses, where it is assumed that α increases linearly with axial strain ε_{axial}. For a three-dimensional case, microstructural change α is related to the second invariant of the total strain. The relation between α and II_ε, which corresponding with a linear relation between α and ε_{axial}, can be written as:

$$\alpha(\boldsymbol{\varepsilon}) = \left(\frac{II_{\boldsymbol{\varepsilon}}}{II_{\varepsilon}^{\max}} \right)^{0.505} \tag{162}$$

As discussed in Eq. (149), the permanent strain can be related to the maximum irreversible deformation through microstructural change α. Figure 41 shows the calibration of maximum irreversible strain $\varepsilon_p^{\max}$ corresponding with $\alpha = 1$. As depicted in Figure 41(top), under temperature 80℃, when the material is loaded to its final configuration ($\varepsilon = 4.2\%$), upon unloading, the remaining permanent strain $\varepsilon_p^{\max} = 1.3\%$. Note that it is assumed no recovery of microstructural change occurs during unloading (α remains the same during unloading). For quasi-static tests depict in Figure 42, the total strain can be reduced to the summation of elastic strain and permanent strain, due to the fast loading rate:

$$\boldsymbol{\varepsilon} = \boldsymbol{\varepsilon}_E + \boldsymbol{\varepsilon}_P \tag{163}$$

In Eq. (163), elastic strain tensor $\boldsymbol{\varepsilon}_E$ depends on parameter β, while $\boldsymbol{\varepsilon}_p$ depends on parameter κ. As shown in Eq. (149), exponent parameter κ describes the rate of the generation of permanent strain. In this study, κ and β are adjusted simultaneously till the prediction fits well with the experimental data, as shown in Figure 42. The calibrated values are listed in Table 8. Parameter β is modeled with an exponential function of temperature, while κ is assumed as a linear function of temperature:

$$\begin{aligned} \beta(T) &= 0.0053e^{0.014T} \\ \kappa(T) &= 2.05 - 0.0125T \end{aligned} \tag{164}$$

The calibrations of Poisson's ratio for both initial and final configurations are depicted in Figure 42(right). For lateral responses under uniaxial loading in 90° direction, Poisson's ratio ν_{TL} of both configurations are adjusted until the prediction of lateral response fits well with experimental data. From Figure 42(right), it can be seen that Poisson's ratio of initial configuration is temperature-independent. We have $\nu_{TL}^{in}(20^oC) = \nu_{TL}^{in}(80^oC) = 0.2$. Poisson's ratio of final configuration shows

small increase with increased temperature. By assuming a linear relation with temperature, we have:

$$\nu_{TL}^{f}(T) = 0.1433 - 3.33\times10^{-4}T \tag{165}$$

Note that due to the symmetricity of compliance tensor, Poisson's ratio in longitudinal direction ν_{LT} can be directly calculated from Eq. (158), once elastic moduli in longitudinal and transverse directions and Poisson's ratio ν_{TL} are calibrated. Substitute Eqs. (161)-(165) into Eqs. (152) and (156), the anisotropic elastic responses under both 0° and 90° loadings can be determined.

5.2.2. Calibration of Material Parameters Associated with Viscoelastic Network

Material parameters related to the dissipative components of the model, as shown in Eqs. (154) and (159), are determined from creep-recovery tests under uniaxial loading in both 0° and 90° directions, at temperature 80℃. In longitudinal direction, elastic moduli of m^{th} viscoelastic component associated with the initial and final microstructures, $E_{Lim}(T), E_{Lfm}(T)$, and the corresponding viscosities, $\mu_{Lim}(T), \mu_{Lfm}(T)$, are calibrated from creep responses at stress levels 10MPa and 50MPa, as depicted in Figure 43. The creep response at 10MPa gives a relatively small strain, which is used to calibrate parameters E_{Lim} and μ_{Lim}, while creep response at 50MPa gives a larger strain, which is used to determine parameters at final configuration. Note that the values of E_{Lim} and E_{Lfm} must be adjusted simultaneously until a completed set of E_{Lim} and E_{Lfm} which can capture both responses at 10MPa and 50MPa are found. The calibrated values of elastic moduli of viscoelastic components are listed in Table 9. The viscosities μ_{Lim} and μ_{Lfm} are related to elastic moduli through characteristics of creep time τ_m:

$$\mu_{Lim} = \tau_m E_{Lim}; \quad \mu_{Lfm} = \tau_m E_{Lfm} \tag{166}$$

Table 9 Material parameters for viscoelastic network

Individual network m	τ_m (s)	Elastic modulus in longitudinal (0°) direction		Elastic modulus in transverse (90°) direction	
		E_{Lim} (GPa)	E_{Lfm} (GPa)	E_{Tim} (GPa)	E_{Tim} (GPa)
1	10	153.85	16.67	47.62	14.29
2	100	105.26	20	64.52	17.24
3	1000	100	23.81	28.57	15.38
4	10000	50	35.71	16.13	14.29
5	100000	100	76.92	100	37.04
6	500000	50	40	50	28.57

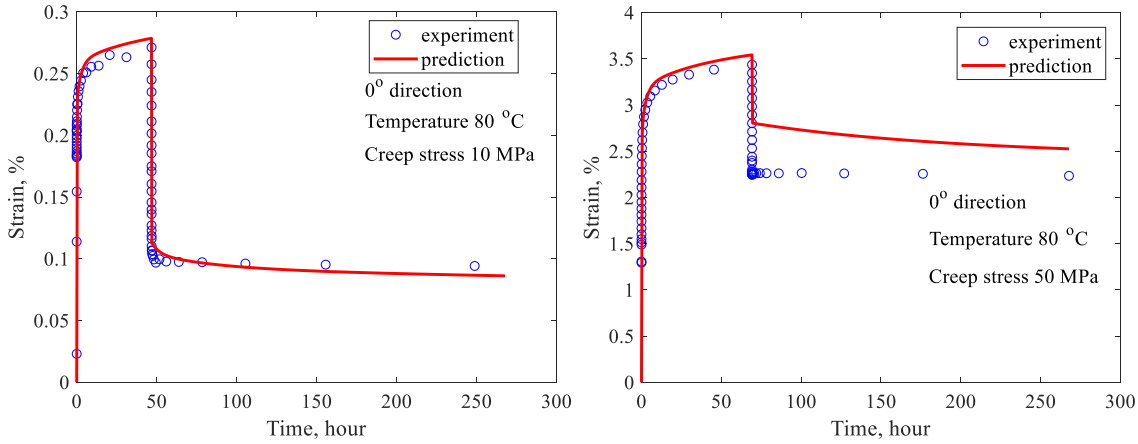

Figure 43 Calibration of elastic moduli for viscoelastic components in longitudinal (0°) direction

For the viscoelastic components, it is assumed that the temperature-dependent parameters in Eq. (154) can be written as the multiplication of a variable ($d_i(T)$, $d_f(T)$, etc.) and a constant (E^0_{Lim}, E^0_{Lfm}, etc.). Therefore, axial strain in Eq. (154) can be rewritten as follow:

$$\varepsilon_{V,axial} = \varepsilon_{V,11} = \sum_{m=1}^{N} \varepsilon_{Vm,11} = \sum_{m=1}^{N} \left[(1-\alpha) d_i(T) \frac{1}{E^0_{Lim}} \sigma^E_{Vm,11} + \alpha d_f(T) \frac{1}{E^0_{Lfm}} \sigma^E_{Vm,11} \right]$$
$$\dot{\varepsilon}_{V,axial} = \dot{\varepsilon}_{V,11} = \sum_{m=1}^{N} \dot{\varepsilon}_{Vm,11} = \sum_{m=1}^{N} \left[(1-\alpha) b_i(T) \frac{1}{\mu^0_{Lim}} \sigma^D_{Vm,11} + \alpha b_f(T) \frac{1}{\mu^0_{Lfm}} \sigma^D_{Vm,11} \right] \quad (167)$$

In Eq. (167), E_{Lim}^0 and E_{Lfm}^0 are elastic moduli of viscoelastic components under temperature 80℃, as listed in Table 9. From Eq. (167), we have:

$$\begin{aligned} \frac{d_i(T)}{b_i(T)}\frac{\mu_{Lim}^0}{E_{Lim}^0} = \tau_m(T) \rightarrow \frac{\mu_{Lim}^0}{E_{Lim}^0} = a_i(T)\tau_m(T) \\ \frac{d_f(T)}{b_f(T)}\frac{\mu_{Lfm}^0}{E_{Lfm}^0} = \tau_m(T) \rightarrow \frac{\mu_{Lfm}^0}{E_{Lfm}^0} = a_f(T)\tau_m(T) \end{aligned} \tag{168}$$

where $a_i(T)$ and $a_f(T)$ are the time-temperature shift factors for initial and final configurations, respectively.

As shown in Figure 44, shift factors $a_i(T)$ and $a_f(T)$ are calibrated by fitting the creep responses under temperatures ranging from 20℃ to 100℃. The reference temperature is 80℃, (i.e., the values E_{Lim}^0, E_{Lfm}^0, etc. in Eq. (168) are parameters corresponding with temperature 80℃). Shift factors $a_i(T)$ and $a_f(T)$ describe the change of viscosity from 80℃ to temperature T. The calibrated values are listed in Table 10. Shift factors of both configurations are related to temperature through exponential functions, as depicted in Eq. (169) below:

$$\begin{aligned} a_i(T) &= 2.494\times10^5 e^{-0.276T} + 1 \\ a_f(T) &= 1.6\times10^9 e^{-0.4952T} + 1 \end{aligned} \tag{169}$$

Table 10 Time-temperature shift factors of initial and final configurations

Temperature, ℃	a_i	a_f
20	1000	80000
40	5	5
60	1	1
80	1	1
100	1	1

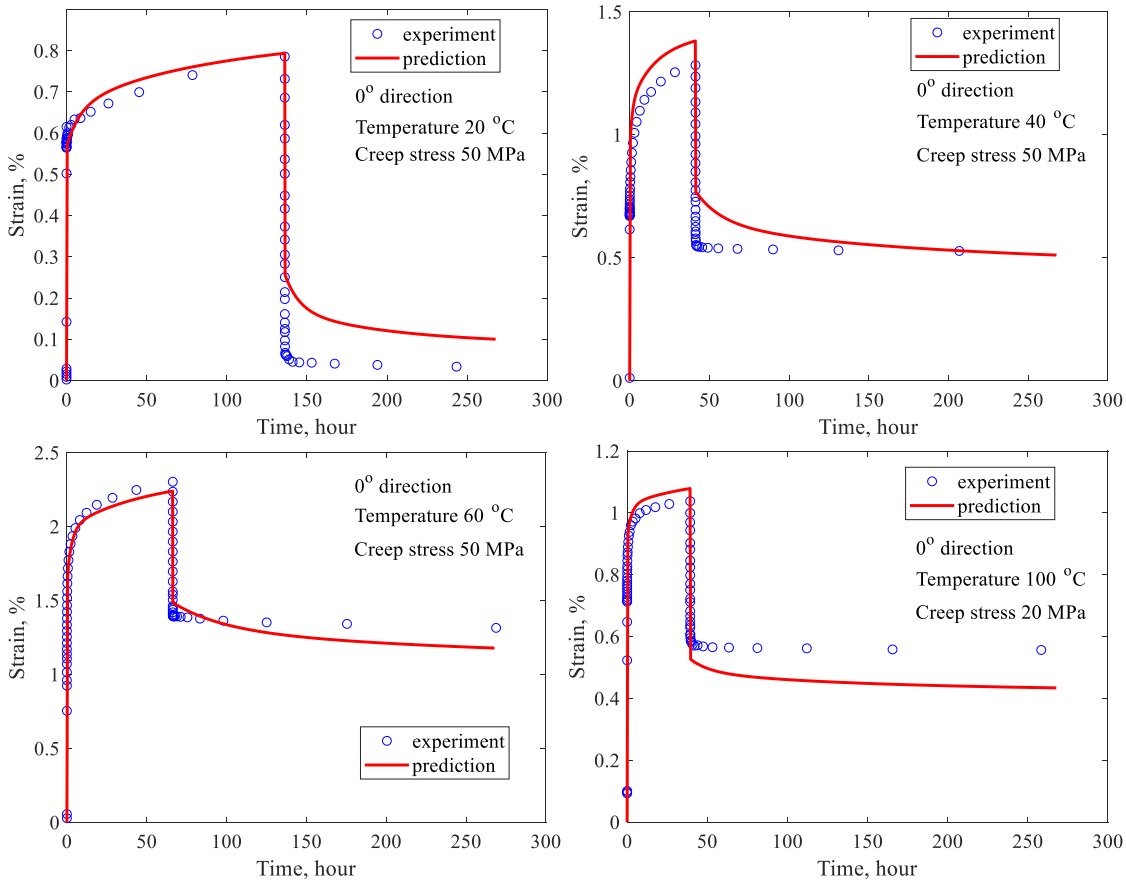

Figure 44 Calibration of time-temperature shift factor

The calibration of time-dependent parameters in 90° direction follows the same idea. By writing the temperature-dependent parameters in Eq. (159) as the multiplication of a temperature dependent variable and a constant, axial strain and its rate in Eq. (159) can be expressed as follow:

$$\begin{aligned}\varepsilon_{V,axial} &= \varepsilon_{V,22} = \sum_{m=1}^{N}\varepsilon_{Vm,22} = \sum_{m=1}^{N}\left[(1-\alpha)d_i(T)\frac{1}{E^0_{Tim}}\sigma^E_{Vm,22} + \alpha d_f(T)\frac{1}{E^0_{Tfm}}\sigma^E_{Vm,22}\right] \\ \dot{\varepsilon}_{V,axial} &= \dot{\varepsilon}_{V,22} = \sum_{m=1}^{N}\dot{\varepsilon}_{Vm,22} = \sum_{m=1}^{N}\left[(1-\alpha)b_i(T)\frac{1}{\mu^0_{Tim}}\sigma^D_{Vm,22} + \alpha b_f(T)\frac{1}{\mu^0_{Tfm}}\sigma^D_{Vm,22}\right]\end{aligned} \tag{170}$$

Note that in Eq. (170), time-temperature shift factors for initial and final configurations, $a_i(T)=\dfrac{b_i(T)}{d_i(T)}$ and $a_f(T)=\dfrac{b_f(T)}{d_f(T)}$, are the same with the shift factors in Eqs. (167)-(168) under loadings in 0° direction. i.e., the dependency of viscosity on temperature does not change with

loading directions. Substitute expressions of shift factors shown in Eq. (169) into Eq. (170), for uniaxial loadings in transverse (90°) direction, elastic moduli of m^{th} viscoelastic component associated with the initial and final microstructures, $E_{Tim}(T)$ and $E_{Tfm}(T)$, can be determined from creep responses under temperature 40℃ and stress levels 10MPa and 50MPa, as shown in Figure 45. Creep response under 10MPa with relatively small strain is used to determine elastic moduli and viscosities of initial configuration, while response under 50MPa with larger strain is used to calibrate parameters for final configuration. The calibrated values are listed in Table 9.

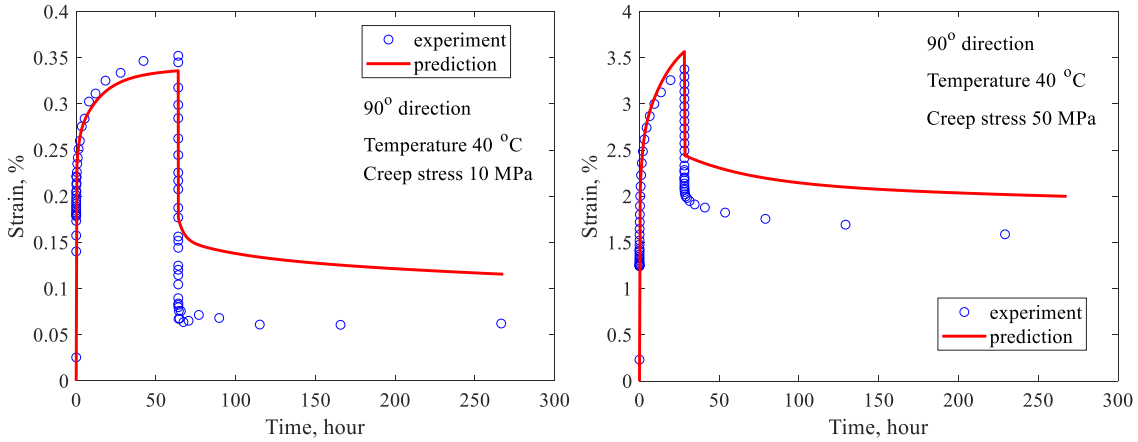

Figure 45 Calibration of elastic moduli for viscoelastic components in transverse (90°) direction

The lateral creep responses can be related to axial responses through Poisson's ratio, as shown in Eqs. (159)-(160). For creep-recovery responses under 90° loading, for all viscoelastic components, Poisson's ratios of initial and final configurations are assumed the same with the Poisson's ratios calibrated from quasi-static tests given in Eq. (165):

$$\begin{aligned} \nu_{TLm}^{in}(T) &= 0.2 \\ \nu_{TLm}^{f}(T) &= 0.1433 - 3.33\times10^{-4}T \end{aligned} \tag{171}$$

For lateral creep-recovery responses under 0° direction loading, Poisson's ratio of each viscoelastic component can be determined from the symmetricity of compliance tensor. For each component, we have:

$$\nu_{LTm}^{in} = \frac{\nu_{TLm}^{in} E_{Lim}}{E_{Tim}}; \quad \nu_{LTm}^{f} = \frac{\nu_{TLm}^{f} E_{Lfm}}{E_{Tfm}} \tag{172}$$

Substitute the values of E_{Tim} and E_{Tfm} listed in Table 9 and Poisson's ratio given in Eq. (171) into Eq. (172), lateral creep responses under loadings in 0° fiber direction can be determined from Eqs. (154)-(155). Predictions of creep-recovery responses under various temperatures, stress levels and loading directions are presented in the following section.

5.3. Prediction of Anisotropic Response under Various Loading Conditions

In this section, quasi-static responses, cyclic responses and creep-recovery responses of PA6GF40 under uniaxial loadings in both 0° and 90° fiber directions are simulated with the constitutive model discussed above, and compared with experimental results under various temperatures. Figure 46 - Figure 49 depict the quasi-static responses under various loading rates and temperatures. For uniaxial loadings in 0° fiber direction, Figure 46 and Figure 47 present the quasi-static axial and lateral responses under temperature 20℃ and 80℃, respectively. From Figure 46 - Figure 47, we can see that for tests under higher temperature, the time-dependency is more pronounced, i.e., under slower loading rate, the quasi-static response shows significant softening compared with response under faster loading rate. Overall, the constitutive model is capable to capture the quasi-static responses in both axial and lateral directions, under different temperatures and loading rates. Figure 48 and Figure 49 depict the quasi-static responses under uniaxial loadings in 90° fiber direction. Similarly with loadings in longitudinal direction, the constitutive model

gives reasonable predictions for quasi-static responses under various loading rates and temperatures, which indicates that the model can capture the anisotropic responses of PA6GF40 in both directions.

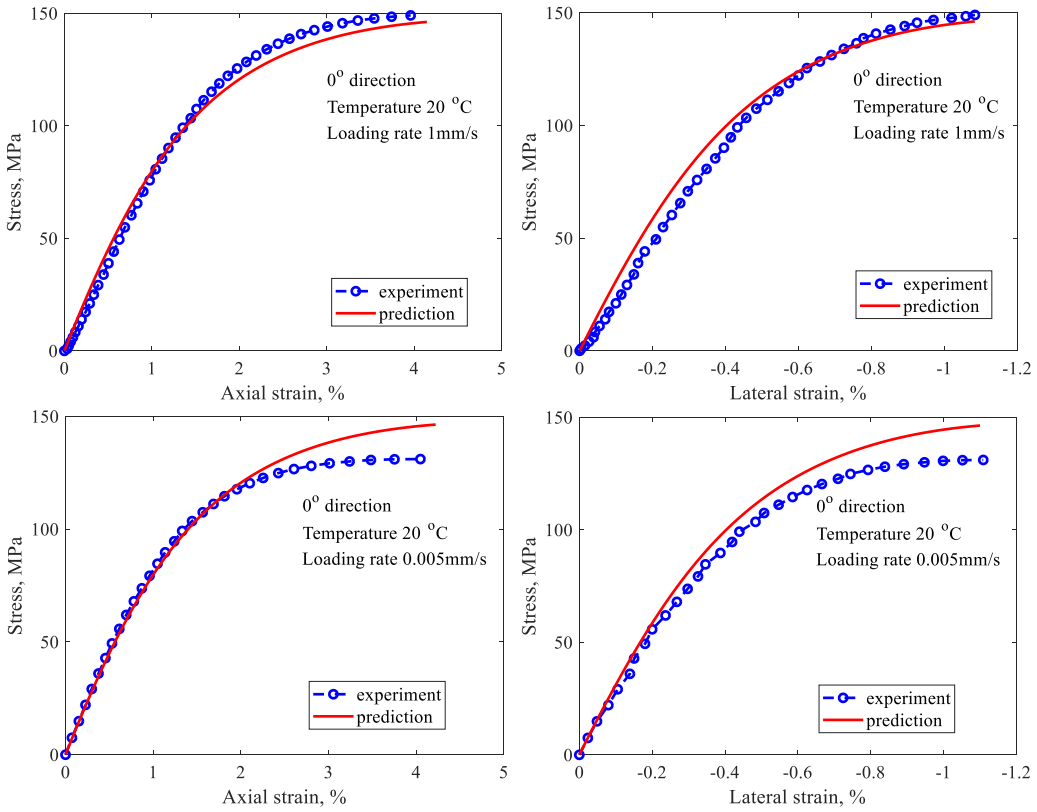

Figure 46 Prediction of quasi-static response under room temperature, 0° fiber direction

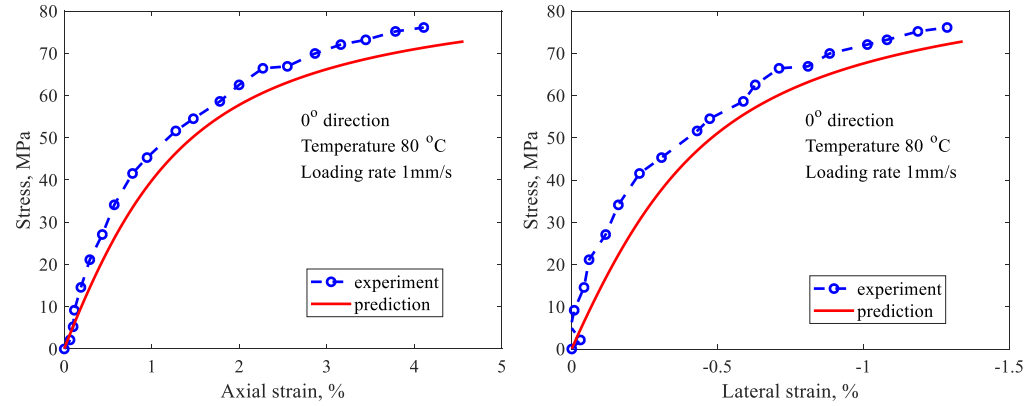

Figure 47 Prediction of quasi-static response under high temperature (80°C), 0° fiber direction

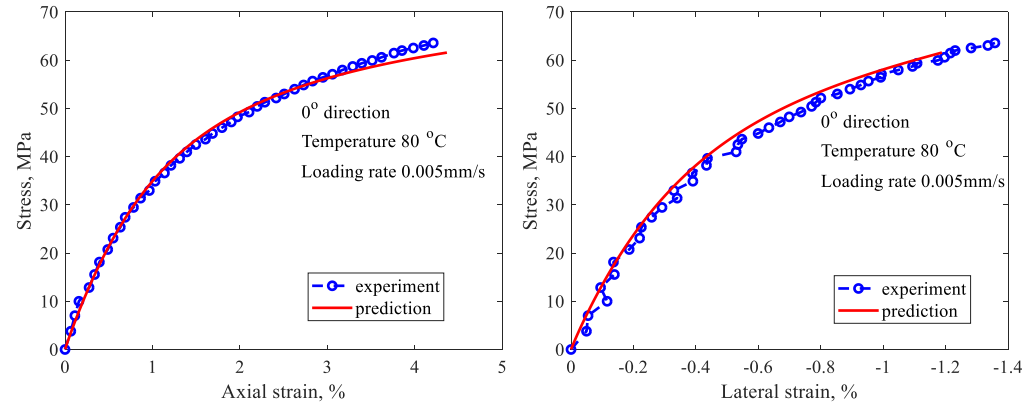

Figure 47 Continued

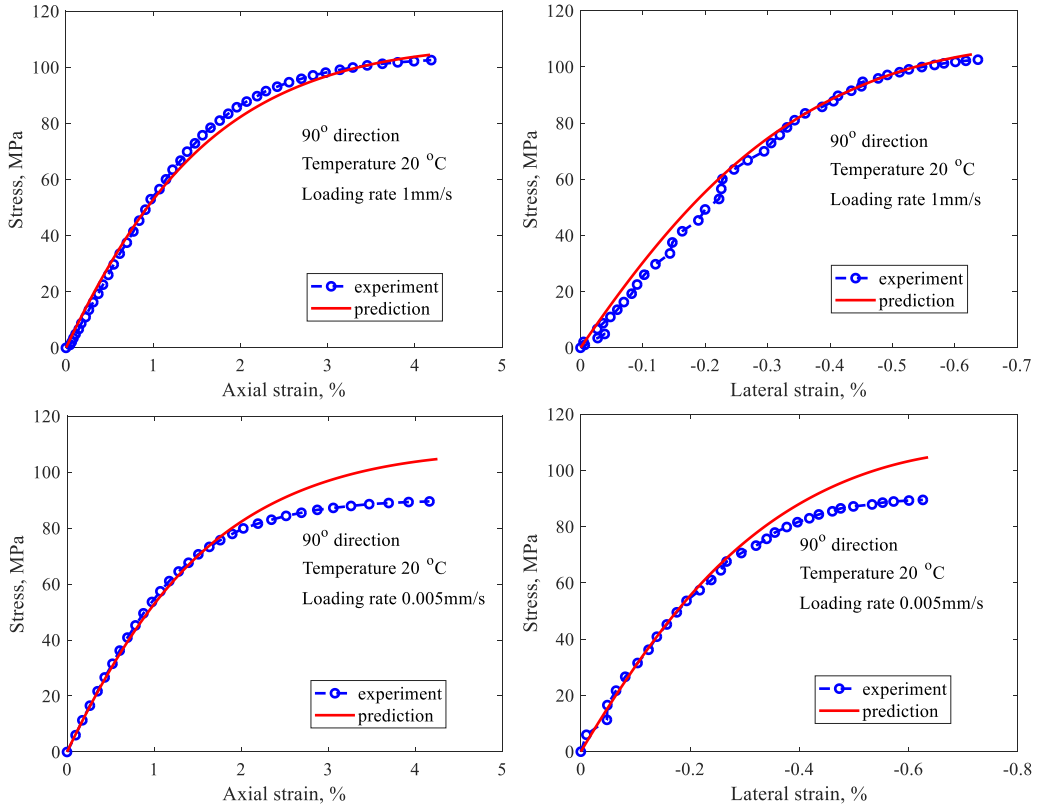

Figure 48 Prediction of quasi-static response under room temperature, 90° fiber direction

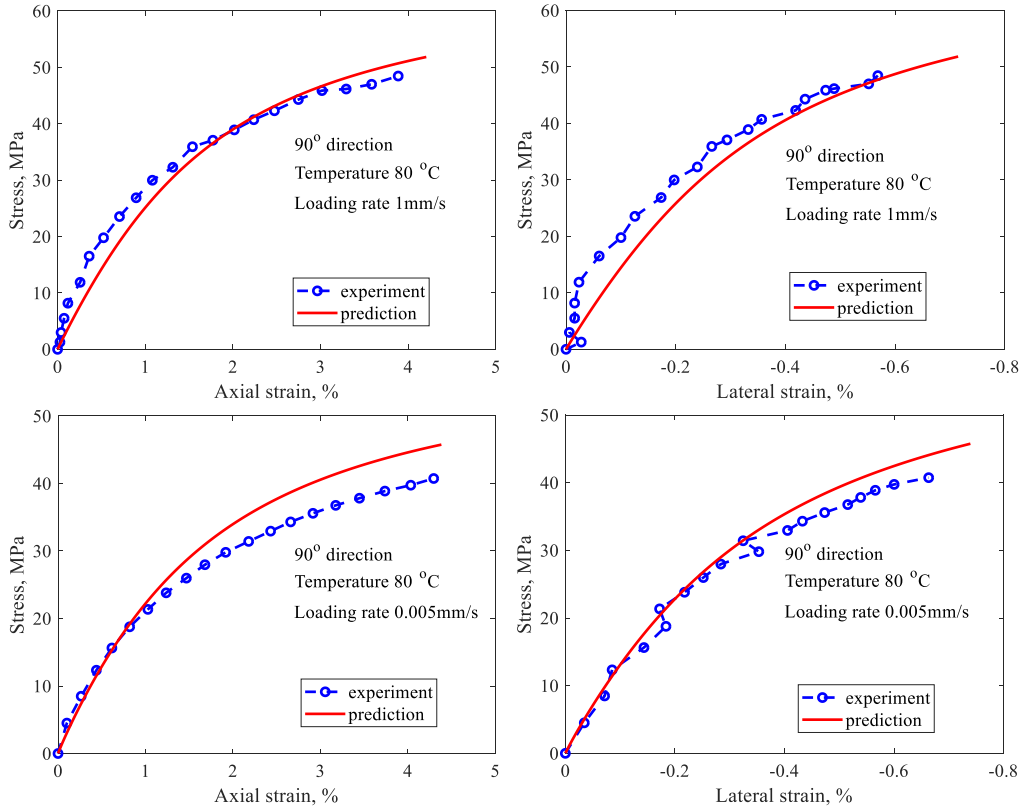

Figure 49 Prediction of quasi-static response under high temperature (80℃), 90° fiber direction

Figure 50 and Figure 51 depict the simulation results for cyclic tests, under uniaxial loadings in 0° fiber direction and 90° fiber direction, respectively. Note that it is assumed during unloading, microstructural change *a* remains unaltered (no healing). The area of the hysteresis loop of first loading cycle is significantly larger than the area of hysteresis loops after initial loading, since the initial loading includes energy dissipation caused by both microstructural change and viscosity. It can be seen that the energy dissipated by both viscosity and microstructural change could be reasonably captured by the model. From Figure 50 - Figure 51, anisotropic cyclic responses in both longitudinal and transverse directions, under both 20℃ and 80℃, can be captured by the constitutive model.

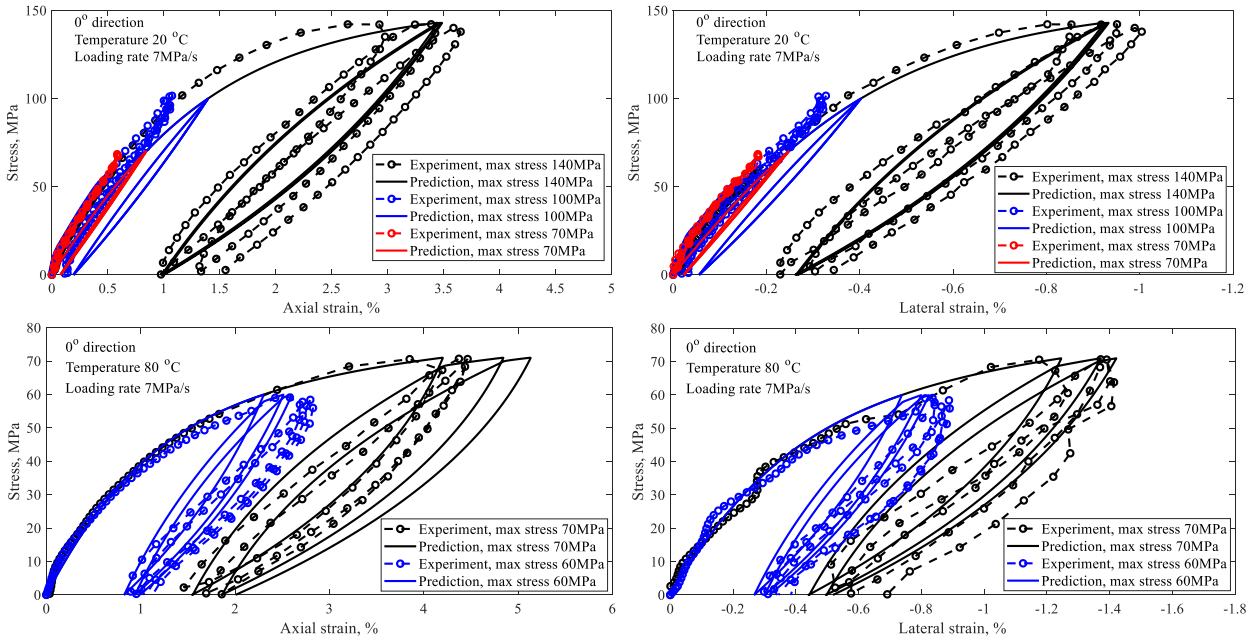

Figure 50 Prediction of cyclic response under loadings in 0° fiber direction

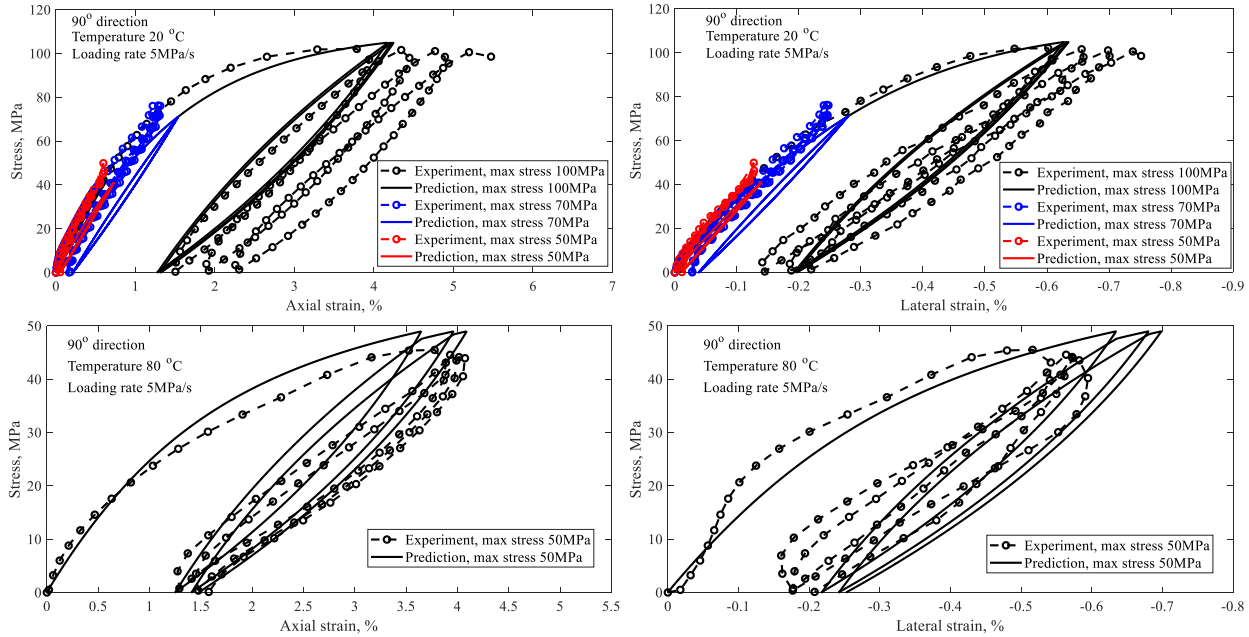

Figure 51 Prediction of cyclic response under loadings in 90° fiber direction

Figure 52 and Figure 53 depict the predictions of creep-recovery responses under various temperatures and stress levels, for 0° fiber direction and 90° fiber direction, respectively. The

recovery experimental tests are conducted at room temperature (20℃), therefore, it is assumed that during unloading, the temperature drops from maximum temperature to 20℃ in 1.5s. From Figure 52 - Figure 53, for temperatures ranging from 20℃ to 100℃ and stress levels ranging from 10MPa to 50MPa, the anisotropic model can give reasonable predictions for loadings in both longitudinal and transverse directions. With relatively small number of material parameters, the anisotropic multiple configurations based constitutive model can predict time- and temperature-dependent responses reasonably well for PA6GF40.

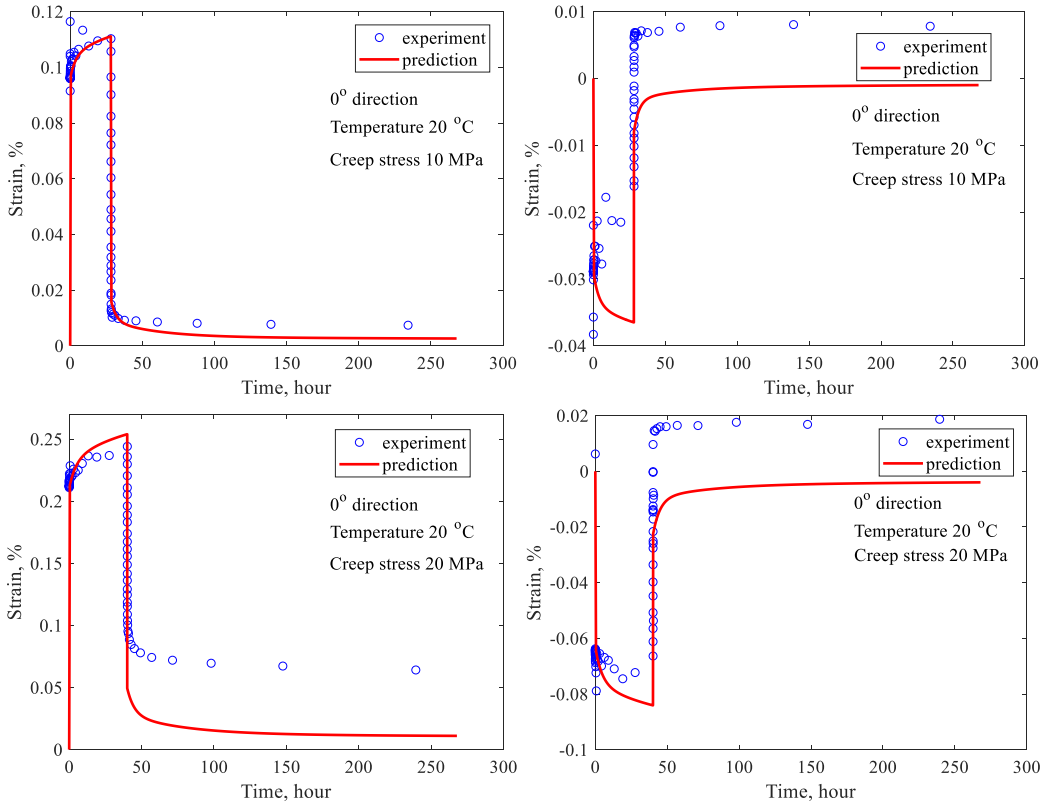

Figure 52 Prediction of creep-recovery response under loadings in 0° fiber direction

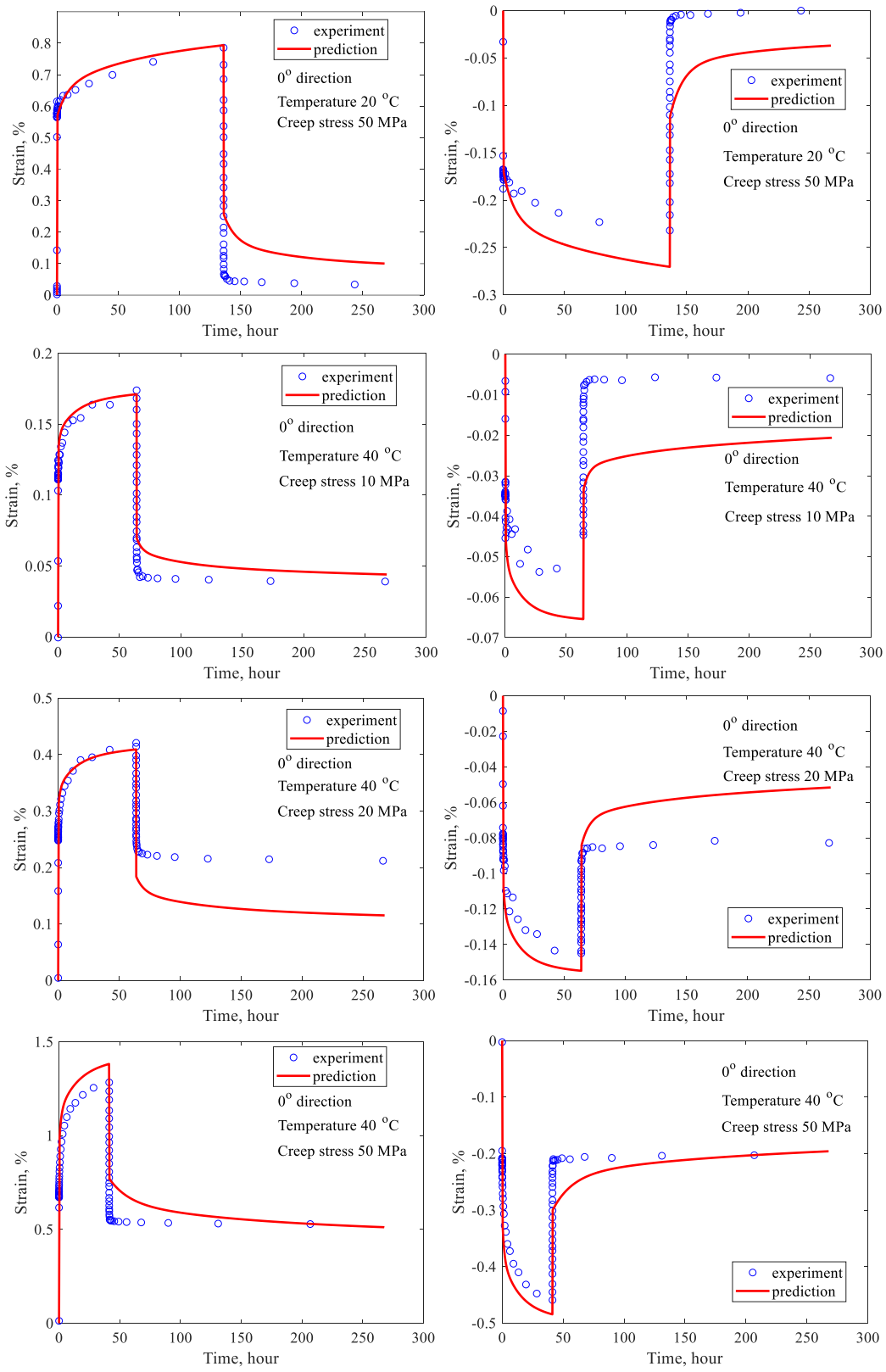

Figure 52 Continued

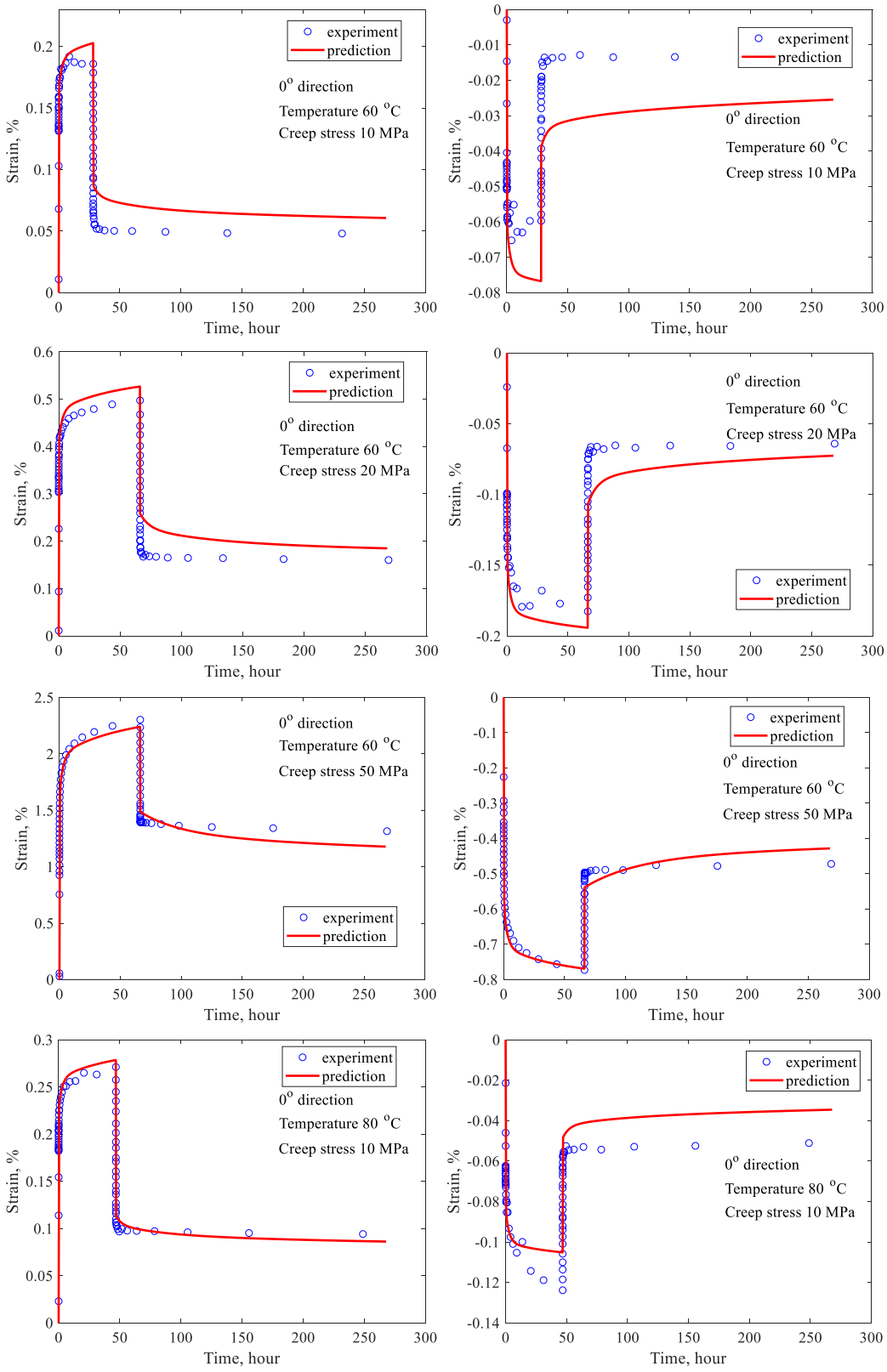

Figure 52 Continued

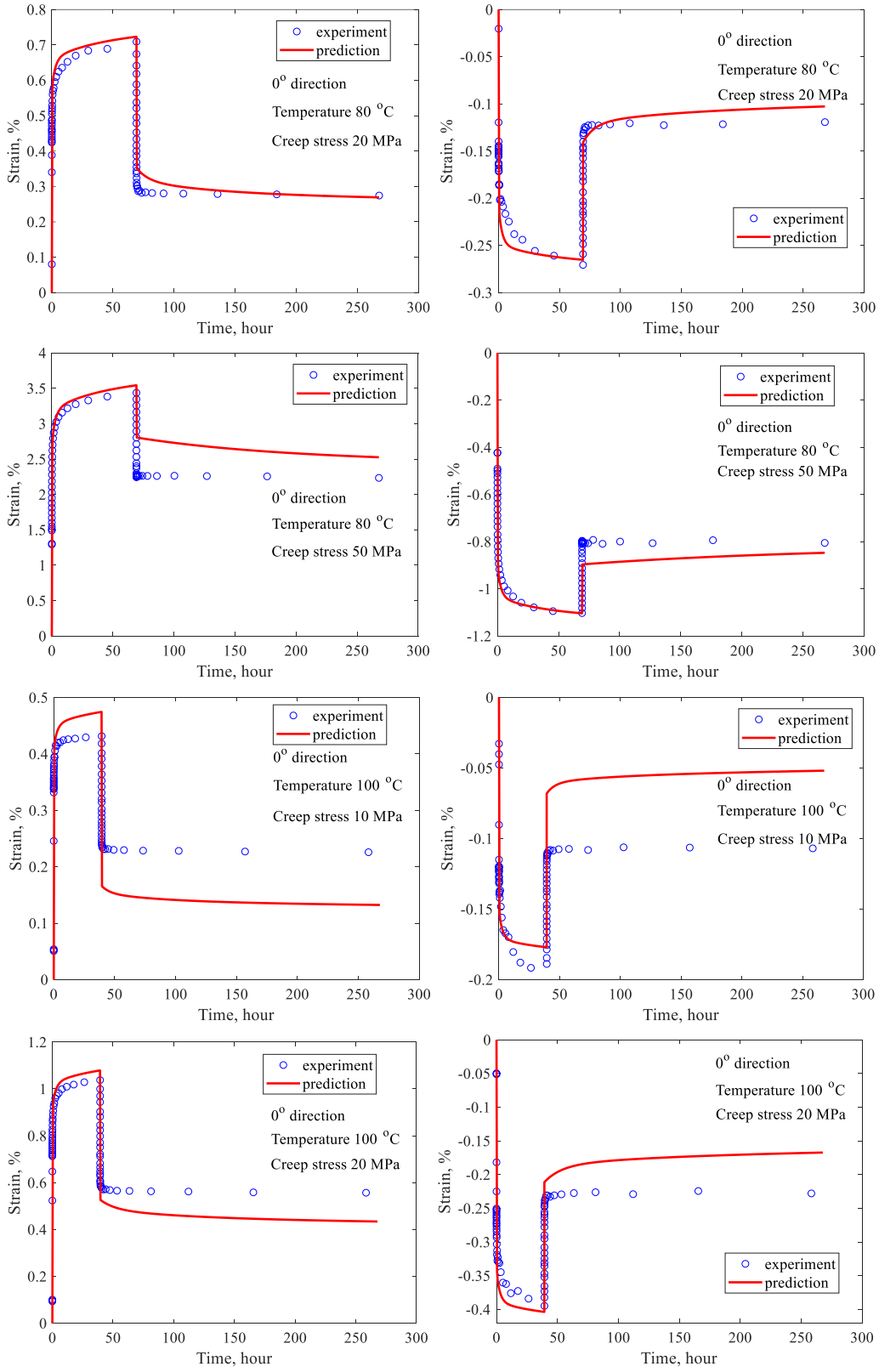

Figure 52 Continued

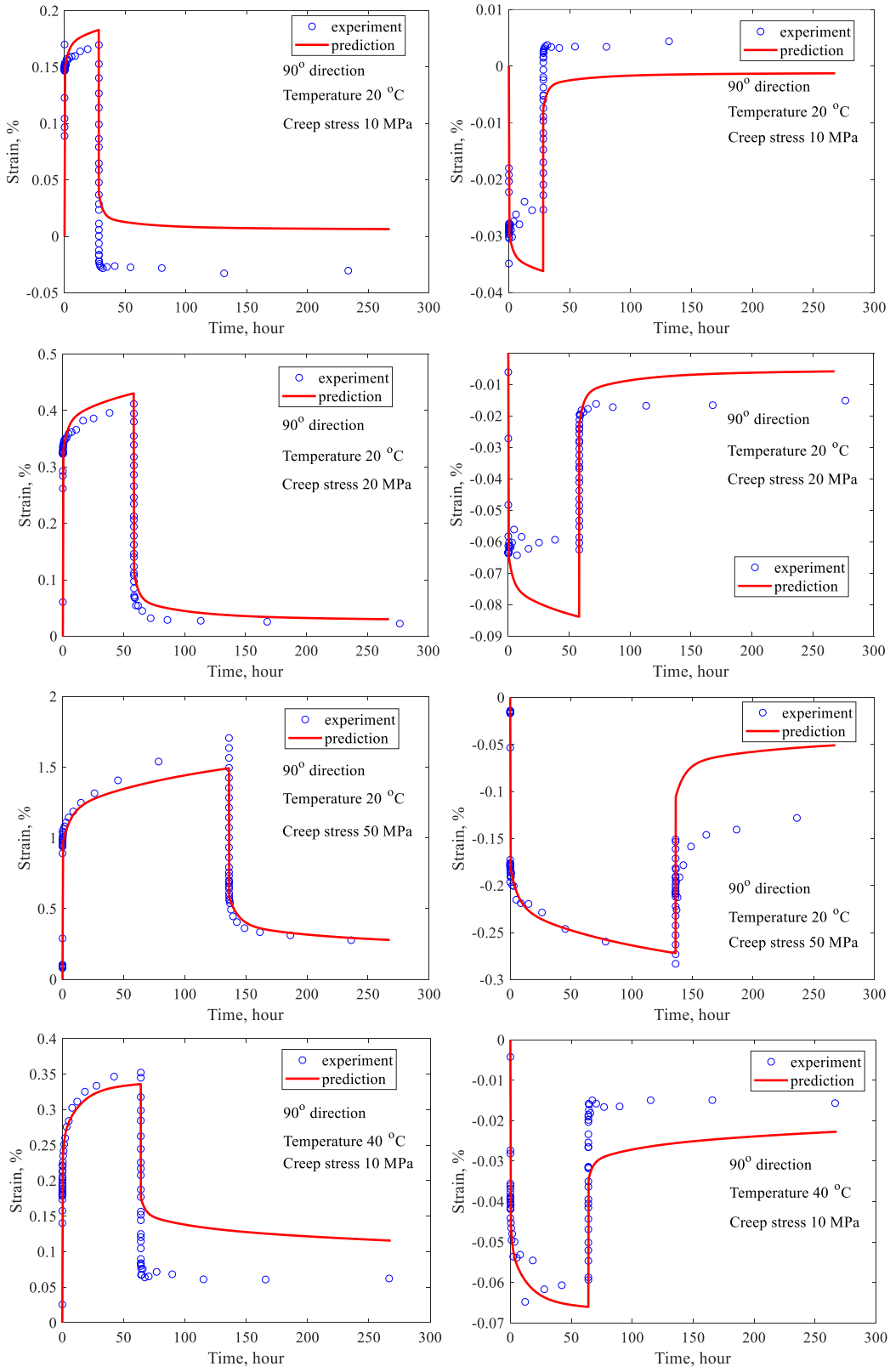

Figure 53 Prediction of creep-recovery response under loadings in 90° fiber direction

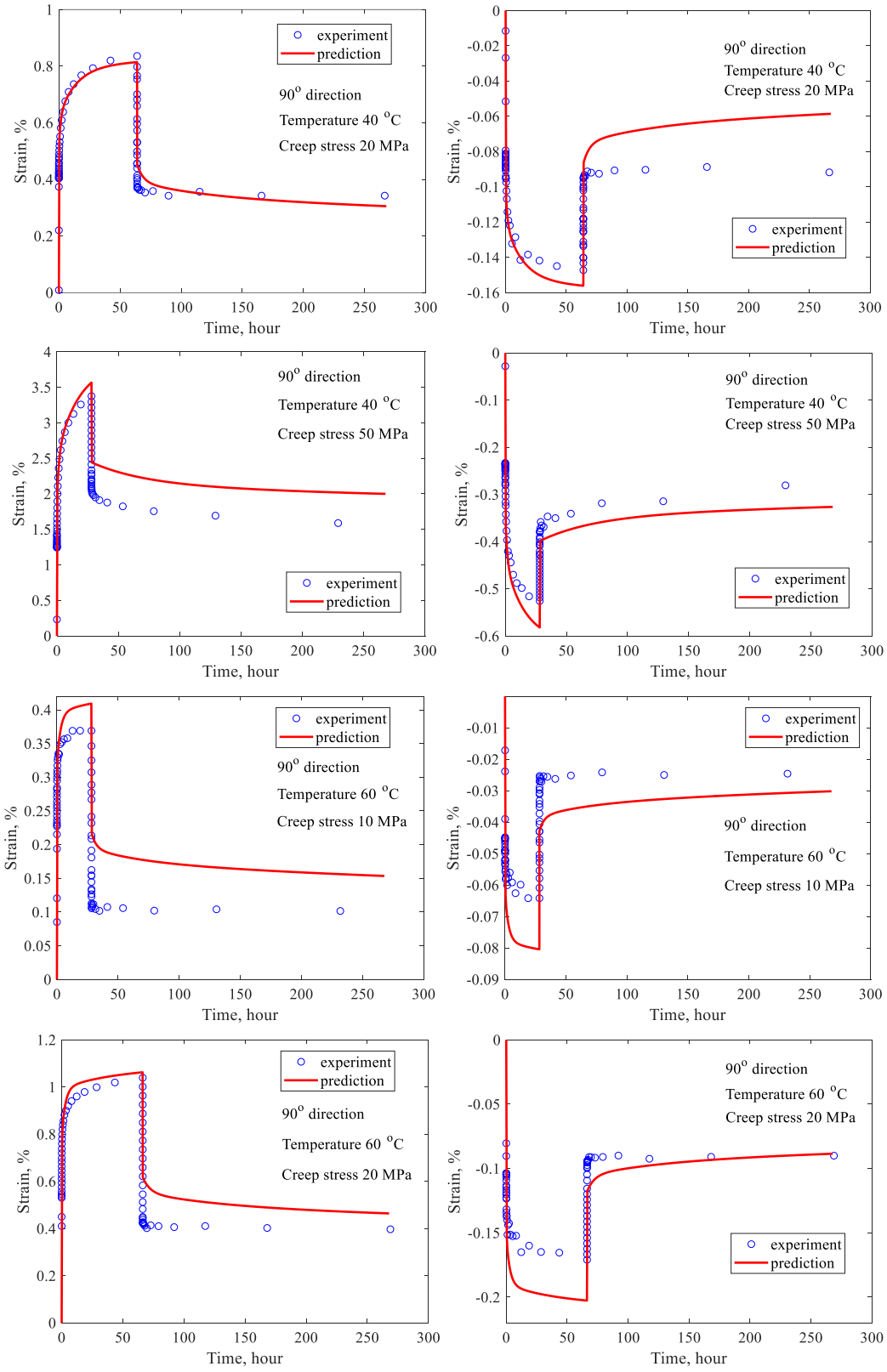

Figure 53 Continued

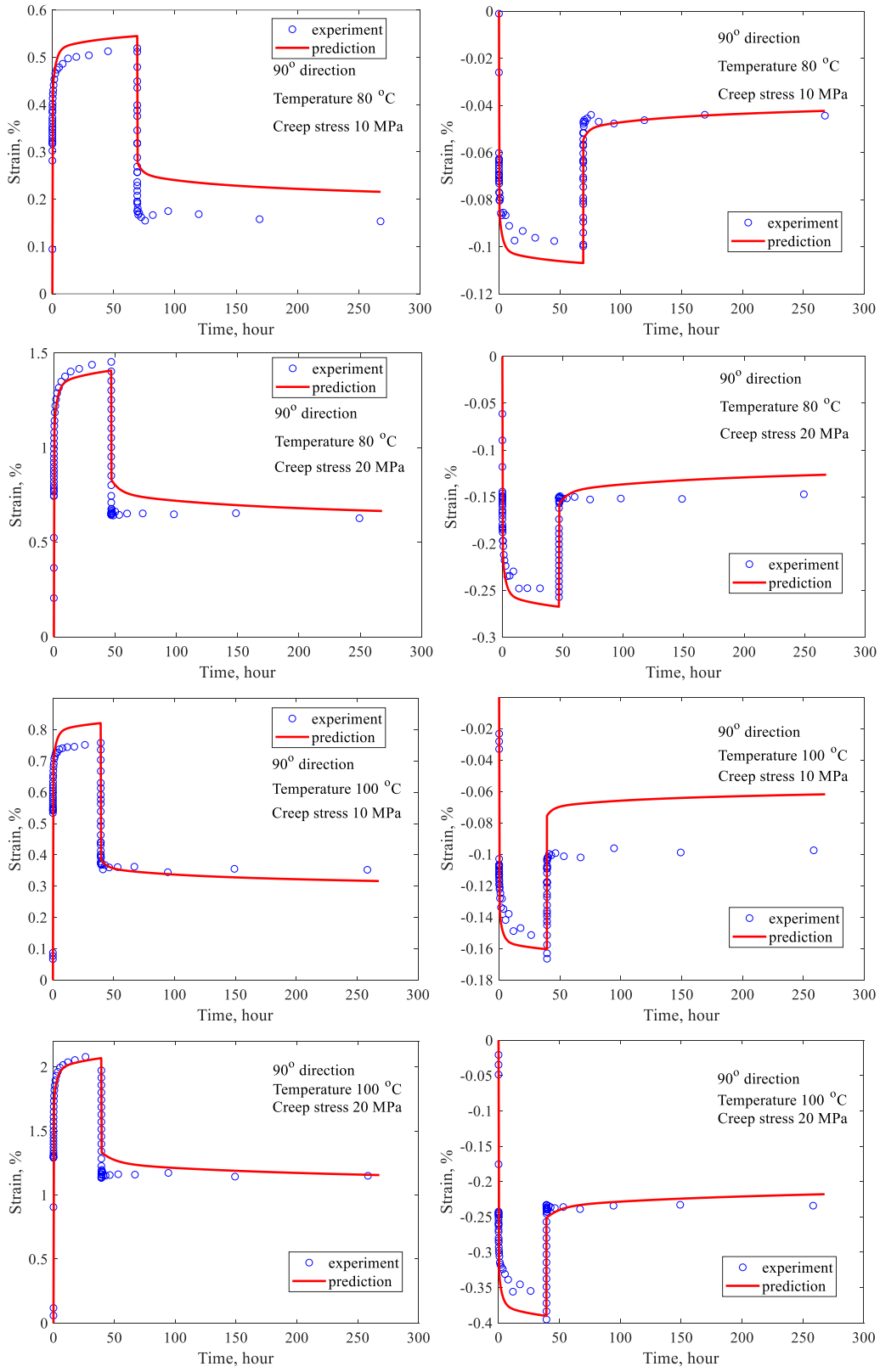

Figure 53 Continued

CHAPTER VI

STRUCTURAL ANALYSIS OF THIN LAYERED POLYMERS UNDERGOING MICROSTRUCTURAL CHANGES FROM NON-MECHANICAL STIMULI[*]

This chapter presents examples of structural analyses of viscoelastic polymers undergoing microstructural changes due to non-mechanical stimuli. As examples of structural analyses, thin multi-layers of polymers, each with different physical and mechanical properties, are studied and upon prescribing external stimuli (thermal, chemical, electrical, etc.) the layers will experience different in-plane stretch and hence inducing shape changes. In this study, we develop numerical models to describe shape reconfigurations of thin multi-layered polymers exposed to non-mechanical stimuli. We investigate the influence of microstructural changes in the polymer layers due to prescribing external stimuli and their effects on the shape configurations of the multi-layered polymers. For this purpose, the constitutive material model derived based on the multiple natural configuration approach is integrated within shell finite elements and the co-rotational finite element (FE) method is used to solve for the governing differential equation that describe the shape reconfiguration of the thin multi-layered polymers.

6.1. Mathematical Formulation of Thin-Multi-Layered Composites

Typical thin multi-layered active composites comprise of three or two layers, see illustrations in Figure 54. In the three-layer system, active materials are usually placed on the top and bottom layers while the middle substrate is made of an inactive material. Prescribing a non-mechanical stimulus, e.g., electric or magnetic field, to the active layer(s), induces in-plane stretching or

[*] Reprinted with permission from "Modeling and Simulation of Thin Layered Composites under Non-mechanical Stimuli" by Song, R., Tajeddini, V., & Muliana, A., 2020. *Front. Mater.*, 7, 97, Copyright [2020] by Frontiers.

contraction. Different in-plane stretching/contraction in these two active layers generates axial stretching and curvature in the thin composite. The inactive substrate is added to increase the distance between the two active layers, and hence increasing the corresponding moment. However, adding an inactive substrate can also increase the overall rigidity of the composite, making the composite less compliant. An alternative arrangement is to consider bilayer systems, comprising of active and inactive layers or two active layers. This study considers attaining three-dimensional shape reconfigurations (or folding) out of a planar system, and hence it is necessary for the different layers in the multi-layer systems to have different in-plane stretching/contraction upon prescribing external stimuli. As will be discussed later, in a thin composite plate the out of plane deformations due to prescribing non-mechanical stimuli are governed by large rotations and the magnitude of the axial stretching is usually small (negligible with respect to the overall rotations). For this reason, it is convenient to map the neutral surface, which does not experience in-plane stretching and contraction, in order achieve shape reconfiguration. Therefore, the shape reconfigurations that can be achieved spontaneously by prescribing the non-mechanical stimuli are associated with zero Gaussian curvature.

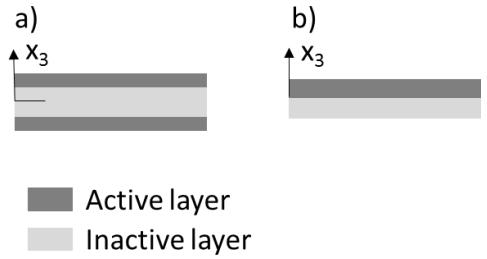

Figure 54 Multi-layered active composites of different arrangements: a) sandwich system, b) bilayer of active and inactive materials

In this section a spontaneous application of an electric field input in the thin bilayer composite is considered. Other types of stimuli, i.e., uniform temperature or moisture change, can

also be considered due to the similar shape reconfiguration mechanisms. Prescribing an electric potential difference along the thickness of the active layer generates a uniform electric field in the active layer and hence a uniform in-plane stretching/contraction along the layer. In principle, out of plane deformations by a spontaneous temperature change can be achieved in a bilayer composite. Polymers generally have low thermal conductivity; thus, practically it might not be possible to achieve spontaneous shape changes by a thermal stimulus. In such situation, a transient diffusion process (thermal field various in space and time) is required in simulating shape reconfigurations in thin polymer bilayers. The transient process is also applicable for bilayers undergoing diffusion of fluid, e.g., experimental studies by Stoychev et al. [62, 63]. Different shape reconfigurations can occur in the same polymers bilayers when subjected to spontaneous and transient thermal stimuli. Likewise, the transient process can be simulated for the electro-mechanical responses in composites by prescribing electric field that varies in time and space; however, this process might not be practical.

Consider a bilayer thin composite plate comprising of active and inactive layers (Figure 54b), and the thicknesses of the active and inactive layers are t_a and t_s, respectively. The surface of the composite is described along the plane x_1-x_2. The out of the plane is described by x_3, measured from the interface between the active and inactive layers. This study concerns with thin active composites, in which the in-plane dimension ($L_1 \times L_2$) of the composite is much larger than its thickness (t), i.e., $L_1 \sim L_2; L_1 \gg t$. In this situation, the out of plane shape reconfiguration is governed by large rotation and the contribution of the in-plane stretch to the overall deformation is small. It is also assumed that an application of an external stimulus is considered to induce only free expansion/contraction, which is a normal (or axial) component of the deformation. In a thin composite, only the in-plane free expansion or contraction strain components, i.e., H_{11}, H_{22}, are

considered when the non-mechanical stimuli are prescribed. The shape reconfiguration of the bilayer composite is defined by the following deformation vector $\{u_1, u_2, u_3 = w\}$, where u_1, u_2 are the axial deformations of the interface along the x_1 and x_2 axes, respectively, and w is the out of plane deformation of the interface. The normal strains of the planar surface undergoing out of plane deformations are described by the following relations:

$$\begin{aligned} \varepsilon_{11} &= \varepsilon_1^o - x_3 \kappa_{11} \\ \varepsilon_{22} &= \varepsilon_2^o - x_3 \kappa_{22} \end{aligned} \tag{173}$$

where $\varepsilon_{11}, \varepsilon_{22}$ are the axial strain components along the in-plane directions x_1 and x_2, respectively, $\varepsilon_1^o, \varepsilon_2^o$ are the axial strains of the interface (at x_3=0) in the directions x_1 and x_2, respectively, and κ_{11}, κ_{22} are the curvatures of the interface about the x_1 and x_2 axes, respectively.

When each layer in the composite plate is modeled as linear elastic and isotropic with regards to its mechanical properties, the constitutive relations for the inactive (substrate) and active layers are given as:

$$\begin{aligned} \sigma_{11}^s &= \frac{E_s}{1-\nu_s^2}\left(\varepsilon_{11} + \nu_s \varepsilon_{22}\right) \\ \sigma_{22}^s &= \frac{E_s}{1-\nu_s^2}\left(\nu_s \varepsilon_{11} + \varepsilon_{22}\right) \\ \sigma_{12}^s &= \frac{E_s}{1+\nu_s}\varepsilon_{12} \end{aligned} \tag{174}$$

$$\begin{aligned} \sigma_{11}^a &= \frac{E_a}{1-\nu_a^2}\left(\varepsilon_{11} + \nu_a \varepsilon_{22} - H_{11}^a - \nu_a H_{22}^a\right) \\ \sigma_{22}^a &= \frac{E_a}{1-\nu_a^2}\left(\nu_a \varepsilon_{11} + \varepsilon_{22} - \nu_a H_{11}^a - H_{22}^a\right) \\ \sigma_{12}^a &= \frac{E_a}{1+\nu_s}\varepsilon_{12} \end{aligned} \tag{175}$$

In the above equations E_s, E_a are the elastic moduli of the substrate and active layers, respectively, and ν_s, ν_a are the Poisson's ratios of the substrate and active layers, respectively. Prescribing non-

mechanical stimulus to the active layer induces free expansion/contraction H_{11}^a, H_{22}^a . Finally, imposing the following equilibrium equations to the thin bilayer plate (in absence of any mechanical stimulus and ignoring twisting and shearing) leads to:

$$\int_{A_1} \sigma_{11} dA = 0; \quad \int_{A_2} \sigma_{22} dA = 0; \quad \int_{A_1} \sigma_{11} x_3 dA = 0; \quad \int_{A_2} \sigma_{22} x_3 dA = 0 \tag{176}$$

where A_1 and A_2 are the transverse cross-sectional areas of the bilayer plate with normal in the x_1 and x_2 axes, respectively.

Substituting Eqs. (90), (174), and (175) into Eq. (176), results in the following relations:

$$\begin{aligned}
&B_1\varepsilon_1^o + B_2\varepsilon_2^o - C_1\kappa_{11} - C_2\kappa_{22} = N_1 \\
&B_2\varepsilon_1^o + B_1\varepsilon_2^o - C_2\kappa_{11} - C_1\kappa_{22} = N_2 \\
&C_1\varepsilon_1^o + C_2\varepsilon_2^o - D_1\kappa_{11} - D_2\kappa_{22} = M_1 \\
&C_2\varepsilon_1^o + C_1\varepsilon_2^o - D_2\kappa_{11} - D_1\kappa_{22} = M_2
\end{aligned} \tag{177}$$

where

$$\begin{aligned}
&B_1 = \frac{E_s t_s}{1-\nu_s^{\,2}} + \frac{E_a t_a}{1-\nu_a^{\,2}}; \qquad B_2 = \frac{\nu_s E_s t_s}{1-\nu_s^{\,2}} + \frac{\nu_a E_a t_a}{1-\nu_a^{\,2}} \\
&C_1 = \frac{-E_s}{1-\nu_s^{\,2}}\left(\frac{t_s^{\,2}}{2}\right) + \frac{E_a}{1-\nu_a^{\,2}}\left(\frac{t_a^{\,2}}{2}\right); \qquad C_2 = \frac{-\nu_s E_s}{1-\nu_s^{\,2}}\left(\frac{t_s^{\,2}}{2}\right) + \frac{\nu_a E_a}{1-\nu_a^{\,2}}\left(\frac{t_a^{\,2}}{2}\right) \\
&D_1 = \frac{E_s}{1-\nu_s^{\,2}}\left(\frac{t_s^{\,3}}{3}\right) + \frac{E_a}{1-\nu_a^{\,2}}\left(\frac{t_a^{\,3}}{3}\right); \qquad D_2 = \frac{\nu_s E_s}{1-\nu_s^{\,2}}\left(\frac{t_s^{\,3}}{3}\right) + \frac{\nu_a E_a}{1-\nu_a^{\,2}}\left(\frac{t_a^{\,3}}{3}\right) \\
&N_1 = \left(H_{11}^a + \nu_a H_{22}^a\right) t_a \frac{E_a}{1-\nu_a^{\,2}}; \qquad N_2 = \left(H_{22}^a + \nu_a H_{11}^a\right) t_a \frac{E_a}{1-\nu_a^{\,2}} \\
&M_1 = \left(H_{11}^a + \nu_a H_{22}^a\right) \frac{t_a^{\,2}}{2} \frac{E_a}{1-\nu_a^{\,2}}; \qquad M_2 = \left(H_{22}^a + \nu_a H_{11}^a\right) \frac{t_a^{\,2}}{2} \frac{E_a}{1-\nu_a^{\,2}}
\end{aligned} \tag{178}$$

It can be seen from Eqs. (177) and (178) that prescribing non-mechanical stimulus to the active layer is comparable to the composite plate being subjected to the corresponding in-plane normal forces and bending moments.

In order to explore the magnitude of the in-plane strains in bilayer thin composites when subjected to spontaneous non-mechanical stimuli, a case study utilizing electric field input and water diffusion input are presented. Electric field is generated by prescribing an electric potential difference through the thickness of the active layer. Various electro-active materials can be considered for the active layer. When a piezoelectric material such as, lead zirconate titanate (PZT), polyvinylidene (PVDF), or active fiber composite (AFC), the in-plane deformation due to the electric field input (E_e) is obtained using the piezoelectric coupling (d), and thus $H_{11}^a = H_{22}^a = dE_e$. In this situation, positive and negative electric field inputs generate expansion and contraction, respectively, to the active layer. When an electrostrictive material, such as P(VDF-TrFE-CTFE) electrostrictive terpolymer (Celli et al. [64]), is considered, the coupling is obtained using the coefficient of electrostriction (β), and thus the in-plane strain is $H_{11}^a = H_{22}^a = \beta\left(E_e\right)^2$. In this case only free expansion is possible, and hence the out of plane shape change can be achieved for the composites with arrangements in Figure 54a and Figure 54b. When the sandwich composite in Figure 54a is considered, only one of the active layers should be activated to induce out of plane shape changes.

This study considers a bilayer composite (Figure 54b) comprising of terpolymer active layer and PDMS substrate, following a previous study by Celli, Gonella [64]. The mechanical properties of the PDMS and terpolymer are $E_s = 2\text{MPa}; \nu_s = 0.5$; $E_a = 200\text{MPa}$; $\nu_s = 0.48$, the thickness of the terpolymer is 0.01mm, the coefficient of electrostriction $\beta = 3\text{x}10^{-18}\text{m}^2/\text{V}^2$, and the maximum electric field that can be prescribed is $E_{e\_\max} = 350\text{MV/m}$. Different thickness of the substrate, i.e., 0.05, 0.1, and 0.2mm, and an electric field input $E_e = 100\text{MV/m}$, which give free expansion of $H_{11}^a = H_{22}^a = \beta\left(E_e\right)^2 = 0.0675$, are considered. From Eqs. (177) and (178), the axial

strains $\varepsilon_1^o = \varepsilon_2^o$ and curvatures $\kappa_{11} = \kappa_{22}$ of the interface of the bilayer can be obtained for the composite with different substrate thickness. The corresponding axial strains are $0.0261;\ 0.0272;\ 0.0276$ for the substrate thickness 0.05, 0.1, and 0.2mm, respectively. These values are relatively small, and the in-plane deformations resulting from the above axial strains are rather insignificant compared to the out of plane deformation. The corresponding curvatures for the above substrate thickness are -0.6989, -0.4041, -0.2086 mm^{-1}, which can result in large out of plane deformations, as will be shown later in the results. This analysis justifies that the large out of plane deformations are governed by large rotation and the in-plane stretch contributions are negligible. It is noted that the analyses of the active bilayers presented using the piezoelectric materials and electrostictive materials are also applicable to magnetostrictive materials.

When the deformation of the neutral surface is considered, the strain in Eq. (173) can be written as:

$$\begin{aligned} \varepsilon_{11} &= -x_3\kappa_{11} \\ \varepsilon_{22} &= -x_3\kappa_{22} \end{aligned} \tag{179}$$

where x_3 is measured from the neutral surface of the plate. The neutral surface of the plate is determined by imposing $\int_{A_1} \sigma_{11} dA = \int_{A_2} \sigma_{22} dA = 0$ only for the bending response, which yield to

$$\begin{aligned} \sum_{k=1}^{N} \left[\frac{E_k}{1-\nu_k^{\,2}} \left(\kappa_{11} + \nu_k \kappa_{22} \right) \int_{A_1} x_3 dA \right] &= 0 \\ \sum_{k=1}^{N} \left[\frac{E_k}{1-\nu_k^{\,2}} \left(\kappa_{22} + \nu_k \kappa_{11} \right) \int_{A_2} x_3 dA \right] &= 0 \end{aligned} \tag{180}$$

The governing equations in Eq. (178) reduce to:

$$\begin{aligned} -\hat{D}_1\kappa_{11} - \hat{D}_2\kappa_{22} &= \hat{M}_1 \\ -\hat{D}_2\kappa_{11} - \hat{D}_1\kappa_{22} &= \hat{M}_2 \end{aligned} \tag{181}$$

where

$$\begin{aligned}
\hat{D}_1 &= \frac{E_s}{1-\nu_s{}^2}\left(\frac{\hat{z}^3}{3}-\frac{\left(\hat{z}-t_s\right)^3}{3}\right)+\frac{E_a}{1-\nu_a{}^2}\left(\frac{\left(\hat{z}+t_a\right)^3}{3}-\frac{\hat{z}^3}{3}\right)\\
\hat{D}_2 &= \frac{\nu_s E_s}{1-\nu_s{}^2}\left(\frac{\hat{z}^3}{3}-\frac{\left(\hat{z}-t_s\right)^3}{3}\right)+\frac{\nu_a E_a}{1-\nu_a{}^2}\left(\frac{\left(\hat{z}+t_a\right)^3}{3}-\frac{\hat{z}^3}{3}\right)\\
\hat{M}_1 &= \frac{E_a}{1-\nu_a{}^2}\left(H_{11}^a+\nu_a H_{22}^a\right)\left(\frac{\left(\hat{z}+t_a\right)^2}{2}-\frac{\hat{z}^2}{2}\right)\\
\hat{M}_2 &= \frac{E_a}{1-\nu_a{}^2}\left(H_{22}^a+\nu_a H_{11}^a\right)\left(\frac{\left(\hat{z}+t_a\right)^2}{2}-\frac{\hat{z}^2}{2}\right)
\end{aligned} \tag{182}$$

where $\hat{z}$ represents the distance between neutral surface of the plate and the interface of the bilayer. The value of $\hat{z}$ can be found by solving Eq. (180).

In analyzing the deformations of the bilayer due to non-mechanical stimuli, the constitutive relation is implemented in shell elements within finite element (FE). For this purpose, a homogeneous planar surface out of the inactive layer (substrate) is considered and external moments to the planar surface are prescribed. A co-rotational (CR) finite element approach, which splits the large rotation from the in-plane deformations, following Felippa and Haugen [65] and Tajeddini and Muliana [66], is used in order to determine the shape reconfiguration of the substrate. This approach is considered since prescribing non-mechanical stimuli only cause free expansion/contraction in the active layer and the substrate does not undergo free expansion/contraction due to an application of the non-mechanical stimuli. However, the through thickness deformation gradient leads to curvature changes of the systems. The bending moments per unit length, m_1 and m_2 that are prescribed to the substrate surface induce normal stresses:

$$\begin{aligned}
\int_{\hat{z}-t_s}^{\hat{z}} \sigma_{11}^s x_3 dx_2 dx_3 &= m_1 dx_2\\
\int_{\hat{z}-t_s}^{\hat{z}} \sigma_{22}^s x_3 dx_1 dx_3 &= m_2 dx_2
\end{aligned} \tag{183}$$

These moments are obtained from prescribing the external electric field to the active layer, which are:

$$m_1 = -\int_{\hat{z}}^{\hat{z}+t_a} \left(\frac{E_a}{1-\nu_a{}^2} \left(\left(-\kappa_{11} - \nu_a \kappa_{22} \right) x_3 - H_{11} - \nu_a H_{22} \right) \right) x_3 dx_3$$
$$m_2 = -\int_{\hat{z}}^{\hat{z}+t_a} \left(\frac{E_a}{1-\nu_a{}^2} \left(\left(-\kappa_{22} - \nu_a \kappa_{11} \right) x_3 - H_{22} - \nu_a H_{11} \right) \right) x_3 dx_3 \tag{184}$$

Upon solving the integral in Eq. (184), the moments are expressed as:

$$m_1 = -\left(\frac{E_a}{1-\nu_a{}^2} \left(-\kappa_{11} - \nu_s \kappa_{22} \right) \right) \left(\frac{\left(\hat{z} + t_a \right)^3}{3} - \frac{\hat{z}^3}{3} \right) + \hat{M}_1$$
$$m_2 = -\left(\frac{E_a}{1-\nu_a{}^2} \left(-\kappa_{22} - \nu_s \kappa_{11} \right) \right) \left(\frac{\left(\hat{z} + t_a \right)^3}{3} - \frac{\hat{z}^3}{3} \right) + \hat{M}_2 \tag{185}$$

where $\hat{M}_1$ and $\hat{M}_2$ are given in Eq. (182). In this study, the shell elements are comprised of a homogeneous substrate material (inactive layer) and the external stimuli, i.e., electric field input, are incorporated as external (prescribed distributed and uniform moments) given in Eq. (185).

6.2. Modeling Bilayers with Viscoelastic Layer

For multi-layered polymer smart structures, the material properties, geometrical shapes and layer arrangements all contribute to the controlling of shape reconfigurations. In this section, different polymer properties are considered to model the deformed shapes. For applications that require precise time and shape controls, it is important to include the viscoelastic properties of polymers. Thus, the time-dependent reconfiguration of the bilayer systems is studied in this section. The substrate layer (inactive) is modeled as a linear viscoelastic, isotropic material. The constitutive relations for the inactive substrate layer can be written as:

$$
\begin{aligned}
\sigma_{11}^{s} &= \frac{1}{1-\nu_s^{\,2}}\int_0^t E_s(t-\tau)\left(\frac{d\varepsilon_{11}}{d\tau}\right)d\tau + \frac{\nu_s}{1-\nu_s^{\,2}}\int_0^t E_s(t-\tau)\left(\frac{d\varepsilon_{22}}{d\tau}\right)d\tau \\
\sigma_{22}^{s} &= \frac{\nu_s}{1-\nu_s^{\,2}}\int_0^t E_s(t-\tau)\left(\frac{d\varepsilon_{11}}{d\tau}\right)d\tau + \frac{1}{1-\nu_s^{\,2}}\int_0^t E_s(t-\tau)\left(\frac{d\varepsilon_{22}}{d\tau}\right)d\tau \\
\sigma_{12}^{s} &= \frac{1}{1+\nu_s}\int_0^t E_s(t-\tau)\left(\frac{d\varepsilon_{12}}{d\tau}\right)d\tau
\end{aligned}
\tag{186}
$$

In the above equations, $E_s(t-\tau)$ is the relaxation modulus. The constitutive relations for the active layer and the equilibrium equations are the same with the relations given in Eqs. (175)-(176). Similar with the procedures discussed in section 5.1, substitute constitutive relations shown in Eqs. (175), (186) into equilibrium equation Eq. (176) results in the following relation:

$$
\begin{aligned}
&B_1(t)*d\varepsilon_1^o(t) + B_2\varepsilon_1^o(t) + \nu_s B_1(t)*d\varepsilon_2^o(t) + \nu_a B_2\varepsilon_2^o(t) \\
&-C_1(t)*d\kappa_{11}(t) - C_2\kappa_{11}(t) - \nu_s C_1(t)*d\kappa_{22}(t) - \nu_a C_2\kappa_{22}(t) = N_1(t) \\
&\nu_s B_1(t)*d\varepsilon_1^o(t) + \nu_a B_2\varepsilon_1^o(t) + B_1(t)*d\varepsilon_2^o(t) + B_2\varepsilon_2^o(t) \\
&-\nu_s C_1(t)*d\kappa_{11}(t) - \nu_a C_2\kappa_{11}(t) - C_1(t)*d\kappa_{22}(t) - C_2\kappa_{22}(t) = N_2(t) \\
&C_1(t)*d\varepsilon_1^o(t) + C_2\varepsilon_1^o(t) + \nu_s C_1(t)*d\varepsilon_2^o(t) + \nu_a C_2\varepsilon_2^o(t) \\
&-D_1(t)*d\kappa_{11}(t) - D_2\kappa_{11}(t) - \nu_s D_1(t)*d\kappa_{22}(t) - \nu_a D_2\kappa_{22}(t) = M_1(t) \\
&\nu_s C_1(t)*d\varepsilon_1^o(t) + \nu_a C_2\varepsilon_1^o(t) + C_1(t)*d\varepsilon_2^o(t) + C_2\varepsilon_2^o(t) \\
&-\nu_s D_1(t)*d\kappa_{11}(t) - \nu_a D_2\kappa_{11}(t) - D_1(t)*d\kappa_{22}(t) - D_2\kappa_{22}(t) = M_2(t)
\end{aligned}
\tag{187}
$$

where

$$
\begin{aligned}
&B_1 = \frac{E_s(t)t_s}{1-\nu_s^{\,2}}; \qquad B_2 = \frac{E_a t_a}{1-\nu_a^{\,2}}; \qquad C_1 = \frac{-E_s(t)}{1-\nu_s^{\,2}}\left(\frac{t_s^{\,2}}{2}\right); \\
&C_2 = \frac{E_a}{1-\nu_a^{\,2}}\left(\frac{t_a^{\,2}}{2}\right); \qquad D_1 = \frac{E_s(t)}{1-\nu_s^{\,2}}\left(\frac{t_s^{\,3}}{3}\right); \qquad D_2 = \frac{E_a}{1-\nu_a^{\,2}}\left(\frac{t_a^{\,3}}{3}\right) \\
&N_1 = \left(H_{11}^a + \nu_a H_{22}^a\right)t_a\frac{E_a}{1-\nu_a^{\,2}}; \qquad N_2 = \left(H_{22}^a + \nu_a H_{11}^a\right)t_a\frac{E_a}{1-\nu_a^{\,2}} \\
&M_1 = \left(H_{11}^a + \nu_a H_{22}^a\right)\frac{t_a^{\,2}}{2}\frac{E_a}{1-\nu_a^{\,2}}; \qquad M_2 = \left(H_{22}^a + \nu_a H_{11}^a\right)\frac{t_a^{\,2}}{2}\frac{E_a}{1-\nu_a^{\,2}}
\end{aligned}
\tag{188}
$$

In Eq. (187), operator '$*$' stands for convolution integral over time [0, t], while operator *d* denotes the time derivative. Eq. (187) can be solved analytically in Laplace domain. The following equation depicts the Laplace transformation of Eq. (193) in Laplace domain:

$$\begin{aligned}
&\tilde{B}_1 d\tilde{\varepsilon}_1^o + B_2\, d\tilde{\varepsilon}_1^o/s + \nu_s \tilde{B}_1 d\tilde{\varepsilon}_2^o + \nu_a B_2\, d\tilde{\varepsilon}_2^o/s - \tilde{C}_1 d\tilde{\kappa}_{11} - C_2\, d\tilde{\kappa}_{11}/s - \nu_s \tilde{C}_1 d\tilde{\kappa}_{22} - \nu_a C_2\, d\tilde{\kappa}_{22}/s = \tilde{N}_1 \\
&\nu_s \tilde{B}_1 d\tilde{\varepsilon}_1^o + \nu_a B_2\, d\tilde{\varepsilon}_1^o/s + \tilde{B}_1 d\tilde{\varepsilon}_2^o + B_2\, d\tilde{\varepsilon}_2^o/s - \nu_s \tilde{C}_1 d\tilde{\kappa}_{11} - \nu_a C_2\, d\tilde{\kappa}_{11}/s - \tilde{C}_1 d\tilde{\kappa}_{22} - C_2\, d\tilde{\kappa}_{22}/s = \tilde{N}_2 \\
&\tilde{C}_1 d\tilde{\varepsilon}_1^o + C_2\, d\tilde{\varepsilon}_1^o/s + \nu_s \tilde{C}_1 d\tilde{\varepsilon}_2^o + \nu_a C_2\, d\tilde{\varepsilon}_2^o/s - \tilde{D}_1 d\tilde{\kappa}_{11} - D_2\, d\tilde{\kappa}_{11}/s - \nu_s \tilde{D}_1 d\tilde{\kappa}_{22} - \nu_a D_2\, d\tilde{\kappa}_{22}/s = \tilde{M}_1 \\
&\nu_s \tilde{C}_1 d\tilde{\varepsilon}_1^o + \nu_a C_2\, d\tilde{\varepsilon}_1^o/s + \tilde{C}_1 d\tilde{\varepsilon}_2^o + C_2\, d\tilde{\varepsilon}_2^o/s - \nu_s \tilde{D}_1 d\tilde{\kappa}_{11} - \nu_a D_2\, d\tilde{\kappa}_{11}/s - \tilde{D}_1 d\tilde{\kappa}_{22} - D_2\, d\tilde{\kappa}_{22}/s = \tilde{M}_2
\end{aligned} \tag{189}$$

In Eq. (189), operator '~' above the time-dependent functions indicate the transformation of the function in Laplace domain. By solving Eq. (189), the transformed expressions of $d\tilde{\varepsilon}_1^o$, $d\tilde{\varepsilon}_2^o$, $d\tilde{\kappa}_{11}$, $d\tilde{\kappa}_{22}$ can be found; then by taking the inverse of Laplace transformation, the time-dependent expressions of in-plane strains at interface and the corresponding curvatures can be determined.

Similar with the discussion in section 6.1, an electric field is generated by prescribing an electric potential difference through the thickness of the active layer. It is assumed that the electric field is spontaneously applied to the active layer, then held constant for a few seconds. To analyze the deformation of the bilayer system and the snap-though behavior caused by the viscosity of substrate layer, shell elements in a CF-FE formulation is applied to simulate the deformation of the neutral surface of the bilayer system. From Eq. (187), the prescribed electrical stimulus can be equivalent with an in-plane normal force and bending moments applied to the interface of the two layers. The bending moments per unit length prescribed to the neutral surface can be determined from the following expression:

$$\begin{aligned}
&\int_{\hat{z}-t_s}^{\hat{z}} \sigma_{11}^s x_3 dx_2 dx_3 = m_1 dx_2 \\
&\int_{\hat{z}-t_s}^{\hat{z}} \sigma_{22}^s x_3 dx_1 dx_3 = m_2 dx_2
\end{aligned} \tag{190}$$

In Eq. (190), stress σ_{11}^{s} and σ_{22}^{s} can be related to the in-plane strains through constitutive relations shown in Eq. (186). $\hat{z}$ in Eq. (196) indicates the location of neutral axis. The bending moments per unit length in Laplace domain can be expressed as:

$$\begin{aligned}\tilde{m}_1 &= \frac{1}{1-\nu_s^2}\left(\frac{\hat{z}^2-t_s^2}{2}\right)\tilde{E}_s d\tilde{\varepsilon}_1 - \frac{1}{1-\nu_s^2}\left(\frac{\hat{z}^3-t_s^3}{3}\right)\tilde{E}_s d\tilde{\kappa}_{11} + \frac{\nu_s}{1-\nu_s^2}\left(\frac{\hat{z}^2-t_s^2}{2}\right)\tilde{E}_s d\tilde{\varepsilon}_2 - \frac{\nu_s}{1-\nu_s^2}\left(\frac{\hat{z}^3-t_s^3}{3}\right)\tilde{E}_s d\tilde{\kappa}_{22} \\ \tilde{m}_1 &= \frac{\nu_s}{1-\nu_s^2}\left(\frac{\hat{z}^2-t_s^2}{2}\right)\tilde{E}_s d\tilde{\varepsilon}_1 - \frac{\nu_s}{1-\nu_s^2}\left(\frac{\hat{z}^3-t_s^3}{3}\right)\tilde{E}_s d\tilde{\kappa}_{11} + \frac{1}{1-\nu_s^2}\left(\frac{\hat{z}^2-t_s^2}{2}\right)\tilde{E}_s d\tilde{\varepsilon}_2 - \frac{1}{1-\nu_s^2}\left(\frac{\hat{z}^3-t_s^3}{3}\right)\tilde{E}_s d\tilde{\kappa}_{22}\end{aligned} \quad (191)$$

Eq. (191) above gives the time-dependent functions of bending moments applied to the neutral surface in Laplace domain. Taking the reverse transformation of Eq. (191), the external moments prescribed to the neutral surface can be determined and implemented into the co-rotational finite element model.

6.3. Modeling Bilayers with Electro-active and Shape Memory Layers

This section presents a constitutive model for bilayers comprising of two different active materials, i.e., electro-active polymer and shape memory polymer. The shape reconfiguration in the bilayer is achieved by prescribing electric fields. The motivation of using shape memory polymer as a substrate is that the shape can be partially (or fully) retained upon removal of the electric field. This study uses a light activated shape memory polymer (LASMP), whose phase transformation is achieved by light irradiation. The discussion of LASMPs can be found in Lendlein, Jiang [67], Scott, Schneider [68], and Long, Scott [69]. In this study, the constitutive model for the LASMP is based on the work of Yuan et al. [49, 70].

Yuan et al. [49, 70] used a multiple natural configuration approach to describe the deformations of LASMPs. In LASMPs, light irradiation induces microstructural changes from the original molecular network to a newly formed network due to radiation. In order to describe the

deformations of LASMPs comprising of two phases, a model of a constrained mixture is adopted, which is given as:

$$\boldsymbol{\sigma} = (1-\alpha)\boldsymbol{\sigma}_o + \alpha\boldsymbol{\sigma}_n \tag{192}$$

where the subscripts *o* and *n* represent the original and newly formed networks, respectively, α is the volume fraction of the second network. The stress of the original network is expressed in terms of the deformation gradient associated with the original network $\mathbf{F}_o$, i.e., $\boldsymbol{\sigma}_o(\mathbf{F}_o)$, and the stress associated with the new configuration is expressed in terms of the deformation gradient that maps the original network to the newly formed network $\mathbf{F}_n$, i.e., $\boldsymbol{\sigma}_n(\mathbf{F}_n)$, where $\mathbf{F}_n = \mathbf{F}_a^{*-1}\mathbf{F}_a$ and $\mathbf{F}_a^*$ is the deformation gradient associated with the original network when the radiation starts.

For a substrate made of LASMP, the axial stresses upon light irradiation from the multiple natural configuration approach are then written as follow:

$$\begin{aligned}
\sigma_{11}^s &= (1-\alpha)\frac{E_s}{1-\nu_s{}^2}\left[\left(\lambda_1^0 - 1 - x_3\kappa_{11}\right) + \nu_s\left(\lambda_2^0 - 1 - x_3\kappa_{22}\right)\right] \\
&+ \alpha\frac{E_s^*}{1-\nu_s{}^2}\left[\left(\frac{\lambda_1^0}{\lambda_1^*} - 1 - x_3\left(\kappa_{11} - \kappa_{11}^*\right)\right) + \nu_s\left(\frac{\lambda_2^0}{\lambda_2^*} - 1 - x_3\left(\kappa_{22} - \kappa_{22}^*\right)\right)\right] \\
\sigma_{22}^s &= (1-\alpha)\frac{E_s}{1-\nu_s{}^2}\left[\left(\lambda_2^0 - 1 - x_3\kappa_{22}\right) + \nu_s\left(\lambda_1^0 - 1 - x_3\kappa_{11}\right)\right] \\
&+ \alpha\frac{E_s^*}{1-\nu_s{}^2}\left[\left(\frac{\lambda_2^0}{\lambda_2^*} - 1 - x_3\left(\kappa_{22} - \kappa_{22}^*\right)\right) + \nu_s\left(\frac{\lambda_1^0}{\lambda_1^*} - 1 - x_3\left(\kappa_{11} - \kappa_{11}^*\right)\right)\right]
\end{aligned} \tag{193}$$

where E_s and E_s^* are the elastic moduli of the original and newly generated networks, respectively, of the LASMP substrate. The stretches and curvatures of the neutral plane are λ_1^0, λ_2^0 and κ_{11}, κ_{22}, respectively. In this study, the Poisson's ratios of the original and newly form networks are assumed the same, $\nu_s = \nu_s^*$. The variables λ_1^*, λ_2^* and $\kappa_{11}^*, \kappa_{22}^*$ are the axial stretches and curvatures of the neutral plane, associated with the original network, when the radiation starts, which in this

study they are obtained from prescribing an electric field input. Since the stretch of the neutral plane is negligible, the axial stretches $\lambda_1^* = \lambda_2^* = 1$. The neutral plane was determined from prescribing the electric field input (Eq. (180)). After radiation, the stresses in Eq. (174) is written as:

$$\begin{aligned}\sigma_{11}^s &= \frac{FE_s}{1-\nu_s^{\,2}}\left(\varepsilon_{11}+\nu_s\varepsilon_{22}\right)+\frac{GE_s}{1-\nu_s^{\,2}}\left(x_3\kappa_{11}^*+\nu_s x_3\kappa_{22}^*\right)\\ \sigma_{22}^s &= \frac{FE_s}{1-\nu_s^{\,2}}\left(\varepsilon_{22}+\nu_s\varepsilon_{11}\right)+\frac{GE_s}{1-\nu_s^{\,2}}\left(x_3\kappa_{22}^*+\nu_s x_3\kappa_{11}^*\right)\end{aligned} \tag{194}$$

where

$$F = \frac{\left(1-\alpha\right)E_s+\alpha E_s^*}{E_s}\ ;\ G = \frac{\alpha E_s^*}{E_s}$$

$$\varepsilon_{11} = \varepsilon_1^o - x_3\kappa_{11} = \lambda_1^o - 1 - x_3\kappa_{11}\ ;\ \varepsilon_{22} = \varepsilon_2^o - x_3\kappa_{22} = \lambda_2^o - 1 - x_3\kappa_{22}$$

Consider a bilayer comprising of terpolymer electro-active layer and LASMP substrate. The thicknesses of the active and substrate layers are t_a and t_s, respectively. It is noted that the initial elastic properties of the active and substrate layers are $E_a,\ \nu_a, E_s,\ \nu_s$. Substituting Eq. (194) into the equilibrium equations, Eq. (176), the equilibrium equations for the bilayer after the substrate irradiation are:

$$\begin{aligned}\tilde{B}_1\varepsilon_1^o+\tilde{B}_2\varepsilon_2^o-\tilde{C}_1\kappa_{11}-\tilde{C}_2\kappa_{22} &= \tilde{N}_1\\ \tilde{B}_2\varepsilon_1^o+\tilde{B}_1\varepsilon_2^o-\tilde{C}_2\kappa_{11}-\tilde{C}_1\kappa_{22} &= \tilde{N}_2\\ \tilde{C}_1\varepsilon_1^o+\tilde{C}_2\varepsilon_2^o-\tilde{D}_1\kappa_{11}-\tilde{D}_2\kappa_{22} &= \tilde{M}_1\\ \tilde{C}_2\varepsilon_1^o+\tilde{C}_1\varepsilon_2^o-\tilde{D}_2\kappa_{11}-\tilde{D}_1\kappa_{22} &= \tilde{M}_2\end{aligned} \tag{195}$$

where

$$\tilde{B}_1=\frac{FE_st_s}{1-\nu_s^{\,2}}+\frac{E_at_a}{1-\nu_a^{\,2}};\qquad \tilde{B}_2=\frac{F\nu_sE_st_s}{1-\nu_s^{\,2}}+\frac{\nu_aE_at_a}{1-\nu_a^{\,2}}$$

$$\tilde{C}_1=\frac{FE_s}{1-\nu_s^{\,2}}\left(\frac{\hat{z}^2}{2}-\frac{\left(\hat{z}-t_s\right)^2}{2}\right)+\frac{E_a}{1-\nu_a^{\,2}}\left(\frac{\left(\hat{z}+t_a\right)^2}{2}-\frac{\hat{z}^2}{2}\right);\quad \tilde{C}_2=\frac{F\nu_sE_s}{1-\nu_s^{\,2}}\left(\frac{\hat{z}^2}{2}-\frac{\left(\hat{z}-t_s\right)^2}{2}\right)+\frac{\nu_aE_a}{1-\nu_a^{\,2}}\left(\frac{\left(\hat{z}+t_a\right)^2}{2}-\frac{\hat{z}^2}{2}\right) \tag{196}$$

$$\tilde{D}_1=\frac{FE_s}{1-\nu_s^{\,2}}\left(\frac{\hat{z}^3}{3}-\frac{\left(\hat{z}-t_s\right)^3}{3}\right)+\frac{E_a}{1-\nu_a^{\,2}}\left(\frac{\left(\hat{z}+t_a\right)^3}{3}-\frac{\hat{z}^3}{3}\right);\quad \tilde{D}_2=\frac{F\nu_sE_s}{1-\nu_s^{\,2}}\left(\frac{\hat{z}^3}{3}-\frac{\left(\hat{z}-t_s\right)^3}{3}\right)+\frac{\nu_aE_a}{1-\nu_a^{\,2}}\left(\frac{\left(\hat{z}+t_a\right)^3}{3}-\frac{\hat{z}^3}{3}\right)$$

$$\begin{aligned}
\tilde{N}_1&=\left(H_{11}^a+\nu_aH_{22}^a\right)t_a\frac{E_a}{1-\nu_a^{\,2}}-\frac{GE_s}{1-\nu_s^{\,2}}\left(\kappa_{11}^*+\nu_s\kappa_{22}^*\right)\left(\frac{\hat{z}^2}{2}-\frac{\left(\hat{z}-t_s\right)^2}{2}\right)\\
\tilde{N}_2&=\left(H_{22}^a+\nu_aH_{11}^a\right)t_a\frac{E_a}{1-\nu_a^{\,2}}-\frac{GE_s}{1-\nu_s^{\,2}}\left(\kappa_{22}^*+\nu_s\kappa_{11}^*\right)\left(\frac{\hat{z}^2}{2}-\frac{\left(\hat{z}-t_s\right)^2}{2}\right)\\
\tilde{M}_1&=\left(H_{11}^a+\nu_aH_{22}^a\right)\left(\frac{\left(\hat{z}+t_a\right)^2}{2}-\frac{\hat{z}^2}{2}\right)\frac{E_a}{1-\nu_a^{\,2}}-\frac{GE_s}{1-\nu_s^{\,2}}\left(\kappa_{11}^*+\nu_s\kappa_{22}^*\right)\left(\frac{\hat{z}^3}{3}-\frac{\left(\hat{z}-t_s\right)^3}{3}\right)\\
\tilde{M}_2&=\left(H_{22}^a+\nu_aH_{11}^a\right)\left(\frac{\left(\hat{z}+t_a\right)^2}{2}-\frac{\hat{z}^2}{2}\right)\frac{E_a}{1-\nu_a^{\,2}}-\frac{GE_s}{1-\nu_s^{\,2}}\left(\kappa_{22}^*+\nu_s\kappa_{11}^*\right)\left(\frac{\hat{z}^3}{3}-\frac{\left(\hat{z}-t_s\right)^3}{3}\right)
\end{aligned} \tag{197}$$

The curvatures and axial strains at the neutral plane can be solved from equilibrium equations Eq. (195)-(197). It is noted that in Eqs. (195)-(197), the deformations are obtained for the neutral surface, which was determined initially from prescribing the electric field input (Eq. (180)). Due to the irradiation of the substrate, the elastic modulus of the LASMP substrate changes, and thus the neutral surface also changes with irradiation. As mentioned above, in a thin composite the variation in the neutral surface due to irradiation is negligible. This has been shown by determining the axial strains $\varepsilon_1^0,\varepsilon_2^0$ in Eq. (195), which are small[5]. As discussed above that the axial strains generated by the application of external stimuli are negligible, therefore the equilibrium equation can be reduced to:

[5] When the elastic modulus of newly generated network is taken as $E_s^*=10E_s$, the curvatures and axial strains corresponding to electric field 100 MV/m are $\kappa_{11}=\kappa_{22}=-0.1392$ and $\varepsilon_1^0=\varepsilon_2^0=1.33\times10^{-6}$, for a LASMP substrate with thickness 0.3mm. The variation in neutral plane $\Delta z=-2.31\times10^{-4}$ mm, which is negligible compare to the thickness of substrate. Increasing E_s^* will further reduce the values for $\varepsilon_1^0,\varepsilon_2^0$ and Δz.

$$
\begin{aligned}
-\tilde{D}_1\kappa_{11} - \tilde{D}_2\kappa_{22} &= \tilde{M}_1 \\
-\tilde{D}_2\kappa_{11} - \tilde{D}_1\kappa_{22} &= \tilde{M}_2
\end{aligned}
\tag{198}
$$

Following the discussion in Section 6.1, the shape reconfigurations of the LASMP substrate are simulated using shell elements in a CF-FE formulation. For this reason, distributed bending moments are prescribed to the substrate, which are:

$$
\begin{aligned}
m_1 &= \left(\frac{FE_s}{1-\nu_s{}^2}\left(-\kappa_{11} - \nu_s\kappa_{22}\right) + \frac{GE_s}{1-\nu_s{}^2}\left(-\kappa_{11}^* - \nu_s\kappa_{22}^*\right) \right)\left(\frac{\hat{z}^3}{3} - \frac{\left(\hat{z}-t_s\right)^3}{3} \right) \\
m_2 &= \left(\frac{FE_s}{1-\nu_s{}^2}\left(-\kappa_{22} - \nu_s\kappa_{11}\right) + \frac{GE_s}{1-\nu_s{}^2}\left(-\kappa_{22}^* - \nu_s\kappa_{11}^*\right) \right)\left(\frac{\hat{z}^3}{3} - \frac{\left(\hat{z}-t_s\right)^3}{3} \right)
\end{aligned}
\tag{199}
$$

where κ_{11}, κ_{22} are determined from solving Eq. (198). Upon removal of the electric field input, the corresponding bending moments in Eq. (198) are reduced to the following amounts:

$$
\begin{aligned}
\tilde{M}_1 &= -\frac{GE_s}{1-\nu_s{}^2}\left(\kappa_{11}^* + \nu_s\kappa_{22}^*\right)\left(\frac{\hat{z}^3}{3} - \frac{\left(\hat{z}-t_s\right)^3}{3} \right) \\
\tilde{M}_2 &= -\frac{GE_s}{1-\nu_s{}^2}\left(\kappa_{22}^* + \nu_s\kappa_{11}^*\right)\left(\frac{\hat{z}^3}{3} - \frac{\left(\hat{z}-t_s\right)^3}{3} \right)
\end{aligned}
\tag{200}
$$

Thus, the amount of curvature springs back upon the removal of the electric field are written as:

$$
\Delta\kappa_1 = \Delta\kappa_2 = \Delta\kappa = \frac{-\left(H_{11}^a + \nu_a H_{22}^a\right)\left(\frac{\left(\hat{z}+t_a\right)^2}{2} - \frac{\hat{z}^2}{2} \right)\frac{E_a}{1-\nu_a{}^2}}{\frac{FE_s}{1-\nu_s}\left(\frac{\hat{z}^3}{3} - \frac{\left(\hat{z}-t_s\right)^3}{3} \right) + \frac{E_a}{1-\nu_a}\left(\frac{\left(\hat{z}+t_a\right)^3}{3} - \frac{\hat{z}^3}{3} \right)}
\tag{201}
$$

Recall from Eq. (181), the curvature of neutral plane before radiation starts can now be written as:

$$
\kappa_1^* = \kappa_2^* = \kappa^* = \frac{-\left(H_{11}^a + \nu_a H_{22}^a\right)\left(\frac{\left(\hat{z}+t_a\right)^2}{2} - \frac{\hat{z}^2}{2} \right)\frac{E_a}{1-\nu_a{}^2}}{\frac{E_s}{1-\nu_s}\left(\frac{\hat{z}^3}{3} - \frac{\left(\hat{z}-t_s\right)^3}{3} \right) + \frac{E_a}{1-\nu_a}\left(\frac{\left(\hat{z}+t_a\right)^3}{3} - \frac{\hat{z}^3}{3} \right)}
\tag{202}
$$

Comparing Eq. (202) with Eq. (201), it can be seen that $\kappa^* > \Delta\kappa$ for $\alpha > 0$, which means the bilayer with LASMP substrate is still deformed after the removal of electric field input.

6.4. Results

Shape reconfigurations in the bilayer plane actuated by a uniform application of electric field input are first examined. The studied bilayer plates comprise of terpolymer active layer and PDMS substrate. The electro-mechanical properties of the terpolymer and PDMS are discussed above, which are summarized in Table 11. The nonlinear electro-mechanical constitutive model is defined for the free expansion/contraction strains H_{11}^a, H_{22}^a. The planar dimension of the plate is defined along the x_1-x_2 axes, while the out of plane direction is defined along the x_3 axis. The thickness of the terpolymer and PDMS are 0.01 mm and 0.3 mm, respectively.

Table 11 Material and geometrical properties

	Terpolymer	PDMS
Modulus E (MPa)	200	2
Poisson's ratio ν	0.48	0.5
thickness (mm)	0.01	0.3
Electrostrictive β (m^2/V^2)	$3x10^{-18}$	-

First study concerns with the shape reconfigurations of bilayer plates of a rectangular shape. Bilayer plates with three different planar dimensions, 50x50 mm^2, 50x25 mm^2, and 50x5 mm^2 are subjected to a continuous increase of electric field in the terpolymer layer. Figure 55 illustrates the corresponding shape reconfigurations in the square bilayer plate at different electric fields. It is noticed that in a square plate at low electric field inputs (Figure 55a and b) the deformations are seen by uniform folding of the four corners to achieve a dome-like shape. This is expected as the electric field input generates the same axial stretch in the terpolymer layer along the planar axes.

The in-plane stretch gradient through the bilayer plate thickness generates the same curvatures along both planar axes. It is noted that the folded surface is the neutral surface of the bilayer plate, which is determined from Eq. (180), as discussed in Section 6.1. This has a consequence that only shapes with zero Gaussian curvature can be attained by prescribing the electric field input to the terpolymer layer. This is seen by snap-through shape reconfigurations when the electric field input is increased (Figure 55c-e) in order to achieve developable surfaces. The stable configuration with zero Gaussian curvature is associated with bending about a single planar axis. After the stable shape from the snap-through deformation is achieved, increasing electric field will lead to a rolling of the plate about the single planar axis. Figure 56 illustrates the corresponding Gaussian curvature of the square bilayer plate. It is seen that close to the snap-through state (Figure 57b-c), the Gaussian curvature has nearly zero magnitude. Once the stable configuration is achieved, the Gaussian curvature is zero (Figure 57d-e), except near the edges. Unlike the square plate, the rectangular plates immediately achieve a stable bending configuration about the axis with shorter dimension (Figure 57 and Figure 58). It is noted that the edge warping leads to a corkscrew-like shape, which can be clearly seen from a top view angle in all cases (Figure 59).

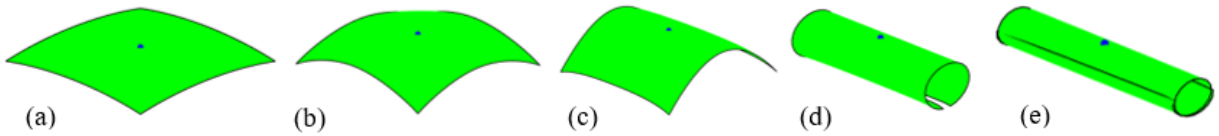

Figure 55 Bistable folding of square plate. (a): electric field 9MV/m; (b): electric field 15MV/m; (c): electric field 18MV/m; (d): electric field 68MV/m; (e): electric field 86MV/m

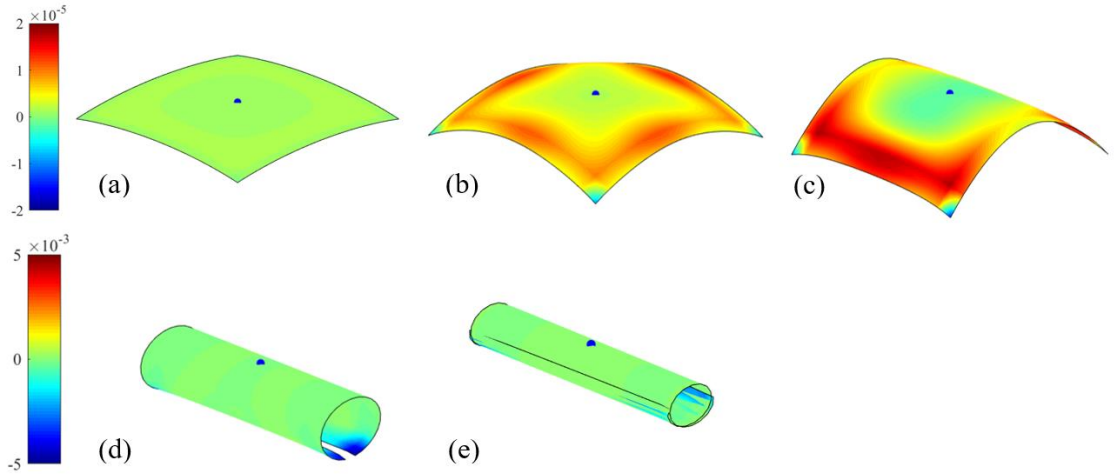

Figure 56 Gaussian curvature of folded square plate. (a): electric field 9MV/m; (b): electric field 15MV/m; (c): electric field 18MV/m; (d): electric field 68MV/m; (e): electric field 86MV/m

Figure 57 Folding of 50×25 rectangular plate. (a): electric field 25MV/m; (b): electric field 43MV/m; (c): electric field 68MV/m; (d): electric field 86MV/m

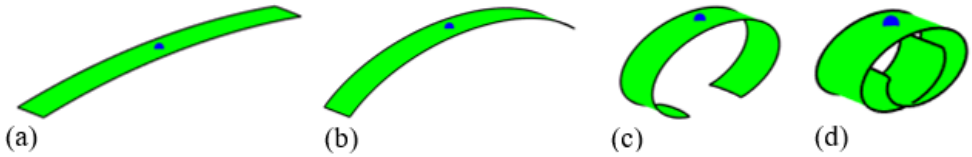

Figure 58 Folding of 50×5 rectangular plate. (a): electric field 25MV/m; (b): electric field 43MV/m; (c): electric field 68MV/m; (d): electric field 86MV/m

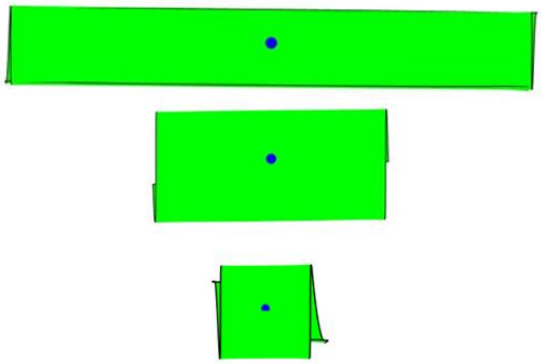

Figure 59 Top view of folded shapes of rectangular plates showing corkscrew shapes

To further illustrate the influence of single or double curvature changes of bilayer plates, parametric studies on both square and rectangular plates are presented. Figure 60 shows the shape reconfigurations of square plates when the through thickness electric field input is assumed to only create an in-plane stretching about one planar axis. It is seen that the plate immediately bends about a single axis perpendicular to the in-plane stretching axis. The effect of Poisson's ratio on the shape reconfigurations is also examined, as shown in Figure 60. The Poisson's effect results in a slight edge outward bending, perpendicular to the global rotation axis, due to the contraction of the plate perpendicular to the stretching direction. Comparing the cases with and without Poisson's effect, the Poisson's effect results in more pronounced folding, as shown by the first principal curvature contours in Figure 61. The second principal curvatures are nearly zero and thus are not reported here. Figure 62 illustrates shape changes in a rectangular plate when the electric field input induces stretching only along the longitudinal axis of the plate. The influence of the Poisson's ratio is also studied. As expected, a simple bending is seen in all cases. When the influence of the Poisson's ratio is removed, the response reduces to bending of a beam. Comparing the shape changes in Figure 57 and Figure 62, it is seen that the beam model can give a reasonable approximation of the deformation when the plate has a relatively large in-plane aspect ratio. Ignoring the influence

of Poison's effect shows a negligible effect when the plate is under small curvatures (Figure 62a). Figure 63 presents the shape reconfigurations of a rectangular plate when the electric field input induces stretching only along the lateral axis of the plate. The influence of Poisson's ratio is also investigated. It is seen that in this example, the longitudinal contraction of the bilayer plate due to stretching of the terpolymer layer in the lateral direction induces an anticlastic shape with one axis of bending dominates the shape changes.

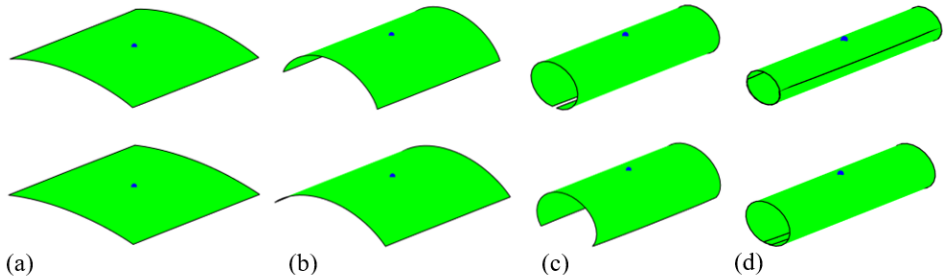

Figure 60 Folding of square plate, $m_y = 0$. Top: with Poisson's effect; Bottom: without Poisson's effect. (a): electric field 25MV/m; (b): electric field 43MV/m; (c): electric field 68MV/m; (d): electric field 86MV/m

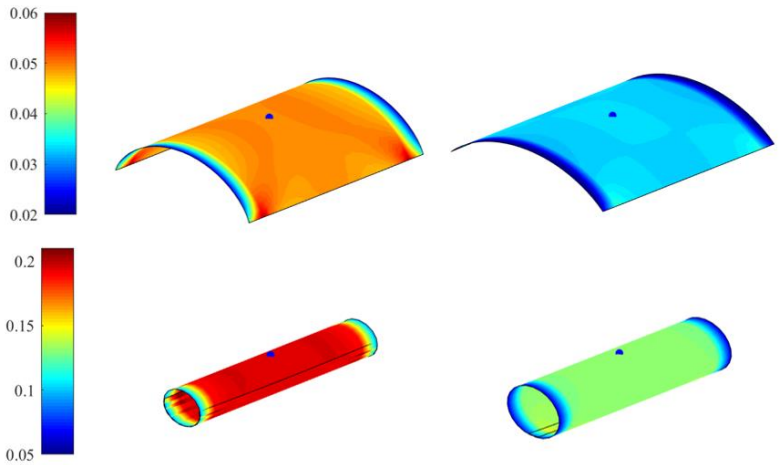

Figure 61 The corresponding first principal curvature with $m_y = 0$. Top: electric field 43MV/m; Bottom: electric field 86MV/m. The figures on the left are responses with Poisson's effect and figures on the right are responses without Poisson's effect

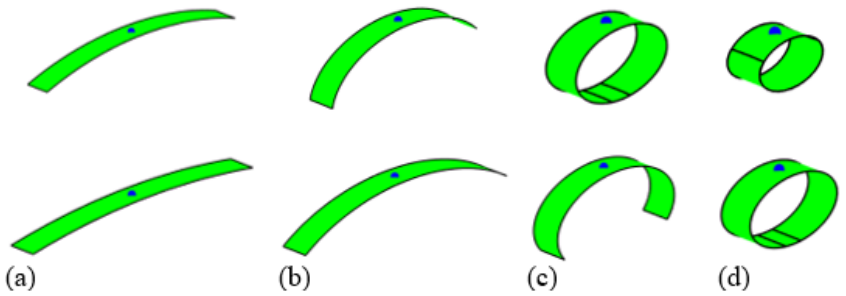

Figure 62 Folding of 50×5 rectangular plate, $m_x = 0$. Top: with Poisson's effect; Bottom: without Poisson's effect. (a): electric field 25MV/m; (b): electric field 43MV/m; (c): electric field 68MV/m; (d): electric field 86MV/m

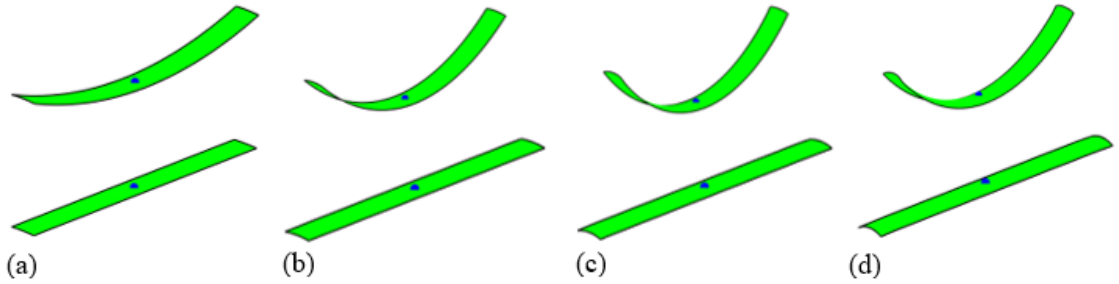

Figure 63 Folding of 50×5 rectangular plate, $m_y = 0$. Top: with Poisson's effect; Bottom: without Poisson's effect. (a): electric field 25MV/m; (b): electric field 43MV/m; (c): electric field 68MV/m; (d): electric field 86MV/m

Another case of folding of a triangular plate is shown in Figure 64. A snap-through behavior to form a rolling shape is also observed in order to maintain a stable shape with zero (or nearly zero) Gaussian curvature. Multi-stable shapes associated with snap-through mechanisms can also be achieved by prescribing different amplitude of electric field. For this purpose, a circular bilayer disk of a radius 25 mm is studied. Two different histories of prescribed electric field inputs are considered, referred as small and large increments. In the small increment input, a first stable shape configuration, which is associated with the lowest strain energy, can be achieved (see Figure 65(a)-(c) right). Once the stable configuration is achieved, increasing an electric field input will further fold the disk following this configuration. When a large increment input is considered, a

different stable shape configuration is attained as the large increment input missed the electric field that drive the first mode, as shown in Figure 65(a)-(c) left. Further increasing the electric field yield to further folding of this stable shape. Figure 65(d) summaries the electric field inputs with small and large increments, and highlights the critical electric fields that induce snap-through mechanisms associated with the first and second stable configurations. The corresponding Gaussian curvatures of the disks, which indicate that the stable shapes have to attain zero Gaussian curvature, are depicted in Figure 66.

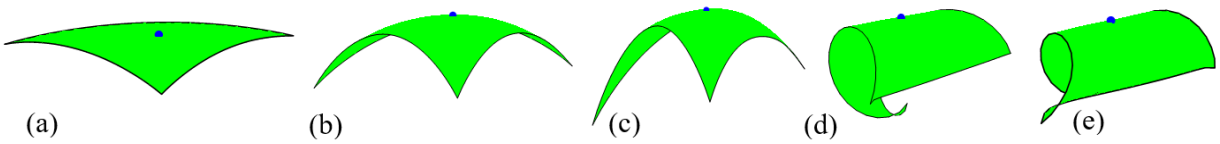

Figure 64 Folding of equilateral triangle plate. (a): electric field 9MV/m; (b): electric field 15MV/m; (c): electric field 20MV/m; (d): electric field 68MV/m; (e): electric field 86MV/m

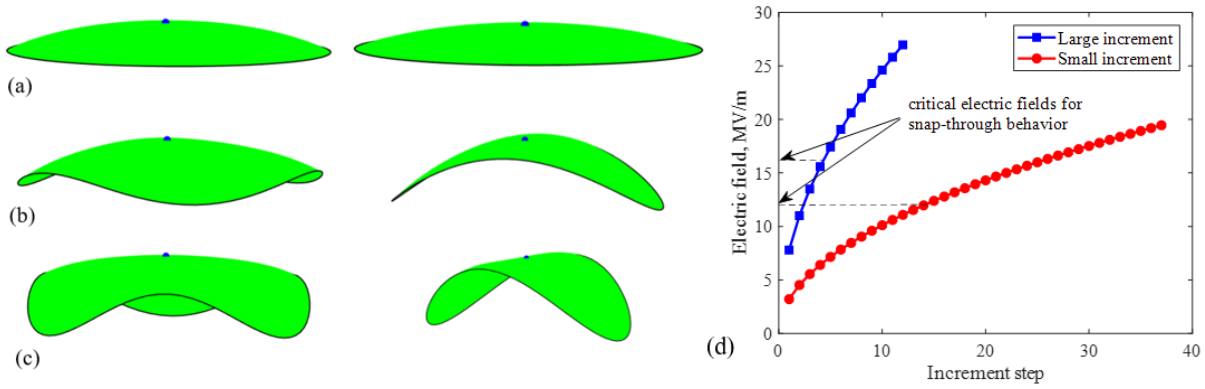

Figure 65 Folding of disk shape plate. Left: with large electric field increment; Right: with small electric field increment. (a): electric field 11MV/m; (b): electric field 17MV/m; (c): electric field 19MV/m; (d): Critical electric fields for the snap-through behavior under different increment.

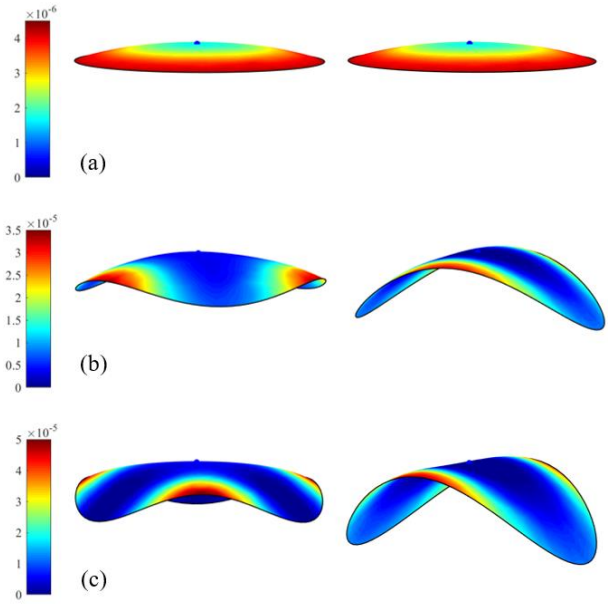

Figure 66 Gaussian curvature of folded disk shape plate. Left: with large electric field increment; Right: with small electric field increment. (a): electric field 11MV/m; (b): electric field 17MV/m; (c): electric field 19MV/m

The proposed approach is also capable in capturing an overall twisting shape reconfiguration of an active planar bilayer by arranging the placement of the active components in the bilayer. Figure 67 shows an example of a twisting of the active bilayer upon prescribing electric field input. It is seen that small magnitude of electric field induces initial bending deformations (Figure 67a-c), and increasing the non-uniform bending in the plate by increasing electric field in the active layers generates overall twisting shapes (Figure 67d-e). This twisting shape is attributed to the bending moments prescribed with off-axis angle from the longitudinal axis of the bilayer, which correspond to the placement of the active layer in the composite plate.

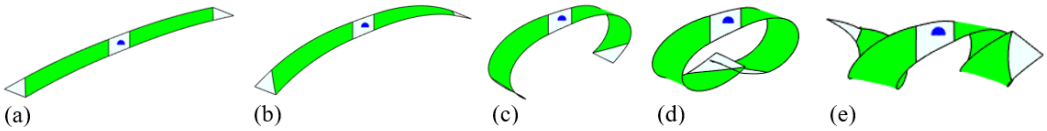

Figure 67 Twisting of 50×5 rectangular plate. (a): electric field 25MV/m; (b): electric field 43MV/m; (c): electric field 68MV/m; (d): electric field 86MV/m; (e): electric field 105MV/m

The time-dependent shape reconfigurations of the bilayer system are depicted in Figure 68-Figure 70 below. Three cases with different geometries are studied. The relaxation modulus of the viscoelastic substrate is assumed as follow:

$$E_s(t) = E_s^e + E_s^{ve} \exp(-t/\tau) \tag{203}$$

The material properties of the viscoelastic substrate are assumed as: $E_s^e = 10MPa$, $E_s^{ve} = 190MPa$, $\tau = 1s$. Figure 68 shows the time-dependent deformation of a square bilayer plate with length 50mm. An electric field of 45MV/m is prescribed to active the bilayer system. While the electric field remains constant, the shape of the bilayer system continues evolving due to the viscosity of the substrate. As shown in Figure 68(a), at very beginning when time *t*=0.1s, the four corners of the plate are deformed uniformly to form a dome-like shape. This is expected since the prescribed electric field would generate the same bending moments in the two in-plane axes. Due to the viscoelastic nature of the substrate, the deformed shape continues to change with constant electric field input. Since only neutral surfaces are mapped in this chapter, where the in-plane stretching is absent, a snap-through shape reconfiguration is seen in order to continually achieve developable surfaces. As depicted in Figure 68(b)-(c), the dome-like shape snapped to rolling about one axis, as time increases. The shape reconfigurations can be seen more clearly from the Gaussian curvature plots, as shown in Figure 68(bottom). Figure 69 and Figure 70 depict the shape reconfigurations evolving with time for an equilateral triangle plate with length 50mm and a disk shape plate with radius 25mm, respectively. The electrical stimuli applied to the triangle plate and disk plate are 65MV/m and 50MV/m, respectively. Same with the square plate, the deformed shapes of the triangle plate and dish shape plate continue evolving under constant electrical stimuli, due to the viscosity of the substrate. Shape reconfiguration can be observed from Figure 69 and

Figure 70. In both cases, the plate snapped to form a stable, rolling shape in order to maintain a zero Gaussian curvature.

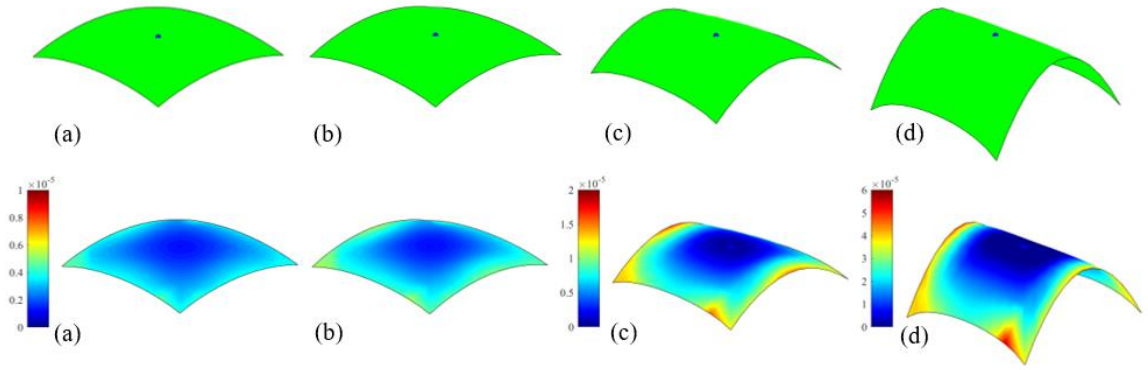

Figure 68 Shape reconfiguration of square plate with viscoelastic substrate. Top: deformed shape; Bottom: corresponding Gaussian curvature. (a): time t=0.1s; (b): time t=0.5s; (c): time t=5s; (d): time t=20s.

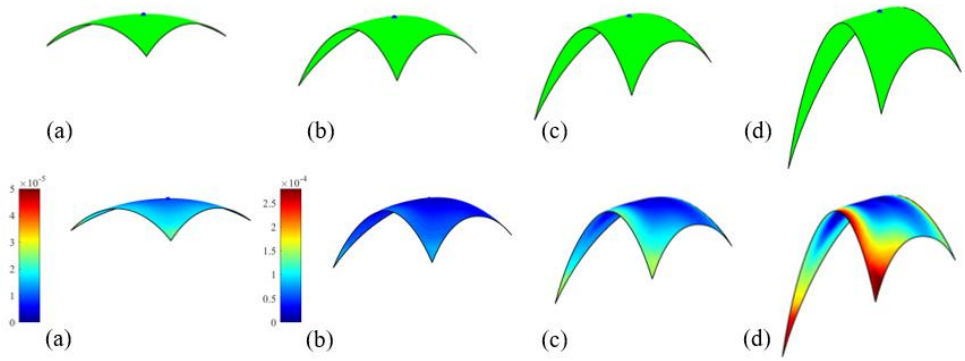

Figure 69 Shape reconfiguration of equilateral triangle plate with viscoelastic substrate. Top: deformed shape; Bottom: corresponding Gaussian curvature. (a): time t=0.1s; (b): time t=5s; (c): time t=10s; (d): time t=20s.

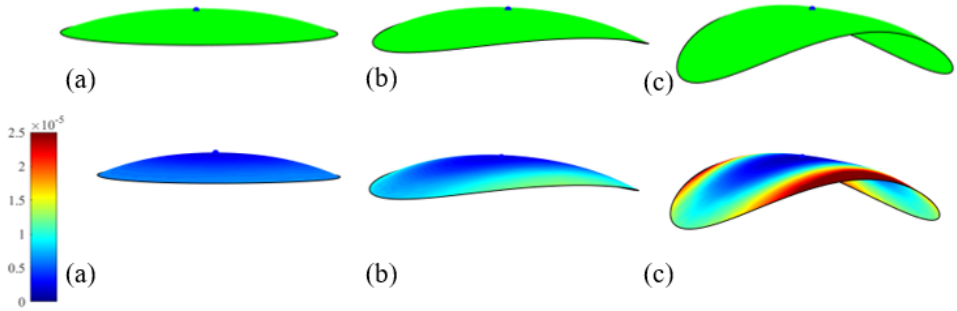

Figure 70 Shape reconfiguration of disk shape plate with viscoelastic substrate. Top: deformed shape; Bottom: corresponding Gaussian curvature. (a): time t=0.1s; (b): time t=0.5s; (c): time t=1.5s.

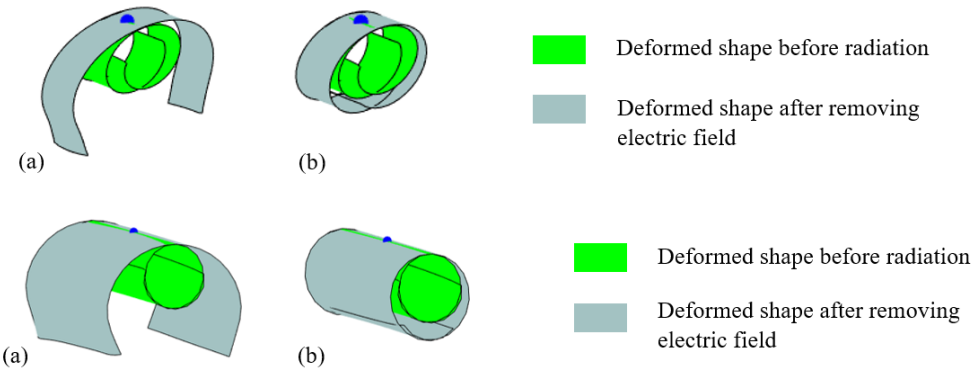

Figure 71 Deformed shapes of rectangular (top) and square (bottom) bilayers, comprising of LASMP substrate, after removing electric field. (a) $E_s^* = 10E_s = 20\text{MPa}$; (b) $E_s^* = 50E_s = 100\text{MPa}$

Finally, shape reconfigurations and retentions of bilayer plates comprising of terpolymer and LASMP layers are simulated. An electric field is first prescribed to the terpolymer layer to reconfigure the shapes of the bilayer, followed by radiating the LASMP layer. Upon radiation, the electric field input is removed and permanent shapes can be achieved. The properties of the terpolymer is given in Table 11. For the LASMP layer, the initial elastic properties are considered the same as the ones of PDMS layer, shown in Table 11. A parametric study is performed in order to investigate the effect of elastic modulus of the radiated LASMP on the overall shape retention behaviors. Figure 71 shows shape retentions of a 50x5 mm^2 (rectangular) and 50x50 mm^2 (square)

bilayers from prescribing electric field 86 MV/m and complete irradiation (α=1). It is seen that the shape retention depends strongly on the modulus of the LASMPs after irradiation. Stiffening the LASMPs by radiation will increase shape retention due to a minimal amount of spring back deformation. The shape retention can also be achieved in case of snap-through shape reconfiguration, as demonstrated for the square plate.

CHAPTER VII

SUMMARY AND CONCLUSIONS

In this study, we have presented a thermodynamic framework for materials undergoing microstructural changes, by assuming such material as a body possessing multiple natural configurations. When subjected to external stimuli, the material experiences microstructural changes and evolves between two natural configurations. Only the net effect of any possible microstructural changes is incorporated into the constitutive model using an internal state variable, which quantifies percent amount of microstructural changes. The multiple configuration approach simplifies the calibration process and reduces the number of material parameters, and are capable of predicting the mechanical responses for materials undergo microstructural changes under varies loading histories and loading environments.

In Chapter II, use POM polymer as example, a multiple configuration based constitutive model is developed from the thermodynamic framework to simulate the mechanical response of isotropic, homogeneous material. Creep-recovery responses of POM polymers under various loading amplitudes and creep durations are predicted by the constitutive model and compared with experimental tests. The model has a relatively small number of material parameters and these material parameters are associated with specific physical mechanisms (material compliance and inverse viscosity). This study also assumes that the microstructural changes are governed by the magnitude of the deformation in the polymer. The material parameters can be easily calibrated from limited experimental tests, as demonstrated in Chapter II. The model and calibrated material parameters are in good agreement with experimental data for various loading histories.

The nonlinear hysteretic responses of plant tissues and stems subjected to cyclic mechanical loadings are modeled in Chapter III. In Chapter III, the thermodynamic framework is extended to incorporate general anisotropic and heterogeneous materials. A constitutive model is formulated by taking into account the net effect of microstructural changes in describing the macroscopic response of the cell wall. The proposed model correlates well with the typical experimental tests since the detailed processes or information of the microstructural aspects that influence the macroscopic response of plant tissues are often not available, and only the net effect is being accounted for. It is also demonstrated that the proposed approach can be extended easily to include responses of different tissues in the plant stem in predicting the overall mechanical response of the stem, whose mechanical behavior is anisotropic and heterogeneous. This will be useful for examining the contributions of different constituents in the plant stem on their macroscopic mechanical response, which can shed light into understanding deformation mechanisms in plant stem.

Chapter IV extends the thermodynamic framework to include temperature as a new state variable. Same with Chapter II, the temperature-dependent response of thermoplastic polymer POM is modeled with a multiple configuration based constitutive model. The evolution of microstructural change and permanent deformation are assumed the same with the relations found in Chapter II, while in this chapter both natural configurations are assumed temperature-dependent. The predictions given by the constitutive model agree well with experimental data under varies loading conditions, including quasi-static tests, cyclic tests and creep-recovery tests. Other than temperature, the mechanical properties of thermoplastic polymers such as POM vary dramatically for different macromolecular characteristics. Three different POM materials with trademark names Delrin 100, Delrin 500 and Delrin 900 are studied in this chapter. It is seen that longer

macromolecular chains would slightly increases the microstructural changes both for tension and compression.

The Constitutive model discussed in Chapter IV can be extended to simulate mechanical responses of general anisotropic materials, as discussed in Chapter V. The compliance tensors and inverse viscosity tensors in Gibbs free energy are extended to include five independent parameters, in order to capture the mechanical response of transversely isotropic material PA6GF40. Two temperature-dependent natural configurations are assumed, and the microstructure evolves from initial configuration to final configuration as deformation increases. Also, same with POM polymer discussed in Chapter IV, the evolution of microstructural change generates permanent deformation. Different loading histories including quasi-static, cyclic, creep-recovery, under different loading rates, loading amplitudes, ambient temperatures are predicted by the developed constitutive model and compared with experimental results. Both axial and lateral responses under uniaxial loadings in 0° fiber direction and 90° fiber direction are analyzed. It can be seen that the model could capture the material symmetry of transversely isotropic material, and give reasonable prediction under different loading histories and loading conditions.

From the constitutive models discussed in Chapter II-V, it can be concluded that the constitutive model developed in this study can capture mechanical response under varies loading conditions with relatively small amount of material parameters, which presents high computation efficiency. A structural analysis of thin bilayer composites undergoing shape reconfigurations prescribed by an external electric field is discussed in Chapter VI. The thin composites comprise of one active and one inactive (substrate) layers and the electric field input causes expansion/contraction in the active layer. Three different types of material are considered for the inactive substrate layer, including elastic, viscoelastic, and light activated shape memory polymer

(LASMP), whose constitutive relation is modeled by multiple configuration approach. Several cases involving shape reconfigurations and snap-through behaviors of the neutral surfaces of various geometries have been presented. It can be concluded that in all cases the reconfigured shapes have zero (or nearly zero) Gaussian curvature. The snap-through behavior could be caused by increased electrical stimulus, or by the viscoelastic nature of the substrate. For bilayer system with LASMP substrate, it has been demonstrated that the shape retentions in the systems can be achieved upon removal of the electric field input.

REFERENCES

[1]. Song, R., A. Muliana, and K. Rajagopal, *A Thermodynamically Consistent Model for Viscoelastic Polymers undergoing Microstructural Changes*. under preparation, 2019.

[2]. Pawlak, A. and A. Galeski, *Cavitation during tensile deformation of polypropylene.* Macromolecules, 2008. **41**(8): p. 2839-2851.

[3]. Kobayashi, M., *Ultrasonic nondestructive evaluation of microstructural changes of solid materials under plastic deformation—Part I. Theory*. International Journal of Plasticity, 1998. **14**(6): p. 511-522.

[4]. Rajagopal, K.R. and A.S. Wineman, *A constitutive equation for nonlinear solids which undergo deformation induced microstructural changes.* International Journal of Plasticity, 1992. **8**(4): p. 385-395.

[5]. Meng, H. and J. Hu, *A brief review of stimulus-active polymers responsive to thermal, light, magnetic, electric, and water/solvent stimuli.* Journal of Intelligent Material Systems and Structures, 2010. **21**(9): p. 859-885.

[6]. Elhadrouz, M., T.B. Zineb, and E. Patoor, *Constitutive law for ferroelastic and ferroelectric piezoceramics.* Journal of intelligent material systems and structures, 2005. **16**(3): p. 221-236.

[7]. Jiles, D.C. and D.L. Atherton, *Theory of ferromagnetic hysteresis.* Journal of magnetism and magnetic materials, 1986. **61**(1-2): p. 48-60.

[8]. Ambard, D. and F. Cherblanc, *Mechanical behavior of annulus fibrosus: a microstructural model of fibers reorientation.* Annals of biomedical engineering, 2009. **37**(11): p. 2256-2265.

[9]. Schmidt, T., D. Balzani, and G.A. Holzapfel, *Statistical approach for a continuum description of damage evolution in soft collagenous tissues.* Computer methods in applied mechanics and engineering, 2014. **278**: p. 41-61.

[10]. Freed, A., K. Walker, and M. Verrilli, *Extending the theory of creep to viscoplasticity.* Journal of pressure vessel technology, 1994. **116**(1): p. 67-75.

[11]. Freed, A.D. and K.P. Walker, *Viscoplastic model development with an eye toward characterization.* Journal of engineering materials and technology, 1995. **117**(1): p. 8-13.

[12]. Green, A.E. and R.S. Rivlin, *The mechanics of non-linear materials with memory.* Archive for Rational Mechanics and Analysis, 1957. **1**(1): p. 1-21.

[13]. Findly, W., J. Lai, and K. Onaran, *Creep and relaxation of nonlinear viscoelastic materials*. 1976, North Holland, Toronto.

[14]. Pipkin, A.C., *Lectures on viscoelasticity theory*. Vol. 7. 2012: Springer Science & Business Media.

[15]. Christensen, R., *Theory of Viscoelasticity*. 2013: Courier Corporation.

[16]. Amin, K.E., A.K. Mukherjee, and J.E. Dorn, *A universal law for high-temperature diffusion controlled transient creep.* Journal of the Mechanics and Physics of Solids, 1970. **18**(6): p. 413-426.

[17]. Sherby, O. and J. Weertman, *Diffusion-controlled dislocation creep: a defense.* Acta Metallurgica, 1979. **27**(3): p. 387-400.

[18]. Frost, H.J. and M.F. Ashby, *Deformation mechanism maps: the plasticity and creep of metals and ceramics.* 1982.

[19]. Gabb, T. and G. Welsch, *The high temperature deformation in cyclic loading of a single crystal nickel-base superalloy.* Acta Metallurgica, 1989. **37**(9): p. 2507-2516.

[20]. Orlova, A., *On the relation between dislocation structure and internal stress measured in pure metals and single phase alloys in high temperature creep.* Acta metallurgica et materialia, 1991. **39**(11): p. 2805-2813.

[21]. Ashby, M.F., *A first report on deformation-mechanism maps.* Acta Metallurgica, 1972. **20**(7): p. 887-897.

[22]. Anand, M. and K. Rajagopal, *A shear-thinning viscoelastic fluid model for describing the flow of blood.* Int. J. Cardiovasc. Med. Sci, 2004. **4**(2): p. 59-68.

[23]. Wineman, A., *Nonlinear viscoelastic solids—a review.* Mathematics and mechanics of solids, 2009. **14**(3): p. 300-366.

[24]. De Pascalis, R., I.D. Abrahams, and W.J. Parnell, *On nonlinear viscoelastic deformations: a reappraisal of Fung's quasi-linear viscoelastic model.* Proceedings of the Royal Society A: Mathematical, Physical and Engineering Sciences, 2014. **470**(2166): p. 20140058.

[25]. de Souza Neto, E.A., D. Peric, and D.R. Owen, *Computational methods for plasticity: theory and applications*. 2011: John Wiley & Sons.

[26]. Lubliner, J., *Plasticity theory*. 2008: Courier Corporation.

[27]. Chaboche, J.-L., *A review of some plasticity and viscoplasticity constitutive theories.* International Journal of Plasticity, 2008. **24**(10): p. 1642-1693.

[28]. Lubliner, J., et al., *A plastic-damage model for concrete.* International Journal of solids and structures, 1989. **25**(3): p. 299-326.

[29]. Simo, J.C. and J. Ju, *Strain-and stress-based continuum damage models—I. Formulation.* International journal of solids and structures, 1987. **23**(7): p. 821-840.

[30]. Haddag, B., F. Abed-Meraim, and T. Balan, *Strain localization analysis using a large deformation anisotropic elastic–plastic model coupled with damage.* International journal of Plasticity, 2009. **25**(10): p. 1970-1996.

[31]. Tobolsky, A., I. Prettyman, and J. Dillon, *Stress relaxation of natural and synthetic rubber stocks.* Rubber Chemistry and Technology, 1944. **17**(3): p. 551-575.

[32]. Andrews, R., A. Tobolsky, and E. Hanson, *The theory of permanent set at elevated temperatures in natural and synthetic rubber vulcanizates.* Journal of Applied Physics, 1946. **17**(5): p. 352-361.

[33]. Leaderman, H., *Large longitudinal retarded elastic deformation of rubberlike network polymers.* Transactions of the Society of Rheology, 1962. **6**(1): p. 361-382.

[34]. Wineman, A. and J. Shaw, *A correspondence principle for scission-induced stress relaxation in elastomeric components.* Journal of applied mechanics, 2004. **71**(6): p. 769-773.

[35]. Wineman, A. and J. Shaw, *Combined deformation-and temperature-induced scission in a rubber cylinder in torsion.* International Journal of Non-Linear Mechanics, 2007. **42**(2): p. 330-335.

[36]. Arruda, E.M. and M.C. Boyce, *A three-dimensional constitutive model for the large stretch behavior of rubber elastic materials.* Journal of the Mechanics and Physics of Solids, 1993. **41**(2): p. 389-412.

[37]. Wu, P. and E. Van Der Giessen, *On improved network models for rubber elasticity and their applications to orientation hardening in glassy polymers.* Journal of the Mechanics and Physics of Solids, 1993. **41**(3): p. 427-456.

[38]. Nguyen, T.D., et al., *A thermoviscoelastic model for amorphous shape memory polymers: incorporating structural and stress relaxation.* Journal of the Mechanics and Physics of Solids, 2008. **56**(9): p. 2792-2814.

[39]. Kuhl, E., et al., *Remodeling of biological tissue: mechanically induced reorientation of a transversely isotropic chain network.* Journal of the Mechanics and Physics of Solids, 2005. **53**(7): p. 1552-1573.

[40]. Krairi, A. and I. Doghri, *A thermodynamically-based constitutive model for thermoplastic polymers coupling viscoelasticity, viscoplasticity and ductile damage.* International Journal of Plasticity, 2014. **60**: p. 163-181.

[41]. Guo, Q., F. Zaïri, and X. Guo, *A thermo-viscoelastic-damage constitutive model for cyclically loaded rubbers. Part I: Model formulation and numerical examples.* International Journal of Plasticity, 2018. **101**: p. 106-124.

[42]. Rajagopal, K. and A. Srinivasa, *Mechanics of the inelastic behavior of materials—Part 1, theoretical underpinnings.* International Journal of Plasticity, 1998. **14**(10-11): p. 945-967.

[43]. Lapczyk, I., K. Rajagopal, and A. Srinivasa, *Deformation twinning during impact of a titanium cylinder–numerical calculations using a constitutive theory based on multiple natural configurations.* Computer methods in applied mechanics and engineering, 2000. **188**(1-3): p. 527-541.

[44]. Rajagopal, K. and A. Srinivasa, *Inelastic behavior of materials. Part II. Energetics associated with discontinuous deformation twinning.* International Journal of Plasticity, 1997. **13**(1-2): p. 1-35.

[45]. Lapczyk, I., K. Rajagopal, and A. Srinivasa, *Deformation twinning during impact–numerical calculations using a constitutive theory based on multiple natural configurations.* Computational Mechanics, 1998. **21**(1): p. 20-27.

[46]. Rajagopal, K. and A. Srinivasa, *Modeling anisotropic fluids within the framework of bodies with multiple natural configurations.* Journal of Non-Newtonian Fluid Mechanics, 2001. **99**(2-3): p. 109-124.

[47]. Rajagopal, K.R. and A.R. Srinivasa, *A thermodynamic frame work for rate type fluid models.* Journal of Non-Newtonian Fluid Mechanics, 2000. **88**(3): p. 207-227.

[48]. Rajagopal, K. and A. Srinivasa, *On the thermomechanics of shape memory wires.* Zeitschrift für angewandte Mathematik und Physik ZAMP, 1999. **50**(3): p. 459-496.

[49]. Yuan, Z., A. Muliana, and K. Rajagopal, *Quasi-linear viscoelastic modeling of light-activated shape memory polymers.* Journal of Intelligent Material Systems and Structures, 2017. **28**(18): p. 2500-2515.

[50]. Barot, G., I. Rao, and K. Rajagopal, *A thermodynamic framework for the modeling of crystallizable shape memory polymers.* International Journal of Engineering Science, 2008. **46**(4): p. 325-351.

[51]. Xing, J., M. Radovic, and A. Muliana, *A nonlinear constitutive model for describing cyclic mechanical responses of $$\hbox {BaTiO} _ {3}/\hbox {Ag} $$ BaTiO 3/Ag composites.* Acta Mechanica, 2017. **228**(6).

[52]. Song, R., et al., *Hysteretic electro-mechanical coupling response of PZT fibers: Constitutive modeling and experiments.* Ferroelectrics, 2018. **526**(1): p. 95-119.

[53]. De Tommasi, D., G. Puglisi, and G. Saccomandi, *A micromechanics-based model for the Mullins effect.* Journal of Rheology, 2006. **50**(4): p. 495-512.

[54]. Ambrosi, D. and F. Mollica, *On the mechanics of a growing tumor.* International journal of engineering science, 2002. **40**(12): p. 1297-1316.

[55]. Muliana, A., K. Rajagopal, and D. Tscharnuter, *A nonlinear integral model for describing responses of viscoelastic solids.* International Journal of Solids and Structures, 2015. **58**: p. 146-156.

[56]. Muliana, A., et al., *A nonlinear viscoelastic constitutive model for polymeric solids based on multiple natural configuration theory.* International Journal of Solids and Structures, 2016. **100**: p. 95-110.

[57]. Burgert, I., *Exploring the micromechanical design of plant cell walls.* American journal of botany, 2006. **93**(10): p. 1391-1401.

[58]. Mayergoyz, I., *Mathematical models of hysteresis.* IEEE Transactions on magnetics, 1986. **22**(5): p. 603-608.

[59]. Mayergoyz, I.D., *Mathematical models of hysteresis and their applications*. 2003: Academic Press.

[60]. Köhler, L. and H.-C. Spatz, *Micromechanics of plant tissues beyond the linear-elastic range.* Planta, 2002. **215**(1): p. 33-40.

[61]. Spencer, A.J.M., *Continuum theory of the mechanics of fibre-reinforced composites*. Vol. 282. 1984: Springer.

[62]. Stoychev, G., et al., *Shape-programmed folding of stimuli-responsive polymer bilayers.* ACS nano, 2012. **6**(5): p. 3925-3934.

[63]. Stoychev, G., et al., *Hierarchical multi-step folding of polymer bilayers.* Advanced Functional Materials, 2013. **23**(18): p. 2295-2300.

[64]. Celli, P., et al., *Wave control through soft microstructural curling: bandgap shifting, reconfigurable anisotropy and switchable chirality.* Smart Materials and Structures, 2017. **26**(3): p. 035001.

[65]. Felippa, C.A. and B. Haugen, *A unified formulation of small-strain corotational finite elements: I. Theory.* Computer Methods in Applied Mechanics and Engineering, 2005. **194**(21-24): p. 2285-2335.

[66]. Tajeddini, V. and A. Muliana, *Deformations of flexible and foldable electro-active composite structures.* Composite Structures, 2017. **160**: p. 280-291.

[67]. Lendlein, A., et al., *Light-induced shape-memory polymers.* Nature, 2005. **434**(7035): p. 879-882.

[68]. Scott, T.F., et al., *Photoinduced plasticity in cross-linked polymers.* Science, 2005. **308**(5728): p. 1615-1617.

[69]. Long, K.N., et al., *Photo-induced deformation of active polymer films: Single spot irradiation.* International journal of solids and structures, 2011. **48**(14-15): p. 2089-2101.

[70]. Yuan, Z., A. Muliana, and K.R. Rajagopal, *Modeling the response of light-activated shape memory polymers.* Mathematics and Mechanics of Solids, 2017. **22**(5): p. 1116-1143.